

Phosphonic Acid-Containing Molecules as Proton Conductors and Linkers for Hybrid Materials

Dissertation zur Erlangung des Grades
“Doktor der Naturwissenschaften”
am Fachbereich Chemie, Pharmazie und Geowissenschaften
der Johannes Gutenberg-Universität Mainz

Lucía Jiménez García
geboren am 14. Mai 1984 in Madrid, Spanien
Mainz im Jahr 2011

Dedicated to my family

“The more *outré* and grotesque an incident is
the more carefully it deserves to be examined,
and the very point which appears to complicate a case is,
when duly considered and scientifically handled,
the one which is most likely to elucidate it.”

Sir Arthur Conan Doyle
(*The Hound of the Baskervilles*)

Contents

1	Introduction	1
1.1	The Phosphonic Acid Group as a Structural Motif	1
1.1.1	General Considerations.....	1
1.1.2	The Phosphonic Acid Group.....	2
1.2	Fuel Cell Technology	4
1.2.1	Principles of Fuel Cell Operation	4
1.2.2	Types of Fuel Cells.....	6
1.2.3	The Proton Transport Mechanisms.....	7
1.2.4	Proton-Conducting Materials for Intermediate Temperature Fuel Cells.....	11
1.2.5	Proton Conductivity Measurements	14
1.3	Phosphonic Acid based Organic-Inorganic Hybrid Materials	19
1.3.1	General Considerations.....	19
1.3.2	Physisorption of gases	19
1.3.3	Carboxylic Acid based MOFs	23
1.3.4	Phosphonic acid based organic-inorganic hybrid materials	24
1.4	Bibliography	28
2	Motivation and Objectives	33
2.1	Phosphonic Acid based Solid State Proton Conductors	33

2.2	Phosphonic Acid based Organic-Inorganic Hybrid Materials	37
2.3	Bibliography	40
3	Phosphonic Acid based Solid State Proton Conductors	41
3.1	Introduction.....	41
3.2	Hexakis(<i>p</i> -phosphonatophenyl)benzene	43
3.2.1	Synthesis and Characterization	43
3.2.2	Proton Conductivity	47
3.2.3	Thermal Stability.....	56
3.2.4	Water Uptake	59
3.2.5	Crystallinity.....	62
3.2.6	Acidity	71
3.2.7	Solid-State NMR Investigations	73
3.2.8	Summary.....	82
3.3	The Influence of Geometry and the Number of Acidic Functions.....	83
3.3.1	General Remarks	83
3.3.2	Synthesis and Characterization	84
3.3.3	Proton Conductivity	90
3.3.4	Water Uptake	95
3.3.5	Crystallinity.....	99
3.3.6	Solid-State NMR Investigations	103
3.3.7	Discussion.....	114
3.3.8	Summary.....	116
3.4	Substituted Hexaphenylbenzene Molecules.....	118
3.4.1	General Remarks	118
3.4.2	Hexakis(<i>m</i> -phosphonatophenyl)benzene.....	119

3.4.3	1,3,5-Tris(3,5-biphosphonatophenyl)-2,4,6-tris(4-dodecylphenyl)-benzene	128
3.4.4	Hexakis(<i>p</i> -sulfonatophenyl)benzene.....	139
3.4.5	Hexakis(3,5-biphosphonatophenyl)benzene.....	142
3.4.6	Summary.....	147
3.5	Expanding the Periphery of the Hexaphenylbenzene.....	149
3.5.1	General remarks.....	149
3.5.2	Para and Meta substituted Molecules.....	150
3.5.3	Hexakis[<i>p</i> -(3,5-bisphosphonatophenylethynyl)phenyl]benzene.....	167
3.5.4	Summary.....	168
3.6	Conclusions.....	170
3.7	Bibliography.....	172
4	Phosphonic Acid based Organic-Inorganic Hybrid Materials.....	175
4.1	Introduction.....	175
4.2	Synthesis.....	177
4.3	Structural Characterization.....	181
4.3.1	Infrared Spectroscopy.....	181
4.3.2	Thermal Analysis.....	184
4.3.3	Solid-State NMR.....	185
4.4	Morphology Characterization.....	188
4.4.1	X-Ray Analysis.....	188
4.4.2	Electron Microscopy.....	196
4.5	Textural Characterization.....	200
4.5.1	Divalent Metals as Connectors.....	200
4.5.2	Trivalent Metal as Connector.....	202
4.5.3	Tetravalent Metals as Connectors.....	207

4.6	Hydrogen Storage.....	212
4.6.1	Hydrogen as a Future Energy Carrier.....	212
4.6.2	The Storage of Hydrogen.....	212
4.6.3	Trisphosphonate Hybrid Materials for Hydrogen Storage.....	215
4.7	Discussion.....	217
4.7.1	Divalent Metals as Connectors.....	217
4.7.2	Aluminum as Connector.....	217
4.7.3	Tetravalent Metals as Connectors.....	219
4.8	Conclusion.....	221
4.9	Bibliography.....	223
5	Conclusions and Outlook.....	225
5.1	Solid State Proton-Conducting Materials.....	225
5.2	Linkers for Porous Hybrid Materials.....	228
6	Experimental Part.....	231
6.1	General Methods.....	231
6.1.1	Chemicals and Solvents.....	231
6.1.2	Chromatography.....	231
6.1.3	Inert Atmosphere.....	231
6.2	Analytical Techniques.....	232
6.2.1	Mass Spectrometry.....	232
6.2.2	NMR Spectroscopy.....	232
6.2.3	Elemental Analysis.....	232
6.2.4	Infrared Spectroscopy.....	232
6.2.5	X-Ray Scattering.....	233

6.2.6	Wide Angle X-Ray Scattering	233
6.2.7	Two-Dimensional Wide Angle X-Ray Scattering	233
6.2.8	Thermal Gravimetric Analysis	233
6.2.9	Melting Points	233
6.2.10	Single Crystal Analysis	234
6.2.11	Impedance Spectroscopy	234
6.2.12	Water Uptake	234
6.2.13	Potentiometric Titration	235
6.2.14	Nitrogen Sorption	235
6.2.15	Electron Microscopy	235
6.3	Hexakis(<i>p</i> -phosphonatophenyl)benzene	236
6.3.1	Bis(4-diethylphosphonatophenyl)acetylene	236
6.3.2	Hexakis(<i>p</i> -diethylphosphonatophenyl)benzene	236
6.3.3	Hexakis(<i>p</i> -phosphonatophenyl)benzene	237
6.4	The Influence of Geometry and the Number of Acidic Functions	238
6.4.1	4,4'-Diiido- <i>p</i> -terphenyl ^[4]	238
6.4.2	4,4'-Diethylphosphonato- <i>p</i> -terphenyl	238
6.4.3	(<i>p,p'</i> -Terphenyl-4,4''-diyl)bisphosphonic acid	239
6.4.4	1,3,5-Tris(<i>p</i> -diethylphosphonatophenyl)benzene	240
6.4.5	1,3,5-Tris(<i>p</i> -phosphonatophenyl)benzene	240
6.4.6	1,3,5-Tris-2'-bromophenylbenzene ^[5]	241
6.4.7	1,3,5-Tris[4''-(trimethylsilyl)-2'-biphenyl]ylbenzene ^[5]	242
6.4.8	1,3,5-Tris[4''-(iodo)-2'-biphenyl]ylbenzene ^[5]	242
6.4.9	1,3,5-Tris[4''-(diethylphosphonato)-2'-biphenyl]ylbenzene	243
6.4.10	1,3,5-Tris[4''-(phosphonato)-2'-biphenyl]ylbenzene	244
6.4.11	1,2,4,5-Tetrakis(4-trimethylsilylphenyl)benzene	244
6.4.12	1,2,4,5-Tetrakis(<i>p</i> -iodophenyl)benzene	245

6.4.13	1,2,4,5-Tetrakis(<i>p</i> -diethylphosphonatophenyl)benzene	245
6.4.14	1,2,4,5-Tetrakis(<i>p</i> -phosphonatophenyl)benzene	246
6.4.15	1,3,5,7-Tetrakisphenyladamantane ^[6]	247
6.4.16	1,3,5,7-Tetrakis(<i>p</i> -iodophenyl)adamantane ^[6]	248
6.4.17	1,3,5,7-Tetrakis(<i>p</i> -diethylphosphonatophenyl)adamantane ^[7]	249
6.4.18	1,3,5,7-Tetrakis(<i>p</i> -phosphonatophenyl)adamantane	250
6.5	Substituted Hexaphenylbenzene Molecules	251
6.5.1	((3-Bromophenyl)ethynyl)trimethylsilane.....	251
6.5.2	1-Bromo-3-ethynylbenzene	251
6.5.3	1,2-Bis(3-bromophenyl)ethyne	252
6.5.4	1,2-Bis(3-diethylphosphonatophenyl)ethyne	252
6.5.5	Hexakis(<i>m</i> -diethylphosphonatophenyl)benzene	253
6.5.6	Hexakis(<i>m</i> -phosphonatophenyl)benzene.....	254
6.5.7	[(4-Dodecylphenyl)ethynyl]trimethylsilane.....	254
6.5.8	1-Dodecyl-4-ethynylbenzene	255
6.5.9	1,3-Dibromo-5-[(4-dodecylphenyl)ethynyl]benzene	255
6.5.10	Tetraethyl 5-[(4-dodecylphenyl)ethynyl]-1,3- phenylene	256
	diphosphonate.....	256
6.5.11	1,3,5-Tris(3,5-bidiethylphosphonatophenyl)-2,4,6-tris(4-	257
	dodecylphenyl)-benzene	257
6.5.12	1,3,5-Tris(3,5-biphosphonatophenyl)-2,4,6-tris(4-dodecyl	258
	phenyl)-benzene	258
6.5.13	Hexaphenylbenzene hexasulfonyl chloride ^[8]	259
6.5.14	Hexakis(<i>p</i> -sulfonatophenyl)benzene	259
6.5.15	[(3,5-Dibromophenyl)ethynyl]trimethylsilane.....	260
6.5.16	1,3-Dibromo-5-ethynylbenzene	260
6.5.17	1,2-Bis(3,5-dibromophenyl)ethyne	261

6.5.18	Octaethyl 5,5'-(ethyne-1,2-diyl)bis(benzene-5,3,1-triyl)	261
	tetraphosphonate	261
6.6	Expanding the Periphery of the Hexaphenylbenzene	263
6.6.1	Diethyl 4-[(trimethylsilyl)ethynyl]phenylphosphonate	263
6.6.2	Diethyl 4-ethynylphenylphosphonate	263
6.6.3	Hexakis[<i>p</i> -(<i>p</i> -diethylphosphonatophenylethynyl)phenyl]	264
	benzene	264
6.6.4	Hexakis[<i>p</i> -(<i>p</i> -phosphonatophenylethynyl)phenyl]benzene	265
6.6.5	Diethyl 3-[(trimethylsilyl)ethynyl]phenylphosphonate	266
6.6.6	Diethyl 3-ethynylphenylphosphonate	266
6.6.7	Hexakis[<i>p</i> -(<i>m</i> -diethylphosphonatophenylethynyl)phenyl]	267
	benzene	267
6.6.8	Hexakis[<i>p</i> -(<i>m</i> -phosphonatophenylethynyl)phenyl]benzene	268
6.6.9	Tetraethyl 5-[(trimethylsilyl)ethynyl]-1,3-phenylene	269
	diphosphonate.....	269
6.6.10	Tetraethyl 5-ethynyl-1,3-phenylenediphosphonate.....	269
6.7	Crystal Structures	271
6.7.1	Hexakis(<i>p</i> -diethylphosphonatophenyl)benzene (3)	271
6.7.2	Hexakis(<i>p</i> -phosphonatophenyl)benzene (4)	272
6.7.3	(<i>p,p'</i> -Terphenyl-4,4''-diyl)bisphosphonic acid (9).....	273
6.7.4	Hexakis[<i>p</i> -(<i>p</i> -diethylphosphonatophenylethynyl).....	274
	phenyl]benzene (58).....	274
6.8	Phosphonic Acid based Organic-Inorganic Hybrid Materials	275
6.8.1	Copper based Organic-Inorganic Hybrid Materials	275
6.8.2	Zinc based Organic-Inorganic Hybrid Materials	276
6.8.3	Aluminum based Organic-Inorganic Hybrid Materials	277
6.8.4	Zirconium based Organic-Inorganic Hybrid Materials	278

6.8.5 Tin based Organic-Inorganic Hybrid Materials	279
6.10 Bibliography	280
7 List of Publications	281

Index of Abbreviations

2D-WAXS	two-dimensional wide-angle X-ray scattering
a.c.	alternating current
AFC	alkaline fuel cell
BaBa	back-to-back
BET	<i>Brunauer, Emmett and Teller</i>
COF	covalent organic framework
CP	cross polarization
d	doublet (NMR)
d.c.	direct current
DCM	dichloromethane
DFT	density functional theory
DMAP	<i>p</i> -dimethylaminopyridine
DMFC	direct methanol fuel cell
DMSO	dimethylsulfoxide
dppe	1,2-bis(diphenylphosphino)ethane
EIS	electrochemical impedance spectroscopy
Et	ethyl
FC	fuel cell
FD	field desorption
FTIR	Fourier transform infrared spectroscopy
GPC	gel permeation chromatography
h	hour
HCP	hypercrosslinked polymer
HPB	hexaphenylbenzene

HPLC	high performance liquid chromatography
IS	impedance spectroscopy
PBI	polybenzimidazole
m	multipllett (NMR)
MAS	magic angle spinning
MCFC	molten carbonate fuel cell
MEA	membrane electrode assembly
min	minute
MOF	metal-organic framework
MS	mass spectrometry
NMP	N-methylpyrrolidinone
NMR	nuclear magnetic resonance
PAFC	phosphoric acid fuel cell
PEEK	poly(ether ether ketone)
PEFC	polymer electrolyte fuel cell
PEM	proton-exchanging membrane
Ph	phenyl
PIM	polymers of intrinsic microporosity
ppm	parts per million
PVPA	poly(vinylphosphonic acid)
PVTz	poly(vinyl triazole)
q	quartet (NMR)
REPT-HSQC	recoupled polarization transfer-heteronuclear single-quantum correlation
RH	relative humidity
RT	room temperature
s	singlet (NMR)
SAXS	small angle X-ray scattering
SEM	scanning electron microscopy
SOFC	solid oxide fuel cell
SPE	single pulse excitation
t	triplet (NMR)
TBAF	tetra-iso-butyl ammonium fluoride
TEM	transmission electron microscopy

THF	tetrahydrofuran
TGA	thermo-gravimetric analysis
TMS	trimethylsilyl-
tt	triplet of triplets (NMR)
VT	variable temperature
WAXS	wide angle X-ray scattering

1 Introduction

1.1 The Phosphonic Acid Group as a Structural Motif

1.1.1 General Considerations

Organic compounds possessing $-P(O)(OH)_2$ groups are called phosphonic acids (see Figure 1.1). 2-Aminoethylphosphonic acid is the first identified natural phosphonate whereas bis- or polyphosphonates are not naturally occurring. 2-Aminoethylphosphonic acid was first identified in 1959 in plants and many animals, where it is localized in membranes.^[1-5] Phosphonates are quite common among different organisms, like fungi and mollusks, however their biological role is still poorly understood.^[6]

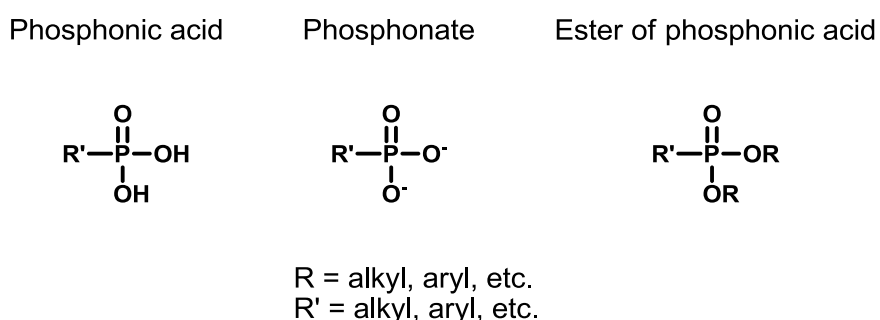


Fig. 1.1: General chemical structure of phosphonic acids, phosphonates and esters of phosphonic acid.

Phosphonates can be used for medical and non-medical applications. In pharmacology, bisphosphonates (or diphosphonates) are a class of drugs preventing the loss of bone mass applied to treat osteoporosis and similar diseases.^[7-9] Bisphosphonates were first synthesized in 1897 by *von Baeyer* and *Hofmann*. Most recently phosphonates have found to serve as carriers for radionuclides in bone cancer

treatments.^[10, 11] Another application of phosphonates is as chelating agents to prevent the formation of insoluble precipitates (also called scale). Phosphonates can bind tightly to di- and trivalent metal ions and have therefore an important industrial use in cooling waters, desalination systems and in oil fields to inhibit scale formation.^[12, 13] Furthermore in pulp and paper manufacturing and in textile industry they serve as "peroxide bleach stabilizers," by chelating metals that could inactivate the peroxide.^[14] In detergents they are used as a combination of chelating agent, scale inhibitor and bleach stabilizer.^[15] Besides, phosphonic acid is also employed as an anchor group to bind a wide range of molecules to surfaces like e.g. small molecules and polymers to metal oxide surfaces.^[16-18]

1.1.2 The Phosphonic Acid Group

As can be observed in Table 1.1, the chemical and physical properties of the divalent phosphonic acid differ distinctly from those of the monovalent carboxylic and sulfonic acid.

Table 1.1: Properties of aromatic carboxylic, sulfonic and phosphonic acids.^[19]

Property	Phenyl-COOH*	Phenyl-SO ₃ H	Phenyl-PO ₃ H ₂
Melting point (°C)**	121	85 ^[20]	170 ^[21]
Boiling point (°C)	249 (ambient pressure)	171 ^[22] (13 mbar)	n.a. (decomposition)
pK _a (in water)	4.2	- 0.7	1.8 / 7.0 ^[23]
Water solubility*** (g)	2.9	93 ^[24]	47 ^[19]

* MSDS-Data sheet; ** anhydrous form; *** per 100 mg solution at RT

When compared to the carboxylic acid group, the phosphonic acid moiety is of superior acid strength; however it possesses a lower dissociation constant (higher pK_a) than the sulfonic acid group. This means that the number of available charge carriers will be lower in the case of phosphonic acid derivatives compared to the sulfonic acid compounds.

The rise of the melting points in the series sulfonic < carboxylic < phosphonic acid is an evidence of the increase of polarity and/or hydrogen bonding in the same order. The high melting point of phenylphosphonic acid as well as its involatility are attributed to its high capacity to form hydrogen bonds (see Figure 1.2). An additional benefit of

hydrogen bonded networks of phosphonic acid groups is the possibility of cooperative proton transport phenomena. Therefore phosphonic acid-containing polymers have found applications as proton conductors in fuel cell membranes.^[25]

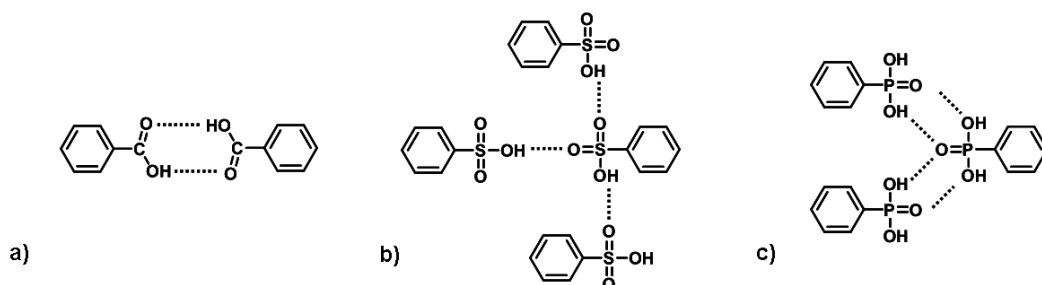


Fig. 1.2: Schematic illustration of the hydrogen bonding in a) phenylcarboxylic acid, b) phenylsulfonic acid and c) phenylphosphonic acid.

However, there is also another type of non-covalent interaction which comprises phosphonic acid based molecules and gives rise to networks exhibiting porous properties. In this case, the interaction is ionic and involves a phosphonated species and a metal cation. These ionic networks, called phosphonic acid based organic-inorganic hybrid materials, have centered the interest of many research groups on account of their porous properties and their potential for rational design of their structure and functionality.^[26]

Thus it can be deduced that phosphonic acid based small molecules can form two types of non-covalent networks:

- Hydrogen bonded networks: they are formed due to the hydrogen bonds between phosphonic acid-containing molecules. Within these networks it is possible to have a cooperative proton transport phenomena so that the materials could be used as proton conductors for fuel cells. This topic is introduced in Section 1.2 and treated in Chapter 3.
- Ionic networks: they are formed due to the ionic interactions between a negatively charged phosphonic acid-containing molecule and a positively charged metal cation. Porous solids are obtained. This topic is introduced in Section 1.3 and treated in Chapter 4.

1.2 Fuel Cell Technology

The objective of this section is to present the general function of a fuel cell as well as the different proton transport mechanisms which can take place through the membrane. Moreover, the various types of proton conductors which can be used as separator materials are also described with an emphasis on phosphonic acid based polymers.

1.2.1 Principles of Fuel Cell Operation

Fuel cells (FCs) may help to reduce our dependence on fossil fuels and diminish poisonous emissions into the atmosphere because by using pure hydrogen, they only produce water.^[27]

FCs are one of the oldest electrical energy conversion technologies known to man. However, even if they were described in the first century by *C. F. Schönbein*,^[28] their development was impeded during the first century due to the abundance of unrestricted and inexpensive primary energy sources. The first successful technical application of the FC was the use of alkaline fuel cells (AFC) in the NASA Gemini space program during 1960 - 1965.

A FC is a single-step energy conversion device. As in other electro-chemical devices, the physical detachment of electron and ion flux of a redox reaction provides an electric current. Even if there is a variety of FCs, they all obey to the same principle (Figure 1.3). An electrolyte, which can be either a solid or a liquid, is sandwiched between two electrodes. Its nature varies with the type of FC but it should be fuel-impermeable but ion-conductive. Oxygen is flushed at the cathode while at the anode hydrogen or a hydrocarbon fuel (e.g. methanol) is split into electrons and protons taking different pathways to the cathode. The electrons create an usable electric current, and the protons pass through the electrolyte to be recombined with the electrons at the cathode and provided oxygen to produce water, electricity and heat.

In a FC, the combination of electrolyte, catalyst and electrodes is called membrane electrode assembly (MEA) (see Figure 1.3).

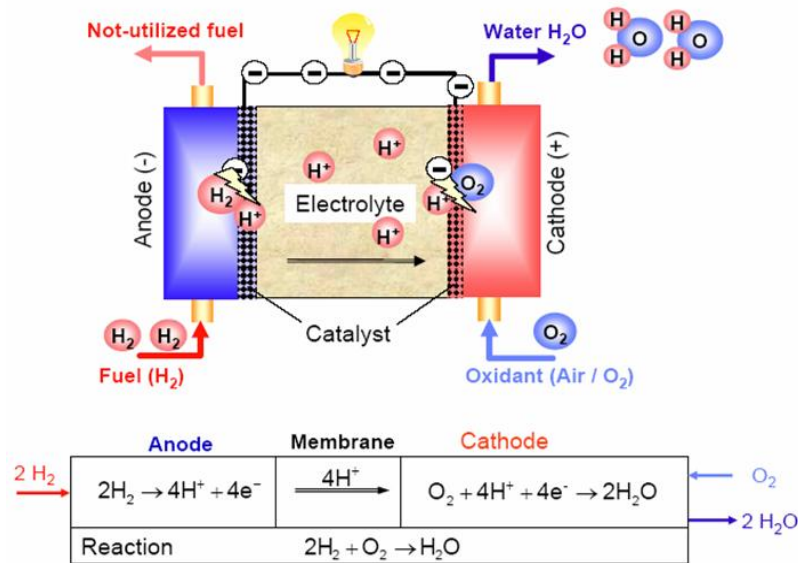


Fig. 1.3: Schematic diagram of a MEA.

In contrast to a detonating gas reaction, the electrochemical reaction between hydrogen and oxygen taking place in a FC is controlled and produces not only thermal but electrical energy.

Commonly discussed FC fuels are hydrogen and methanol, the overall electrode reactions of which are given in Table 1.2.

Table 1.2: Reactions at the anode and the cathode in two FC types.

	PEMFC (polymer electrolyte fuel cell)	DMFC (direct methanol fuel cell)
Anode	$\text{H}_2 \rightarrow 2\text{H}^+ + 2\text{e}^-$	$\text{CH}_3\text{OH} + \text{H}_2\text{O} \rightarrow \text{CO}_2 + 6\text{H}^+ + 6\text{e}^-$
Cathode	$0.5\text{O}_2 + 2\text{H}^+ + 2\text{e}^- \rightarrow \text{H}_2\text{O}$	$1.5\text{O}_2 + 6\text{H}^+ + 6\text{e}^- \rightarrow 3\text{H}_2\text{O}$

Four important features must be taken into account when designing a FC. The first one is the electrolyte substance, which usually defines the type of FC, followed by the fuel that is used (the most common is hydrogen). The two last characteristics are the electrodes catalysts: the anode catalyst, which breaks down the fuel into electrons and ions, is usually made up of very fine platinum powder whereas the cathode catalyst, which turns the ions into the waste chemicals like water or carbon dioxide, is frequently composed of nickel.

At full rated load, typically a FC produces a voltage from 0.6 V to 0.7 V. While increasing the current, a voltage decrease is observed. This is due to three factors: the activation loss, the ohmic loss (voltage drop due to resistance of the cell components and interconnects) and the mass transport loss (depletion of reactants at catalyst sites under high loads, causing rapid loss of voltage).^[29]

Often, a FC alone does not deliver the desired amount of energy, therefore FCs are combined in series and parallel circuits. Such a design is called a FC stack. Stacking the cells in series yields higher voltage whereas cells stacked in parallel allow a higher current to be supplied. The cell surface area can be increased to allow stronger current from each cell. The potential power generated by a FC stack depends on the number and size of the individual fuel cells that comprise the stack and the surface area of the MEA.

1.2.2 Types of Fuel Cells

FCs are principally divided into two groups based on their operating temperature, which is imposed by the electrolyte: the low ($T \leq 120^\circ\text{C}$) and high temperature ($T = 600 - 1000^\circ\text{C}$) types (Table 1.2).^[30] Low-temperature FCs are the Alkaline Fuel Cell (AFC), the Polymer Electrolyte Fuel Cell (PEFC), the Direct Methanol Fuel Cell (DMFC) and the Phosphoric Acid Fuel Cell (PAFC). There are two types of high-temperature FC: the Molten Carbonate Fuel Cell (MCFC) and the Solid Oxide Fuel Cell (SOFC). Except for the Direct Methanol Fuel Cell (DMFC), names are derived from the employed electrolyte.^[28]

Three problems presented by FCs operating at low temperatures must be addressed:^[25, 31]

- The use of expensive platinum and platinum alloys catalysts to promote the electrochemical reactions at the electrodes;
- The requirement of hydrogen of high purity (i.e. without any CO present);
- The complicated water and heat management.

The limited operation temperature makes it necessary to use expensive platinum and platinum alloy catalysts to promote the electrochemical reactions at the electrodes. But even with platinum, only hydrogen of high purity can be converted at sufficient rates. At low temperature, the rates of oxidation of methanol (which is frequently considered as an environmentally friendly fuel) are not high enough and even traces of

CO present in hydrogen rich reformats poison platinum based catalysts by absorbing on and thus blocking the reaction sites.^[32] The CO poisoning effect has been shown to be very temperature-dependent, i.e., CO adsorption is less pronounced with increasing temperature. For example, at 80 °C, the typical operational temperature of a PFSA polymer membrane electrolyte fuel cell, a CO content as low as 20 ppm in the fuel steam will result in a significant loss in the cell performance. As a consequence very pure hydrogen is needed for operation of PEFCs. In the case of high temperature FCs, no CO poisoning is observed, while cheaper catalysts like nickel can be used.^[33] The humidification requirements, along with the high electroosmotic drag of water and methanol in conventional proton-exchanging membranes complicate the water and heat management and lead to a significant chemical short-circuiting, i.e. parasitical chemical oxidation of methanol at the cathode.

Therefore, the overall performance and cost efficiency of the FC system can be expected to be significantly improved by operating the FC at high temperatures since this fact increases the kinetics of the electrode reactions, reduces the risk of catalyst poisoning, lowers the amount of catalyst needed and reduces cathode flooding.^[34]

Table 1.3: Overview of the different types of FC and their characteristics.^[27]

FC type	Electrolyte	Charge carrier	Fuel/Oxidant	T _{op} (°C)	Efficiency (%)	Application Output
AFC	30 % KOH	OH ⁻	high grade H ₂ / O ₂	80 - 90	60 - 70	space 5 - 150 kW
PEFC	Polyelectrolyte	H ⁺	high grade H ₂ / air	80 +	50 - 70	mobile 5 - 250 kW
DMFC	Polyelectrolyte	H ⁺	CH ₃ OH / air	60 +	50 - 70	mobile 5 kW
PAFC	100 % H ₃ PO ₄	H ⁺	techn. H ₂ / air	200	55	stationary 50 kW +
SOFC	ZrO ₂ /Y ₂ O ₃	O ₂ ⁻	CH ₄ , H ₂ / air	650	65	stationary 100 kW +
MCFC	Na ₂ CO ₃ /K ₂ CO ₃	CO ₃ ²⁻	CH ₄ , H ₂ / air	800 - 1000	60 - 65	stationary 100 - 250 kW

1.2.3 The Proton Transport Mechanisms

Proton conductivity and mobility have been extensively studied by chemists, physicists as well as biologists due to their importance in chemical (like electricity

generation in a hydrogen FC), as well as in biological processes (like photosynthesis or adenosine 5'-triphosphate (ATP) production^{[35],[36]}).

Two sorts of proton transport mechanisms have been detailed in the literature^[37, 38]: the vehicle mechanism^[39] and the *Grotthuss*-type mechanism^[40], also called structure diffusion. In most of the cases, both types contribute to the overall proton transport. In this section, the two types of mechanisms are described.

The vehicle mechanism implies the diffusion of hydrated protons or proton containing groups (e.g. H_3O^+ , NH_4^+) as a whole in a medium of low viscosity and high diffusion coefficient such as water. Actually it should be noted that the inherent protonic charge carriers (H^+) are solvated by little number of species. The most known are water (in hydrated polymeric membranes like Nafion®)^[41] and oxo-acids like phosphoric acid (in basic membranes containing doped with phosphoric acid).^[42] However, other kinds of species are also able to solvate protons, like e.g. oxo-acid anions (in CsHSO_4)^[43-48] and heterocycles (intercalated into acidic polymers^[49] or immobilized via flexible spacers^[50]).

Since hydrogen bonding is a common characteristic of all these species, it is logical to think that it is also the key to understand long-range proton transport in these environments. Strong and weak hydrogen bonding are at the same time needed for proton transport: strong hydrogen bonding is considered as a precursor of proton transfer reactions^[51] whereas long-range proton transfer is only likely to occur in weakly hydrogen bonded systems.

One also has to keep in mind that the self-diffusion coefficient of the species able to solvate protons plays an important role in the vehicle mechanism. Species with high self-diffusion coefficient will allow a faster proton transport than species which possess lower self-diffusion coefficient.

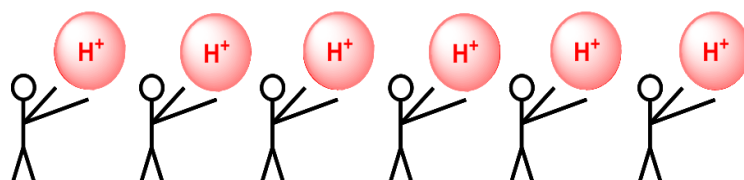


Fig. 1.4: Schematic illustration of the proton conductivity based on the vehicle mechanism for proton conduction.

It can be concluded that in the case of the vehicle mechanism:

- The charge transport is equivalent to the mass transport;
- The transport of protons is influenced by the electrolyte viscosity;
- Size effects have a strong influence on mobility (importance of the hydration shell).

The *Grotthuss*-type mechanism, also called structure diffusion or intrinsic proton conductivity, consists of the diffusion of protonic defects (inherent protonic charge carriers).

Protons have an unusual high mobility in water, which is at ambient conditions nine times higher than that for Li^+ and five times higher than that for K^+ . The theory of water conductivity was first proposed by *De Grotthuss* in 1806,^[52] who described it as a 'bucket line' where each oxygen atom simultaneously passes and receives a single hydrogen atom. Even if in *De Grotthuss* description the empirical formula of water was incorrect, he depicted the cooperative proton transport between neighboring water molecules in a very clairvoyant way.

Since the *Grotthuss* theory, water conductivity has been extensively studied.^[53, 54] *Eigen* and *De Meyer* demonstrated that the rate-limiting step is the "structure diffusion" in which the excess proton is "tunneling" back and forth.^[55, 56] The region with a single excess proton within the hydrogen-bond network (protonic defect) corresponds to either a *Zundel* ion or an *Eigen* ion (see Figure 1.5), which are limiting configurations. This type of mechanism is termed "structure diffusion", as suggested by *Eigen*, because the protonic charge follows a propagating hydrogen-bond arrangement or structure.

However, in the case of proton mobility in water, the hydrodynamic diffusion of protonated water clusters (vehicle mechanism) plays also a role due to the high diffusion-coefficient of the medium and the mechanism cannot only be described, as it has been done for many years in classical textbook explanations, as being only *Grotthuss*-type.^[37, 54]

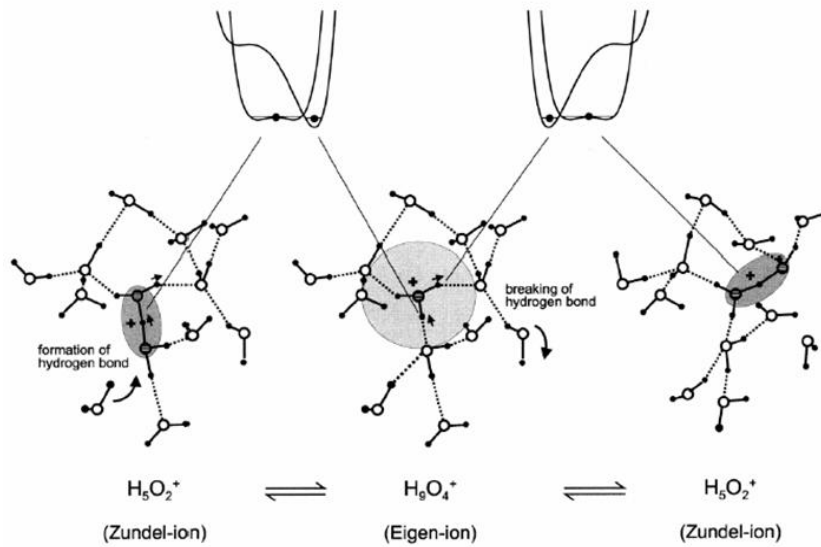


Fig. 1.5: Schematic representation of the “structure diffusion” of a protonic defect in water.^[37]

Protonic defects can be either generated extrinsically by doping with a *Brønsted* acid or base or intrinsically by self-dissociation of the species participating in their solvation (e.g. phosphoric acid and imidazole^[25, 57]). As above mentioned, the protonic defects diffuse through the medium by hydrogen-bond breaking and forming processes. In the particular case of a solid, the vehicle mechanism consists of the formation of an ion adduct composed of a proton and a diffusible carrier molecule (e.g. H_2O). On the contrary, the *Grotthuss*-type mechanism in a solid is the transport of protons from site to site without a carrier molecule, its activation energy depending on the hydrogen bond breaking energy and the distance between hopping sites.^[40]

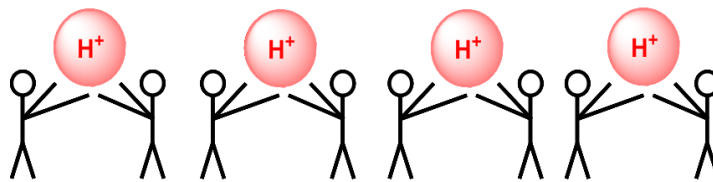


Fig. 1.6: Schematic illustration of proton conductivity based on the *Grotthuss*-type mechanism for proton conduction.

It can be concluded that in the case of the *Grotthuss*-type mechanism for proton conduction:

- The charge transport is decoupled from the mass transport;
- The charge transport is independent of the hydration shell.

1.2.4 Proton-Conducting Materials for Intermediate Temperature Fuel Cells

Proton-conducting membranes for intermediate-temperature FC have found applications in three main fields: automotive, stationary and portable power. Even if the operating conditions and material demands are unique for each of the implementation fields, all membranes must meet the following requirements:^[58, 59]

- High proton conductivity (around $1 \cdot 10^{-1}$ S/cm);
- Low electron conductivity;
- Constant performance;
- Low permeability with respect to fuel and oxidant;
- Low water transport through diffusion and electro-osmosis;
- High chemical (oxidative and hydrolytic) and mechanical stability for long-term operation under severe conditions (over 2000 h for electric vehicle applications);
- Low cost;
- Capability for fabrication into MEAs.

The current state-of-the-art membrane materials for PEFC are perfluorinated sulfonic acids (PFSA). The polymers possess a perfluorinated main chain like Teflon and side chains containing sulfonic acid groups. They are produced from different companies; a summary is presented in Table 1.4.

Table 1.4: Overview of the different types of perfluorinated sulfonic acid membranes.^[33]

Company	Name	Chemical structure	
DuPont	Nafion®	$\left(\text{CF}_2-\text{CF}_2 \right)_x \left(\text{CF}-\text{CF}_2 \right)_y$ $\left(\text{O}-\text{CF}_2-\text{CF} \right)_z \text{O}(\text{CF}_2)_2\text{SO}_3\text{H}$	$x = 6 - 10; y = z = 1$
Asahi Glas	Flemion®		
Asahi Chemicals	Acidiplex®	$\left(\text{CF}_2-\text{CF}_2 \right)_x \left(\text{CF}-\text{CF}_2 \right)_y$ $\left(\text{O}-\text{CF}_2-\text{CF} \right)_z \text{O}(\text{CF}_2)_2\text{SO}_3\text{H}$ CF_3	
Dow Chemical	Dow®	$\left(\text{CF}_2-\text{CF}_2 \right)_x \left(\text{CF}-\text{CF}_2 \right)_y$ $\text{O}-(\text{CF}_2)_2\text{SO}_3\text{H}$	$x = 3 - 10; y = 1$

Almost all commercially available membranes are based on Nafion®, which presents moreover the largest number of literature studies and was originally

developed as anion-impermeable separator in chlorine-alkali-electrolysis. These membranes present excellent long-term chemical stability due to the Teflon-like polymer backbone (demonstrated lifetime of Nafion® under FC conditions: 60 000 h). Moreover, they possess good mechanical properties and very high proton conductivity. In the case of Nafion®, values of 40 MPa tensile strength at 23°C and 50 % relative humidity and of 0.1 S/cm for the proton conductivity at full hydration have been achieved.^[34, 60]

However, one of the major disadvantages of this kind of membrane materials is that at elevated temperatures the performance decreases. At low water contents (or high temperatures), the proton conductivity diminishes and the membrane loses its mechanical strength). This is due to the proton transport mechanism taking place through the membrane. Small angle X-ray scattering (SAXS) experiments have revealed that the materials consist of interpenetrating nanophase-separated apolar backbone and polar ionic domains.^[49] The perfluorinated backbone provides high hydrophobicity while the sulfonic acid functional groups are responsible for the hydrophilicity. In the presence of water, this gives rise to some hydrophobic/hydrophilic nano-separation. Proton conductivity assisted by water dynamics occurs through the channels within the hydrophilic domains, thus the vehicle mechanism is responsible for the proton transport through these types of membranes. Therefore, when water is lost due for example to a temperature increase, the performance drops down. On the other hand, the hydrophobic domain is responsible for the morphological stability of the polymer and prevents it from dissolving in water.

Poly(perfluorosulfonic acid) membranes present then several disadvantages like the high humidification conditions required which complicate heat management, water and methanol cross-over as a reason of the electroosmotic drag, high cost (target: 20 \$/m², currently: 200 - 600 \$/m²) and the common problem of CO poisoning which has been above mentioned. Moreover at high temperatures, desulfonation, i.e. the loss of the sulfonic acid unit through hydrolysis, may become a critical issue.^[34] Therefore the search for alternative protogenic groups has increased in the past years. The ideal protogenic group should exhibit the following characteristics:^[58, 59]

- Proton donor and acceptor properties (it should be amphoteric);
- High degree of self-dissociation;
- High dielectric constant to enhance charge separation;
- Tendency to form hydrogen bonds;
- Stability under FC operation conditions.

The carboxylic acid moiety -COOH has been investigated in the form of perfluorocarboxylic polyelectrolytes^[61] and carboxylated copoly(arylene sulfone)s.^[62, 63] However, the conductivity of both ionic materials was reported to be insufficient for FC operations. This is most probably due to the low acid strength (pKa of benzoic acid = 4.2).

Aromatic heterocycles, e.g. imidazole, pyrazole and benzimidazole are interesting alternatives to acid moieties.^[64] These hydrogen bonding substances and their more leaching resistant oligomers^[65] has been examined as non-volatile, ion-conductive liquids in sulfonated polyelectrolytes. However, as above mentioned upon immobilization of the moieties the obtained materials do not give conductivities high enough for FC operation.

Among the few remaining acidic moieties capable of bonding to organic substrates, the phosphonic acid group has been intensely discussed as alternative for proton conductive polyelectrolytes.^[25, 59, 66-73] In order to identify the most suitable proton solvent for PEFC working at intermediate temperatures, sulfonic acid, phosphonic acid, and imidazole functionalized model compounds with an identical alkyl chain were compared in terms of their proton conductivity, proton diffusion coefficient, thermo-oxidative and electrochemical stability.^[25, 31] From these studies, it can be stated that the phosphonic acid based compound exhibited the most advantageous behavior under low humidity conditions and at intermediate temperatures. The sulfonic acid functionalized model compound showed low conductivity in its dry state, which was expected from a highly proton donating (acidic), but poor proton accepting (basic) property of the sulfonic acid function. The imidazole based system displayed the largest electrochemical stability window, but its conductivity and thermo-oxidative stability were low. Phosphonic acid based systems offer the possibility to obtain high proton conductivities over a wide temperature range between RT to 200 °C. After the drying of the material at higher temperatures, the proton conduction mechanism may be dominated by structure diffusion within a hydrogen bonded network formed by phosphonic acid functionality alone. Phosphonic acid based systems proved to have a high number of charge carrier as expected from its pronounced amphoteric character.

Even though phosphonic acid units are less acidic than sulfonic acid units, ionomers with these alternative moieties have higher chemical and thermal stabilities than sulfonic acid-based.^[74] Phosphonic acid-containing aliphatic or semi-aliphatic^[73, 86-88] and fluoro- or perfluoroaliphatic^[61, 66, 67, 72, 74] polymers have been mostly synthesized by the radical polymerization of phosphonated monomers. The use of the materials as

proton conductors,^[61, 74, 75] protective metal coatings^[76] and ion exchange materials^[77] has been investigated. Since the aliphatic and semi-aliphatic phosphonated polymers do not present long-term stability to FC conditions, this material class will not be discussed further. On the other hand, perfluorophosphonic polyelectrolytes present relatively high proton conductivities (at 80 °C between $6 \cdot 10^{-3}$ and $7.6 \cdot 10^{-2}$ S/cm, while the conductivity of Nafion® under the same conditions is of $7 \cdot 10^{-3}$ - 0.1 S/cm) but due to the high price inherent to perfluorinated backbones the materials have not been commercialized.^[61, 74]

Arylphosphonic acid-functionalized polyelectrolytes have been recognized as attractive candidates to replace poly(perfluorosulfonic acid) membranes as PEMFC.^[19] The aromatic phosphonated polyelectrolytes present high proton conductivity, unusually low water uptake at elevated temperatures and good resistance to fuel permeation.^[25, 38, 68, 78-83] The nickel catalyzed arylphosphonation of brominated educts in non-coordinating solvents was found to be the best preparative approaches due to the high reaction yields, the economy of the catalyst and attainable degrees of functionalization.^[19]

Studies on non-aromatic polyelectrolytes containing phosphonic acid groups such as poly(vinylphosphonic acid) (PVPA) have been also performed.^[68, 84-86] The polymer was obtained by free radical polymerization of vinylphosphonic acid. The material exhibits high proton conductivity ($1 \cdot 10^{-3}$ S/cm at 150 °C under 1 bar H₂O atmosphere), limited however by condensation reactions between the phosphonic acid groups.^[86] Moreover, even after annealing and drying the material, water (free water and self-condensation water) takes part in the conductivity mechanism. This material can therefore not be seen as alternative to poly(perfluorosulfonic acid) membranes since it requires high water content to achieve high proton conductivity.

1.2.5 Proton Conductivity Measurements

To determine the proton conductivity properties of electrolytes impedance spectroscopy (IS) measurements are commonly performed. While formerly conductivity was measured by direct current (d.c.) techniques using reversible electrodes (e.g. H_xTi, H_xPd) and low voltages or just by electrolyzing the sample at voltages above the decomposition potential, nowadays alternating current (a.c.) impedance spectroscopy is a standard method for the measurement of ionic conductivities in general.^[87]

The electrical impedance describes a measure of opposition to an alternating current and extends the concept of resistance to a.c. circuits. When the circuit is driven

with direct current there is no distinction between impedance and resistance, however when the current applied is alternating, one talks about impedance. The impedance describes not only the relative amplitudes of the voltage and current but also the relative phases whereas the resistance can be seen as impedance with zero phase angle.^[88] Two main categories of IS have been described in the literature.^[88] The first type is called electrochemical IS (EIS) and involves measurements and analysis of materials in which ionic conduction strongly predominates. EIS is valuable in the study of FCs and rechargeable batteries. The remaining category of IS applies to dielectric materials: solid or liquid nonconductors whose electrical characteristics involve dipolar rotation, and to materials with predominantly electronic conduction.

Alternating current EIS makes use of an alternating current to measure the electric properties of a sample. By this method, information not only about the long range migration of ions but also about the polarization phenomena occurring within the cell, such as relaxation of the trapped ions, is obtained. The measurements can be performed either in-plane or through-plane as a function of the material. In case of polymer films, the inert electrodes are most commonly placed at the two ends of the film (in-plane measurements). To obtain a membrane, the sample has to be dissolved in a suitable solvent and afterwards it has to be coated on a surface. In the case of solid materials with no film-forming properties, pellets are pressed and sandwiched between the two inert electrodes (through-plane measurements). To ensure efficient contact to the electrodes, the rough surface of the pellet has to be sputtered with gold. However, since in the majority of the cases the recycling of the material is desired, flexible carbon cloth electrodes loaded with platinum particles are used to ensure the contact. In both in- and through-plane measurements, the application of an external current leads to a flow of protons through the material towards the other electrode (see Figure 1.7).

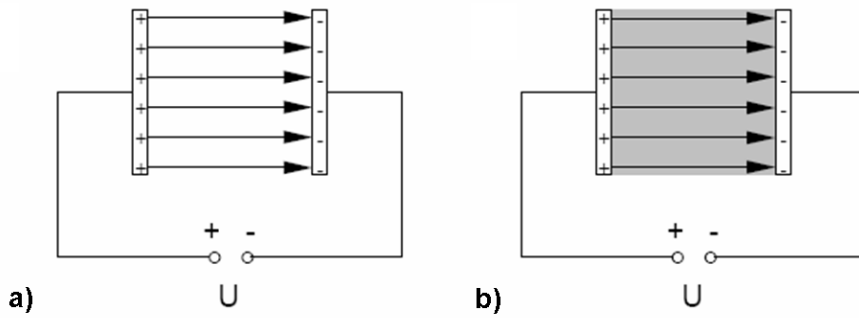


Fig. 1.7: Schematic pictures of plate capacitors a) without sample, b) with dielectric sample in close contact. The dielectric is shown in grey.^[89]

In an a.c. experiment, a sinusoidal voltage $V(t)$ is applied to a cell and the resulting sinusoidal current $I(t)$ passing through the cell is recorded (Figure 1.8).

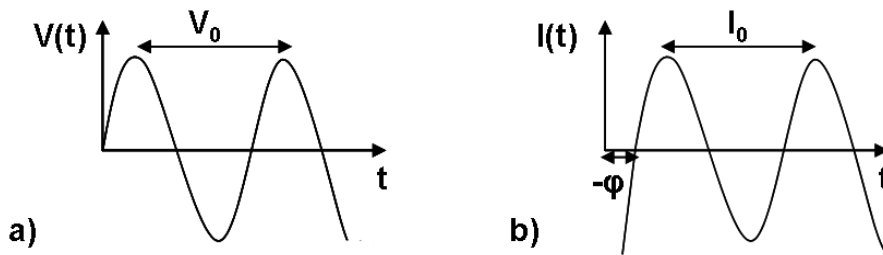


Fig. 1.8: Representation of a) the sinusoidal voltage applied and b) the sinusoidal current obtained at a given frequency.

The resulting current $I(t)$ is measured as a function of the frequency ω and the amplitude I_0 and the phase shift θ between voltage and current of the resulting current:

$$I(t) = I_0 \cdot \sin(\omega \cdot t + \theta)$$

The impedance $Z(\omega)$ is the complex a.c. resistance and it is measured as a function of the frequency of the applied signal over a wide frequency range, typically from 1 mHz to 1 MHz. Impedance is a vectorial quantity which possesses both magnitude and phase as well as a real Z' and a imaginary part Z'' .^[90, 91] In case of linearity, it can be described as:

$$Z(\omega) = \frac{U_0}{I_0} \exp(-i \cdot \theta) = Z' - i \cdot Z''$$

To reveal the conductivity of a sample, it is of importance to calculate the complex conductivity $Y(\omega)$, which is reciprocal to the impedance $Z(\omega)$ and can be expressed as:

$$Y(\omega) = \frac{1}{Z(\omega)}$$

In order to obtain the specific conductivity $\sigma(\omega)$, it is necessary to know the cell constant K from the surface area A and the sample thickness d of the cell:

$$K = \frac{A}{d}$$

Once the cell constant is known, the specific conductivity $\sigma(\omega)$, which is a measure of the carried charge per time, can be defined with the help of the following formula:

$$\sigma(\omega) = \frac{1}{K} \cdot Y(\omega) = \frac{1}{K \cdot Z(\omega)}$$

A typical a.c. experiment consists of the determination of the complex impedance of a cell as a function of the signal frequency. When the electrodes are not smoothly in contact to the samples surface or block the ion/proton flow during the measurement, a polarization of the electrodes is obtained, leading to a decrease in conductivity. Three typical isotherm areas can be observed in a typical a.c. conductivity plot vs frequency (see Figure 1.9):^[92]

- The low frequency regime determined by the electrode polarization;
- The frequency-independent plateau (d.c. plateau) reflecting the wanted transport phenomena;
- The high frequency regime (dispersive regime) caused by the relaxation effects.

To calculate the d.c. conductivity $\sigma_{d.c.}$ from the isotherms of $\sigma'(\omega)$, the conductivity values have to be derived from the frequency-independent plateaus. The d.c. plateau region is shifted to higher frequencies with increased temperature. Within this region, the dynamic processes are determined by random mobility due to an overall increase of energy in the system.

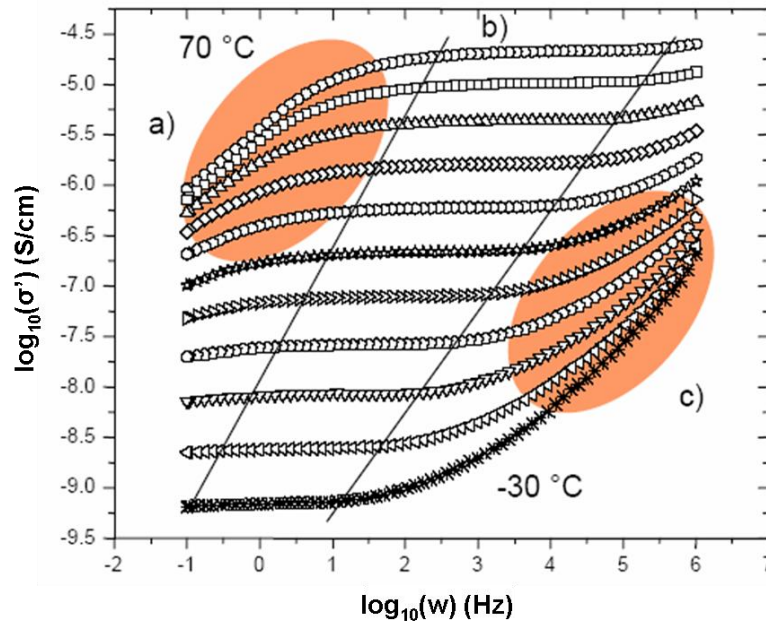


Fig. 1.9: Typical conductivity plots showing three areas: a) the regime determined by electrode polarization, b) the d.c. plateau and c) the dispersive regime.^[93]

1.3 Phosphonic Acid based Organic-Inorganic Hybrid

Materials

In this section it is aimed to present the characteristics of porous open-framework structures, the main focus being a description of phosphonic acid based organic-inorganic hybrid materials. In addition, the physisorption of gases is shortly described.

1.3.1 General Considerations

In order to obtain robust porous solid materials, “molecular scaffolds” of rigid rod-like organic moieties (called linkers) connected to inflexible inorganic clusters (metal ions) (called connectors or secondary building units SBU) have been synthesized.^[94] A variety of names has been given to these compounds: metal-organic frameworks (MOFs), coordination polymers, hybrid organic-inorganic materials and organic zeolite analogues with unavoidable overlap.^[95-99] Distinctions are made based on the composition, i.e. on the type of linker and connector composing the material.^[100, 101]

Usually transition metal ions are used as connectors. The coordination number depends on the metal and the valence state and goes from 2 to 7.^[102]

In case of the linkers, there is an enormous selection with adjustable bonding strength and bonding directions available:^[102]

- Inorganic ligands: halogenides and cyanometals;
- Neutral organic ligands;
- Anionic organic ligands;
- Cationic organic ligands.

These compounds have found applications as gas storage materials on account of their porous properties and their potential for rational design of their structure and functionality.

1.3.2 Physisorption of gases

Adsorption can be described as the adhesion of atoms, ions or molecules in the gas, liquid or solid state (called adsorptive) to a surface (called adsorbent) forming a film. In

contrast to chemisorption, which involves covalent or ionic bonds between two species and in which the electronic structure of bonding atoms or molecules are changed, physisorption is the physical adsorption of an atom or molecule caused by the *van der Waals* forces. During this process, the electronic structure of the atom or molecule is only barely perturbed.^[103] The intermolecular forces involved are of the same kind as those responsible for the imperfection of real gases and the condensation of vapors. In addition to the attractive dispersion forces and the short range repulsive forces, specific molecular interactions (e.g. polarization, field-dipole, field gradient-quadrupole) usually occur as a result of particular geometric and electronic properties of the adsorbent and adsorptive.^[104, 105]

Within the scope of physisorption, different types of pores are considered, which have been classified according to their sizes:^[106, 107]

- Macropores: pores with widths exceeding 50 nm;
- Mesopores: pores with widths between 2 and 50 nm;
- Micropores: pores with widths inferior to 2 nm.

In the particular case of micropores, the entire accessible volume can be considered as adsorption space and the process which then occurs is called micropore filling and may be regarded as a primary physisorption process. On the contrary, in the case of macropores and mesopores, surface coverage takes place on the walls of the open pores and the process of physisorption occurs in two or less distinct steps: monolayer-multilayer adsorption and capillary condensation.

In monolayer adsorption all the adsorbed molecules are in direct contact with the surface layer of the adsorbent whereas in the case of multilayer adsorption the adsorption space accommodates more than one layer of molecules so that not all adsorbed molecules are in direct contact with the surface layer of the adsorbent.

After multilayer adsorption, the residual pore space is filled with condensate separated from the gas phase by menisci. This process is called capillary condensation and is often accompanied by hysteresis. In the case of micropore filling, the physisorption process is not accompanied by the formation of liquid menisci; thereof the term capillary condensation should not be employed.

The interaction between a gas molecule and a surface can be explained by the *Lennard-Jones* potential (also referred to as the L-J potential, 6-12 potential or, less commonly, 12-6 potential), which is a mathematical model that describes the

interaction between a pair of neutral atoms or molecules. A form of the potential was first proposed in 1924 by *John Lennard-Jones*. The most common expression of the *Lennard-Jones* potential is:

$$V(r) = 4 \cdot \varepsilon \cdot \left[\left(\frac{\sigma}{r} \right)^{12} - \left(\frac{\sigma}{r} \right)^6 \right]$$

where ε is the depth of the potential well, σ is the (finite) distance at which the inter-particle potential is zero, and r is the distance between the particles.

The r^{-12} term describes *Pauli* repulsion at short ranges due to overlapping electron orbitals and the r^{-6} term describes attraction at long ranges (*van der Waals* force, or dispersion force). The *Lennard-Jones* potential is an approximation. The form of the repulsion term has no theoretical justification. Its physical origin is related to the Pauli principle: when the electronic clouds surrounding the atoms start to overlap, the energy of the system increases abruptly. The exponent 12 was chosen exclusively because of ease of computation.

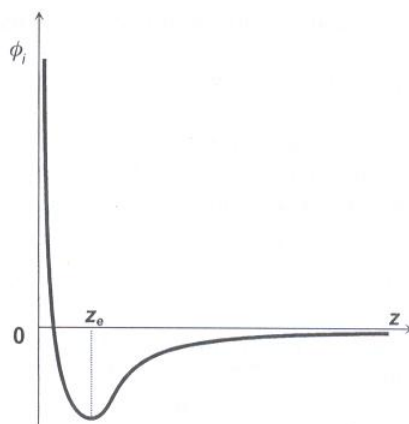


Fig. 1.10: Schematic representation of the run of the *Lennard-Jones* potential.^[103]

As a result, in the particular case of the physisorption of an atom, ion or molecule by a surface, the minimum energy of physisorption must be found by the balance between the long-range *van der Waals* attraction and short-range *Pauli* repulsion.

The exothermic adsorption of gases in surfaces is favored by low temperatures and high pressures, while the correspondent desorption by high temperatures and low pressures. The adsorption enthalpy depends on the concrete adsorptive/adsorbent pair. In the case of the physisorption of hydrogen in most of the cases values between -

4 and - 8 kJ/mol are found and in the case of methane between - 12 and - 19 kJ/mol.^[108] The adsorption enthalpy has to be high enough to facilitate the fixation of the gas molecules in the surface by the respective pressure storage of the system. However, at the same moment this parameter must not be too elevated to avoid the occurrence of high heat quantities and to assure the complete desorption of gases by moderate temperature rises.

Physisorption measurements have to be employed for the determination of surface area and/or porosity. Prior to the measurement, all of the physisorbed species should be removed from the surface of the adsorbent by outgassing the sample. In this dissertation, adsorption measurements were performed with commercially available equipment using nitrogen sorption at 77 K (- 196 °C). This method consists of the measurement of the amount of gas (nitrogen) adsorbed at constant temperature by increasing the relative pressure p/p_0 .

Adsorption is usually described through isotherms, that is, the amount of adsorbate on the adsorbent as a function of its pressure (if gas) or concentration (if liquid) at constant temperature. The quantity adsorbed is nearly always normalized by the mass of the adsorbent to allow comparison of different materials. Six types of physisorption isotherms have been described by the IUPAC^[106] (see Figure 1.11). All the isotherm types are reversible, excepting type IV and V.

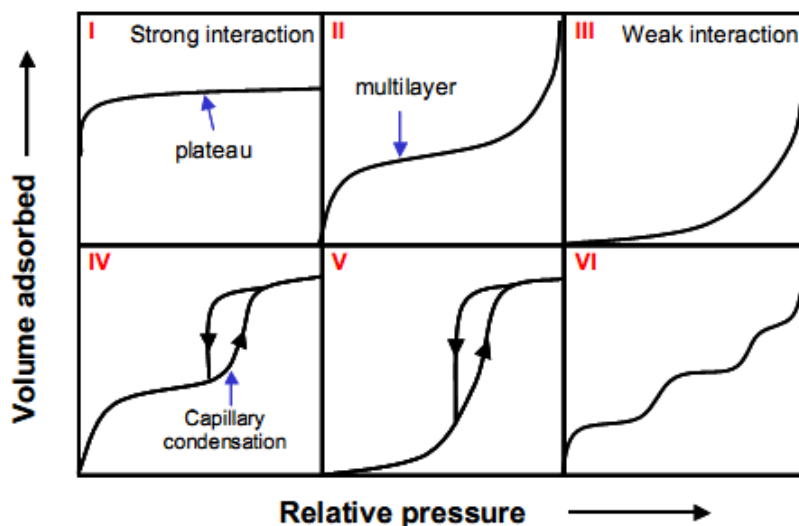


Fig. 1.11: IUPAC classification of the types of physisorption isotherms.^[106]

Microporous adsorbents show physisorption isotherms of type I whereas the isotherms of type II usually correspond to non-porous or macroporous adsorbents. For

mesoporous materials, an isotherm curve of type IV is usually observed. The sorption hysteresis which is due to capillary condensation taking place in the mesopores is characteristic of this type of isotherm. The hysteresis depends on the exact pore size distribution of the system.

To be able to compare the porosity of different materials, two values are calculated from the adsorption isotherms: the surface area and the pore volume. The *Langmuir* model, which assumes that a homogenous monolayer of the adsorbate is formed on the walls of the adsorbent, can be used to describe type I isotherms.^[109, 110] On the other hand multilayer adsorption can be described by the commonly used *Brunauer, Emmett and Teller* (BET) equation, which is primarily used to determine the point at which monolayer coverage is obtained.^[111, 112] In the two cases, the apparent surface area is calculated as the product of the estimated value of monolayer uptake and an accepted value for the area occupied by an adsorbate molecule. Both models allow a simple comparison of microporous materials even if their assumptions are not always suitable, especially since pore-filling is the predominant mode of uptake.

1.3.3 Carboxylic Acid based MOFs

A MOF has been described as a highly crystalline solid which possesses strong bonds providing robustness and linking units that are available for modification by organic synthesis.^[113] These materials have been proposed as candidates for hydrogen storage since they present high porosity and facile syntheses. Moreover, they are reproducible and chemical modification can be done for targeting desired properties.

In the two past decades, a large variety of MOFs have been synthesized and characterized. The majority of the compounds are based on dicarboxylic acids or polyfunctional carboxylic acids. *Yaghi* et al. developed a system of porous materials in which the pore size can be varied based on the choice of the dicarboxylic acid.^[114, 115] Cubic open framework structures were formed upon reaction of zinc-oxygen clusters with aryl dicarboxylic acids in diethylformamide. These compounds were found to store H₂ and CH₄ providing for their potential commercial use.^[116]

The group of *Férey* has also prepared many open framework carboxylates. They were able to synthesize three new Cr(III) compounds.^[117] The reactions were carried out hydrothermally at 220 °C and HF additions were necessary to achieve sufficient crystallinity for structure solutions from powders. Nitrogen physisorbed surface areas of 1500 and 1150 m²/g respectively were obtained. Subsequently, *Férey* et al. prepared two additional chromium terephthalates containing pores of 25 to 29 Å and *Langmuir*

surface areas of around 3100 m²/g.^[118] MIL-101 had even larger pores and a surface area of 5900 ± 300 m²/g. Until this discovery the largest reported surface area was 4500 m²/g obtained with MOF-177.^[119]

However, despite their porous and crystalline properties carboxylic acid based MOFs are chemically unstable.^[95, 99, 120, 121] MOFs exhibiting some of the best performance characteristics, such as Zn₄O(BDC)₃ and Mn₃[(Mn₄Cl)₃(BTT)₈]₂, are known to decompose in air,^[122-124] a serious disadvantage in the design of a storage system. Therefore there is a need to produce open-frameworks featuring strong metal-ligand bonds, as occurs for example in metal-imidazolate^[125, 126] and metal-triazolate,^[127, 128] frameworks, in order to obtain materials exhibiting improved chemical stability.

1.3.4 Phosphonic acid based organic-inorganic hybrid materials

Phosphonic acid-containing molecules have been proposed as linkers to obtain “molecular scaffolds” and in contrast to the carboxylate analogues they possess strong metal-ligand bonds, i.e. higher chemical stability. Most of the work on this field has been performed by A. Clearfield^[26] who has directed his research toward obtaining materials with high surface areas and pore diameters between 10 and 20 Å which would bridge the gap between the zeolites and the newer mesoporous materials.^[129, 130]

The phosphonate anions may function as linkers connecting inorganic oxide and organic groups giving a great variety of structure types: 1D chains, 2D layers, 3D network, and 3D network with channels.^[131] Due to the tetrahedral nature of the phosphonic acid group and the presence of two protons and three oxygens, the obtained compounds differed greatly from the carboxylic analogues. No structure solution of these compounds is possible by X-ray or neutron diffraction techniques since the cross-linked compounds form particles that precipitate rapidly into nanoparticles that exhibit only short range order. Therefore, they must be understood on the basis of modeling and indirect data from EM, NMR, and additional spectroscopic and textural studies.^[26] One refers to organic-inorganic hybrid materials or metal phosphonate open-framework materials instead of MOFs when porous compounds are synthesized using phosphonic acid based linkers.^[132, 133]

Commonly mesoporous metal phosphonates are obtained by adapting the methodology employed for obtaining MCM-41 (a mesoporous solid prepared by calcination of aluminosilicate gels in the presence of surfactants),^[129] and therefore, using organic surfactant molecules as templates (MCM-type approach).

An alternative procedure to obtain porous materials consists of reacting a diphosphonic acid, $\text{H}_2\text{O}_3\text{P-R-PO}_3\text{H}_2$, with a suitable metallic cation to form inorganic layers of the metal and PO_3 groups and then to cross-link these layers with the alkyl or aryl groups (R) and space these pillars (which cross-link the layers) with phosphate (POH) or phosphite (PH) groups (see Figure 1.12). The main advantage of this approach is that materials with pores ranging between 12 and 20 Å can be prepared and functionalized. This porous range is very important because it is too large to be obtained by crystalline zeolites but too small to be achieved by MCM-type approaches. In fact, metal organophosphonate open-framework materials can be regarded as intermediate compounds between zeolite-like materials and MOF compounds.^[133, 134] This strategy, conceived by *Dines et al.*^[135] has been followed by several research groups which have reported the synthesis of several microporous metal phosphate–phosphonates.

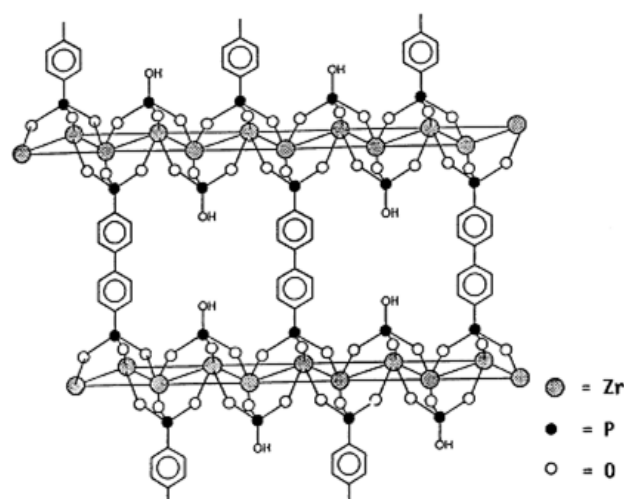


Fig. 1.12: Idealized representation of α -zirconium phosphate type layers pillared by diphenyl groups. The pillars are spaced 10.6 Å apart by mono-hydrogen phosphate groups to create microporosity.^[136]

Most usually, bisphosphonates are used as linkers and the following metals as connectors:

- Me(II): ZnCl_2 , $\text{Cu}(\text{NO}_3)_2 \cdot 2.5 \text{H}_2\text{O}$, $\text{CuSO}_4 \cdot 5\text{H}_2\text{O}$;
- Me(III): $\text{Al}(\text{NO}_3)_3 \cdot 9\text{H}_2\text{O}$;
- Me(IV): $\text{ZrOCl}_2 \cdot 8\text{H}_2\text{O}$, $\text{SnCl}_4 \cdot 5\text{H}_2\text{O}$.

Metals of coordination number II, like Zn^[137, 138] and Cu^[139], give highly crystalline materials which do not present porosity.^[140] On the contrary, the use of metals of higher coordination number provided materials which present porosity, although no crystal structure determination was possible.

Aluminum has been used as connector to obtain micro and mesoporous metal phosphonates. Aluminum phenylphosphonates are layered materials with low specific surface areas in which the aluminum is octahedrally coordinated.^[141, 142] Mesoporous aluminum phosphonates showing 2D-hexagonal structures can be produced by the MCM-type approach. Surface areas of 650 - 700 m²/g, and a pore diameter of ca. 33 Å for the pure methylphosphonate or 1,2-ethylenediphosphonate have been published.^[143, 144]

A series of biphosphonic acids have been used as cross-linking groups and microporous aluminum biphosphonates have been prepared.^[145] The materials present BET surface areas between 100 and 400 m²/g and micropore size distributions centered between 7 and 20 Å. A schematic drawing of how micropores may be formed in the aluminum biphenylenbisphosphonates is shown in Figure 1.13. In the aluminum biphenyldiphosphonates materials, no spacer groups are include as reactant thus the model proposed in Figure 1.12 cannot be applied. In these compounds, the formation of microporosity is a consequence of the coming together of layers of unequal length around the DMSO molecules. These DMSO molecules act as template agents during the crystal growth and after their washings of the samples microporosity is developed.

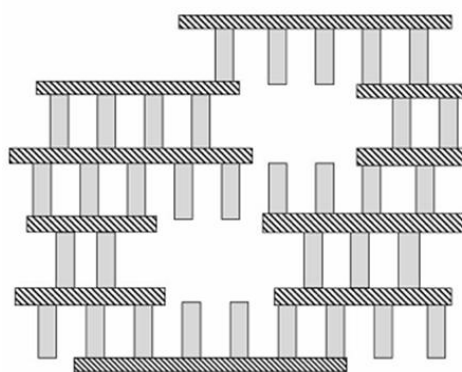


Fig. 1.13: Conceptual model of pore formation in aluminum, zirconium and tin biphenyldiphosphonates.^[136] The double vertical lines represent biphenyl groups and the horizontal striped bars the inorganic layers.

Numerous cross-linking zirconium phosphate-like layers based on several types of aryl- and alkylidiphosphonic acids have been described in the literature.^[136, 146, 147] They

have been synthesized by using the second synthetic approach and microporous materials for which no crystal solution is possible have been obtained.

In the case of pillared zirconium aryldiphosphonates microporosity was observed. Surface areas of 300 - 400 m²/g was obtained by using DMSO and DMSO/ethanol mixtures at 90 °C.^[147, 148] A number of spacer groups were used to separate the pillars to determine what effect this would have on porosity; however there appears to be only a slight correlation of surface area with the amount of phenyl groups replacing pillars. Since no spacer groups are included as reactants, it was proposed by *A. Clearfield* that the pores developed by a coming together of layers of unequal size during particle growth so that the schematic representation of the pore formation depicted in Fig 1.12 can be also applied in this case.^[136]

In the case of zirconium alkylidiphosphonates, mesoporous materials of surface areas between 100 and 200 m²/g were obtained.^[149] *Derouane* and *Jullien-Lardot* proposed three possible models to account for the structure of these mixed derivatives but only the third one was accepted (see Figure 1.14). This model explains the two interlayer spacings and the internal porosity.

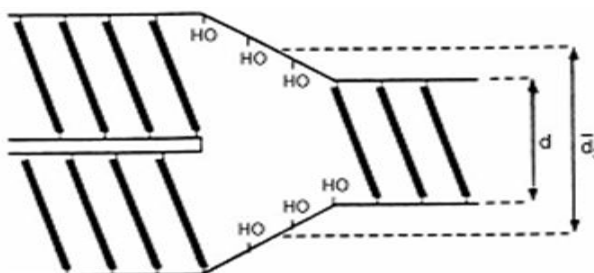


Fig. 1.14: Structural model explaining the generation of mesoporosity and larger interlayer spacings in zirconium n-alkyl-diphosphonates.^[149]

The first synthesis of a porous tin phosphonate compound in the presence of a surfactant was reported in 2005 by *Mal* et al.^[150] The obtained MCM-type materials were mesoporous with BET surface areas of around 300 m²/g after calcinations. Since then, a large number of monophosphonates of tin(IV) have been prepared without surfactant, all of which are microporous and form spherical globules with surface areas between 200 - 500 m²/g.^[151-155] The surface area arises from their layered structure like in the case of zirconium based phosphonates. Moreover, this new family of layered tin phosphonate materials has been proven to be very efficient catalyst in the *Baeyer–Villiger* oxidation of aromatic aldehydes without any solvent and using aqueous H₂O₂ (30 %) as the oxidant.^[156]

1.4 Bibliography

- [1] M. Horiguchi, M. Kandatsu, *Nature* **1959**, *184*, 901
- [2] J. S. Kittredge, E. Roberts, D. G. Simonsen, *Biochemistry* **1962**, *1*, 624
- [3] H. M. Benedict, R. Swidler, J. N. Simons, *Science* **1964**, *144*, 1134
- [4] J. A. Alhadeff, G. D. Daves Jr, *Biochemistry* **1970**, *9*, 4866
- [5] M. W. Baldwin, J. Braven, *J. mar. biol. Ass. U. K.* **1968**, *48*, 603
- [6] D. M. Kariotoglou, S. K. Mastronicolis, *Comp. Biochem. Physiol. B: Biochem. Mol. Biol.* **2003**, *136*, 27
- [7] C. Brumsen, N. A. T. Hamdy, S. E. Papapoulos, *Medicine* **1997**, *76*, 266
- [8] N. B. Watts, *Endocrinol. Metab. Clinics North America* **1998**, *27*, 419
- [9] H. Fleisch, *Hormone and Metabolic Research* **1997**, *29*, 145
- [10] G. R. Mundy, *J. Clin. Oncol.* **2002**, *20*, 3191
- [11] A. Bamias, E. Kastritis, C. Bamia, L. A. Mouloupoulos, I. Melakopoulos, G. Bozas, V. Koutsoukou, D. Gika, A. Anagnostopoulos, C. Papadimitriou, *J. Clin. Oncol.* **2005**, *23*, 8580
- [12] M. M. Reddy, G. H. Nancollas, *Desalination* **1973**, *12*, 61
- [13] J. S. Gill, R. G. Varsanik, *J. Cryst. Growth* **1986**, *76*, 57
- [14] B. Nowack, A. T. Stone, *Water Res.* **2006**, *40*, 2201
- [15] B. Nowack, *Water Res.* **2003**, *37*, 2533
- [16] M. Nilising, S. Lunell, P. Persson, L. Ojamä, *Surf. Sci.* **2005**, *582*, 49
- [17] J. Pahnke, J. Rühle, *Macromol. Rapid Commun.* **2004**, *25*, 1396
- [18] N. Griep-Raming, M. Karger, H. Menzel, *Langmuir* **2004**, *20*, 11811
- [19] T. Bock, H. Möhwald, R. Mülhaupt, *Macromol. Chem. Phys.* **2007**, *208*, 1324
- [20] J. J. Eisch, B. D. Mohammad, K. Suresh, *J. Organomet. Chem.* **1985**, *285*, 121
- [21] Kovaleva, Feshchenko, *J. Gen. Chem. USSR (Engl. Transl.)* **1979**, *49*, 476
- [22] J. v. Braun, E. Anton, K. Weinbach, *Chem. Ber.* **1930**, *63*, 2847
- [23] H. H. Jaffé, L. D. Freedman, G. O. Doak, *J. Am. Chem. Soc.* **1953**, *75*, 2209
- [24] V. A. Kozlov, I. A. Popkova, B. D. Berezin, *Russ. J. Phys. Chem. (Engl. Transl.)* **1981**, *55*, 827
- [25] M. Schuster, T. Rager, A. Noda, K. D. Kreuer, J. Maier, *Fuel Cells* **2005**, *5*, 355
- [26] A. Clearfield, *Dalton Trans.* **2008**, *44*, 6089
- [27] M. Winter, R. J. Brodd, *Chem. Rev.* **2004**, *104*, 4245
- [28] L. Carrette, K. A. K. A. Friedrich, U. Stimming, *Fuel Cells* **2001**, *1*, 5
- [29] C. Rayment, S. Sherwin, *Introduction to FC technology, Department of Aerospace and Mechanical Engineering, University of Notre Dame Notre Dame, IN 46556, U.S.A.* **2003**.
- [30] K. V. Kordesch, G. R. Simade, *Chem. Rev.* **1995**, *95*, 191
- [31] S. J. Paddison, K. D. Kreuer, J. Maier, *Phys. Chem. Chem. Phys.* **2006**, *8*, 4530
- [32] R. Ianniello, V. M. Schmidt, U. Stimming, J. Jumper, A. Wallan, *Electrochim. Acta* **1994**, *39*, 1863
- [33] T. Aigle, WBZU, *PEFC-Course March 10 to 14*, **2008**, Ulm.
- [34] M. Rikukawa, K. Sanui, *Prog. Polym. Sci.* **2000**, *25*, 1463
- [35] A. Chernyshev, K. M. Armstrong, S. Cukierman, *Biophys. J.* **2003**, *84*, 238
- [36] C. H. Yu, S. Cukierman, R. Pomès, *Biophys. J.* **2003**, *84*, 816
- [37] K. D. Kreuer, S. J. Paddison, E. Spohr, M. Schuster, *Chem. Rev.* **2004**, *104*, 4637
- [38] K. D. Kreuer, *Chem. Mater.* **1996**, *8*, 610
- [39] K. D. Kreuer, A. Rabenau, W. Weppner, *Angew. Chem. Int. Ed.* **1982**, *21*, 208
- [40] N. Agmon, *Chem. Phys. Lett.* **1995**, *244*, 456
- [41] Y. Sone, P. Ekdunge, D. Simonsson, *J. Electrochem. Soc.* **1996**, *143*, 1254.
- [42] J. S. Wainright, J. T. Wang, D. Weng, R. F. Savinell, M. Litt, *J. Electrochem. Soc.* **1995**, *142*, 121
- [43] D. J. Stasko, K. J. Perzynski, M. A. Wasil, J. K. Brodbeck, K. Kirschbaum, Y. W. Kim, C. Lind, *Inorg. Chem.* **2004**, *43*, 3786
- [44] E. Ortiz, R. A. Vargas, B. E. Mellander, *J. Phys.: Condens. Matter* **2006**, *18*, 9561
- [45] J. W. Phair, S. P. S. Badwal, *Ionics* **2006**, *12*, 103

- [46] S. M. Haile, C. R. I. Chisholm, K. Sasaki, D. A. Boysen, T. Uda, *Faraday Discussions* **2007**, 134, 17
- [47] S. M. Haile, D. A. Boysen, C. R. I. Chisholm, R. B. Merle, *Nature* **2001**, 410, 910
- [48] S. M. Haile, *Acta Mater.* **2003**, 51, 5981
- [49] K. D. Kreuer, *J. Membr. Sci.* **2001**, 185, 29.
- [50] H. G. Herz, K. D. Kreuer, J. Maier, G. Scharfenberger, M. F. H. Schuster, W. H. Meyer, *Electrochim. Acta* **2003**, 48, 2165
- [51] T. Steiner, *Angew. Chem. Int. Ed.* **2002**, 41, 48
- [52] C. J. T. De Grotthuss, *Ann. Chim.* **1806**, 58, 54
- [53] M. Tuckerman, K. Laasonen, M. Sprik, M. Parrinello, *J. Chem. Phys.* **1995**, 103, 150
- [54] S. Cukierman, *Biochim. Biophys. Acta* **2006**, 1757, 876
- [55] M. Eigen, L. De Maeyer, *Proc. R. Soc. London, Ser. A* **1958**, 247, 505
- [56] M. Eigen, *Angew. Chem.* **1963**, 75, 489
- [57] H. Steininger, M. Schuster, K. D. Kreuer, A. Kaltbeitzel, B. Bingöl, W. H. Meyer, S. Schauff, G. Brunklaus, J. Maier, H. W. Spiess, *Phys. Chem. Chem. Phys.* **2007**, 9, 1764
- [58] A. L. Rusanov, D. Yu Likhatchev, K. Müllen, *Russ. Chem. Rev.* **2002**, 71, 761
- [59] M. A. Hickner, H. Ghassemi, Y. S. Kim, B. R. Einsla, J. E. McGrath, *Chem. Rev.* **2004**, 104, 4587
- [60] Q. Li, R. He, J. O. Jensen, N. J. Bjerrum, *Chem. Mater.* **2003**, 15, 4896
- [61] M. Yamabe, K. Akiyama, Y. Akatsuka, M. Kato, *Eur. Polym. J.* **2000**, 36, 1035
- [62] D. Poppe, H. Frey, K. D. Kreuer, A. Heinzl, R. Mülhaupt, *Macromolecules* **2002**, 35, 7936
- [63] D. Poppe, *Dissertation, Freiburg* **2002**.
- [64] K. D. Kreuer, A. Fuchs, M. Ise, M. Spaeth, J. Maier, *Electrochim. Acta* **1998**, 43, 1281
- [65] M. Schuster, W. H. Meyer, G. Wegner, H. G. Herz, M. Ise, M. Schuster, K. D. Kreuer, J. Maier, *Solid State Ionics* **2001**, 145, 85
- [66] R. Souzy, B. Ameduri, *Prog. Polym. Sci.* **2005**, 30, 644
- [67] K. Kanamura, A. Tanaka, V. Kennedy, R. Adzic, E. B. Yeager, D. Burton, R. Guneratne, *J. Electrochem. Soc.* **1996**, 143, 2765
- [68] M. Yamada, I. Honma, *Polymer* **2005**, 46, 2986
- [69] M. Yamada, I. Honma, *Electrochim. Acta* **2003**, 48, 2411
- [70] M. Yamada, I. Honma, *Chem. Phys. Lett.* **2005**, 402, 324
- [71] I. Honma, M. Yamada, *Bull. Chem. Soc. Jpn* **2007**, 80, 2110
- [72] R. Souzy, B. Ameduri, B. Boutevin, G. Gebel, P. Capron, *Solid State Ionics* **2005**, 176, 2839
- [73] T. Bock, *Dissertation, Freiburg* **2007**.
- [74] S. V. Kotov, S. D. Pedersen, W. Qiu, Z. M. Qui, D. J. Burton, *J. Fluor. Chem.* **1997**, 82, 13
- [75] B. A. R. Souzy, B. Boutevin, D. Virieux, , *J. Fluor. Chem.* **2004**, 125, 1317
- [76] B. Boutevin, B. Hamoui, J. P. Parisi, B. Améduri, *Eur. Polym. J.* **1996**, 32, 159
- [77] F. M. B. Coutinho, V. G. Teixeira, C. C. R. Barbosa, *J. Appl. Poly. Sci.* **1998**, 67, 781
- [78] B. Lafitte, P. Jannasch, *J. Polym. Sci., Part A: Polym. Chem.* **2005**, 43, 273
- [79] K. Miyatake, A. S. Hay, *J. Polym. Sci., Part A: Polym. Chem.* **2001**, 39, 3770
- [80] B. Liu, G. P. Robertson, M. D. Guiver, Z. Shi, T. Navessin, S. Holdcroft, *Macromol. rapid commun.* **2006**, 27, 1411
- [81] T. Rager, M. Schuster, H. Steininger, K. D. Kreuer, *Adv. Mater.* **2007**, 19, 3317
- [82] J. Parvole, P. Jannasch, *J. Mater. Chem.* **2008**, 18, 5547
- [83] K. Jakoby, K. V. Peinemann, S. P. Nunes, *Macromol. Chem. Phys.* **2003**, 204, 61
- [84] B. Bingöl, *Dissertation, Mainz* **2007**.
- [85] B. Bingöl, W. H. Meyer, M. Wagner, G. Wegner, *Macromol. Rapid Commun.* **2006**, 27, 1719
- [86] A. Kaltbeitzel, S. Schauff, H. Steininger, B. Bingöl, G. Brunklaus, W. H. Meyer, H. W. Spiess, *Solid State Ionics* **2007**, 178, 469
- [87] K. D. Kreuer, *Proton conductors-Solid membranes and gels-Materials and devices* **1992**, Edited by Philippe Colomban, Cambridge University Press, 409
- [88] J. R. Macdonald, *Annals of Biomedical Engineering* **1992**, 20, 289
- [89] W. Göpel, C. Ziegler, *Struktur und Materie: Grundlagen, Mikroskopie und Spektroskopie*, Teubner **1994**.
- [90] C. H. Lee, H. B. Park, Y. M. Lee, R. D. Lee, *Ind. Eng. Chem. Res.* **2005**, 44, 7617

-
- [91] M. Ciureanu, S. D. Mikhailenko, S. Kaliaguine, *Catalysis Today* **2003**, 82, 195
- [92] J. R. Macdonald, W. B. Johnson, *Impedance spectroscopy. Theory, experiment, and applications, 2 Edition* **2005**, Edited by Evgenij Barsoukov and J. Ross Macdonald, John Wiley and Sons, 1
- [93] S. Schauff, *Dissertation, Mainz* **2007**.
- [94] M. Eddaoudi, D. B. Moler, H. Li, B. Chen, T. M. Reineke, M. O'Keeffe, O. M. Yaghi, *Acc. Chem. Res.* **2001**, 34, 319
- [95] H. Li, M. Eddaoudi, T. L. Groy, O. M. Yaghi, *J. Am. Chem. Soc.* **1998**, 120, 8571
- [96] Y. Aoyama, *Top. Curr. Chem.* **1998**, 198, 131
- [97] P. J. Hagrman, D. Hagrman, J. Zubieta, *Angew. Chem. Int. Ed.* **1999**, 38, 2638
- [98] B. Moulton, M. J. Zaworotko, *Curr. Opin. Solid State Mater. Sci.* **2002**, 6, 117
- [99] S. L. James, *Chem. Soc. Rev.* **2003**, 32, 276
- [100] G. Férey, *Chem. Mater.* **2001**, 13, 3084
- [101] C. Janiak, *Dalton Trans.* **2003**, 2003, 2781
- [102] S. Kitagawa, R. Kitaura, S. Noro, *Angew. Chem. Int. Ed.* **2004**, 43, 2334
- [103] F. Rouquerol, J. Rouquerol, K. Sing, *Adsorption by Powders and Porous Solids; Academic Press: London*, **1999**.
- [104] P. A. Webb, C. Orr, *Analytical Methods in Fine Particle Technology; Micromeritics Instrument Corporation* **1997**.
- [105] S. Lowell, J. E. Shields, M. A. Thomas, M. Thommes, *Characterization of Porous Solids and Powders: Surface Area, Pore Size and Density; Kluwer Academic Publishers: Dordrecht* **2004**.
- [106] K. S. W. Sing, D. H. Everett, R. A. W. Haul, L. Moscou, R. A. Pierotti, J. Rouquerol, T. Siemieniowska, *Pure Appl. Chem.* **1985**, 57, 603
- [107] B. D. Zdravkov, J. J. Čermák, M. Sefara, J. Janku, *Central European J. Chem.* **2007**, 5, 385
- [108] S. K. Bhatia, A. L. Myers, *Langmuir* **2006**, 22, 1688
- [109] I. Langmuir, *J. Am. Chem. Soc.* **1916**, 38, 2221
- [110] I. Langmuir, *Chem. Rev.* **1933**, 13, 147
- [111] S. Brunauer, P. H. Emmett, E. Teller, *J. Am. Chem. Soc.* **1938**, 60, 309
- [112] S. Brunauer, L. S. Deming, W. E. Deming, E. Teller, *J. Am. Chem. Soc.* **1940**, 62, 1723
- [113] J. L. C. Rowsell, O. M. Yaghi, *Microporous Mesoporous Mater.* **2004**, 73, 3
- [114] M. Eddoudi, J. Kim, N. Rosi, D. Vodak, J. Wachter, M. O'Keeffe, O. M. Yaghi, *Science* **2002**, 295, 469
- [115] O. M. Yaghi, M. O'Keeffe, N. W. Ockwig, H. K. Chae, M. Eddaoudi, J. Kim, *Nature* **2003**, 423, 705
- [116] J. L. C. Rowsell, A. R. Millward, K. S. Park, O. M. Yaghi, *J. Am. Chem. Soc.* **2004**, 126, 5666
- [117] F. Millange, C. Serre, G. Férey, *Chem. Commun.* **2002**, 822
- [118] G. Férey, C. Mellot-Draznieks, C. Serre, F. Millange, J. Dutour, S. Surblé, I. Margiolaki, *Science* **2005**, 309, 2040
- [119] H. K. Chae, D. Y. Siberio-Pérez, J. Kim, Y. B. Go, M. Eddaoudi, A. J. Matzger, M. O'Keeffe, O. M. Yaghi, *Nature* **2004**, 427, 523
- [120] U. Mueller, M. Schubert, F. Teich, H. Puetter, K. Schierle-Arndt, J. Pastré, *J. Mater. Chem.* **2006**, 16, 626
- [121] L. J. Murray, M. Dinc, J. R. Long, *Chem. Soc. Rev.* **2009**, 38, 1294
- [122] S. S. Kaye, A. Dailly, O. M. Yaghi, J. R. Long, *J. Am. Chem. Soc.* **2007**, 129, 14176
- [123] M. Dinca, A. Dailly, Y. Liu, C. M. Brown, D. A. Neumann, J. R. Long, *J. Am. Chem. Soc.* **2006**, 128, 16876
- [124] M. Dinca, W. S. Han, Y. Liu, A. Dailly, C. M. Brown, J. R. Long, *Angew. Chem., Int. Ed.* **2007**, 45, 1419
- [125] K. S. Park, Z. Ni, A. P. Cote, J. Y. Choi, R. Huang, F. J. Uribe-Romo, H. K. Chae, M. O'Keeffe, O. M. Yaghi, *Proc. Natl. Acad. Sci. U. S. A.* **2006**, 103, 10186
- [126] H. Wu, W. Zhou, T. Yildirim, *J. Am. Chem. Soc.* **2007**, 129, 5314
- [127] C. Yang, X. Wang, M. A. Omary, *J. Am. Chem. Soc.* **2007**, 129, 15454
- [128] Q.-G. Zhai, C.-Z. Lu, X.-Y. Wu, S. R. Batten, *Cryst. Growth Des.* **2007**, 7, 2332
- [129] C. T. Kresge, M. E. Leonowicz, W. J. Roth, J. C. Vartuli, J. S. Beck, *Nature* **1992**, 359, 710

-
- [130] Q. Huo, D. I. Margolese, U. Ciesla, P. Feng, T. E. Gier, P. Sieger, R. Leon, P. M. Petroff, F. Schüth, G. D. Stucky, *Nature* **1994**, 368, 317
- [131] A. Clearfield, *Progress in Inorganic Chemistry*, vol. 47, John Wiley & Sons, Edited by K. D. Karlin **1998**, 371.
- [132] A. Vioux, J. Le Bideau, P. H. Mutin, D. Leclercq, *Top Curr. Chem.* **2004**, 232, 145
- [133] K. Maeda, *Microporous Mesoporous Mater.* **2004**, 73, 47
- [134] M. J. Rosseinsky, *Microporous Mesoporous Mater.* **2004**, 73, 15
- [135] M. D. Dines, P. M. Digiacomio, K. P. Callahan, P. C. Griffith, R. H. Lane, R. E. Cooksey, *Chemically Modified Surfaces in Catalysis and Electrocatalysis*, 192, ACS, Washington, DC **1982**, Edited by J.S. Miller, 223.
- [136] A. Clearfield, Z. Wang, *J. Chem. Soc., Dalton Trans.* **2002**, 2937
- [137] D. M. Poojary, B. Zhang, P. Bellinghausen, A. Clearfield, *Inorg. Chem.* **1996**, 35, 5254
- [138] B. Zhang, D. M. Poojary, A. Clearfield, *Inorg. Chem.* **1998**, 37, 1844
- [139] D. M. Poojary, B. Zhang, P. Bellinghausen, A. Clearfield, *Inorg. Chem.* **1996**, 35, 4942
- [140] M. d. M. Gómez-Alcántara, A. Cabeza, M. Martínez-Lara, M. A. G. Aranda, R. Suau, N. Bhuvanesh, A. Clearfield, *Inorg. Chem.* **2004**, 43, 5283
- [141] J. E. Haky, J. B. Brady, *Mater. Res. Bull.* **1997**, 32, 297
- [142] A. Cabeza, M. A. G. Aranda, S. Bruque, D. M. Poojary, A. Clearfield, J. Sanz, *Inorg. Chem.* **1998**, 37, 4168
- [143] J. El Haskouri, C. Guillem, J. Latorre, A. Beltrán, D. Beltrán, P. Amorós, *Eur. J. Inorg. Chem.* **2004**, 1804
- [144] J. El Haskouri, C. Guillem, J. Latorre, A. Beltrán, D. Beltrán, P. Amorós, *Chem. Mater.* **2004**, 16, 4359
- [145] M. d. M. Gómez-Alcántara, A. Cabeza, L. Moreno-Real, M. A. G. Aranda, A. Clearfield, *Microporous and Mesoporous Materials* **2006**, 88, 293
- [146] A. Clearfield, *Chem. Mater.* **1998**, 10, 2801
- [147] A. Clearfield, Z. Wang, P. Bellinghausen, *J. Solid State Chem.* **2002**, 167, 376
- [148] Z. Wang, J. M. Heising, A. Clearfield, *J. Am. Chem. Soc.* **2003**, 125, 10375
- [149] E. G. Derouane, V. Jullien-Lardot, *Stud. Surf. Sci. Catal.* **1994**, 83, 11
- [150] N. K. Mal, M. Fujiwara, M. Matsukata, *Chem. Commun.* **2005**, 5199
- [151] A. Subbiah, N. Bhuvanesh, A. Clearfield, *J. Solid State Chem.* **2005**, 178, 1321
- [152] J. Huang, A. Subbiah, D. Pyle, A. Rowland, B. Smith, A. Clearfield, *Chem. Mater.* **2006**, 18, 5213
- [153] M. d. M. Gómez-Alcántara, A. Cabeza, P. Olivera-Pastor, F. Fernández-Moreno, I. Sobrados, J. Sanz, R. E. Morris, A. Clearfield, M. A. G. Aranda, *Dalton Trans.* **2007**, 2394
- [154] A. Cabeza, M. d. M. Gómez-Alcántara, P. Olivera-Pastor, I. Sobrados, J. Sanz, B. Xiao, R. E. Morris, A. Clearfield, M. A. G. Aranda, *Microporous and Mesoporous Materials* **2008**, 114, 322
- [155] S. Kirumakki, J. Huang, S. Subbiah, J. Yao, A. Rowland, B. Smith, A. Mukherjee, S. Samarajeewa, A. Clearfield, *J. Mater. Chem.* **2009**, 19, 2593
- [156] S. Kirumakki, S. Samarajeewa, R. Harwell, A. Mukherjee, R. H. Herber, A. Clearfield, *Chem. Commun.* **2008**, 5556

2 Motivation and Objectives

Phosphonic acid-containing molecules have found numerous applications as chelating agents^[1, 2] and drugs.^[3, 4] Furthermore polymers possessing this acidic moiety have been studied as proton conductors owing to the amphoteric character of the acidic group.^[5-8] In addition, phosphonic acid based organic-inorganic hybrid materials have found the interest of many research groups due to the porous properties of the compounds.^[9-11]

In this work, two types of non-covalent networks composed of phosphonic acid based small molecules are presented. On the one hand, it is aimed to use phosphonic acid-containing small molecules as solid state proton conductors in FCs. This is due to the possibility of cooperative proton transport phenomena in hydrogen bonded networks of phosphonic acid groups.^[12] On the other hand, it is targeted to apply phosphonic acid based small molecules to create ionic networks with the help of metal cations. In this case, the phosphonated molecules would act as linkers to obtain porous organic-inorganic hybrid materials which could be used for example for gas storage.

2.1 Phosphonic Acid based Solid State Proton Conductors

A FC is a promising energy device which can provide electrical energy with high efficiency and low environmental impact. The central part of the FC is the electrolyte membrane, also called separator material or proton-exchanging membrane PEM, which should be able to transport the protons from the anode to the cathode. State-of-the-art polymeric electrolytes for low temperature FCs (PEFC) are sulfonic acid-based perfluorinated polymers such as Nafion®. They present high but temperature dependent proton conductivity since proton transport in these materials is governed by the vehicle mechanism which is based on the diffusion of proton-containing groups.^[13-15] This hydration requirement restricts the maximum operating temperature of the corresponding FC to the boiling point of water (i.e. 100 °C at 1 atm) and results in the “cross-over” of significant amounts of water and/or methanol through permeation and

electroosmotic drag.^[16] As a result, the operation of the PEFC is expensive in view of the necessity for using platinum and platinum alloy catalysts, the requirement for hydrogen of high purity (i.e. without any CO present) and a complicated water and heat management setup.^[12, 17] Thus, it is widely recognized that the key to further progress in PEM fuel cell technology is the development of an electrolyte that exclusively conducts protons at high rates and is both chemically (i.e. resistant to oxidation) and mechanically stable at higher operating temperatures and under low humidity conditions.

Up to now, the on-going research has focused on the development of materials which like Nafion® present a nanophase separation between the hydrophobic polymer main chain and the acidic moieties leading to a nanoscopic morphology responsible for the water uptake and proton conduction.^[18] Different synthetic strategies have been applied to obtain polymeric materials with an efficient ionic network, i.e. a defined morphology.^[19-23]

The work presented in Chapter 3 goes into a different direction: it is proposed to increase proton mobility by using small molecules which are able to self-assemble and thus to provide a nanophase separation between a conductive and a non-conductive phase. Phosphonic acid is chosen as protogenic group due to its amphoteric properties.^[8, 17, 24] It has been demonstrated that a high concentration of these acidic groups which are able to aggregate is beneficial for a high intrinsic proton conductivity.^[24] A series of phosphonic acid-containing molecules possessing a carbon-rich hydrophobic core and a protogenic hydrophilic periphery has been synthesized and characterized. The purpose of this chapter is to study the solid state proton transport properties of this novel class of compounds and to determine whether they can be applied as separator materials in FCs working at intermediate temperatures.

One primary goal of this work is to explore the concept of using a phosphonic acid based organic molecule as proton conductor and to prove whether it is applicable as a separator material for intermediate temperature FCs. Therefore, phosphonic acid groups have been introduced in the non-planar structure of hexaphenylbenzene (HPB). The synthesis and characterization of this central compound are described in Section 3.2. The work here focuses heavily on providing insights into the proton transport mechanism taking place through the material and determining the usability of hexakis(*p*-phosphonatophenyl)benzene as PEM for intermediate temperature FCs.

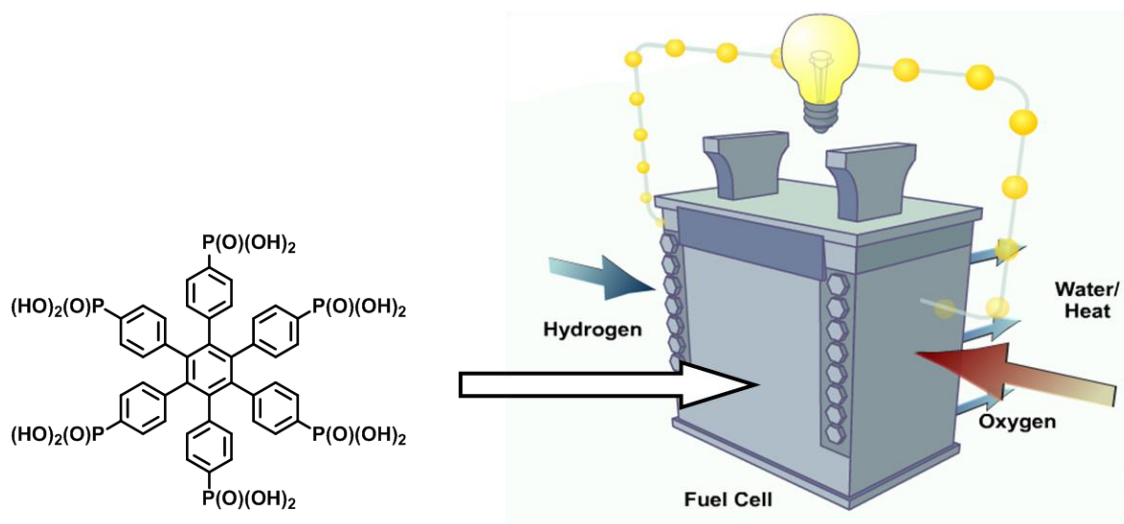


Fig. 2.1: Hexakis(*p*-phosphonatophenyl)benzene as solid state proton conductor.

The main purpose of the following sections is to design rules for more optimized molecular entities which can be used as separator materials for intermediate temperature FCs. For the development of novel separator materials based on organic small molecules which are able to self-assemble and therefore also to provide the nanophase separation leading to proton transport, it is important to understand how geometry and structure determine proton conductivity in this novel type of compounds. Therefore, a deep study has been carried out divided in three main parts.

Section 3.3 focuses on finding the optimum geometry for an organic crystalline material to be a good PEM candidate. The synthesis of five phosphonic acid-containing molecules with different geometry and substitution pattern is described. Proton conductivity, water uptake, crystallinity and solid state NMR studies have been carried out providing insights into the proton-conducting properties of this novel class of materials and the mechanisms involved in proton transport. The question addressed in this section is what effects have the number of phosphonic acid functions, the geometry and the crystallinity on the performance of the materials. Moreover it is aimed to clarify the basic principles which regulate the proton transport in this sort of molecules.

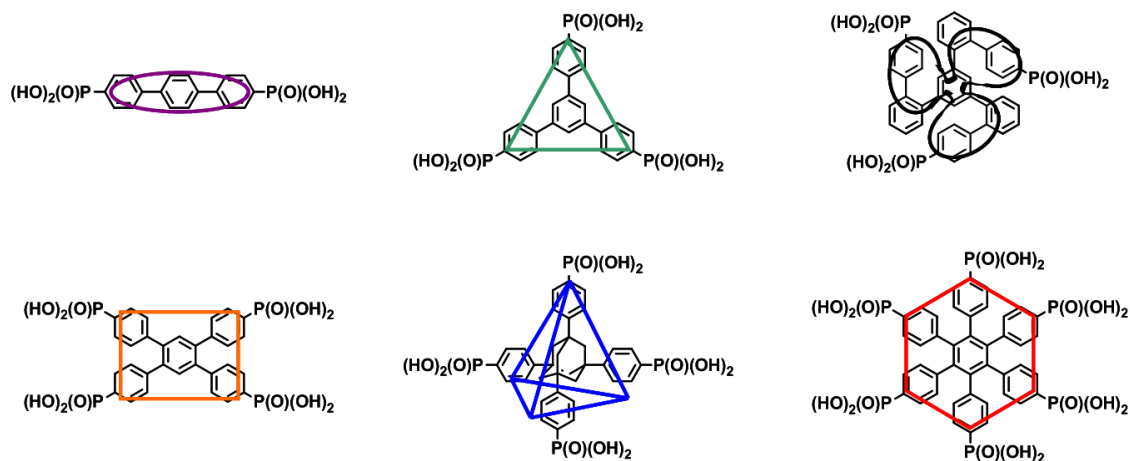


Fig. 2.2: Phosphonic acid-containing small molecules: (*p,p'*-terphenyl-4,4''-diyl)bisphosphonic acid (violet), 1,3,5-tris(*p*-phosphonatophenyl)benzene (green), 1,3,5-tris[4''-(phosphonato)-2'-biphenyl]ylbenzene (black), 1,2,4,5-tetrakis(*p*-phosphonatophenyl)benzene (orange), 1,3,5,7-tetraakis(*p*-phosphonatophenyl)adamantane (blue), hexakis(*p*-phosphonatophenyl)benzene (red).

In the next section the synthesis and proton-conducting properties of HPB derivatives are examined. Three cases center this section: the change of the phosphonic acid groups from the *para* to the *meta* position, the introduction of alkyl chains into the system and the replacement of phosphonic acid functions by sulfonic acid ones. Thermal stability, proton conductivity, water uptake and crystallinity of the materials are compared to these of the model compound treated in Section 3.2. The study presented in this section is a comparison between hexakis(*p*-phosphonatophenyl)benzene and other HPB derivatives through which the impact that the changes of the periphery of the HPB have on proton conductivity are explored. Moreover another aspect considered in this chapter is the improvement of the proton transport properties of model compound hexakis(*p*-phosphonatophenyl)benzene by increasing the phosphonic acid density.

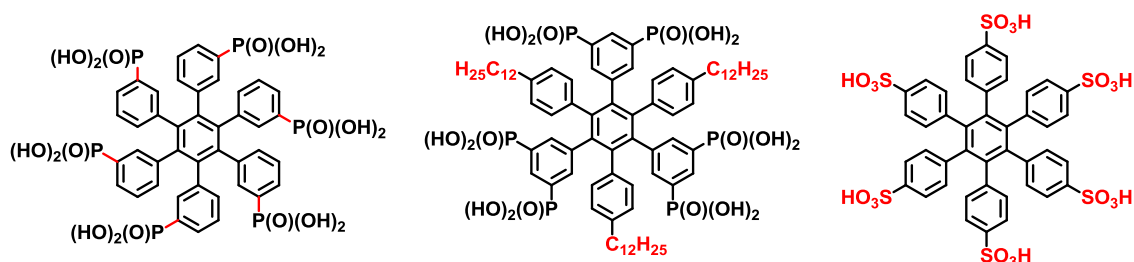


Fig. 2.3: Substituted HPB molecules proposed as solid state separator materials.

The effect of the size expansion of the HPB core in proton conductivity is examined in the last section. For this purpose, two HPB derivatives have been synthesized and characterized and their proton conductivities have been compared to this of their respective analogues. Firstly, the interesting synthesis of these materials is outlined, followed by characterization of the molecule which includes proton conductivity measurements, water uptake and X-ray analysis. These methods can give clues to understand how the molecular ordering and the degree of π -stacking affect the proton conductivity. Furthermore, the increase of the phosphonic acid density in this hydrophobic core is also treated as another way to obtain a molecule with twelve phosphonic acid groups and a hexagonal core.

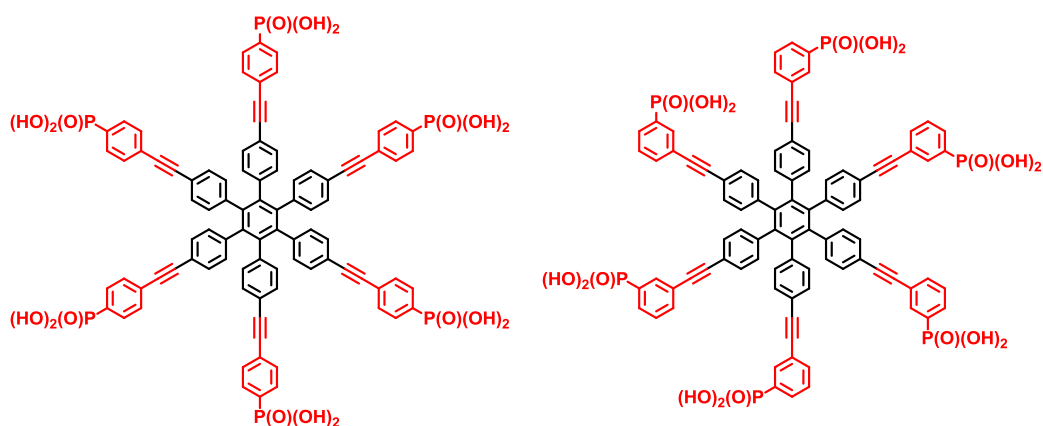


Fig. 2.4: HPB derivatives containing phosphonic acid groups.

2.2 Phosphonic Acid based Organic-Inorganic Hybrid Materials

Metal phosphonates have gained increasing research interest as a result of their potential applications as sorbents,^[25] ion exchangers,^[26] ionic conductors^[27] and catalysts.^[28, 29] Notably, metal phosphonates represent a particularly versatile research field as almost any desired organic compound may be converted to its corresponding phosphonic acid by known reactions.^[30, 31] Moreover, hybrid organic-inorganic compounds in which the phosphonate anions may function as linkers between inorganic groups can be obtained from almost all metals, yielding a great variety of structure types (1D chains, 2D layers, 3D network, and 3D network with channels).^[9-11]

In contrast to the crystalline carboxylic acid based analogues (commonly known as Metal-Organic-Frameworks),^[32] no structure solution of these compounds is possible by X-ray or neutron diffraction techniques since the cross-linked compounds form particles that exhibit only short range order.^[9] Therefore one refers to organic-inorganic hybrid materials or metal phosphonate open-frameworks when porous compounds are synthesized using phosphonic acid based molecules as linkers. However crystallinity is a very important issue since it assures the regularity of the pore sizes through the entire open-framework. A major advantage of phosphonic acid based open frameworks is that in contrast to carboxylic acid based analogues they are chemically stable, i.e. that they feature strong metal-ligand bonds.

However, two issues remain open when discussing porous phosphonated organic-inorganic hybrid materials:

1. Organic-inorganic hybrid materials are most exclusively composed of mono- and bisphosphonates linkers and the use of organic molecules possessing a higher number of phosphonic acid functions remains unexplored.
2. Moreover, the combination of high porosity and crystallinity in those systems has not yet been achieved. Among all known metal phosphonates, layered structures are predominant wherein aryl- or alkylphosphonate molecules are coordinated to the metal oxide layers.^[33-36] Efforts have been made to prevent the formation of simple layers and create phosphonated open-framework structures.^[37, 38] However, all attempts to combine high porosity and crystallinity in those systems have failed.

The work presented in this second part of the dissertation deals with these two concerns. It explores the concept of using a multi-functionalized phosphonic acid based organic molecule and metals of varied coordination numbers with the objective of producing by a non MCM-type approach (i.e., in the absence of surfactant) novel organic-inorganic hybrid materials which can combine crystallinity and porosity.

Two questions are addressed in this section. The first one is whether 1,3,5-tris(*p*-phosphonatophenyl)benzene, which has never been used to obtain phosphonated hybrid materials, is an appropriate choice as linker and can be applied to provide porous solids. The second one is whether one can obtain a phosphonated open-framework which combines porosity and crystallinity. To answer these issues, Chapter 4 details an extensive study of the properties of phosphonated organic-inorganic hybrid

materials obtained by using 1,3,5-tris(*p*-phosphonatophenyl)benzene as linker and various metals as connectors. It is also aimed to propose a mechanism for pore formation in these compounds and to study their application for hydrogen storage.

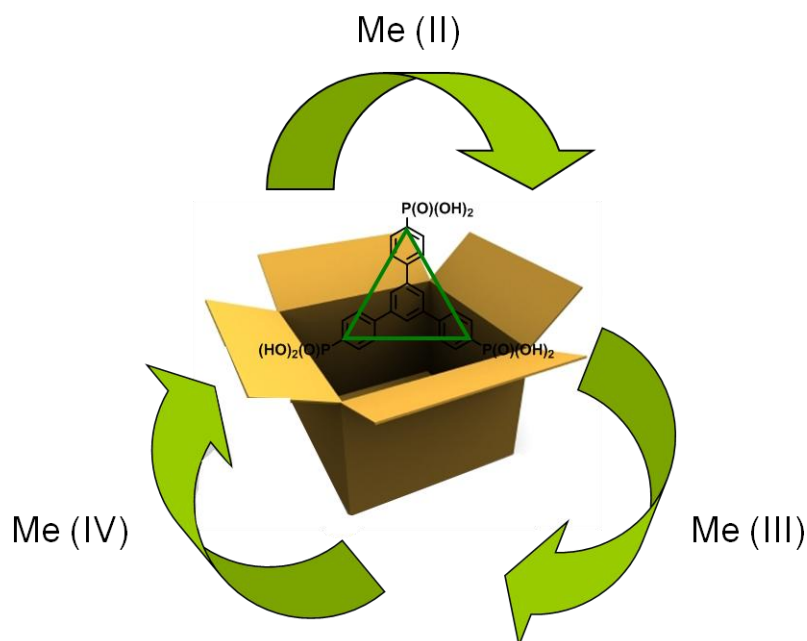


Fig. 2.5: Schematic illustration of the linker and connectors used to produce organic-inorganic hybrid materials.

2.3 Bibliography

- [1] M. M. Reddy, G. H. Nancollas, *Desalination* **1973**, *12*, 61
- [2] B. Nowack, A. T. Stone, *Water Res.* **2006**, *40*, 2201
- [3] C. Brumsen, N. A. T. Hamdy, S. E. Papapoulos, *Medicine* **1997**, *76*, 266
- [4] G. R. Mundy, *J. Clin. Oncol.* **2002**, *20*, 3191
- [5] J. Parvole, P. Jannasch, *J. Mater. Chem.* **2008**, *18*, 5547
- [6] B. Bingöl, W. H. Meyer, M. Wagner, G. Wegner, *Macromol. Rapid Commun.* **2006**, *27*, 1719
- [7] B. Lafitte, P. Jannasch, *J. Polym. Sci., Part A: Polym. Chem.* **2005**, *43*, 273
- [8] B. Lafitte, P. Jannasch, *Advances in Fuel Cells* **2007**, *1*, 119
- [9] A. Clearfield, *Dalton Trans.* **2008**, *44*, 6089
- [10] K. Maeda, *Microporous Mesoporous Mater.* **2004**, *73*, 47
- [11] A. Vioux, J. Le Bideau, P. H. Mutin, D. Leclercq, *Top Curr. Chem.* **2004**, *232*, 145
- [12] S. J. Paddison, K. D. Kreuer, J. Maier, *Phys. Chem. Chem. Phys.* **2006**, *8*, 4530
- [13] K. D. Kreuer, A. Rabenau, W. Weppner, *Angew. Chem. Int. Ed.* **1982**, *21*, 208
- [14] K. D. Kreuer, *J. Membr. Sci.* **2001**, *185*, 29.
- [15] K. D. Kreuer, S. J. Paddison, E. Spohr, M. Schuster, *Chem. Rev.* **2004**, *104*, 4637
- [16] K. D. Kreuer, *ChemPhysChem* **2002**, *3*, 771
- [17] M. Schuster, T. Rager, A. Noda, K. D. Kreuer, J. Maier, *Fuel Cells* **2005**, *5*, 355
- [18] Y. Yang, S. Holdcroft, *Fuel Cells* **2005**, *5*, 171
- [19] J. Ding, C. Chuy, S. Holdcroft, *Adv. Funct. Mater.* **2002**, *12*, 389
- [20] Z. Shi, S. Holdcroft, *Macromolecules* **2005**, *38*, 4193
- [21] L. Rubatat, Z. Shi, O. Diat, S. Holdcroft, B. J. Frisken, *Macromolecules* **2006**, *39*, 720
- [22] T. B. Norsten, M. D. Guiver, J. Murphy, T. Astill, T. Navessin, S. Holdcroft, B. L. Frankamp, V. M. Rotello, J. Ding, *Adv. Funct. Mater.* **2006**, *16*, 1814
- [23] B. Lafitte, P. Jannasch, *Advanced Functional Materials* **2007**, *17*, 2823
- [24] H. Steininger, M. Schuster, K. D. Kreuer, A. Kaltbeitzel, B. Bingöl, W. H. Meyer, S. Schauff, G. Brunklaus, J. Maier, H. W. Spiess, *Phys. Chem. Chem. Phys.* **2007**, *9*, 1764
- [25] A. U. Czaja, N. Trukhan, U. Müller, *Chem. Soc. Rev.* **2009**, *38*, 1284
- [26] A. Clearfield, *Chem. Rev.* **1988**, *88*, 125
- [27] G. Alberti, M. Casciola, E. D'Alessandro, M. Pica, *J. Mater. Chem.* **2004**, *14*, 1910
- [28] G. Alberti, M. Casciola, U. Costantino, R. Vivani, *Adv. Mater.* **1996**, *8*, 291
- [29] D. Deniaud, G. A. Spyroulias, J. F. Bartoli, P. Battioni, D. Mansuy, C. Pinel, F. Odobel, B. Bujoli, *New J. Chem.* **1998**, *22*, 901
- [30] A. K. Bhattacharya, G. Thyagarajan, *Chem. Rev.* **1981**, *81*, 415
- [31] A. L. Schwan, *Chem. Soc. Rev.* **2004**, *33*, 218
- [32] J. L. C. Rowsell, O. M. Yaghi, *Microporous Mesoporous Mater.* **2004**, *73*, 3
- [33] A. Clearfield, *Chem. Mater.* **1998**, *10*, 2801
- [34] M. d. M. Gómez-Alcántara, A. Cabeza, M. Martínez-Lara, M. A. G. Aranda, R. Suau, N. Bhuvanesh, A. Clearfield, *Inorg. Chem.* **2004**, *43*, 5283
- [35] M. d. M. Gómez-Alcántara, A. Cabeza, P. Olivera-Pastor, F. Fernández-Moreno, I. Sobrados, J. Sanz, R. E. Morris, A. Clearfield, M. A. G. Aranda, *Dalton Trans.* **2007**, 2394
- [36] Z. Wang, J. M. Heising, A. Clearfield, *J. Am. Chem. Soc.* **2003**, *125*, 10375
- [37] M. Vasylyev, R. Neumann, *Chem. Mater.* **2006**, *18*, 2781
- [38] J. M. Taylor, A. H. Mahmoudkhani, G. K. H. Shimizu, *Angew. Chem. Int. Ed.* **2007**, *46*, 795

3 Phosphonic Acid based Solid State Proton Conductors

3.1 Introduction

The motivation of this work is to increase proton mobility by a novel concept consisting of the self-assembly and preorganization of phosphonic acid based small molecules. This chapter is directed toward describing the synthesis and studying the properties of hydrogen bonded networks composed of phosphonic acid based small molecules designated to be used as separator materials for FC working at intermediate temperatures.

Fuel cells may help to reduce our dependence on fossil fuels and diminish poisonous emissions into the atmosphere because by using pure hydrogen, they only produce water.^[1] The current state-of-the-art membrane materials for polymer electrolyte fuel cells (PEFCs) are perfluorinated sulfonic acids. These polymers possess a perfluorinated main chain and side chains containing sulfonic acid groups. However one of the major disadvantages of this kind of membrane materials is the performance decrease at elevated temperatures due to the proton transport mechanism taking place through the membrane.

The materials consist of an interpenetrating nanophase-separated apolar backbone and polar ionic domains (see Figure 3.1).^[2] Proton conductivity assisted by water dynamics occurs through the channels within the hydrophilic domains. Therefore, when water is lost due for example to a temperature increase, the performance drops down. However the operation of FCs at high temperatures would simplify the heat and water management and prevent the poisoning of the catalyst by carbon monoxide.^[3] Therefore a membrane material which exclusively transports protons and operates at

elevated temperatures in a low humidity environment is considered the key to further progress in proton-exchanging membrane (PEM) fuel cell technology.

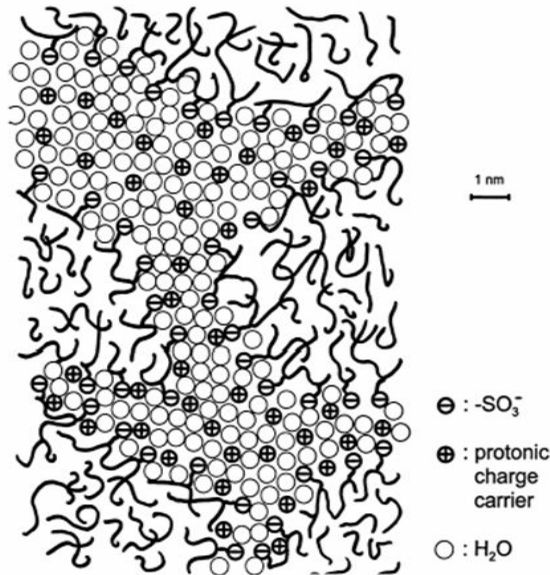


Fig. 3.1: Schematic illustration of the microstructure of Nafion® derived from SAXS experiments.^[2]

Phosphonic acid has been suggested as an alternative protogenic group for intrinsically conducting separator materials due to its amphoteric properties.^{[3],[4],[5]} It has been demonstrated that a high concentration of these acidic groups which are able to aggregate is required to have high intrinsic proton conductivity.^[4]

Up to now, the on-going research has focused on the development of materials which like Nafion® present a nanophase separation between the hydrophobic polymer main chain and the acidic moieties leading to a nanoscopic morphology responsible for the water uptake and proton conduction.^[6] Different synthetic strategies have been applied to obtain polymeric materials with an efficient ionic network, i.e. a defined morphology.^[7-11] In this chapter a novel concept is proposed which consists of using phosphonic acid based small molecules as separator materials for FC applications.

3.2 Hexakis(*p*-phosphonatophenyl)benzene

3.2.1 Synthesis and Characterization

The crystal structure of hexaphenylbenzene (HPB) and its derivatives is known since a long time.^[12, 13] Most recently, crystallographic studies on acidic derivatives have been carried out.^[14-17] It was found that almost all the molecules present multiple hydrogen bonds in the molecular plane and additionally form hydrogen bonds between adjacent sheets in a way that columnar supramolecular networks are formed. The resulting structures can be described as networks of molecules connected by hydrogen bonds.

Inspired by the above mentioned properties of phosphonic acids as well as by the supramolecular self-assembly of HPB derivatives, phosphonic acid groups have been introduced in the non-planar structure of HPB. Hexakis(*p*-phosphonatophenyl)benzene (**4**) is synthesized via a three-step reaction as depicted in Figure 3.2.

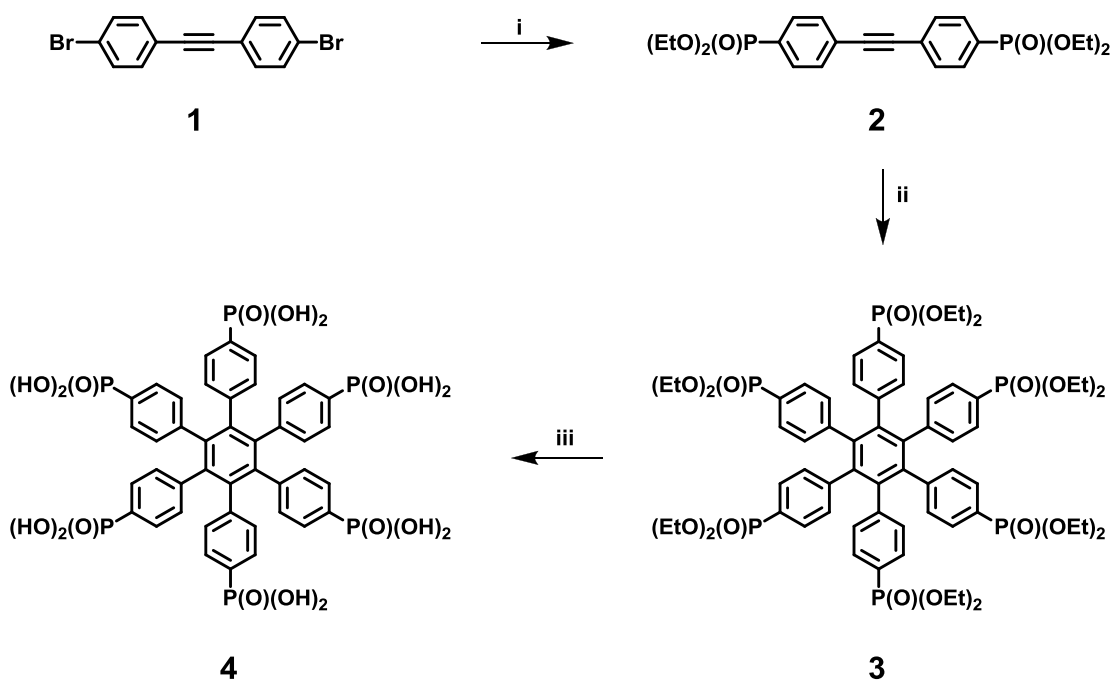


Fig. 3.2: Synthetic route toward hexakis(*p*-phosphonatophenyl)benzene (**4**): i) HP(O)(OEt)_2 , $\text{Pd(PPh}_3)_4$, NEt_3 , toluene, 75 °C, 12 h, 82 %; ii) $\text{Co}_2(\text{CO})_8$, dioxane, reflux, 12 h, 69 %; iii) a. TMS-Br , DCM, RT, 48 h; b. MeOH, RT, 48 h, 97 %.

The phosphonic acid ester groups are introduced into bis(4-bromophenyl)acetylene (1) by a palladium-catalyzed P-C cross-coupling reaction using diethyl phosphite, triethylamine and tetrakis(trisphenylphosphine)palladium.^[18] The principal advantage of this reaction over the commonly used nickel-catalyzed *Michaelis-Arbusov* reaction of an arylbromide or -iodide with triethyl phosphite^[19] is that both temperature and reaction-time are lowered. Subsequently, bis(4-diethylphosphonatophenyl)acetylene (2) is cyclotrimerized using dicobaltoctacarbonyl as catalyst.^[20] The reaction proceeds with moderate yield (69 %) but the educt can be recovered by separation in column chromatography. In the final step, the cleavage of the diethyl phosphonate esters is achieved following a two-step procedure which consists of the treatment by bromotrimethylsilane in DCM at RT followed by methanolysis as shown in Figure 3.3.^{[21],[22]}

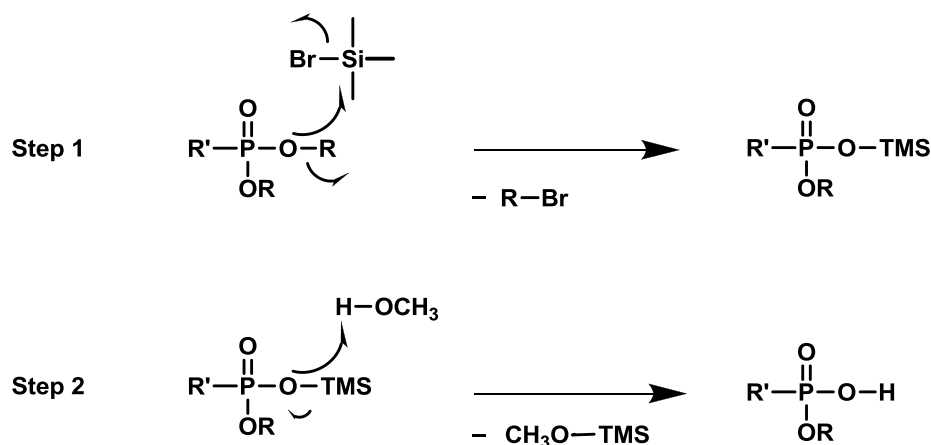


Fig. 3.3: Mechanism of the mild dealkylation and subsequent methanolysis of phosphonate derivatives.

Hydrolysis of diethyl phosphonate esters in solution by normal routes (boiling HCl)^[23] conducts in this case to the rupture of the covalent C-P bond on hexakis(*p*-diethylphosphonatophenyl)benzene (3). After the cleavage of the ester groups, purification by Soxhlet extraction in THF gives a light yellow powder.

The key step of this synthetic strategy is the cyclotrimerization reaction. Since the final product is needed on gram scale, it is necessary to repeat this reaction a high number of times to obtain the desired quantity of material.

An alternative strategy to the above described synthetic procedure is the introduction of the phosphonic acid ester groups on the hexakis(*p*-

bromophenyl)benzene (**5**). However, only a mixture of partially substituted compounds is obtained by using the palladium-catalyzed cross-coupling reaction as well as the analogue *Michaelis-Arbuzov* reaction. This is most probably due to the extremely low solubility of the bromo-substituted HPB both in toluene and mesitylene. The use of microwave conditions does not conduct to the obtainment of the desired product.

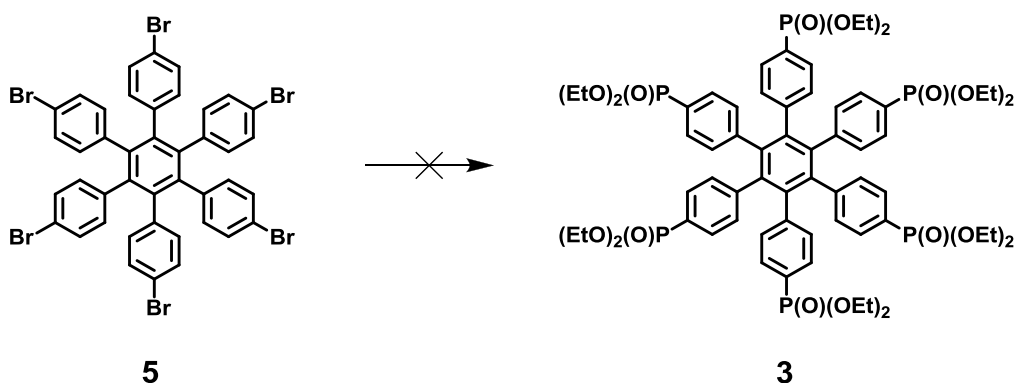


Fig. 3.4: Not-working synthetic route toward hexakis(*p*-phosphonatophenyl)benzene).

Solubility is a crucial issue when preparing novel separator materials for FC applications. The compound designated to be used as proton conductor should not be water soluble to avoid its dissolution during the operation of the cell. The phosphonic acid-containing HPB is poorly soluble in water, water/alcohol mixtures and all kind of organic solvents at RT and only slightly soluble in DMSO at elevated temperatures.

To characterize compound **4**, liquid-state nuclear magnetic resonance (NMR) has been used. The $^1\text{H-NMR}$ spectra of the molecule at different temperatures in deuterated DMSO are depicted in Figure 3.5. In the aromatic region, two peaks can be observed with a ratio 1 to 1: one doublet of doublets at 7.2 ppm and another at 7.0 ppm. However, the shape of the two signals is not identical so that not only the chemical shift but also the shape of the peak serve as indicator to assign the protons of the molecule to the signals of the $^1\text{H-NMR}$ spectrum. The peak at 7.2 ppm corresponds to the proton which is a direct neighbor of the C-P bond (**H1** in Figure 3.5). The peak is split twice (doublet of doublets): firstly since it is coupled with the neighboring proton (**H2**) and secondly because of the coupling with phosphorous. The second peak is a deformed doublet of doublets (**H2** in Figure 3.5): it splits first due to the neighboring proton **H1** and secondly because of the coupling with phosphorous. However, since in this case there is a carbon atom between the C-P and the C-H**2** bonds, the splitting is not so strong like in the case of **H1** and the doublet of doublets is distorted.

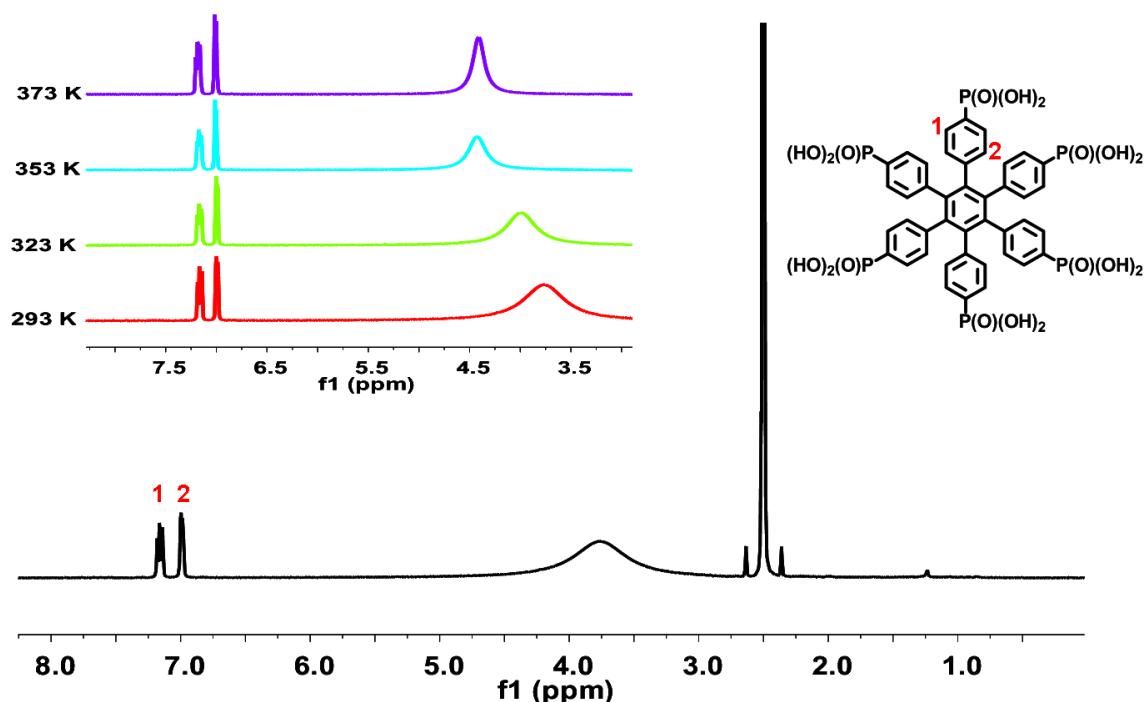


Fig. 3.5: $^1\text{H-NMR}$ spectrum of hexakis(*p*-phosphonatophenyl)benzene in DMSO-d_6 at 373 K and temperature dependent $^1\text{H-NMR}$ spectra recorded at 500 MHz.

The third peak at about 3.8 ppm in the RT $^1\text{H-NMR}$ spectrum is caused by the free protons coming from the acidic groups and the residual water present in the deuterated DMSO. The peak slightly shifts downfield on heating, i.e. from 3.8 ppm at RT to 4.4 ppm at 100 °C.

Figure 3.6 shows the $^{13}\text{C-NMR}$ spin echo spectrum of compound **4** recorded in deuterated DMSO at 373 K. The tertiary carbons appear below the baseline whereas the quaternary above. The two peaks at 131.7 and 130.2 ppm correspond actually to one carbon (C1 in Figure 3.5): the peak is a doublet of spin coupling constant $3J(\text{P,C})$ of 183.3 Hz. The doublet peak at low field with a spin coupling constant $3J(\text{P,C})$ of 3.0 Hz can be attributed to the quaternary carbon labeled C4 in Figure 3.5. Finally the singlet peak at 139.1 ppm corresponds to the quaternary carbon belonging to the unsaturated aromatic ring (C5 in Figure 3.5) which does not couple with the phosphorous atom.

The peaks below the baseline can be attributed to the tertiary carbons C2 and C3 (see Figure 3.5). The peak at about 130 ppm is a doublet of doublets of spin coupling constant $3J(\text{P,C})$ of 9.1 Hz corresponding to C3 whereas the peak at 128.5 ppm

attributed to C2 is a doublet of higher spin coupling constant (10.0 Hz) because it is nearer the phosphorous atom.

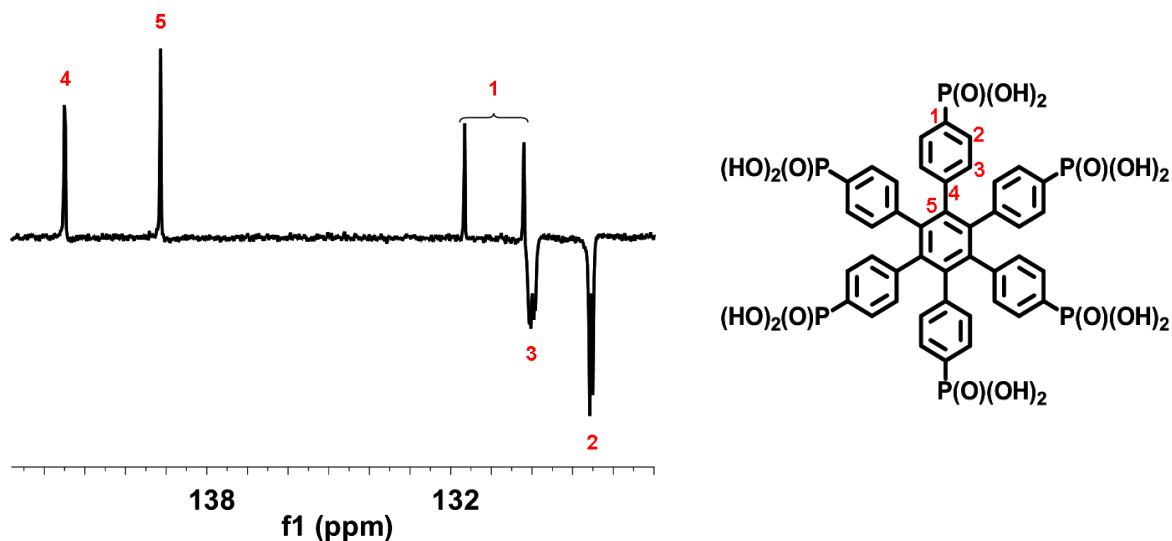


Fig. 3.6: ^{13}C -NMR spin echo spectrum of compound **4** recorded in DMSO- d_6 at 373 K and 126 MHz.

The ^{31}P -NMR spectrum recorded in deuterated DMSO at RT shows one peak at 13.5 ppm which corresponds to the only type of phosphorous atoms present in the molecule.

3.2.2 Proton Conductivity

Through-plane proton conductivity (σ) is the measurement of interest in an operating FC and is usually performed by dielectric impedance spectroscopy (IS). To estimate the possible applications of hexakis(*p*-phosphonatophenyl)benzene as a novel separator material for fuel cells, initial proton conductivity measurements have been performed. In collaboration with Dr. A. Kaltbeitzel from the MPI-P Mainz/Germany, proton conductivity studies have been carried out under different types of conditions. Unlike the commonly used polymeric materials, the synthesized compound has no film-forming properties; therefore like in the case of solid acid proton conductors^[24] hand-pressed pellets (100 mg, 5.5 mm diameter, 2.1 mm thickness) have been used for these measurements. Therefore, through-plane in opposite to in-plane conductivity measurements have been performed. The shape of the pellet remains identical

throughout the entire process for the different measurements performed, indicating that the molecule is stable during fuel cell operating conditions described below.

In order to simulate the working conditions of an intermediate-temperature fuel cell, through-plane proton conductivity has been measured under 1 bar H₂O atmosphere by increasing temperature until 180 °C, i.e. by decreasing relative humidity (RH) until 20 %ⁱ (Figure 3.7). Under these conditions, the temperature dependence of the conductivity is defined by the opposing effects of decreasing RH and increasing thermal activation with increasing temperature. Therefore, the behavior of the conductivity of the compound gives some insights into the proton transport mechanism taking place through the material. On the one hand, a conductivity which decreases with increasing temperature is evidence of a vehicle mechanism.^{[25],[2]} On the other hand, a conductivity which increases with increasing temperature is related to an intrinsic proton transport (*Grotthuss*-type mechanism).^[26]

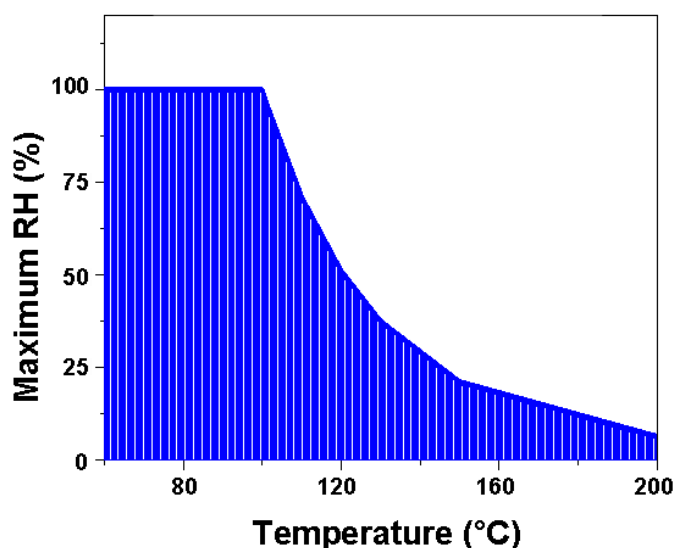


Fig. 3.7: Maximum RH as a function of temperature at 1 bar H₂O pressure.

The proton conductivity of the investigated compound above 100 °C under 1 bar H₂O atmosphere is depicted in Figure 3.8. These investigations show high proton conductivity values ($3.4 \cdot 10^{-3} \text{ S} \cdot \text{cm}^{-1}$ at 180 °C), especially when compared to inorganic hydrates^[27] or some phosphonic acid containing polymers.^[28] The obtained values are

ⁱ The maximum RH of air above 100 °C at 1 bar can be calculated from a steam pressure table.

only slightly inferior to the target conductivity for intermediate temperature separator materials which is between $1 \cdot 10^{-1}$ and $1 \cdot 10^{-2}$ S/cm.^[29, 30] Surprisingly, hexakis(*p*-phosphonatophenyl)benzene presents a proton conductivity which is temperature independent. Contrary to Nafion® 117 and the above mentioned polymers, this rather rigid system has an almost constant proton conductivity with increasing temperature and furthermore exhibits higher values of proton conductivity than Nafion® 117 above 160 °C. The decrease of the proton conductivity of Nafion® with temperature is a known phenomenon explained by the vehicle mechanism, however no clue about the proton transport mechanism taking place through **4** and its high proton conductivity values could be found just by contemplating these data. This absence of any significant temperature dependence has been only observed before for a phosphonated fully aromatic polymer,^[31] which presents however slightly inferior proton conductivity values. Moreover, in the case of compound **4** the temperature region in which the conductivity remains constant is higher than in the case of this phosphonated polymer (from 110 to 180 °C for **4** and from 140 to 170 °C for the polymer). The authors explain the behavior of the polymer by the opposing effects of decreasing RH and increasing temperature at 1 bar H₂O atmosphere: conductivity initially decreases with increasing temperature and then approaches asymptotically the conductivity of the water-free sample. However, no more details of such an uncommon behavior are given in this study and the proton transport mechanism taking place through the polymer is not elucidated. For this all, no clue can be found which can help to explain the performance of compound **4** and the proton transport through the material.

It has been demonstrated that a high concentration of phosphonic acid groups is needed to achieve high proton conductivity.^[4] The density of acidic functions in compound **4** is calculated by using the following equation:

$$d = \frac{6 \cdot M_w(P(O)(OH)_2)}{M_w(Ph)(OH) + 6M_w(Ph)(4H)} = \frac{485.94}{528.69} = 0.92$$

where *d* is the density and Ph a phenyl ring.

This value is very high and is in accordance with the above mentioned relation between density of phosphonic acid groups and proton conductivity. It can be then concluded that hexakis(*p*-phosphonatophenyl)benzene presents so high proton conductivity values because the density (concentration) of phosphonic acid functions is very high (0.92).

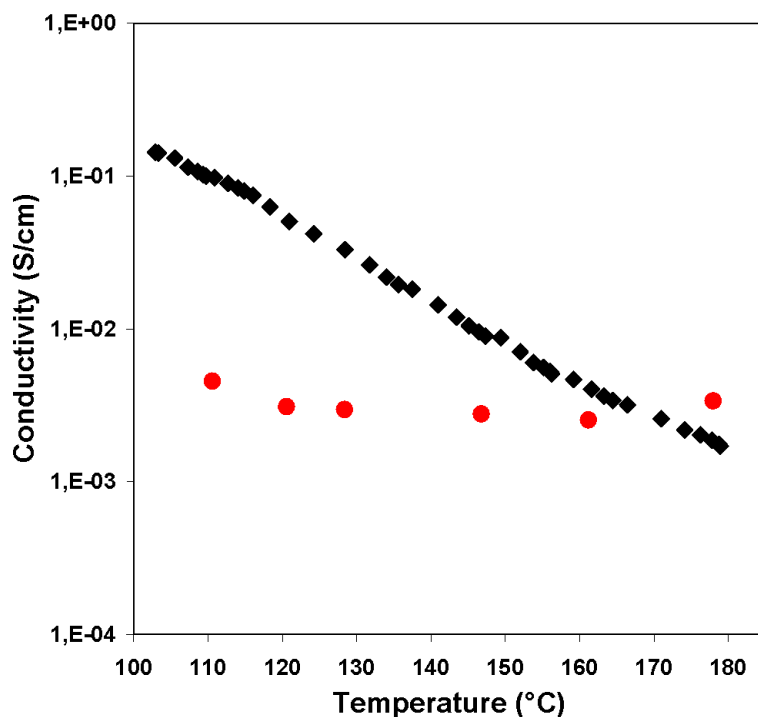


Fig. 3.8: Plots of the proton conductivity vs. temperature under 1 bar H₂O atmosphere for hexakis(*p*-phosphonatophenyl)benzene (●) and Nafion® 117 (◆).

Proton conductivity measurements at 25 °C by increasing and decreasing RH have been conducted to study the behavior of compound **4** only by changing one parameter, the RH (in the previous experiments, both the temperature and the RH are varied). It is expected to gain a deeply knowledge of the proton transport mechanism taking place through the material.

Figure 3.9 shows the proton conductivity of hexakis(*p*-phosphonatophenyl)benzene at RT by increasing and decreasing RH and the one of Nafion® by decreasing RH. A constant increase in proton conductivity is noticed for compound **4** while increasing RH. This is probably due to the macroporous morphology of the pellet, enabling for the proton transport along water molecules that are adsorbed on the pore surfaces. Around 50 % RH, a step in conductivity is observed and could not be explained. At RT and 95 % RH, the examined material has a high proton conductivity of $2.5 \cdot 10^{-2} \text{ S} \cdot \text{cm}^{-1}$ which is comparable to that of mixtures of inorganic acids.^[32]

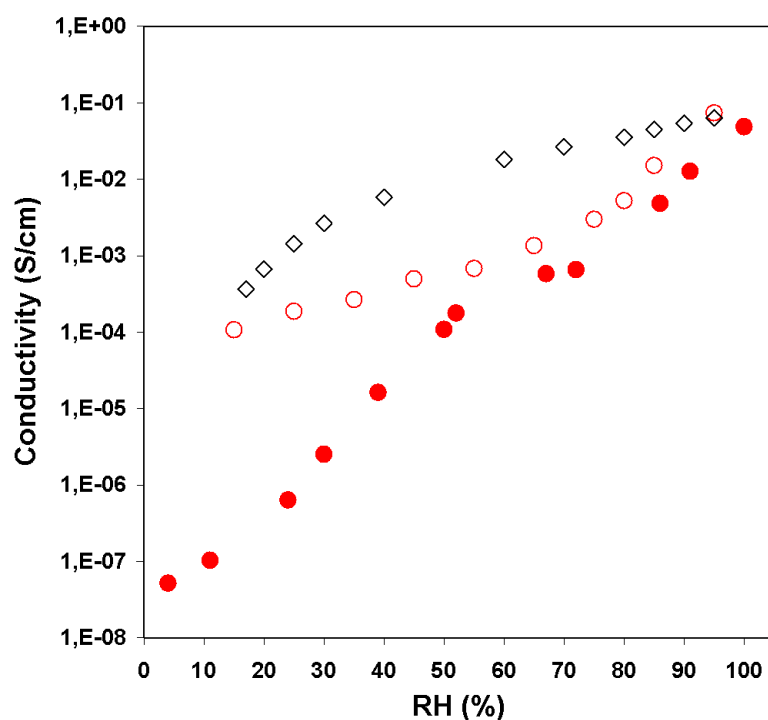


Fig. 3.9: Plots of the proton conductivity of hexakis(*p*-phosphonatophenyl)benzene at RT by increasing (●) and decreasing (○) RH and of Nafion® 117 (◇) by decreasing RH.

A hysteresis can be observed on the conductivity curve of the same pellet by decreasing RH. Moreover, these measurements provide higher conductivity values. This difference is due to the fact that to execute the measurements the pellet has to be at an atmosphere of 100 % RH until equilibrium is reached. During this time, the compound adsorbs water molecules which contribute to proton transport.

The curve of the conductivity by decreasing RH at RT can help to understand why compound **4** presents a constant performance by increasing temperature (Figure 3.8) since both measurements have been performed by decreasing RH. It can be observed that while the conductivity of Nafion® 117 drops off below 40 % RH due to the lower presence of water in the system, compound **4** do not experiments such a pronounced conductivity decrease. This result may indicate that its proton conductivity is not based on the vehicle mechanism.

The transport of a proton from one site to another is a process which involves the passage from a higher to a lower energy configuration through which protons must overcome a certain energy barrier. It is of interest to study the energy barrier which protons have to surmount in hexakis(*p*-phosphonatophenyl)benzene (**4**) since this

value might give some additional information about the type of proton transport mechanism which takes place through the material. On account of this, proton conductivity has to be measured as a function of temperature under anhydrous conditions.

Ion conduction in solid electrolytes has been described by *Funke et al.*^[33, 34] with the use of a modified *Debye-Hückel*-type model. It is described as being a long-distance ion migration which involves at least two steps:

1. Translocation by hopping of the ion from site A to site B (given that the ion is exposed to a gradient of an electrical field).
2. Reorganization of site B to form a lower energy configuration otherwise the proton will hop back to site A. The reason is that the hopping of ion from site A to B creates a local electrical field which will bring the ion back to site A; only if relaxation happens in the same time scale and the energy of site B becomes lower than site A, the ion will stay at site B waiting for the chance to hop to the next vacancy along the field direction (x axis), otherwise, no long-distance ion migration will occur.

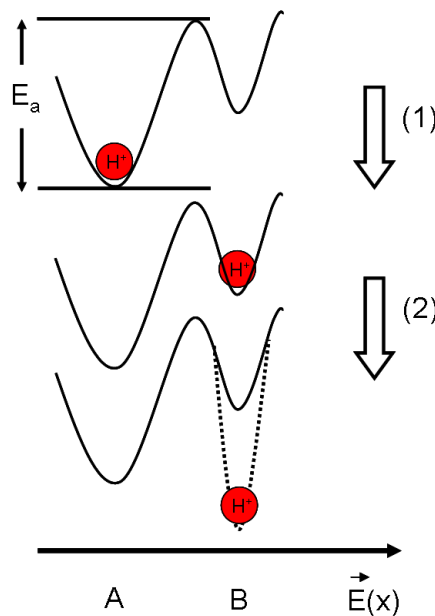


Fig. 3.10: Schematic representation of the two steps necessary for proton hopping in the model of *Funke et al.*

The temperature dependence of the conductivity can be taken as being indicative of a particular type of conduction mechanism. In particular, when a conductivity obeys the *Arrhenius* equation, a plot of $\ln(\sigma)$ versus $1/T$ gives a straight line, whose slope and intercept can be used to determine E_a and σ_0 :

$$\sigma = \sigma_0 \cdot \exp\left(\frac{-E_a}{R \cdot T}\right)$$

where E_a , R , T , σ_0 represent the activation energy, gas constant, temperature and pre-exponential factor respectively.

The activation energy (energy barrier height) is a rate determining factor of the conductivity process. The motion of ions is a thermally activated process and the ions need to have sufficient energy to overcome the energy barrier E_a . The pre-exponential factor σ_0 is the limiting conductivity of the system at infinite temperature ($1/T = 0$).

The proton conductivity of hexakis(*p*-phosphonatophenyl)benzene (**4**) has been measured as a function of temperature under different humidity conditions, i.e. different RH, so that the apparent activation energy of the compound can be calculated at various RH.

The proton conductivity of compound **4** under dry N_2 flux (0 % RH) is plotted in Figure 3.11 together with its corresponding error bar. The pellet is first heated from RT to 160 °C, then cooled to RT and heated again. This is done in order to get rid of the possible water present in the sample. Proton conductivity is recorded during the three temperature cycles; however Figure 3.11 only reports the third cycle which corresponds to the intrinsic proton conductivity.

The *Arrhenius* plot is almost linear in the experimental temperature range (proton conductivity increasing with temperature), indicating that one dominant proton conducting mechanism, with constant activation energy, is present in the material. In other words, ion hopping resulting in the observed conductivity is a thermally activated process. The maximum anhydrous proton conductivity observed for hexakis(*p*-phosphonatophenyl)benzene is $1.10^{-4.3} \text{ S}\cdot\text{cm}^{-1}$ at 160 °C. This value is almost 10 times higher than the one observed for an annealed PVPA sample ($\sim 1.10^{-5.5} \text{ S}\cdot\text{cm}^{-1}$)ⁱⁱ.^[35]

It has been demonstrated that compounds possessing low activation energy will present a fast proton transport and high conductivity.^[25, 36] Since compound **4** and

ⁱⁱ The value is taken from Figure 6.10. The exact value remains unclear since the author does not mention it in the text.

PVPA have the same activation energy, one would expect also that they present the same conductivity under anhydrous conditions. However, compound **4** shows higher proton conductivity values suggesting that the proton transport is faster in its case.

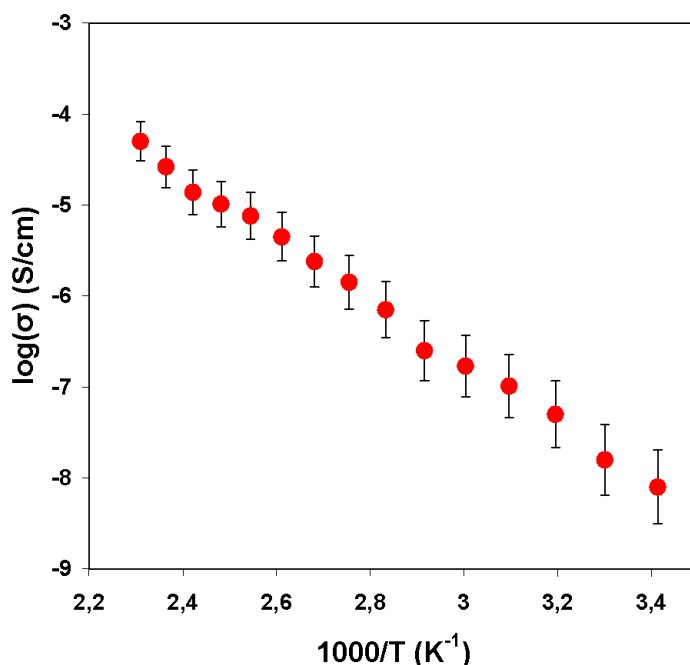


Fig. 3.11: The *Arrhenius* plot of hexakis(*p*-phosphonatophenyl)benzene from measurements performed at 0 % RH and the error bar.

Proton conductivity measurements have also been performed at 15, 50 and 80 % RH and the corresponding activation energies have been calculated from the slope of the *Arrhenius* plots using the above mentioned formula. Figure 3.12 displays the *Arrhenius* plots for the three humidity conditions and the corresponding error bars. It can be observed that the higher the RH applied, the higher the proton conductivity values obtained and the smaller the slope of the *Arrhenius* plot. This indicates that when increasing the RH, the activation energy diminishes and thus the proton conductivity increases.

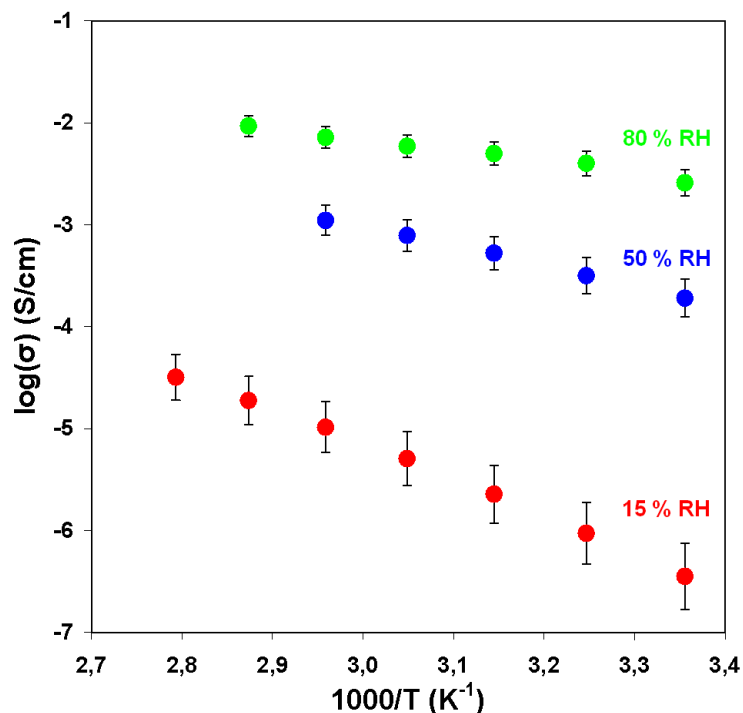


Fig. 3.12: The *Arrhenius* plot of hexakis(*p*-phosphonatophenyl)benzene from measurements performed at 15, 50 and 80 % RH depicted in red, blue and green respectively and the corresponding error bars.

The activation energies are summarized in Table 3.1. Upon increasing the RH from 0 to 15 %, the activation energy stays constant whereas a further increase of the RH to 50 % implies a decrease of the activation energy to almost the half of its initial value. At 80 % RH the activation energy is a third of the value obtained under anhydrous conditions. It can be concluded that only a determined RH the activation energy starts to decrease.

Table 3.1: Activation energies calculated from the slope of the *Arrhenius* plots at different humidities.

RH (%)	E _a (± 5 %) (kJ/mol)
0	65
15	65
50	37
80	21

From these impedance spectroscopy investigations it can be concluded that compound **4** presents:

- very high proton conductivity ($3.2 \cdot 10^{-3} \text{ S} \cdot \text{cm}^{-1}$) under 1 bar H_2O atmosphere due to the high density (0.92) of phosphonic acid groups;
- a smooth conductivity decrease below 40 % RH at RT which indicates that the mechanism for proton transport may be different to the vehicle mechanism;
- an activation energy ($65 \pm 5 \text{ kJ/mol}$) equal to that of PVPA but a conductivity under anhydrous conditions 10 times higher ($1 \cdot 10^{-4.3} \text{ S} \cdot \text{cm}^{-1}$ at 160 °C) ;
- an activation energy that starts to diminish at around 50 % RH.

However, the question as to why under 1 bar H_2O atmosphere this organic molecule attains a proton conductivity which remains constant while increasing the temperature could not be elucidated with just the help of impedance spectroscopy. Therefore, further investigations have been performed.

3.2.3 Thermal Stability

The thermal stability and degradation of **4** have been studied by a combination of analytical techniques including thermogravimetric analysis (TGA) and thermogravimetric analysis coupled to mass ion spectroscopy (TGA-MS) to identify the volatile products which evolve during the degradation of the solid.

Firstly, TGA measurements have been performed under N_2 (Figure 3.13). Three degradation steps are present in the compound at 100, 200 and 450 °C.

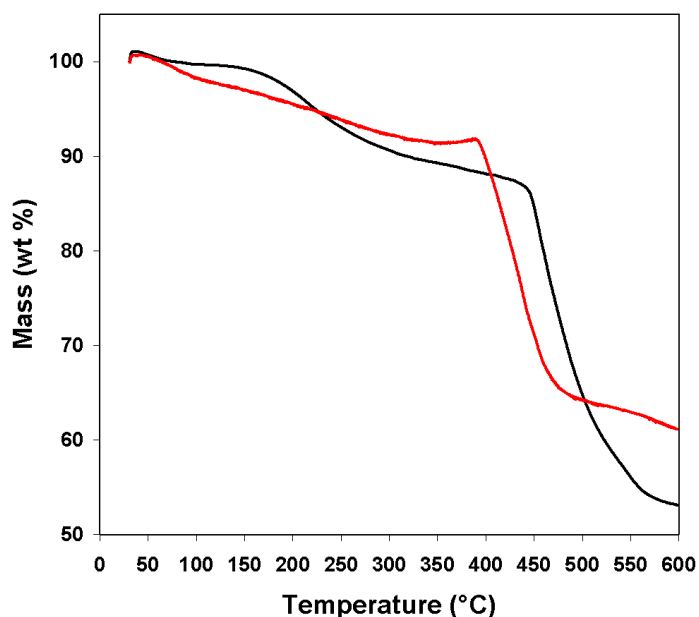


Fig. 3.13: TGA curve of hexakis(*p*-phosphonatophenyl)benzene recorded at 10 K/min under N₂ and under air (black and red curve respectively).

The results from TGA-MS depicted in Figure 3.14a show that only the intensity of the mass corresponding to H₂O and to OH groups is changing as a function of temperature. The intensity of these two signals increases at around 100 and 250 °C. From 25 to 400 °C the mass loss is ~ 12 wt %, which corresponds to ~ 6.7 water molecules per **4**. Since the maximum weight loss due to self-condensation of the acidic groups is limited to 3 water molecules per compound (~ 5 wt %)ⁱⁱⁱ, condensation alone cannot explain the total weight loss. This might then also be due to water “coordinatively” bonded in the structure of the material like it is the case for crystal hydrates.^[37] The water amount lost at around 250 °C suggests that hydrates of **4** (C₄₂H₃₆O₁₈P₆·nH₂O) prevail even after vacuum drying at temperatures below 200 °C.

The third mass loss of 32.7 wt % from 447 to 600 °C is most probably due to the decomposition of the hydrophobic core. An exothermic peak corresponding to a crystallization temperature is observed at around 318 °C and an endothermic one fitting to a melting point at around 329 °C in the cooling and second heating curves of the DSC respectively.

ⁱⁱⁱ Only intramolecular condensation is taken into account even if intermolecular condensation is also likely to occur.

TGA was also performed under O₂ (red curve in Figure 3.14a). No significant differences are observed when these TGA experimental values are compared to those of the TGA performed under N₂. From these data, it is expected that hexakis(*p*-phosphonatophenyl)benzene is stable at intermediate temperatures that are relevant for FC operation.

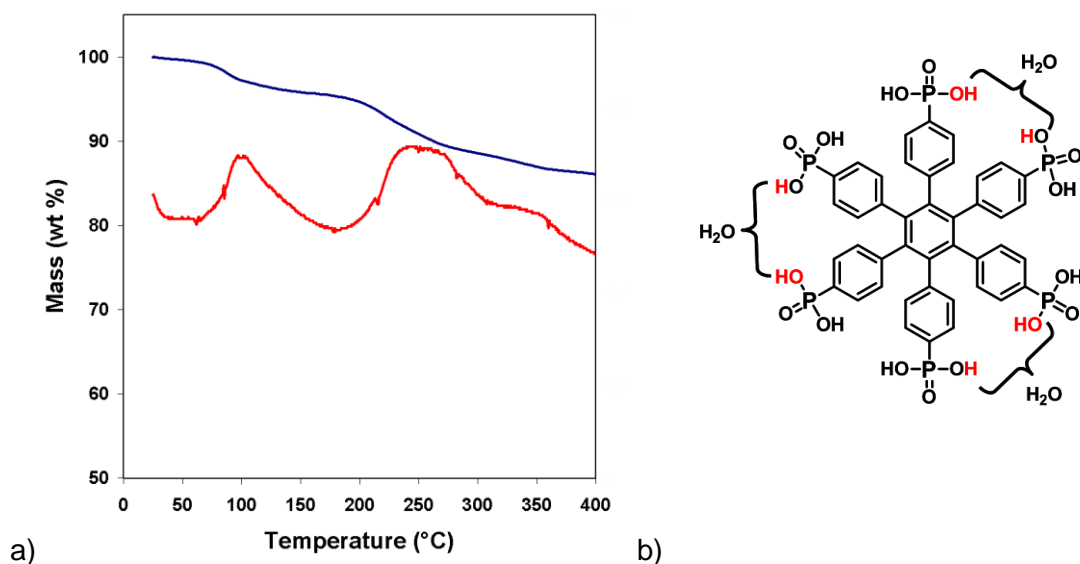


Fig. 3.14: a) The blue curve represents the TGA of hexakis(*p*-phosphonatophenyl)benzene recorded at 10 K/min under He and the red one the H₂O intensity recorded during the TGA-MS measurement. b) Representation of the possible self-condensation reactions in one molecule of compound **4**.

It has been suggested in view of these TGA results that some defined amount of bonded water is incorporated in the structure of hexakis(*p*-phosphonatophenyl)benzene. This fact is characteristic of crystal hydrates. However, it has not been concluded yet whether the examined material is a hydrated crystal and whether these water molecules contribute to proton transport. In case that the answer to the latter question is positive, it would remain to determine what role the water molecules have on the proton transport phenomenon.

Moreover, it has to be taken into account that water molecules interact with the phosphonic acid group as bases or acids. The presence of a basic oxygen atom in P=O with a highly available electronic density is responsible for the interactions where water acts as an acid. The formation of such structures strongly affects the molecular geometry due to the changes in electronic density imposed by the presence of water molecules.

3.2.4 Water Uptake

Water uptake measurements at RT and 80 °C have been conducted to try to determine whether the compound is a hydrated crystal. In order to determine the amount of water adsorbed, the samples have been stored under an atmosphere of fixed RH and temperature for several days until equilibrium weight was reached. No sample morphology changes with increasing and decreasing RH have been noticed.

Water sorption and desorption isotherms at RT are depicted in Figure 3.15. A stepwise hydration/dehydration and hysteresis, also called type VI van der Waals isotherm,^[38] is observed. This behavior is characteristic of crystal hydrates which at each plateau accommodate a certain number of water molecules in their crystalline structure.^[37] Interestingly, the hydration steps are close to integer multiples of water molecules per hexakis(*p*-phosphonatophenyl)benzene (0.5, 1 and 3 water molecules). The pronounced hysteresis isotherm predicts that a considerable amount of loosely bonded water can remain in the material down to 10 % RH. These investigations show that a complex network of hydrogen bonds can be formed to promote a proton transport.

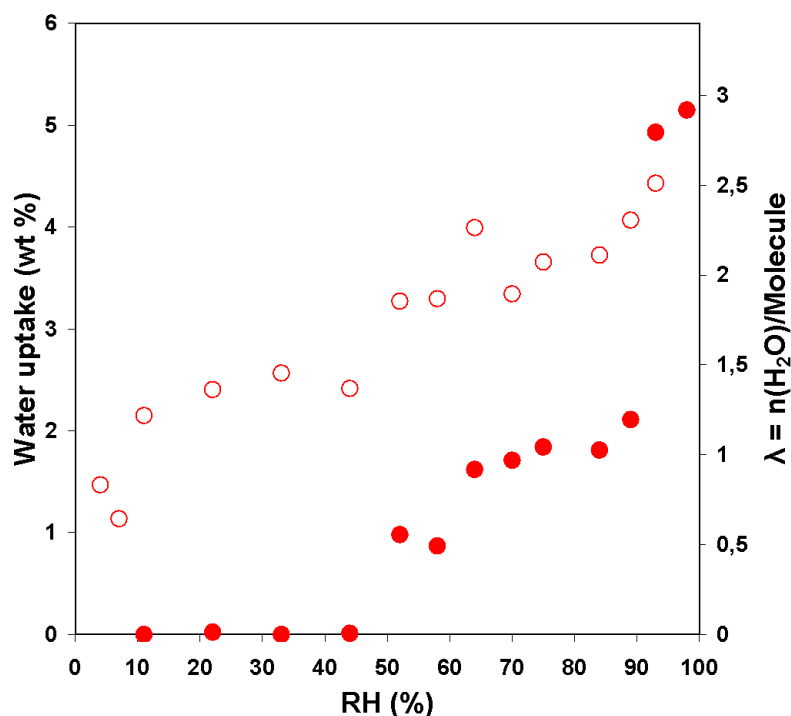


Fig. 3.15: Water sorption (●) and desorption (○) isotherms at RT.

Water uptake has been also measured at 80 °C (Figure 3.16). It can be noticed that the compound starts to take up water at lower RH than at RT, however the maximum water uptake is also lower. A hysteresis is observed like in the case of the measurements performed at RT but indeed the constant water desorption at RH below 50 % is no longer present in this case. In the case of PVPA, the data display little dependence of water sorption on the temperature at fixed RH. This is expected for only weakly bound water that is constantly exchanged with water molecules from the atmosphere.^[28] For compound **4** the difference between the water sorption values at RT and 80 °C might indicate that water is strongly bonded since the temperature increase favors the sorption of water molecules within the material.

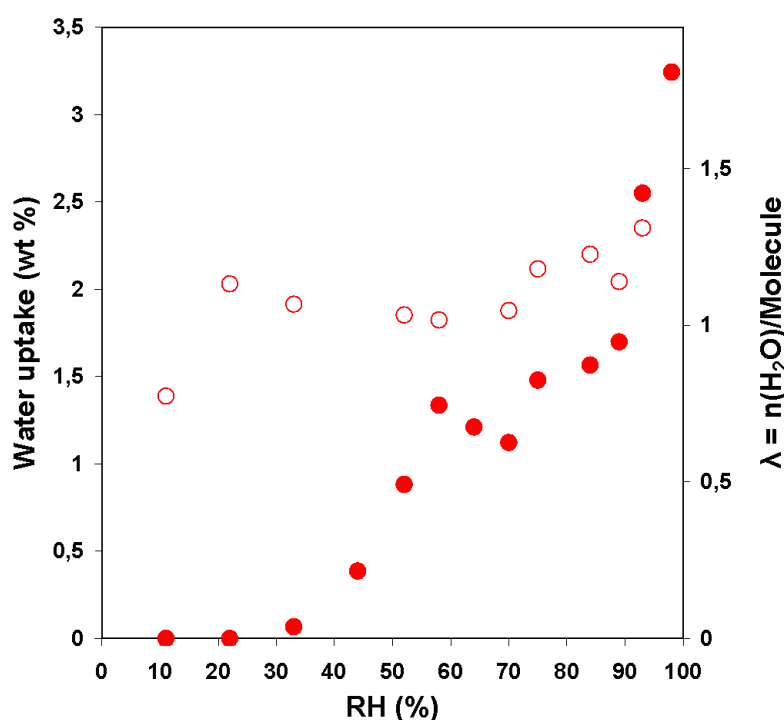


Fig. 3.16: Water sorption (●) and desorption (○) isotherms at 80 °C.

Compared to polymeric electrolyte membranes,^{[39],[40],[41],[28]} hexakis(*p*-phosphonatophenyl)benzene shows very low water adsorption values and very low lambda. Usually, the water uptake values at RT reach a maximum of 25.5 wt % for sulfonic acid based polymers^[42] and of 100 wt % for phosphonic acid based polymers,^[28] whereas in the case of the compound **4** the maximum values is 5 wt %.

From these results it can be concluded that the water uptake measurements corroborate the assumption that the studied compound is a crystal hydrate.

Water uptake measurements not only give a clue to determine the nature of compound **4**, but also to elucidate why its proton conductivity remains constant when the temperature increases under 1 bar H₂O atmosphere. The step-like water desorption isotherm of hexakis(*p*-phosphonatophenyl)benzene is the most likely reason for the flat temperature response of the material. The RH, set by a H₂O atmosphere at 1 bar, decreases with increasing temperature according to the table of vapor pressure. Proton conductivity measurements were realized under 1 bar H₂O atmosphere above 100 °C, which corresponds to a RH lower than 50 %. As can be seen in the desorption isotherm, above 50 % RH hexakis(*p*-phosphonatophenyl)benzene accommodates about 2 water molecules in its structure. It is therefore assumed that these immobilized water molecules act as proton donor and acceptor instead of being diffusible carrier molecules.

Proton conductivity investigations at RT by decreasing RH (Figure 3.9) can also be compared to water uptake studies (Figure 3.15). It is noticed that contrary to the adsorption isotherm, there is a constant increase in conductivity when starting with a well dried material. The step in conductivity observed around 50 % RH is actually in agreement with the plateau of the water uptake study.

From TGA and water uptake analysis, it can be stated that compound **4** has the following characteristics typical of crystal hydrates:

- Weight loss at 200 °C which corresponds to ~ 5 H₂O molecules (TGA-MS);
- Stepwise adsorption and desorption isotherms;
- Pronounced hysteresis of the desorption curve.

Moreover, the role of water in the proton transport through the material could be determined (water is just a donor and acceptor of protons and not a mobile vehicle) and the constant proton conductivity under 1 bar H₂O atmosphere explained with the help of water uptake investigations. In addition, water uptake studies could be correlated to the change of the activation energy while increasing RH. However, it cannot be concluded that the material is a crystal hydrate before having studied its crystalline properties. Therefore, different crystallinity studies have been carried out which will give some light in understanding the system.

3.2.5 Crystallinity

In collaboration with Prof. J. S. Gutmann from the MPI-P Mainz/Germany, wide angle X-ray scattering (WAXS) measurements have been performed at different temperatures and RH. As can be seen in Figure 3.16, the material is crystalline. The degree of crystallinity is determined by calculating the ratio of the integrated peak area to total area. To do so, first the integration of the domain below the peak area has to be assessed followed by the calculation of the total area below the obtained curve. The ratio of the first integral to the second gives the crystallinity degree.^[43] It is found that hexakis(*p*-phosphonatophenyl)benzene is 93 % crystalline at 33 % RH and RT.

The local order is only slightly affected by changing temperature and RH. These changes are attributed to small local packing variations probably caused by the evaporation of water at high temperatures. A notable effect caused by the increase of temperature is the disappearance of one peak at low angles indicated in green in Figure 3.17a. By increasing the RH, it is observed that the two peaks indicated in green in Figure 3.17b become broader.

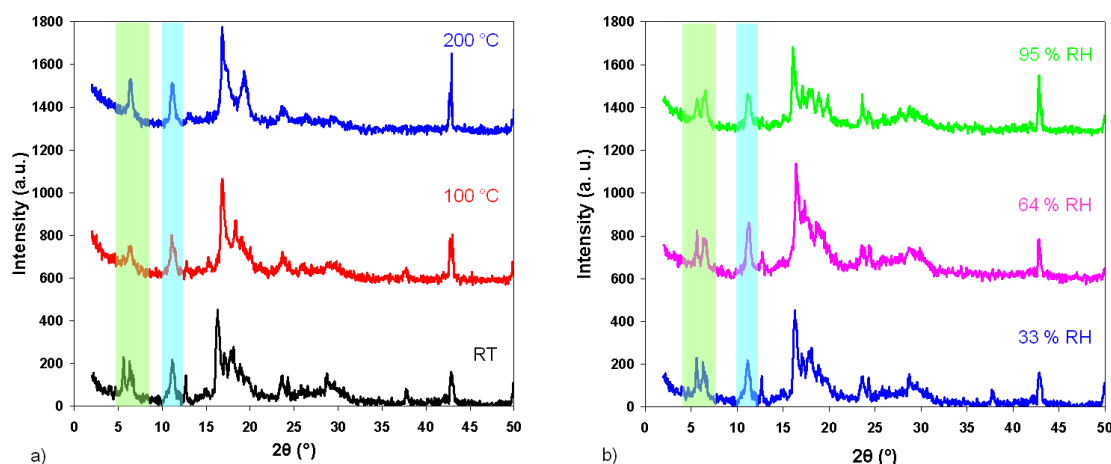


Fig. 3.17: X-ray diffractograms of hexakis(*p*-phosphonatophenyl)benzene a) at 33 % RH and RT, 100 and 200 °C (black, red and blue lines respectively) and b) at RT and 33%, 64 % and 95 % RH (blue, pink and green lines respectively).

The distance d between atomic layers (in angstroms Å) in a crystal can be calculated using *Bragg's law*:

$$n \cdot \lambda = 2 \cdot d \cdot \sin(\theta)$$

where n is an integer (1 is used for most calculations), λ is the wavelength of the X-ray (this is 1.54 Å if copper is the target metal) and θ is the angle between the incident ray and the scattering planes (diffraction angle) in degrees.

The distances at low angles from the diffractograms obtained under different temperatures and RH are calculated by using *Bragg's law*. The results are summarized in Table 3.2. If it is supposed that the molecules arrange into columns, d3 would correspond to the intracolumnar distance whereas d1 and d2 to the intercolumnar ones. So following this supposition it can be noted that the intracolumnar distance remains identical in all experimental conditions applied whereas the intercolumnar one suffers slightly from the change of the external parameters.

Table 3.2: Atomic distances at low angle for compound **4** calculated from the diffractograms of WAXS measured under different conditions.

Experimental conditions	d1 (nm)	d2 (nm)	d3 (nm)
RT and 33 % RH	1.6	1.4	0.8
100 °C and 33 % RH	-	1.4	0.8
200 °C and 33 % RH	-	1.4	0.8
64 % RH and RT	1.6	1.3	0.8
95 % RH and RT	1.5	1.4	0.8

In collaboration with Dr. W. Pisula from the MPI-P Mainz/Germany, two-dimensional wide-angle X-ray scattering (2D WAXS) experiments on mechanically oriented filaments have been performed. In contrast to the previous crystallinity studies, the material is extruded as a fiber resulting in a macroscopically oriented sample which is measured in a temperature dependent 2D X-ray diffractometer (Figure 3.18a). The diffraction pattern in transmission mode is recorded while blocking the primary beam.

2D WAXS is a very important tool for the characterization of liquid crystalline compounds like for example hexa-*peri*-hexabenzocoronene derivatives (HBCs).^[44, 45] The material is extruded as a fiber resulting in a macroscopically oriented sample which is measured in a temperature dependent 2D X-ray diffractometer (Figure 3.18a). The fibers are oriented perpendicular to the incident beam, resulting in 2D diffractograms (Figure 3.18b) which reveal characteristic reflections. Along the vertical (meridional) axis of the spectrum, the reflexes correspond to the intracolumnar stacking

of the discs (Figure 3.18b, c and c'). On the horizontal (equatorial axis), the reflexes can be assigned to the intercolumnar arrangement (Figure 3.18b, a) while the alkyl side-chains provide diffuse reflexes, as they cannot be oriented via extrusion and therefore only allow a diffuse scattering, resulting in a ring on the image (alkyl-halo) (Figure 3.18b, b).

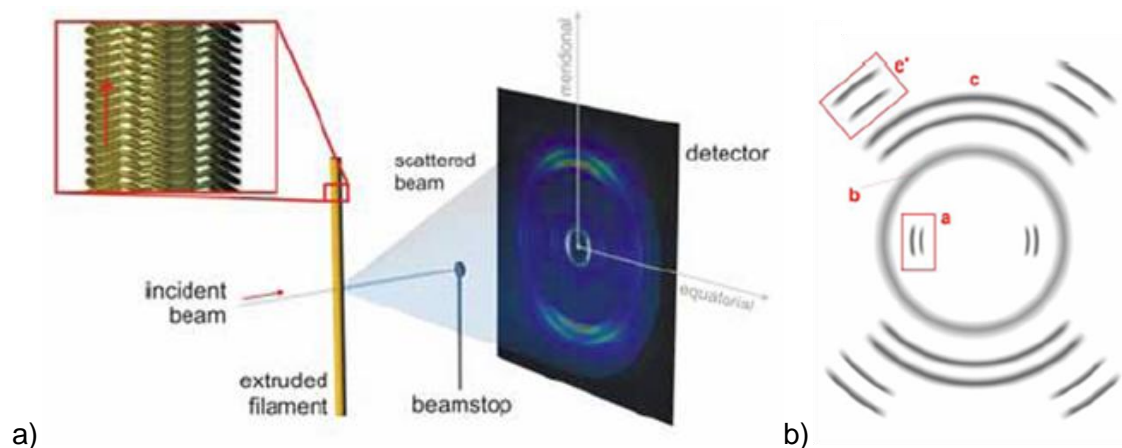


Fig. 3.18: a) Schematic illustration of the experimental setup of the 2D-WAXS scattering on mechanically aligned samples (inset shows the molecular organization within the fiber). b) Typical X-ray pattern of HBCs.

The 2D WAXS pattern of hexakis(*p*-phosphonatophenyl)benzene is depicted in Figure 3.19. Reflections both in the meridional and equatorial axis can be observed corresponding to the intra- and intercolumnar distances (Figure 3.19a). From this pattern, it can be deduced that compound **4** self-assembles into columnar structures in a hexagonal packing (Figure 3.19b). The molecules are stacked on top of each other with a distance of 0.6 nm, and an intercolumnar distance of 1.4 nm.

Moreover, it has been observed that hexakis(*p*-phosphonatophenyl)benzene shows a columnar alignment in the extruded filaments perpendicular to the alignment direction. This unusual orientation behavior has been observed recently for the first time in low-molecular-weight discotic molecules.^[46] Strong hydrogen bond interactions between phosphonic acid groups lead to a perpendicular orientation of the columnar structures. During extrusion, the molecules first assemble into a 2D network due to the hydrogen bonds between the phosphonic acid groups and further into a 3D columnar organization.

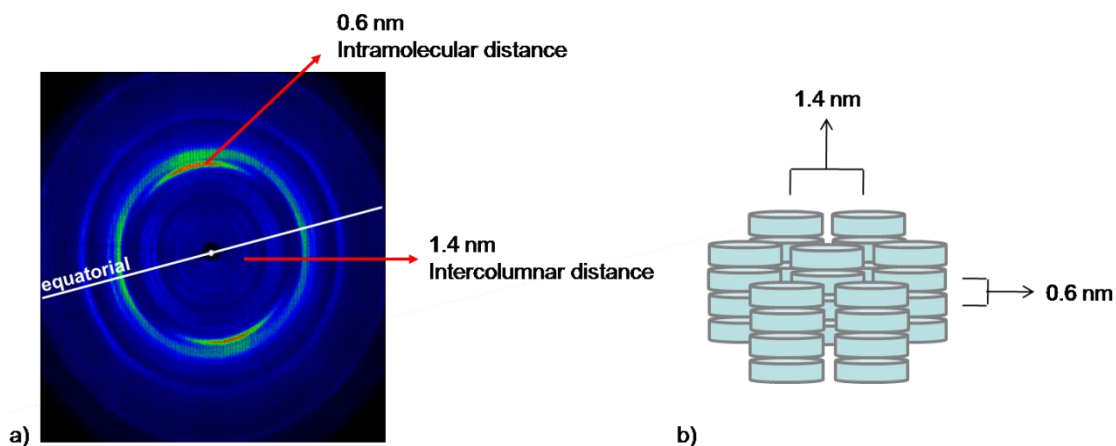


Fig. 3.19: a) 2D WAXS pattern obtained for the extruded filament of compound **4**. b) Schematic representation of the hexagonal packing of compound **4**.

From WAXS and 2D WAXS it is concluded that the material is highly crystalline and that it stacks into columns. Due to its columnar structure containing a proton-conducting periphery and an insulating core, compound **4** can be seen as an inverse proton-conducting cable. It can be deduced that proton conductivity through the crystalline material is possible on the one side due to the amphoteric character, high concentration and preorganization/aggregation of the phosphonic acid groups (assisted by the preorganization of the HPB moieties) and on the other side to the pathways resulting from the self-assembled columns.

However, no information about the location of H_2O molecules in the crystalline structure of the compound could be gained by these two X-ray diffractive methods. To obtain a deeper understanding of the organization of the columns and therefore of the charge transport phenomena through the material, the crystal structure of hexakis(*p*-phosphonatophenyl)benzene must be known.

A crystal structure is composed of a pattern consisting of a set of atoms arranged in a particular way and a lattice exhibiting long-range order and symmetry. In case a single crystal can be grown, the diffraction patterns, which are the patterns that emerge from a sample that is targeted by a beam of some type, can be recorded and analyzed. Since the beam hits the crystal from many different directions, many diffraction patterns are obtained. Crystal planes can be calculated according to Bragg's law using the sharp reflections recorded. The crystal structure can be determined by using a complicated mathematical treatment.^[47] All crystal structures provided in this

dissertation have been measured by Dr. V. Enkelmann from the MPI-P Mainz/Germany.

Spare information exists about the structure and properties of organic phosphonic acids. In the reported compounds,^{[48],[49],[50]} the crystal structure is dominated by the formation of strong hydrogen bonds, each phosphonic acid group being potentially a hydrogen bond acceptor and at the same time a double hydrogen bond donor. Therefore, very robust crystalline solids are produced. A common feature of phosphonic acid-containing organic compounds is that they do not form crystals suitable for conventional X-ray crystallography and only single-crystalline salts with *p*-dimethylaminopyridine (DMAP) can be obtained.^[48, 51, 52]

One of the objectives of the dissertation is to determine the crystal structure of compound **4** so that more information about the proton transport through the material can be gained. However, due to its poor solubility in all kind of solvents difficulties are encountered while attempting to obtain suitable samples for single crystal analysis. On the contrary, hexakis(*p*-diethylphosphonatophenyl)benzene has a high crystallization propensity and crystals of suitable size have been grown from DCM.

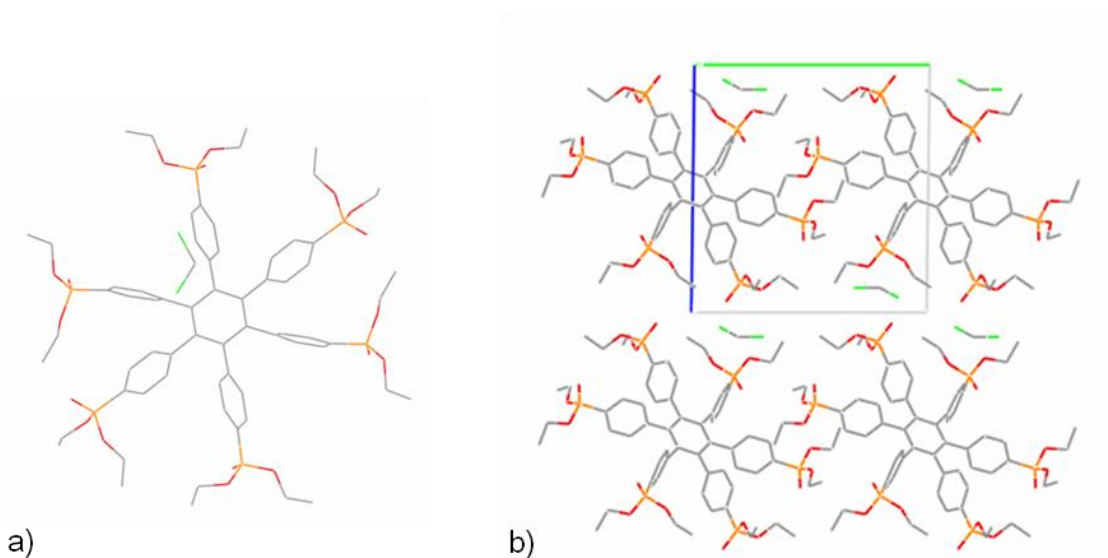


Fig. 3.20: a) Crystal structure of hexakis(*p*-diethylphosphonatophenyl)benzene, H atoms are omitted for clarity. b) View along the axis a.

The molecule is found to crystallize in the *P*1 triclinic space group and the cell parameters are $a = 7.9859(2)$ Å, $b = 14.8979(5)$ Å and $c = 15.7927(4)$ Å. The individual molecules of the crystals are associated by π -stacking and hydrogen bonding into columns. The intracolumnar distance between two molecules is 0.8 nm (axis *a*) and the

intercolumnar distances are 1.3 (axis *b*) and 1.4 nm (axis *c*). A perspective view along the axis *a* is given in Figure 3.20.

From single crystal analysis it can be deduced that the molecules of hexakis(*p*-diethylphosphonatophenyl)benzene arrange into columns. The intracolumnar distance is 0.8 nm (axis *a*) whereas there are two intercolumnar distances since the lattice is not hexagonal: 1.5 nm and 1.6 nm corresponding to the axis *c* and *b* respectively.

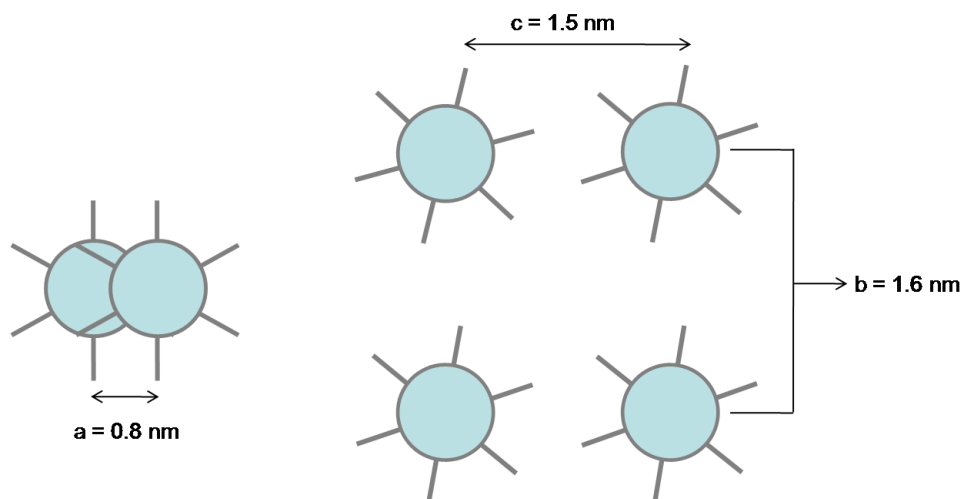


Fig. 3.21: Schematic representation of the organization within hexakis(*p*-diethylphosphonatophenyl)benzene.

Even though compound **4** is not well soluble in water, upon its slow evaporation from a 6:1 H₂O:MeOH solution, a microcrystalline powder is obtained. Some crystals are selected from this powder and proved to be suitable for diffraction. Unfortunately, the compound is found to be a Na⁺ salt. Five Na⁺ ions, three EtOH molecules and two MeOH molecules are found per molecule. Attempts to crystallize the pure acid have so far failed. **6** crystallizes in the triclinic *P* $\bar{1}$ space group and the cell parameters are $a = 7.9133(2) \text{ \AA}$, $b = 12.7498(4) \text{ \AA}$, $c = 13.9783(5) \text{ \AA}$. A perspective view is given in Figure 3.22. The individual molecules of the crystals are associated by π -stacking and hydrogen bonding into columns. The intracolumnar distance is 0.8 nm (axis *a*) and the intercolumnar distances are 1.3 (axis *b*) and 1.4 nm (axis *c*).

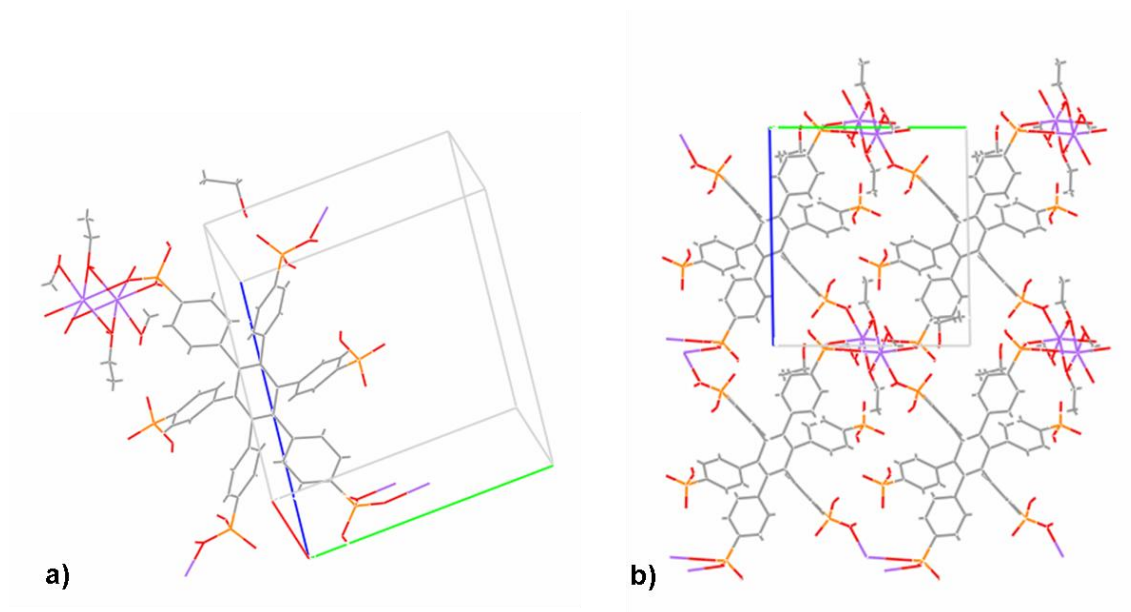


Fig. 3.22: Crystal structure of molecule **4** containing Na^+ ions: a) in the unit cell; b) view along axis a.

The previous results from the 2D WAXS studies are in good agreement with these new outcomes. From 2D WAXS experiments, it has been asserted that the phosphonated HPB molecules stack into columns in a hexagonal lattice. As shown in Figure 3.23a, the inter- and intracolumnar distances are 1.4 and 0.6 nm respectively. From single crystal analysis it has been determined that the molecules in the crystal do not pack in a hexagonal way so that two intercolumnar distances are obtained (axis b and c) (see Figure 3.23b). Moreover, the intracolumnar distance is higher than that found in 2D WAXS (0.8 instead of 0.6 nm) since the molecules stack directly on top of each other and not staggered as in the case of the 2D WAXS (see Figure 3.23b). Two main reasons can be afforded to explain the differences obtained with these two crystallographic studies. In the case of the 2D WAXS experiments, the sample is extruded which means that both thermal energy and mechanical forces are applied so that the molecules during extrusion can adopt the most favorable conformation, i.e. the hexagonal packing. This is not happening in the case of the single crystal structure determination since the molecules are left to crystallize in a solvent and no external forces are exerted. Moreover, in this latter case the solvent molecules (which are not present in the 2D WAXS experiments) disturb the hexagonal columnar packing found in 2D WAXS.

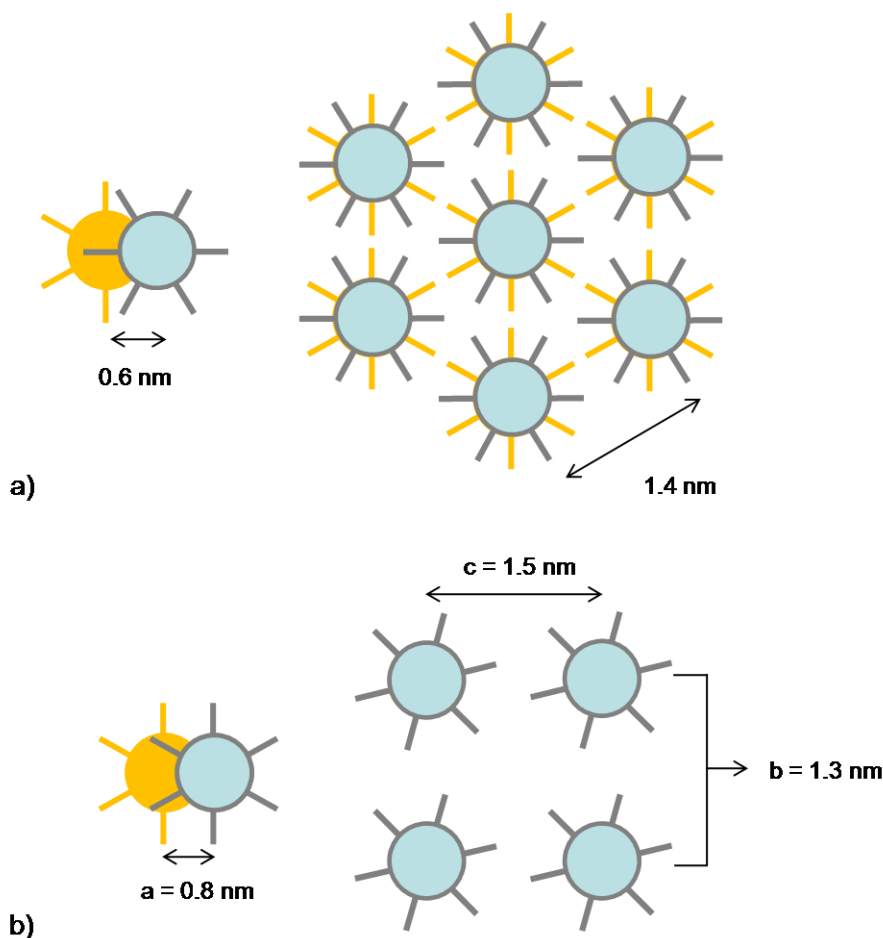


Fig. 3.23: Schematic representation of the organization within a) compound **4** from 2D WAXS experiments and b) compound **4** with five Na^+ from single crystal analysis.

The results from the three different techniques applied to study the crystallinity of compound **4** must be compared. The X-ray diffractograms of the material coming from WAXS and single crystal analysis are displayed in Figure 3.24. It can be observed that the diffractogram from the WAXS measurements shows broader peaks than this of the single crystal analysis since the material obtained after the synthesis is crystalline but is not a single crystal. In both diffractograms the characteristic reflections at low angle corresponding to the inter- and intracolumnar distances are present and can be superposed.

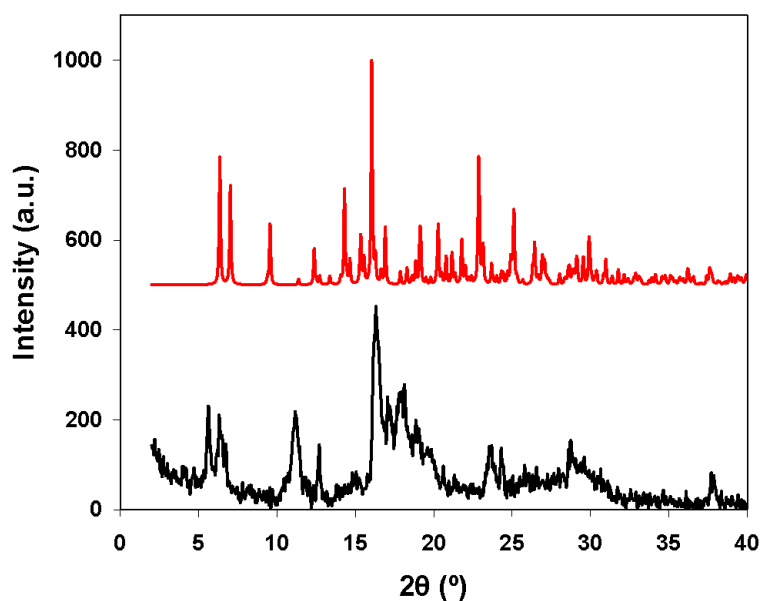


Fig. 3.24: Comparison of the X-ray data for hexakis(*p*-phosphonatophenyl)benzene (**4**) obtained from single crystal grown from a 6:1 H₂O:MeOH solution (red line) with the WAXS data recorded at RT and 33 % RH from the synthesized sample (black line).

Table 3.3 presents the atomic distances at low angle calculated by using *Bragg's* law for the three types of crystal analysis. Since the results obtained are only slightly different from one another it is presumed that hexakis(*p*-phosphonatophenyl)benzene stacks into columns and that the intercolumnar distance must be around 1.4 nm whereas the intracolumnar one between 0.6 and 0.8 nm. The results from the single crystal analysis of hexakis(*p*-diethylphosphonatophenyl)benzene **3** corroborate these findings on account of the columnar structure of the ester and the inter- and intracolumnar distances of 1.6 and 0.8 nm respectively.

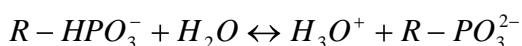
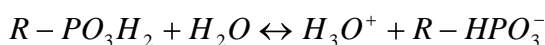
Table 3.3: Atomic distances at low angle for compound **4** calculated from the diffractograms of WAXS, 2D WAXS and single crystal analysis.

Analysis	d1 (nm)	d2 (nm)	d3 (nm)
WAXS (RT and 33 % RH)	1.6	1.4	0.8
2D WAXS	1.4	1.4	0.6
Single crystal	1.5	1.3	0.8

3.2.6 Acidity

Titration experiments have been performed in the group of Prof. Schlögl at the FHI Berlin. Figure 3.25 presents the titration curve of the phosphonated HPB and its corresponding derivative curve. 10.2 mg of compound **4** are allowed to agitate during 48 h at RT in 50 mL of a 3 M KCl solution. Due to the poor solubility of the sample in aqueous solutions, the sample is after 48 h only partially dissolved in this media. Subsequently, the suspension is titrated against a 0.01 M NaOH solution during 52 h. The fact that the titration is effectuated with a suspension plays a minor role: the key is to titrate slowly enough so that the system is always in equilibrium.^{iv}

Every maximum in the derivate plot represents a specific type of protons or acidic centers with different acidity. Since phosphonic acid is a diprotic acid, it is expected that first by lower pH a proton is detached and then by higher pH the second one, so that two maxima in the derivative plot appear.



Interestingly, contrary to what one might expect, hexakis(*p*-phosphonatophenyl)benzene behaves as a monoprotic acid and only one maxima in the derivative plot is observed, i.e. only one dissociation process takes place during titration. The pK_a is found to be 5.37.

In the literature, phosphonic acid-containing small molecules have been described as being diprotic acids. *Crofts* and *Kosolapoff* have investigated the dissociation constants of alkylphosphonic acids^[53, 54] whereas *Bingöl* et al. those of vinyl phosphonic acid (VPA).^[35] The dissociation constants of VPA can be compared with those of alkylphosphonic acid with the same number of carbon atoms, namely ethylphosphonic acid. However, contrary to the monomer, the polymer obtained by its free radical polymerization is described by the same authors as being monoprotic due to electrostatic reasons.

Another example of a phosphonic acid-containing small molecule which presents a titration curve characteristic of diprotic acid is 3,3'-bis(phenylphosphonic acid).^[55] Its

^{iv} At the FHI Berlin they also titrate by this method graphitized samples containing acidic groups which are also suspended in KCl before titration.

polymer analogue (poly(1,3-phenylene-5-phosphonic acid)) is presented in the same manuscript also as diprotic.

In the case of compound **4**, the reasons why it is not possible to dissociate the second proton from the already deprotonated phosphonic acid groups might be manifold. It has been demonstrated above that water is present in the structure of hexakis(*p*-phosphonatophenyl)benzene. These water molecules may form hydrogen bonds with the acidic groups so that the protons are no more dispoable for the reaction with the hydroxyl groups of NaOH. Another and most plausible cause for the partial deprotonation of the phosphonic acid groups may be the increasing of negative charge density while NaOH is being added. There is a moment during titration where the local concentration of negative charges is so high that the protons will not react with the hydroxyl groups of NaOH but with the phosphonate moieties of the compound. This effect has been already observed in the case of poly(methylene amine)^[56] and is due to the high density of phosphonic acid groups present in the compound.

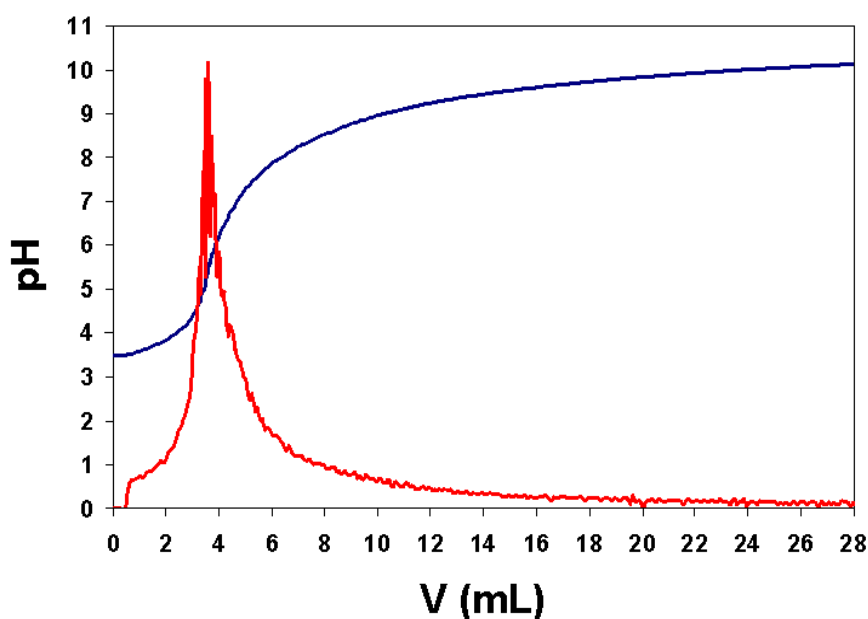


Fig. 3.25: Titration curve of hexakis(*p*-phosphonatophenyl)benzene (blue line) and its derivative plot (red line).

The question arises whether the six phosphonic acid groups present in the molecule give at least one proton during titration, i.e. whether all acidic groups are involved in the acid/base reaction. This issue can be answered if the ion-exchange capacity (IEC) of compound **4** is calculated from these titration data and compared to the theoretical value. The IEC is the capacity of a solid for ion exchange with a solution: “*measure of*

the ability of an insoluble material to undergo displacement of ions previously attached and loosely incorporated into its structure by oppositely charged ions present in the surrounding solution".^[57] IEC can be calculated from the equation below:

$$IEC = \frac{n(H)}{m(\text{compound } 4)} = \frac{2 \cdot n(PO(OH)_2)}{m(\text{compound } 4)} \text{ mmol / g}$$

In the case of these measurements, 10.2 mg of hexakis(*p*-phosphonatophenyl)benzene have been used. This gives a theoretical value for the IEC of 11.8 mmol/g.^v The experimental IEC value from the titration experiments (titrated ion-exchange capacity) is 3.5 mmol/g. The theoretical value is almost 3 times higher than the one obtained by titration methods. This means that in reality more than the half of the 12 protons theoretically disposable to react with NaOH is actually not being involved in the acid/base reaction. This is again due to the high density of phosphonic acid groups.

From these titration measurements it can then be deduced that on the one side the phosphonic acid groups in hexakis(*p*-phosphonatophenyl)benzene behave as monoprotic acids and on the other side not all of the acidic groups participate in the acid/base reaction. These two facts are due to the high density of phosphonic acid groups present in the compound.

3.2.7 Solid-State NMR Investigations

To understand the charge transport mechanism of proton-conducting materials it is crucial to have information concerning both the chemical environment and the proton motion. Impedance spectroscopy, through the measurement of charge transport, yields bulk conductivity data but it does not directly provide information about the local mobility. Therefore, another method is needed to gain this type of knowledge. Through solid-state NMR spectroscopy it is possible to have information about ion motion on the molecular level since the technique allows to selectively observe the nuclei of interest.^[58, 59]

^v For these calculations, the molecular weight of compound **4** used is 1014.57 g/mol, i.e. without incorporated H₂O molecules.

The solid-state nuclear magnetic resonance experiments have been performed in cooperation with the group of Prof. Spiess from the MPI-P Mainz/Germany. All solid-state NMR spectra have been recorded by Dr. B. Faßbender. The results of the solid-state NMR experiments that are important for the discussion of conductivity behavior of hexakis(*p*-phosphonatophenyl)benzene are mentioned in this chapter. The details of the NMR techniques are not given here but can be found elsewhere.^[60]

Liquid-state NMR has been used to characterize hexakis(*p*-phosphonatophenyl)benzene (Section 3.2.1). Since the differences between liquid- and solid-state NMR may reveal information about the solid-state arrangement,^[61] solid-state NMR spectra have been recorded and compared to the liquid-state ones. The chemical shifts in the solid-state are not averaged isotropically and they therefore contain information about the sample orientation. Thus, solid-state magic angle spinning (MAS) NMR spectra often show rather broad spectra compared to the liquid case due to the difference of orientations presents in a powder sample.

In recent years, fast MAS has been used to average the ^1H - ^1H dipolar couplings and thereby achieve high resolution spectra for organic solids. For MAS NMR experiments, the sample is inclined by a specific angle (the magnitude of the magic angle is 54.74°)^[62] with regards to the magnetic field and spun fast during the signal acquisition. This can effectively reduce or removes the anisotropic interactions.

In general, information with respect to assignments is obtained by comparison of liquid-state with solid-state NMR spectra. In addition, ^1H MAS NMR is quantitative, provided that a sufficiently long relaxation delay has been chosen, which facilitates the assignment. The liquid-state ^1H NMR signals of compound **4** are located around 7 ppm (7.16 and 7.0 ppm). Changing to the solid-state, the signals of the molecule stay constant at 7 ppm, however instead of two sharp peaks only one broad peak can be detected (Figure 3.26). A deconvolution results in two different displacements ranging from 1 to 2 ppm. This might be an indication that the shifted proton resonance corresponds to different arrangements of the aromatic rings.

Another difference between liquid- and solid-state spectra is the chemical shift of the acidic protons. In the liquid-state spectrum, the peak appears at 3.8 ppm and corresponds both to the protons of the acidic groups and those of the residual water present in the deuterated DMSO. In the corresponding solid-state spectrum, the peak is shifted toward lower fields (at around 12 ppm) and is much broader than the one in liquid-state.

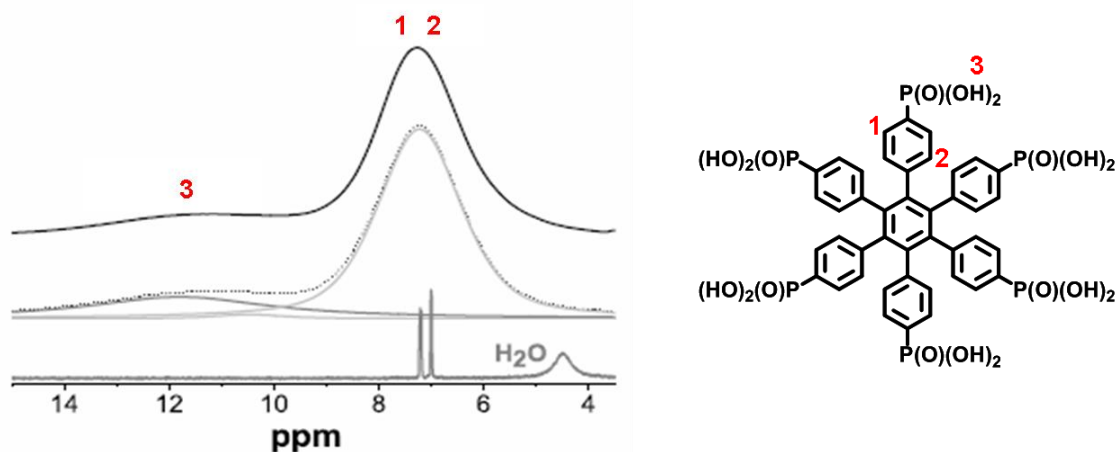


Fig. 3.26: ^1H solid-state MAS NMR spectra recorded at 700 MHz is shown on the top, below the deconvoluted peaks are plotted and at the bottom the liquid spectra recorded in DMSO- d_6 at 373 K (500 MHz).

Insights in the solid-state organization of the samples are also provided by ^{13}C $\{^1\text{H}\}$ cross polarization (CP) MAS NMR. Upon comparison of the liquid and the solid-state NMR spectra, changes in the peaks are observed. In the solid-state spectra peaks are usually broader and shifted to higher or lower ppm values. These changes are due to different effects like packing, limited mobility and π - π stacking.

In general, the three mentioned points have an influence on the chemical shift. However, since the phosphonated HPB includes aromatic systems the effect of π - π stacking is most probable present.^[63] Considering a benzene ring there are two different regions, the first is located above and below the molecular plane and the second orthogonal. These regions will be different in the geometrical structures due to the turning of the aromatic rings and it strongly depends on the location of each ^{13}C next to another ring whether it is shifted to higher or lower chemical shift values.^[64]

Above the plane an atom will experience a deshielding due the induced magnetic field, leading to a difference in the chemical shift values. In contrast, if the atom is located at the side of the aromatic ring the values become smaller.

By comparing the obtained ^{13}C signal from the ^{13}C $\{^1\text{H}\}$ CP MAS spectrum with the 2D ^{13}C $\{^1\text{H}\}$ REPT-HSQC (recoupled polarization transfer-heteronuclear single-quantum correlation) spectrum of compound **4**, a signal loss of the quaternary carbons is observed (Figure 3.27). In the ^{13}C $\{^1\text{H}\}$ CP MAS spectrum, the quaternary carbon C5 shows the lowest intensity representing the carbon of the central aromatic ring. This is supported by the fact that this signal has no corresponding intensity in the ^{13}C $\{^1\text{H}\}$

REPT-HSQC spectrum. There are no protons nearby which may be able to transfer any polarization to quaternary ^{13}C (C5).

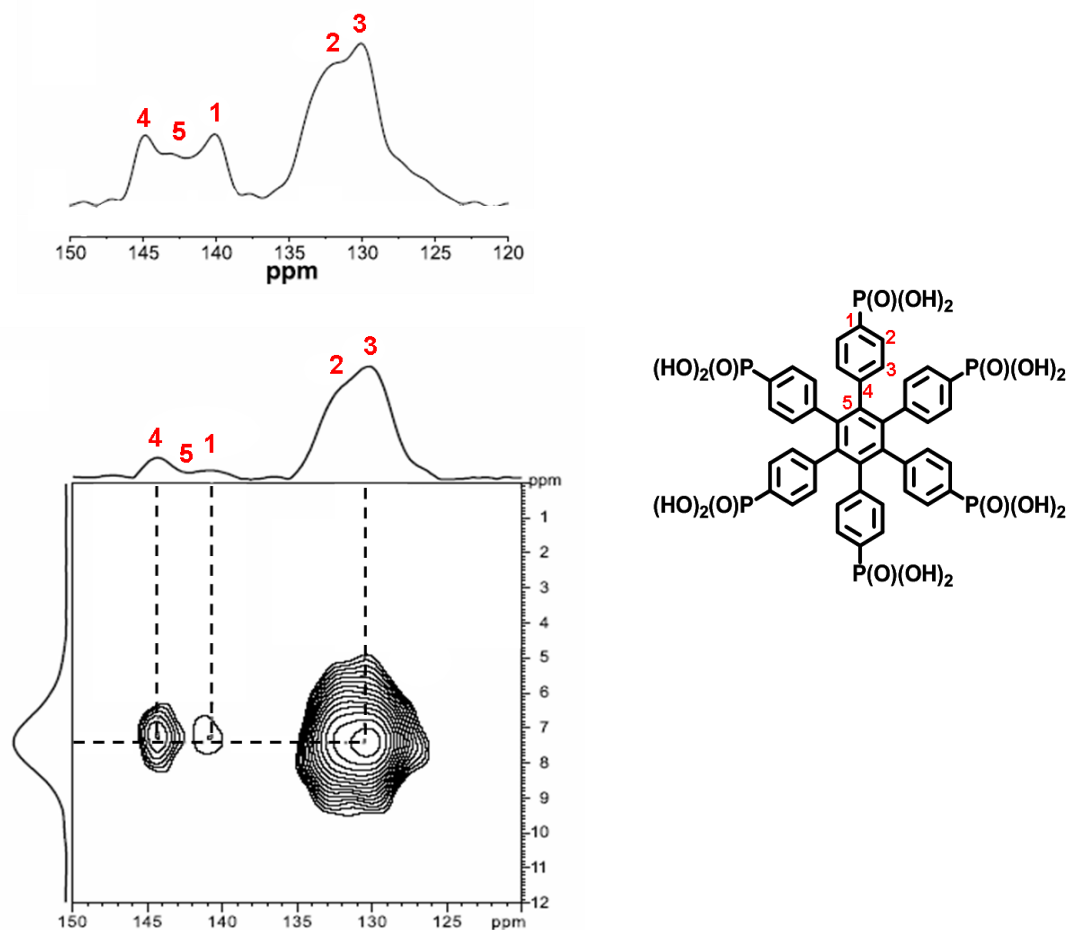


Fig. 3.27: Top: ^{13}C $\{^1\text{H}\}$ CP MAS NMR spectrum of compound **4** recorded at RT and 126 MHz, showing underneath the liquid DEPT-135 spectra in DMSO at 373 K. Bottom: ^{13}C $\{^1\text{H}\}$ MAS REPT-HSQC of compound **4** recorded at RT and 214 MHz plotting projections along the ^{13}C - and ^1H -NMR axis respectively on the top and on the left.

In addition, in the 2D ^{13}C $\{^1\text{H}\}$ REPT-HSQC spectrum a less dramatic but detectable and differential signal reduction of the other two quaternary carbons (C1 and C4) can be noticed. This observation might arise from the location of the aromatic rings in the structure among one another. Hence, the difference in reduction comparing the two quaternary carbons C1 and C4 might result from a more or less strong polarization transfer originating from the protons located at the neighboring ring. Accordingly, the assignment is as follows: the C1 quaternary carbon represents the phosphonic acid

group connection and the C4 carbon the aromatic conjunction between the two aromatic rings (Figure 3.27).

^1H chemical shift values provide information about the chemical environments of the protons and the line widths at various temperatures give an insight into the mobility. On the other hand, signals which might not be present in the liquid, due to fast exchange, i.e. hydrogen bonds, can be detected and analyzed^[65, 66]. This additional information usually is not detectable in the liquid state due to the high dissolution or concurrent interaction with the solvent.

The mobility of protons can be investigated by variable temperature solid-state NMR studies (VT ^1H MAS NMR). If there is a mobile proton, a change in temperature results in a continuous and significant narrowing of the line width.^[67] The chemical exchange process can be described with regard to the NMR time scale,^[68] where the different ranges are characterized by the correlation time, t_c . Slow and fast exchange limits are defined by $t_c > 10^{-5}$ s and $t_c < 10^{-7}$ s, respectively.

The change in transverse relaxation time which is a synonym for the change in the line width as a function of temperature can be correlated with the exchange rate Ω and the transverse relaxation time T_2^* :

$$\Omega = \frac{1}{2 \cdot t_c} = \pi \cdot T_2^*$$

If the line width shows a linear dependence on the inverse temperature scale than the apparent activation energy can be calculated according to the Arrhenius equation:

$$\Omega = \Omega_0 \cdot \exp\left(-\frac{E_a}{R \cdot T}\right)$$

where E_a , R , T and Ω_0 represent the apparent activation energy, gas constant, temperature and pre-exponential factor respectively.

Variable temperature measurements have been conducted in the temperature range of 267 to 409 K to study the dependence of the mobility on the temperature (Figure 3.28a). A significant continuous decrease in line width, while raising the temperature is characteristic for proton mobility.^[69, 70] Compound **4** shows a rather strong effect on the temperature and a complex temperature dependency for the ^1H signal assigned to the

hydrogen bonded protons. In addition to line narrowing, a change of the chemical shift can also be observed for the VT stack. At $-6\text{ }^{\circ}\text{C}$, a broad distribution of different ^1H phosphonic acid group sites can be observed. At around $26\text{ }^{\circ}\text{C}$, the peak shifts 2 ppm towards higher field (from 12 to 10 ppm). A further increase of the temperature leads to a narrowing of the signal. At higher temperatures two signals originating from hydrogen bonds are observed with the minor one located at 8.5 ppm, as seen in Figure 3.28a (light grey arrow).

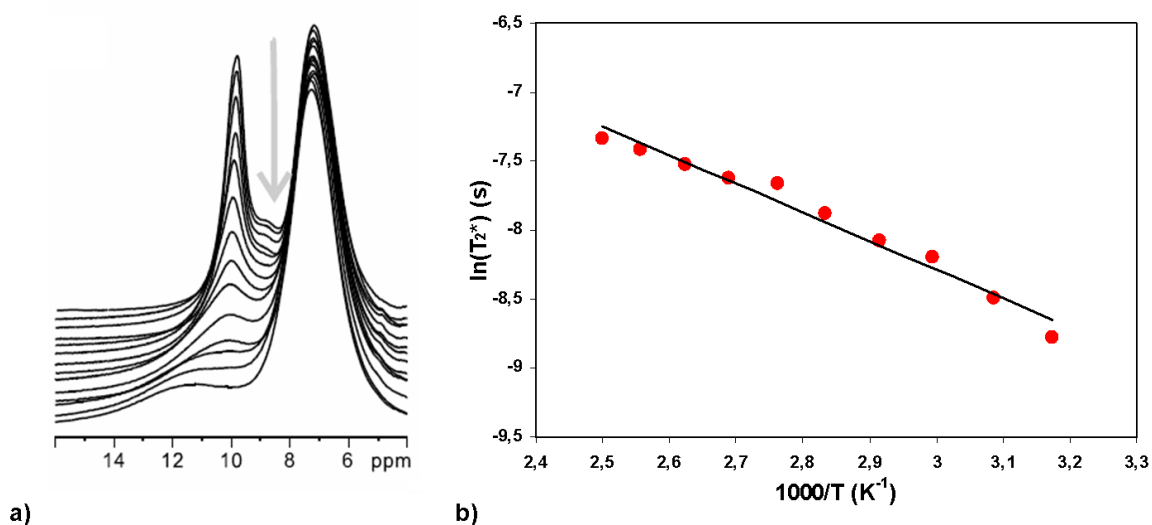


Fig. 3.28: a) VT ^1H MAS NMR spectra of compound **4** at 700 MHz measured at raising temperatures from bottom to top starting with 267 to 409 K in 10 K steps. b) The *Arrhenius* plot shows the change in line width against the inverse temperature.

Figure 3.28b shows the *Arrhenius* plot of hexakis(*p*-phosphonatophenyl)benzene. From the slope of the plot, the apparent activation energy can be calculated. A value of 15 kJ/mol is obtained, which is one-fifth the value of the IS activation energy calculated in Chapter 3.2.2 (65 kJ/mol). The discrepancy between the two measurements is attributed to the fact that the conductivity data represent charge transport on a macroscopic scale, while NMR detects the proton mobility on a microscopic or local scale. Local proton mobilities, however, include different types of motions which do not necessarily contribute to the long-range proton transport that facilitates bulk proton conductivity. Only in rather ideal cases, where the NMR data reflect the proton motions responsible for observable bulk proton conductivity, the activation energies obtained from both the VT ^1H MAS NMR and IS are similar.^[70] Therefore, low NMR activation energies reflect high rotational mobility of the protons and/or fast local proton hopping but do not provide information about proton transfer/hopping in a macroscopic scale.

The fact that in the case of compound **4** the IS activation energy by far exceeds the activation energy calculated from ^1H NMR line width studies reflects proton mobility rather than proton conductivity. Since mobility is a necessary but not a sufficient condition for conductivity, the activation energy of proton conductivity can be higher.

The NMR activation energy of hexakis(*p*-phosphonatophenyl)benzene is smaller than the activation energy of annealed PVPA obtained NMR data (25 kJ/mol).^[28, 35] This fact means that the local processes of proton hopping are faster in the case of compound **4**.

The unassigned signal observed at about 9 ppm in the VT ^1H MAS NMR spectra of compound **4**, indicated by the grey arrow in Figure 3.28a, could be one site with a different dynamic affecting the overall activation energy both in NMR and IS. This different resonance might be due to a phosphonic acid-water interaction, also found in the case of PVPA.^[28]

The formation of phosphonic acid anhydride species may result from either condensation of two phosphonic acid groups within the same molecule, or the condensation of phosphonic acid groups of different molecules (see Figure 3.29). In other words, P-O-P linkages can be either intra- or intermolecular as it has been discussed in Section 3.2.1. In case of being intermolecular, the anhydride bond formation can be between two molecules belonging to the same column (intracolumnar) or two molecules belonging to different columns (intercolumnar).

The presence of anhydride species can be detected by ^{31}P solid-state MAS NMR spectroscopy. The ^{31}P MAS NMR is a quantitative method if a direct detection is used in the relaxation limit. Moreover, ^{31}P MAS NMR is an additional helpful tool to obtain structural information regarding the chemical structure and its surroundings.^[71]

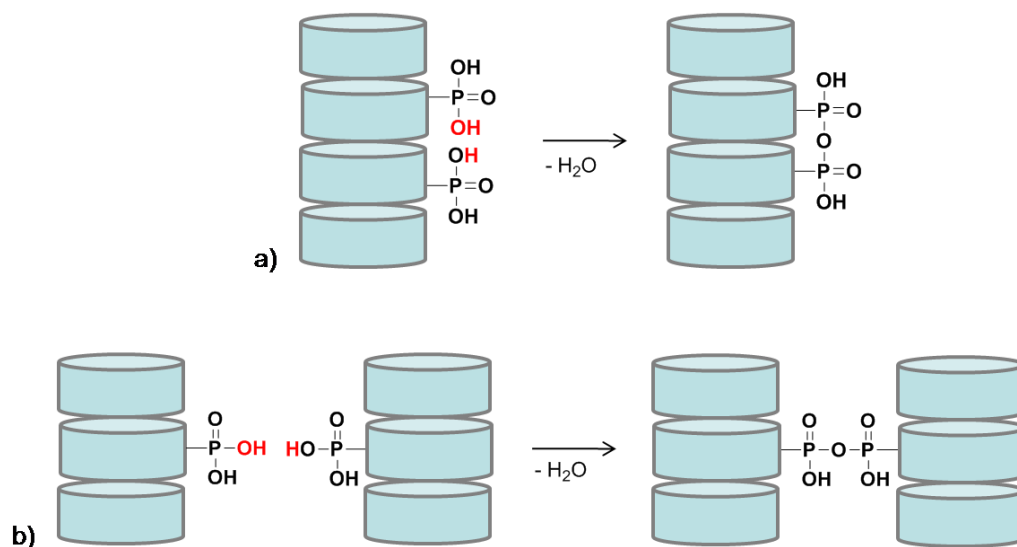


Fig. 3.29: Schematic representation of the a) intracolumnar and b) intercolumnar anhydride formation between two phosphonic acid groups.

In the liquid spectra, compound **4** yields a chemical shift of 13.5 ppm whereas in the solid-state spectra the chemical shift is about 18 ppm (Figure 3.30a). The chemical shift is relatively broad in the case of the solid-state spectrum. Additionally, it can be observed that the solid-state spectrum displays a peak shifted to lower field at around 23 ppm. The broadening can be attributed to a dispersion of isotropic chemical shifts due to conformational differences whereas the shift at lower field can be assigned to crystalline phosphorous species.^[72]

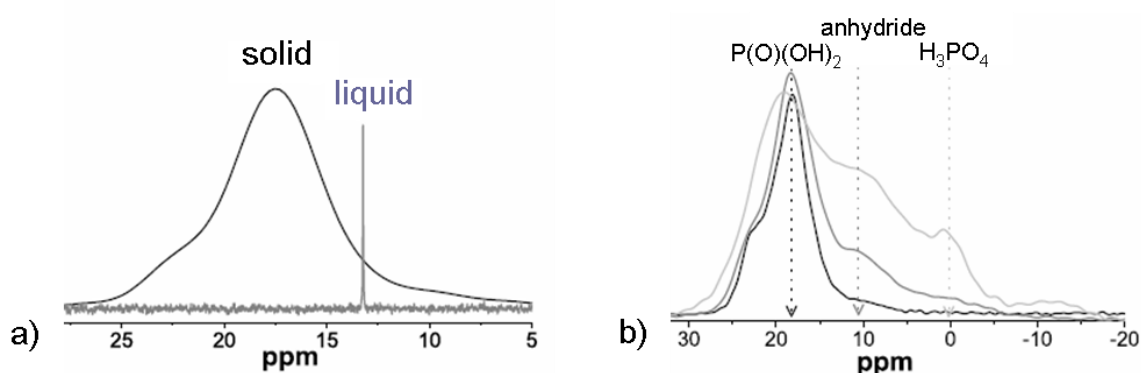


Fig. 3.30: a) ^{31}P solid-state MAS NMR spectrum at 202 MHz, showing underneath the liquid spectrum in DMSO- d_6 at 373 K (202 MHz) of compound **4**. b) ^{31}P MAS NMR spectra recorded at 202 MHz of compound **4** removed from TGA after heating to different temperatures: 298 K (black), 423 K (dark grey) and 623 K (light grey).

Figure 3.30b shows the ^{31}P MAS NMR solid-state spectra of compound **4** at RT and at 150 and 350 °C after the TGA measurements. It can be observed that due to the heating a new peak at 10 ppm can be observed. This is due to the formation of phosphonic acid anhydride while increasing the temperature.^[67] The samples heated to 150 and 350 °C show an additional peak at 0 ppm of 4 and 9 % respectively. This resonance may be assigned to free phosphoric acid.^[73] In the RT spectrum the amount of phosphorous-anhydride species is already 6 %. In the first heating step to 150 °C the anhydride part increases to 24 % and in the last step to 350 °C the anhydride part increases to 44 %. In both cases an anhydride increase of about 19 % is detected. Table 3.4 summarizes the obtained results. It should be noted that the anhydride formation is reversible.

Table 3.4: Amount of different phosphorous species/compounds in hexakis(*p*-phosphonatophenyl)benzene.

	RT	Δ	150 °C	Δ	350 °C
Crystalline P(O)(OH)₂ (23 ppm) (%)	16	- 10	6	-6	
“Amorphous” P(O)(OH)₂ (18 ppm) (%)	78	- 12	66	-12	47
Anhydride species (10 ppm) (%)	6	+18	24	+ 20	44
Free H₃PO₄ (0 ppm) (%)	0	0	4	+ 5	9
Total amount (%)	100	0	100	0	100

If the surrounding is not completely identical for the ^{31}P nucleus, it experiences different chemical shieldings which result in a broad NMR signal. On the contrary, a well-defined structure with different sites gives rise to several narrow signals.

The assumption of different phosphonic acid sites is supported by the comparison of the ^{31}P MAS NMR spectra of compound **4** under dry and wet conditions (Figure 3.31). In the last case, the resolution increases due to higher mobility resulting in a splitting of the broad signal. Additionally, it is observed that the center of the phosphorous chemical shift under wet conditions is located at smaller ppm values. This fact suggests that the phosphorous with higher chemical shift values represents the phosphonic acid groups which are not interacting with water.

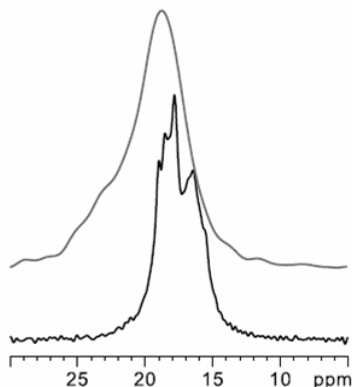


Fig. 3.31: ^{31}P MAS NMR spectra of compound **4** recorded at RT and 15 kHz spinning (202 MHz) as obtained from the synthesis and dried (grey) and after storing the sample under 100 % RH (black).

3.2.8 Summary

A crystalline organic material in which proton conductivity is not a water based diffusion process, as in common amorphous polymer electrolytes, has been presented. Hexakis(*p*-phosphonatophenyl)benzene can be seen as an inverse proton-conducting cable due to its columnar structure containing a proton-conducting periphery and an insulating core. Furthermore it exhibits temperature independent proton conductivity. This behavior has been only observed before for a phosphonated fully aromatic polymer of slightly inferior proton conductivity values.^[31]

It could be shown that proton conductivity through the crystalline material is possible on the one side due to the amphoteric character, high concentration and preorganization/aggregation of the phosphonic acid groups and on the other side to the pathways resulting from the self-assembled columns. In the case of this material, the phase separation providing high proton conduction is achieved at the molecular level so that a 3D proton conductor is formed.

Moreover, it has been demonstrated that the material is a crystal hydrate and that the proton transport is assisted by the presence of immobilized water. In contrast to state-of-the-art polymers and inorganic crystals, hexakis(*p*-phosphonatophenyl)benzene provides high and furthermore constant proton conductivity, satisfying one of the prerequisites for new separator materials in FC systems. In addition its simple three-step synthesis renders its industrial upscaling possible. These results suggest that this compound tested in a MEA should give a good performance with respect to its chemical and thermal stability as well as proton conductivity.

3.3 The Influence of Geometry and the Number of Acidic Functions

3.3.1 General Remarks

As described in Chapter 3.2, hexakis(*p*-phosphonatophenyl)benzene -a small molecule containing phosphonic acid groups- presents proton conducting properties in the solid state because a nanophase separation between the hydrophobic and hydrophilic domains within its structure is possible. For the development of novel separator materials based on organic small molecules which are able to self-assemble and therefore also to provide the nanophase separation leading to proton transport, it is important to understand how geometry and structure determine proton conductivity in this type of compounds. The goal of this section is to examine how the number of phosphonic acid functions, the geometry and the crystallinity influence the proton transport properties of small molecules which contain phosphonic acid functions and are able to form supramolecular structures leading to a nanophase separation between the hydrophilic and the hydrophobic parts.

Firstly the synthesis of five phosphonic acid-containing molecules with different geometry and substitution pattern (see Figure 3.32) is briefly described. Phosphonic acid has been chosen as the protogenic group due to its amphoteric properties. The molecular structure of these molecules consists of a hydrophobic core and a hydrophilic periphery containing a defined number of phosphonic acid functions. Different carbon-rich non-planar cores have been chosen as hydrophobic nodes. At this point it has to be cleared up that the goal of the performed work was neither to optimized well-known or existing procedures or to focus on finding other synthetic pathways. Since for the characterization of the materials a minimum quantity of 1 gram was needed, a central part of the work accomplished during the PhD time dealt with synthesizing the materials in gram-scale

Proton conductivity, water uptake, crystallinity and solid-state NMR studies have been carried out on these organic molecules. These four points are addressed on their corresponding sections which are followed by a summary.

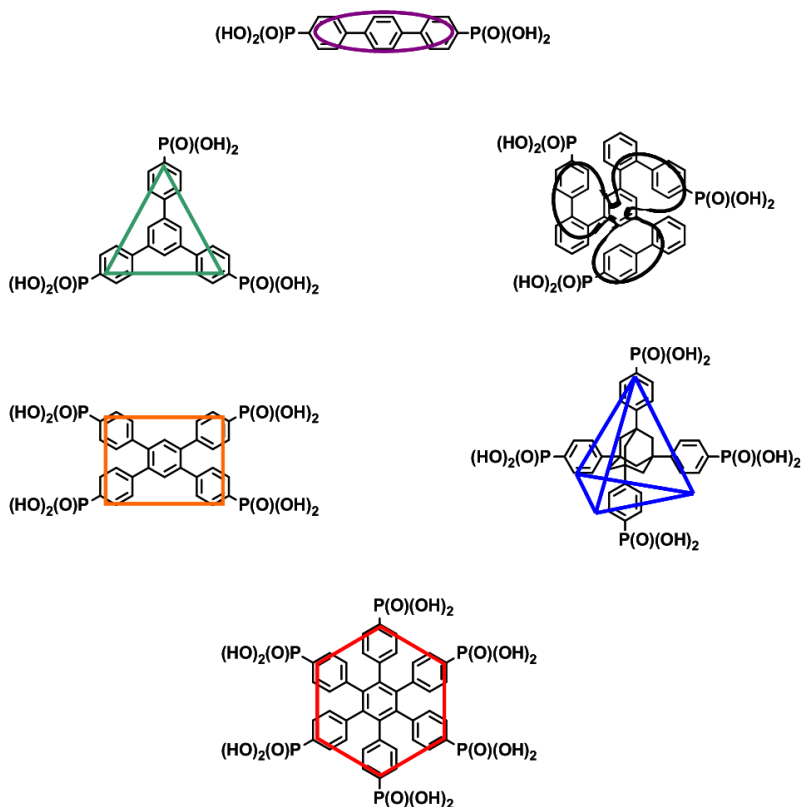


Fig. 3.32: Phosphonic acid-containing small molecules: (*p,p'*-terphenyl-4,4''-diyl)bisphosphonic acid (violet), 1,3,5-tris(*p*-phosphonatophenyl)benzene (green), 1,3,5-tris[4''-(phosphonato)-2'-biphenyl]ylbenzene (black), 1,2,4,5-tetrakis(*p*-phosphonatophenyl)benzene (orange), 1,3,5,7-tetrakis(*p*-phosphonatophenyl)adamantane (blue), hexakis(*p*-phosphonatophenyl)benzene (red).

3.3.2 Synthesis and Characterization

A three-step procedure is used for the synthesis of (*p,p'*-terphenyl-4,4'-diyl)bisphosphonic acid (Figure 3.33). Firstly, iodine is introduced in the two *para* position of the *p*-terphenyl following a synthetic pathway described in the literature.^[74] Secondly, a palladium catalyzed cross-coupling reaction leads to the introduction of phosphonic ester groups. These ester groups are converted into the corresponding phosphonic acids by hydrolysis under mild conditions.

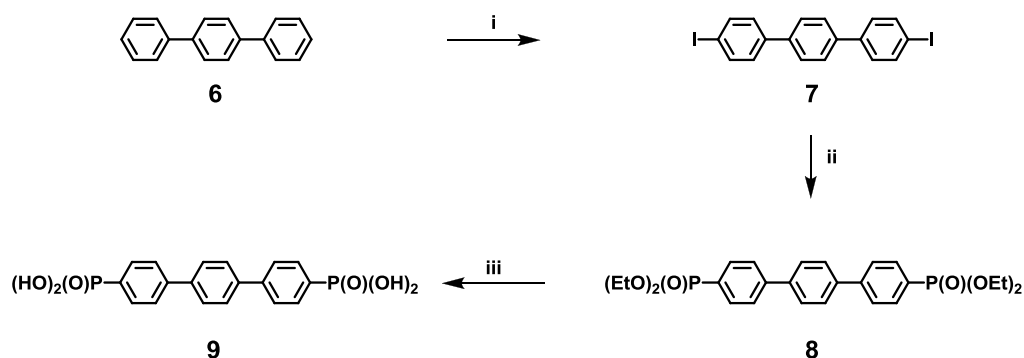


Fig. 3.33: Synthetic route toward (*p,p'*-terphenyl-4,4'-diyl)bisphosphonic acid: i) I_2 , H_5IO_6 , $AcOH/H_2O/H_2SO_4$, 100 °C, 24 h, 60 %; ii) $HP(O)(OEt)_2$, $Pd(PPh_3)_4$, NEt_3 , toluene, 75 °C, 12 h, 97 %; iii) a. $TMS-Br$, DCM , RT, 48 h; b. $MeOH$, RT, 48 h, 72 %.

1,3,5-Tris(*p*-phosphonatophenyl)benzene is synthesized using a two-step procedure. For the first step which consists of the introduction of the phosphonic ester groups, 1,3,5-triphenylbenzene can carry either an iodine or a bromine in the *para* position of the phenyl ring. Unfortunately, a mixture of mono-, di- and trisubstituted molecules is obtained in both cases. Hydrolysis under mild conditions yields the corresponding acid.

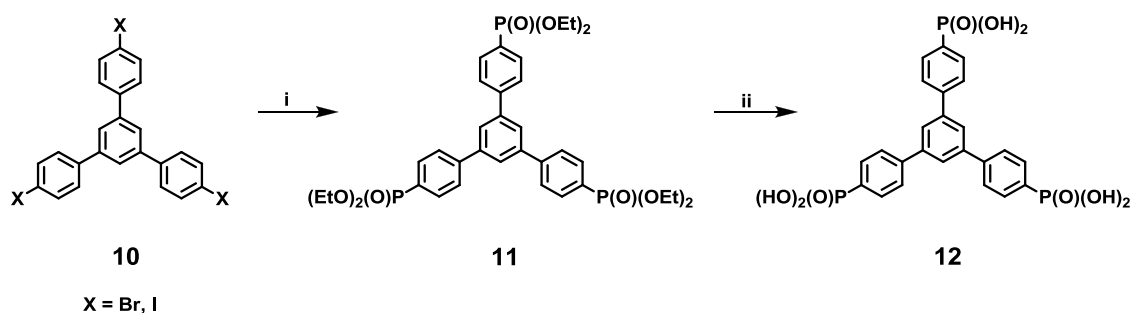


Fig. 3.34: Synthetic route toward 1,3,5-tris(*p*-phosphonatophenyl)benzene: i) $HP(O)(OEt)_2$, $Pd(PPh_3)_4$, NEt_3 , toluene, 75 °C, 12 h, 75 %; ii) a. $TMS-Br$, DCM , RT, 48 h; b. $MeOH$, RT, 48 h, 90 %.

The synthesis of 1,3,5-tris(4''-iodo-2'-biphenyl)ylbenzene is carried out following a procedure described in the literature.^[75] Only the catalytic system of the *Suzuki-Miyaura* coupling used to obtain 1,3,5-tris[4''-(trimethylsilyl)-2'-biphenyl]ylbenzene **15** is different: $Pd(II)$ acetate/tri(*o*-tolyl)phosphine instead of tetrakis(triphenylphosphine)palladium (0). The palladium catalyzed cross-coupling reaction gives the ester of the wanted

molecule. The ester is purified via silica column chromatography and gel permeation chromatography and hydrolyzed under mild conditions.

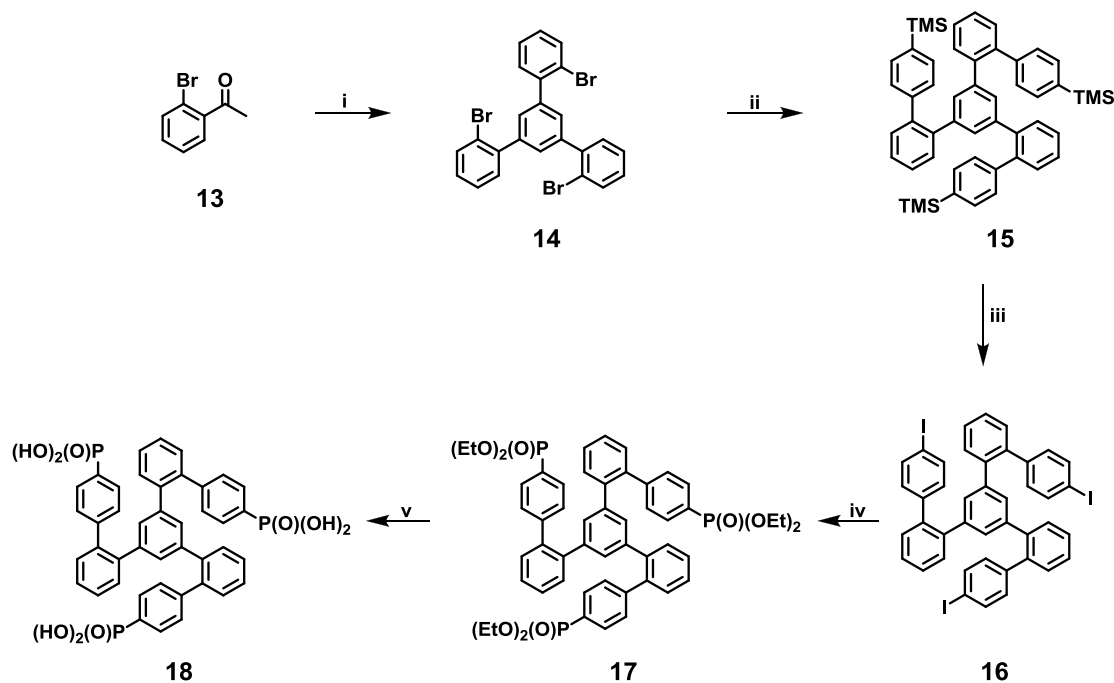


Fig. 3.35: Synthetic route toward 1,3,5-tris[4''-(phosphonato)-2'-biphenyl]ylbenzene: i) trifluoromethanesulfonic acid 10 mol %, 130 °C, 7 h, 72 %; ii) *p*-TMS phenylboronic acid, Pd(PPh₃)₄, K₂CO₃, toluene, EtOH, H₂O, reflux, 12 h, 93 %; iii) ICl, CHCl₃, 1 h, RT, 93 %; iv) HP(O)(OEt)₂, Pd(PPh₃)₄, NEt₃, toluene, 75 °C, 12 h, 63 %; v) a. TMS-Br, DCM, RT, 48 h; b. MeOH, RT, 48 h, 72 %.

The palladium catalyzed *Suzuki-Miyaura* cross-coupling reaction between 1,2,4,5-tetrabromobenzene **19** and 3-trimethylsilylphenylboronic acid in the presence of catalytic system palladium acetate/tri(*o*-tolyl)phosphine affords 1,2,4,5-tetrakis(4-trimethylsilylphenyl)benzene **20**. 1,2,4,5-Tetrakis(*p*-iodophenyl)benzene **21** is obtained after the reaction of **20** with iodine monochloride. The phosphonate ester groups are introduced via a cross-coupling reaction and hydrolyzed under mild conditions to give the desired product.

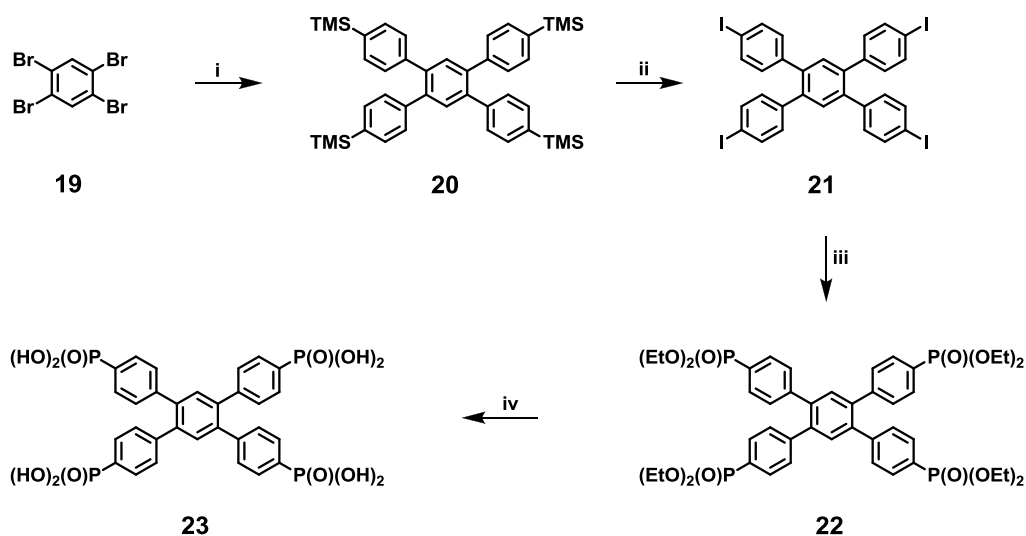


Fig. 3.36: Synthetic route toward 1,2,4,5-tetrakis(*p*-phosphonatophenyl)benzene: i) palladium (II) acetate, tri(*o*-tolyl)phosphine, phenylboronic acid, toluene, MeOH, 2 M K₂CO₃, 75 °C, 12 h, 42 %; ii) ICl, CHCl₃, RT, 1 h, 81 %; iii) HP(O)(OEt)₂, Pd(PPh₃)₄, NEt₃, toluene, 75 °C, 12 h, 68 %; iv) a. TMS-Br, DCM, RT, 48 h; b. MeOH, RT, 48 h, 83 %.

Tetrakis-1,3,5,7-(4-phosphonatophenyl)adamantane **28** is synthesized via a four-step reaction. 1,3,5,7-Tetraphenyladamantane **25** is first prepared by the *Friedel-Crafts* reaction of the commercially available 1-bromoadamantane **24** with benzene in the presence of tert-butyl bromide.^[76] Iodination of **25** gives 1,3,5,7-tetrakis(4-iodophenyl)adamantane **26**. The cross-coupling reaction of **26** with diethyl phosphite in the presence of the catalytic system triethylamine/dichlorobis(triphenylphosphine)palladium (II) gives tetrakis-1,3,5,7-(4-diethylphosphonatophenyl)adamantane^[77] **27** which after hydrolysis under mild conditions affords the desired product **28**.

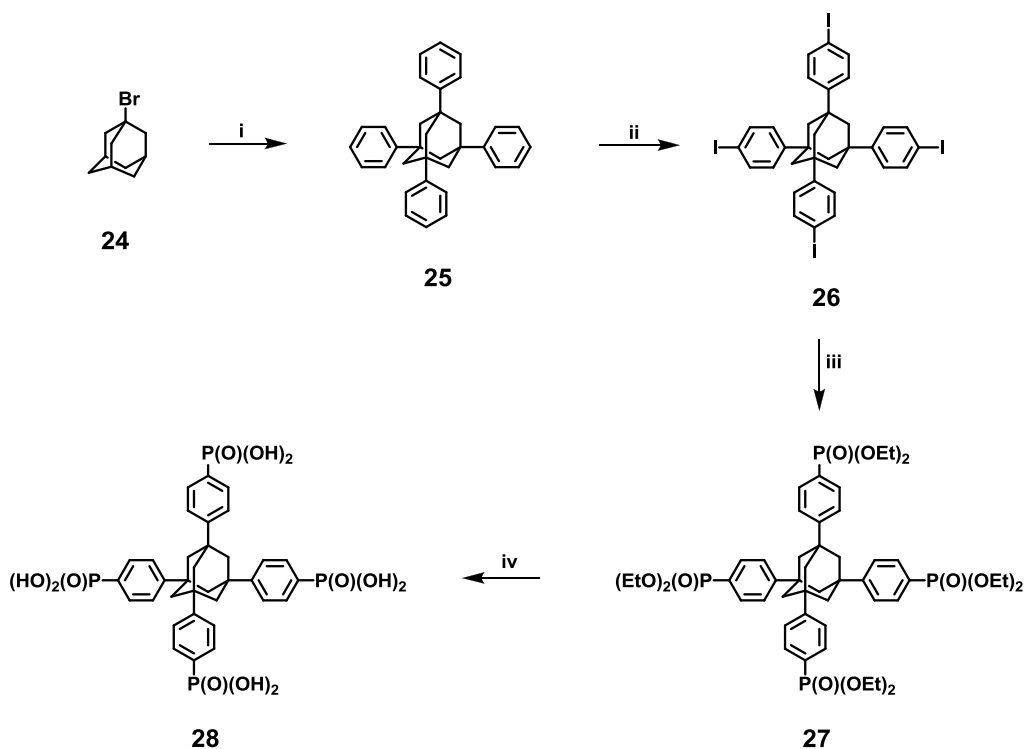


Fig. 3.37: Synthetic route toward 1,3,5,7-tetrakis(*p*-phosphonatophenyl)adamantane: i) benzene, tert-butyl bromide, AlCl_3 , reflux, 1 h, 50 - 70 %; ii) I_2 , BFIB, CHCl_3 , RT, 4 h, 50 - 70 %; iii) HP(O)(OEt)_2 , $\text{Pd(PPh}_3)_4$, NEt_3 , toluene, 80°C , 72 h, 76 %; iv) a. TMS-Br, DCM, RT, 48 h; b. MeOH, RT, 48 h, 72 %.

The thermal stability of the above described compounds has been studied by TGA. The experiments have been performed at 10 K/min under N_2 flux. Figure 3.38 shows the curves for the different materials. The compounds can be divided into two groups with respect to the course of their respective curves:

- Compounds showing the first weight loss at around 250°C : **9** and **18**;
- Compounds showing a progressively loss of weight: **12**, **23**, **28** and **4**.

Belonging to this second group, 1,3,5,7-tetrakis(*p*-phosphonatophenyl)adamantane (**28**) presents the most pronounced weight loss at 600°C (around 51 wt %) while 1,2,4,5-tetrakis(*p*-phosphonatophenyl)benzene (**23**) the less pronounced one (around 32 %).

The continuous weight loss of 1,3,5-tris(*p*-phosphonatophenyl)benzene (**12**) is most probably due to the water enclosed in its structure. The compound is very hygroscopic and water soluble and even if it is dried under vacuum at temperatures above 100°C , it

absorbs water very easily so that a weight loss of 8 wt % is exhibited at temperatures below 200 °C.

1,3,5-Tris[4''-phosphonato-2'-biphenyl]ylbenzene (**18**) can be considered as the best material regarding its thermal properties since it displays its first weight loss at around 250 °C and at 600 °C its weight loss is of around 29 wt %.

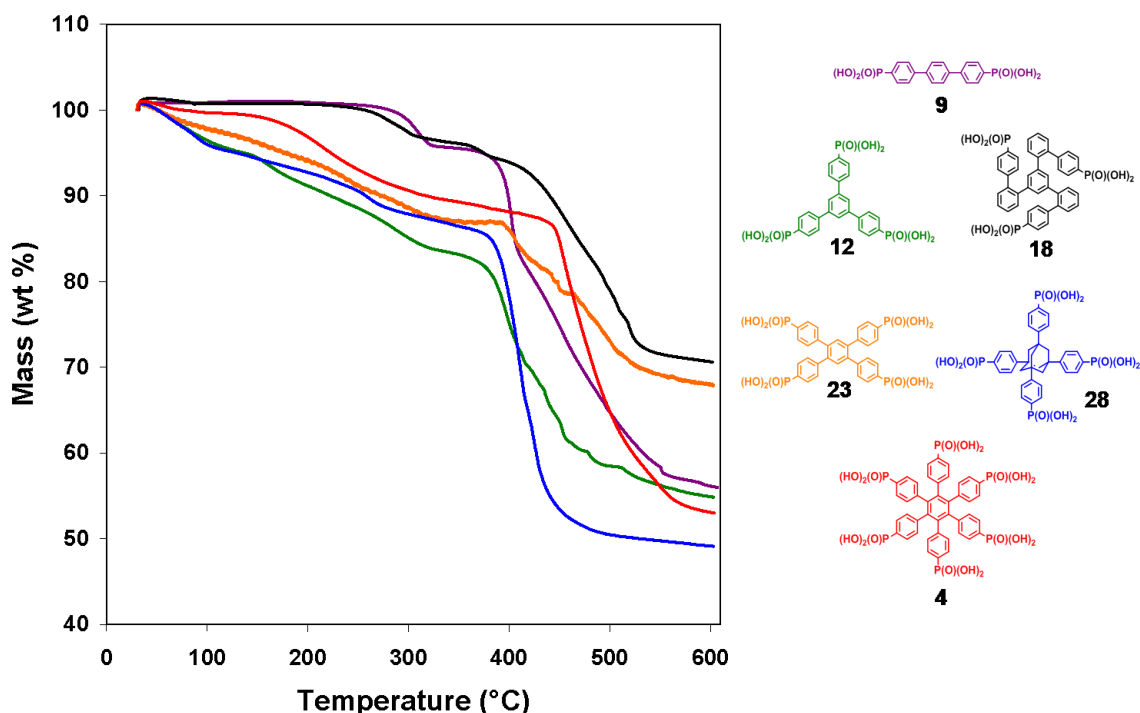


Fig. 3.38: TGA curves for compounds **9**, **12**, **18**, **23**, **28** and **4** recorded at 10 K/min under N₂. Each compound is depicted with a color: (*p,p'*-terphenyl-4,4''-diyl)bisphosphonic acid (**9**) in violet; 1,3,5-tris(*p*-phosphonatophenyl)benzene (**12**) in green; 1,3,5-tris[4''-(phosphonato)-2'-biphenyl]ylbenzene (**18**) in black; 1,2,4,5-tetrakis(*p*-phosphonatophenyl)benzene (**23**) in orange; 1,3,5,7-tetrakis(*p*-phosphonatophenyl)adamantane (**28**) in blue; hexakis(*p*-phosphonatophenyl)benzene (**4**) in red.

Since the weight loss of the materials below 200 °C can be attributed to water, it can be concluded that all the compounds are stable under the experimental conditions used to measure the proton conductivity. Moreover it has to be mentioned that all the molecules except 1,3,5-tris(*p*-phosphonatophenyl)benzene (**12**) are water insoluble, which is a requirement for electrolyte materials in PEMs.

3.3.3 Proton Conductivity

In order to simulate the working conditions of an intermediate-temperature FC, through-plane proton conductivity has been measured under 1 bar H₂O atmosphere by increasing temperature until 180 °C, i.e. by decreasing RH until 20 %. As explained in Section 3.2.2, a conductivity which decreases while increasing temperature is evidence of a vehicle mechanism for proton transport^[25] whereas a conductivity which increases with temperature is related to a *Grotthuss*-type proton transport.^[26] Figure 3.39 presents the plots of the proton conductivity vs. temperature above 100 °C under 1 bar H₂O atmosphere for the six different compounds as well as for Nafion® 117 for comparison.

Under these conditions, three types of proton conductivity curves are observed when the temperature is increased:

- a constant proton conductivity: **12**, **4**, **28** and **9**;
- a decreasing proton conductivity (vehicle mechanism): **23**;
- an increasing proton conductivity (*Grotthuss*-type mechanism): **18**.

Like Nafion® 117, the square-planar molecule **23** presents a conductivity which decreases by increasing the temperature. This is characteristic of compounds in which the vehicle mechanism is responsible for proton transport.^[25] However, the determination of the proton conductivity is hampered by the fact that at 130 °C a continuous but slow decrease of conductivity is observed for more than 20 h which can be most probably attributed to a continuous release of water due to slow condensation of the phosphonic acid groups. These condensation reactions have a profound impact on proton conductivity and are irreversible as can be seen when the conductivity of a pellet before and after exposure to 130 °C at 1 bar H₂O atmosphere are compared. At 150 °C and above the conductivity of the sample again equilibrates faster to the environment.

The proton conductivity of **18** increases by one order of magnitude above 120 °C, i.e. below 50 % RH, reaching a maximum value of $8.5 \cdot 10^{-5} \text{ S} \cdot \text{cm}^{-1}$ at 184 °C. This can be attributed to a *Grotthuss*-type mechanism for proton conduction.

The other compounds present a conductivity which remains constant upon increasing the temperature and which therefore can be neither related to the *vehicle*

nor to the *Grotthuss*-type mechanism. The linear molecule (compound **9**) shows the lowest proton conductivity of all the synthesized materials ($1.4 \cdot 10^{-6} \text{ S}\cdot\text{cm}^{-1}$) while the triangular compound **12** presents the highest ($8 \cdot 10^{-3} \text{ S}\cdot\text{cm}^{-1}$). However, the proton conductivity of **12** can only be measured above $140 \text{ }^\circ\text{C}$, i.e. below 25 % RH, due to its water solubility under these conditions. Above 25 % RH under 1 bar H_2O atmosphere, the substance begins to flow like a fluid of high viscosity.

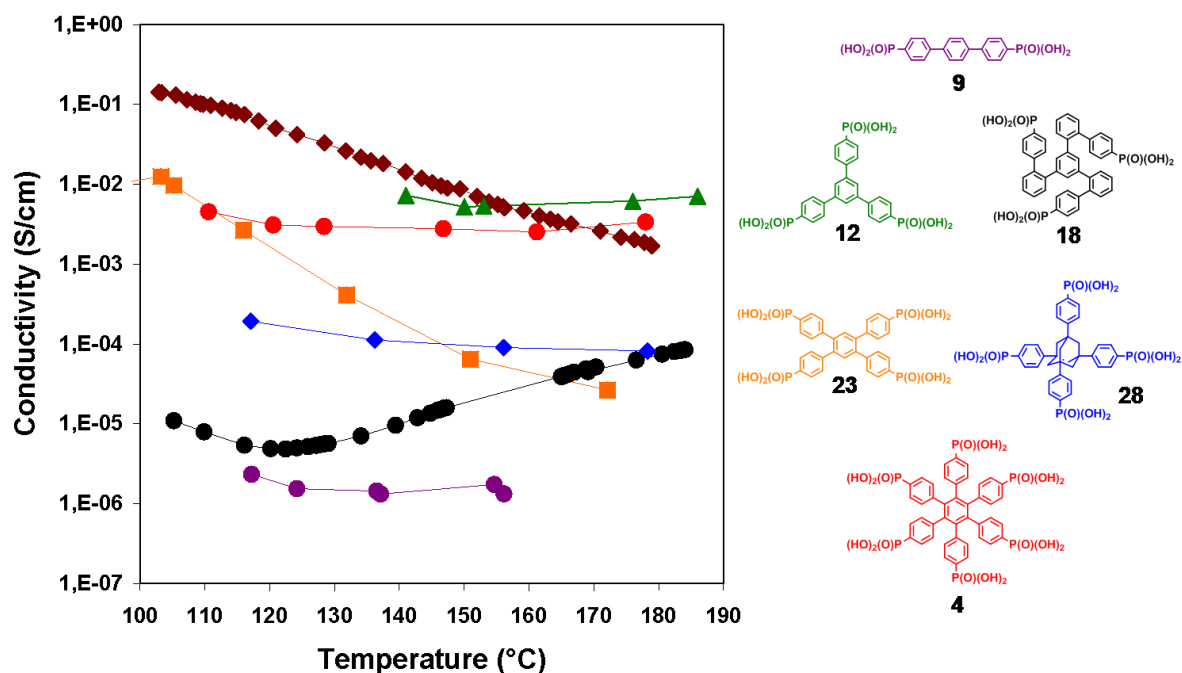


Fig. 3.39: Plots of the proton conductivity vs. temperature under 1 bar H_2O atmosphere for compounds **9**, **12**, **18**, **23**, **28** and **4**. Each compound is depicted with a color: (*p,p'*-terphenyl-4,4''-diyl)bisphosphonic acid (**9**) in violet; 1,3,5-tris(*p*-phosphonatophenyl)benzene (**12**) in green; 1,3,5-tris[4''-(phosphonato)-2'-biphenyl]ylbenzene (**18**) in black; 1,2,4,5-tetrakis(*p*-phosphonatophenyl)benzene (**23**) in orange; 1,3,5,7-tetrakis(*p*-phosphonatophenyl)adamantane (**28**) in blue; hexakis(*p*-phosphonatophenyl)benzene (**4**) in red. The curve of Nafion® 117 (brown) is shown as comparison.

Proton conductivity measurements at $25 \text{ }^\circ\text{C}$ by increasing and decreasing RH have been conducted to study the behavior of the different compounds only by changing one parameter, the RH (in the previous experiments, both the temperature and the RH were varied). It is expected to provide a deep knowledge of the proton transport mechanism taking place through the materials. Figure 3.40 shows the proton conductivity of the materials measured at RT by decreasing RH and this of Nafion® as comparison.

A constant decrease in conductivity is observed for all compounds when the RH is decreased. As expected, the classification of the materials by increasing temperature at 1 bar H₂O atmosphere is the same at 25 °C by decreasing RH. The linear molecule **9** shows the lowest conductivity, followed by the propeller-like compound **18**. On the other hand **12** has the highest proton conductivity; however no measurements could be performed above 80 % RH since the sample started to become fluid above these RH.

Investigations at 25 °C by decreasing the RH have been performed for **23** before and after conductivity measurements under 1 bar H₂O atmosphere.

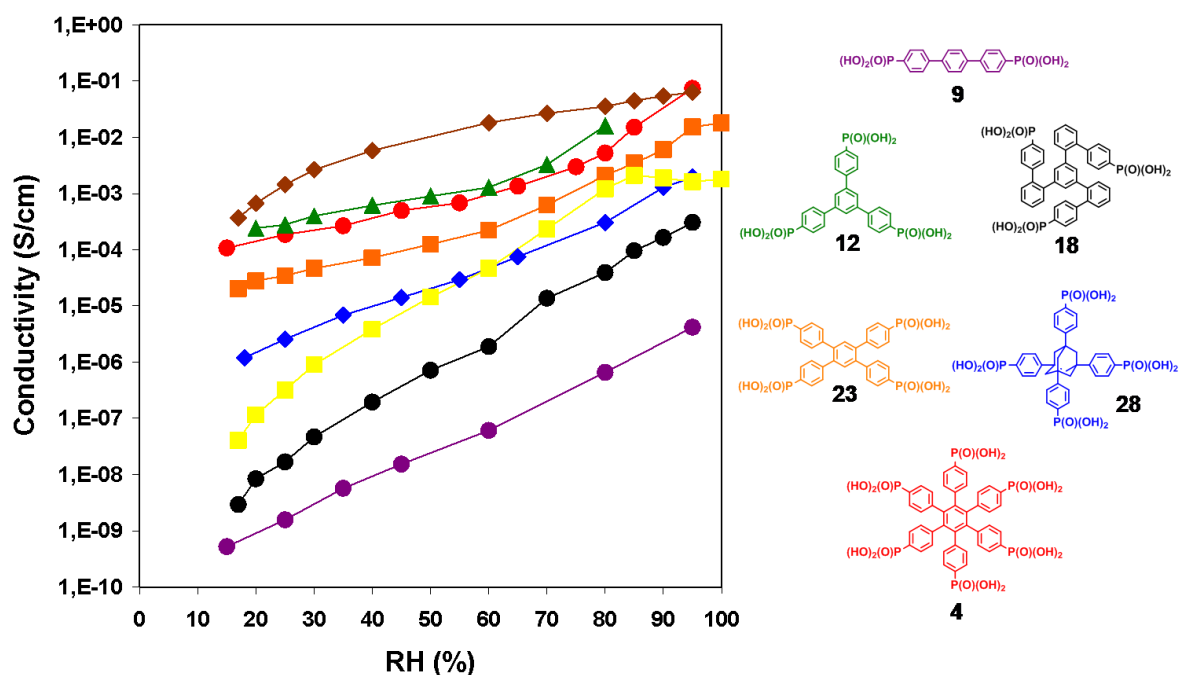


Fig. 3.40: Plots of the proton conductivity vs. RH at RT for compounds **9**, **12**, **18**, **23**, **28** and **4**. Each compound is depicted with a color: (*p,p'*-terphenyl-4,4''-diyl)bisphosphonic acid (**9**) in violet; 1,3,5-tris(*p*-phosphonatophenyl)benzene (**12**) in green; 1,3,5-tris[4''-(phosphonato)-2'-biphenyl]ylbenzene (**18**) in black; 1,2,4,5-tetrakis(*p*-phosphonatophenyl)benzene (**23**)-before “vapor treatment” in orange; 1,2,4,5-tetrakis(*p*-phosphonatophenyl)benzene (**23**)-after “vapor treatment” in yellow; 1,3,5,7-tetrakis(*p*-phosphonatophenyl)adamantane (**28**) in blue; hexakis(*p*-phosphonatophenyl)benzene (**4**) in red. The curve of Nafion® 117 (brown) is shown as comparison.

As can be seen in Figure 3.40, the conductivity of the sample after the “vapor treatment” is lower than that one of the sample which has not been examined under these conditions. This result is in accordance with the above mentioned finding that irreversible condensation reactions between the phosphonic acid groups take place

under 1 bar H₂O atmosphere. The conductivity vs. RH curve to take into account and which can be correlated to the curve at 1 bar H₂O atmosphere is the curve after “vapor treatment”.

Interestingly, for compounds **9** and **4** the drop in conductivity below 50 % is much less pronounced than in the case of Nafion® 117. This can be correlated to the almost constant conductivity by increasing temperature observed above 120 °C at 1 bar H₂O atmosphere corresponding to a RH below 50 %.

The bulk proton conductivities of the different geometrical shapes under dry nitrogen flux are plotted in Figure 3.41. The pellets are first heated from RT to 160 °C, then cooled to RT and heated again. This is done in order to get rid of the possible water present in the sample. Proton conductivity is recorded during the three temperature cycles; however Figure 3.41 only reports the third cycle which corresponds to the intrinsic proton conductivity. The *Arrhenius* plots are almost linear in the experimental temperature ranges (proton conductivity increasing with temperature), indicating that one dominant proton conducting mechanism, with constant activation energy, is present in the different materials. Often, such a dependency is observed for anhydrous proton conductors.^[78]

As already explained in Section 3.2.2, the activation energy of the different compounds can be calculated from the slope of the *Arrhenius* plots. The obtained values are listed in Table 3.5 and range from 65 to 87 kJ/mol. Compound **4** presents the lowest activation energy and the highest conductivity values whereas the higher activation energy belongs to compound **28** which shows very low conductivity values. These results corroborate the above mentioned statement that low activation energies correspond to high proton conductivity values.

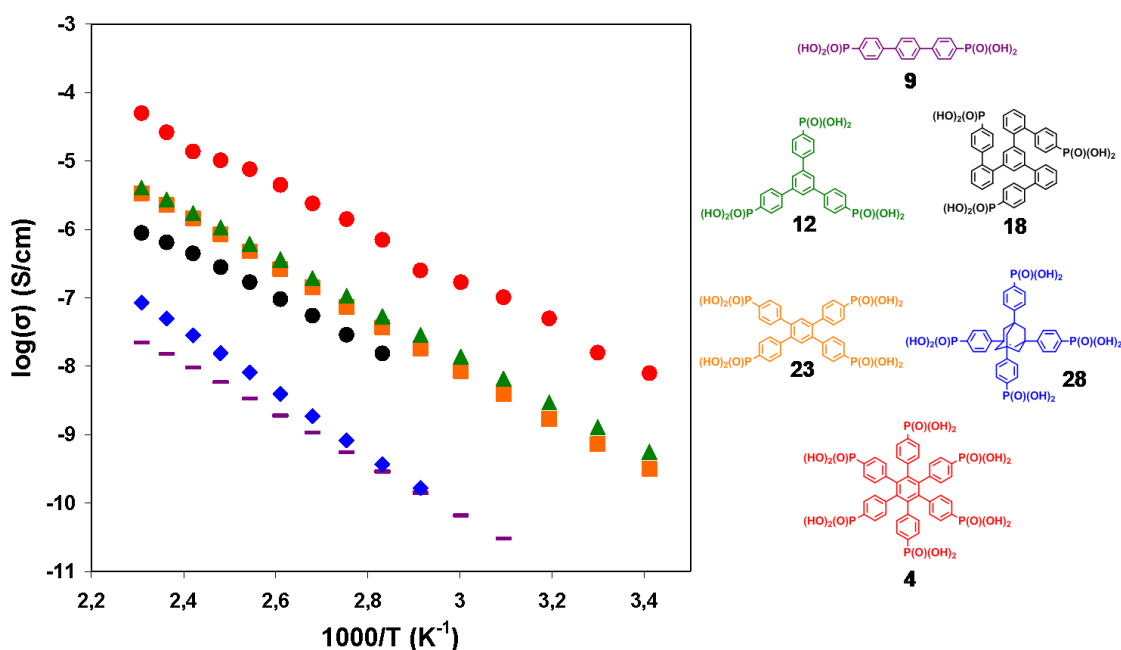


Fig. 3.41: The *Arrhenius* plots of compounds **9**, **12**, **18**, **23**, **28** and **4**. Each compound is depicted with a color: (*p,p'*-terphenyl-4,4''-diyl)bisphosphonic acid (**9**) in violet; 1,3,5-tris(*p*-phosphonatophenyl)benzene (**12**) in green; 1,3,5-tris[4''-(phosphonato)-2'-biphenyl]ylbenzene (**18**) in black; 1,2,4,5-tetrakis(*p*-phosphonatophenyl)benzene (**23**) in orange; 1,3,5,7-tetrakis(*p*-phosphonatophenyl)adamantane (**28**) in blue; hexakis(*p*-phosphonatophenyl)benzene (**4**) in red.

In the dry state both the amount and density of phosphonic acid functions in the sample is expected to strongly affect the conductivity. The phosphonic acid density d has been calculated as described in for compound **4** in section 3.2.2. The obtained values are included in Table 3.5. The highest ratio was found for hexakis(*p*-phosphonatophenyl)benzene. By comparing these values with the conductivity at dry conditions, it can be deduced that the absolute value of the bulk conductivity is smaller for compounds presenting a small density of phosphonic acid functions. The only exception is compound **18** which possess an extremely small density of 0.46 but shows a conductivity under anhydrous conditions which is in the middle of the group.

From these proton conductivity data it can be deduced that the geometry of the molecules and their self-organization play an important role in proton transport since all molecules present different values of proton conductivity and the curves indicate different trends.

Table 3.5: Activation energies of the different materials calculated from the IS data and their corresponding phosphonic acid density *d*.

Compounds	Ea (IS) ($\pm 5\%$) (kJ/mol)	<i>d</i>
(<i>p,p'</i> -Terphenyl-4,4''-diyl)bisphosphonic acid (9)	71	0.71
1,3,5-Tris(<i>p</i> -phosphonatophenyl)benzene (12)	68	0.80
1,3,5-Tris[4''-(phosphonato)-2'-biphenyl]ylbenzene (18)	66	0.46
1,2,4,5-Tetrakis(<i>p</i> -phosphonatophenyl)benzene (23)	71	0.86
1,3,5,7-Tetrakis(<i>p</i> -phosphonatophenyl)adamantane (28)	87	0.74
Hexakis(<i>p</i> -phosphonatophenyl)benzene (4)	65	0.92

3.3.4 Water Uptake

The water uptake of a material determines both its proton conductivity and its mechanical stability and is therefore an important parameter to check the suitability of new compounds as separator materials in PEM.^[30] In the case of the phosphonic acid based organic materials, it is presumed that the compounds with a higher content of phosphonic acid groups will take up more water. As expected, a trend toward increased water uptake when the number of phosphonic acid groups is increased is observed. Figures 3.42 and 3.43 show the variation of the water uptake and the lambda value (number of water molecules per phosphonated molecule) as a function of RH at RT for the different compounds.

For **9** and **23**, the curve of the water uptake against RH was similar to a Type V *van der Waals* adsorption isotherm characterized by an hysteresis loop and a limiting uptake.^[38] Essentially, no water uptake is observed for compound **9** although the molecule possesses two acidic functions. In the case of **23**, the water uptake increases appreciably only above 84 % RH, reaching a maximum value of almost 3 wt % at 98 % RH.

Materials **18** and **28** show a similar trend in their water uptake study at RT when going from low to high values of RH. The curve of the water uptake is similar to a Type IV *van der Waals* adsorption isotherm which is characterized by a hysteresis loop and

a limiting uptake. Only at 98 % RH can a difference be observed since the tetragonal compound **28** presents a higher value of water uptake (1.6 wt %).

The triangular compound **12** becomes sticky and its color changes from yellow to brown above 52 % RH; however, no decomposition of the material is detected by NMR. Most probably, water molecules clustered into the material act as softener. **12** exhibits higher water uptake by lower RH than the other compounds since the water uptake starts to increase from 22 % RH. The water uptake curve is similar to a Type II *van der Waals* adsorption isotherm, which is reversible and has an unlimited uptake. This fits to compound **12** which is water soluble.

4 presents the highest water uptake and also the highest lambda, which can be attributed to the fact that the molecule contains the highest number of phosphonic acid groups. Moreover, **4** is the only compound clearly showing a stepwise hydration isotherm, also called type VI *van der Waals* isotherm;^[38] all the other materials adsorb water continuously.

It should be noted that for all materials, an hysteresis in the water desorption isotherm will be observed due to the shape of the adsorption isotherm.^[38] This has been already observed for compound **4**.

It is known that crystal hydrates can adsorb water either in a stepwise manner or in a continuous way,^[37, 79] contrary to polymers which always adsorb water continuously.^[80] It has previously been determined that **4** belongs to the first type of crystal hydrates which adsorb water in a stepwise way. However, no steps in the adsorption isotherm can be distinguished for **9** and **18** since their water uptake is very low. It is also not possible to determine whether materials **12**, **23** and **28** are crystal hydrates or not since they adsorb water continuously and not in a stepwise manner.

3.3 The Influence of Geometry and the Number of Acidic Functions

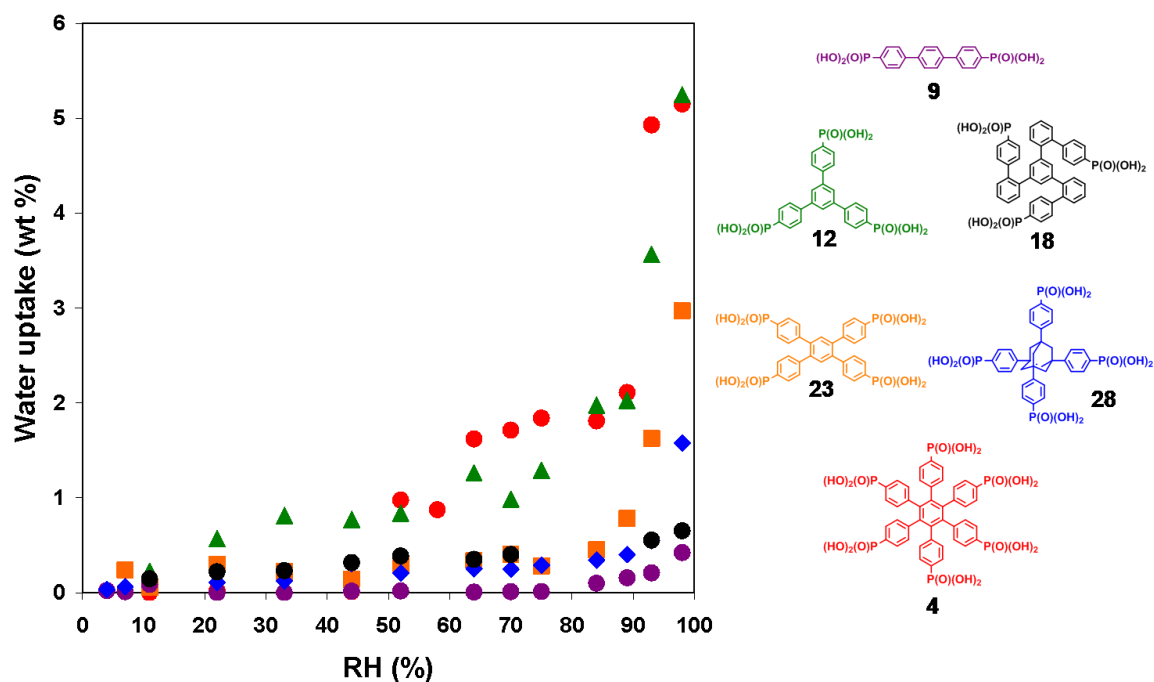


Fig. 3.42: (a) Water uptake of the phosphonic acid containing materials as a function of the RH at RT. Each compound is depicted with a color: (*p,p'*-terphenyl-4,4''-diyl)bisphosphonic acid (**9**) in violet; 1,3,5-tris(*p*-phosphonatophenyl)benzene (**12**) in green; 1,3,5-tris[4''-(phosphonato)-2'-biphenyl]ylbenzene (**18**) in black; 1,2,4,5-tetrakis(*p*-phosphonatophenyl)benzene (**23**) in orange; 1,3,5,7-tetrakis(*p*-phosphonatophenyl)adamantane (**28**) in blue; hexakis(*p*-phosphonatophenyl)benzene (**4**) in red.

In contrast to polymeric electrolyte membranes,^[28, 39] this series of phosphonated crystalline materials showed very low water adsorption values and very low lambda. Usually, the water uptake values at RT reach a maximum of 25.5 wt % for sulfonic acid based polymers^[42] and of 100 wt % for phosphonic acid based polymers,^[28] whereas in the case of the compounds 1 - 6 the maximum values were in the range of 5 to 6 wt %.

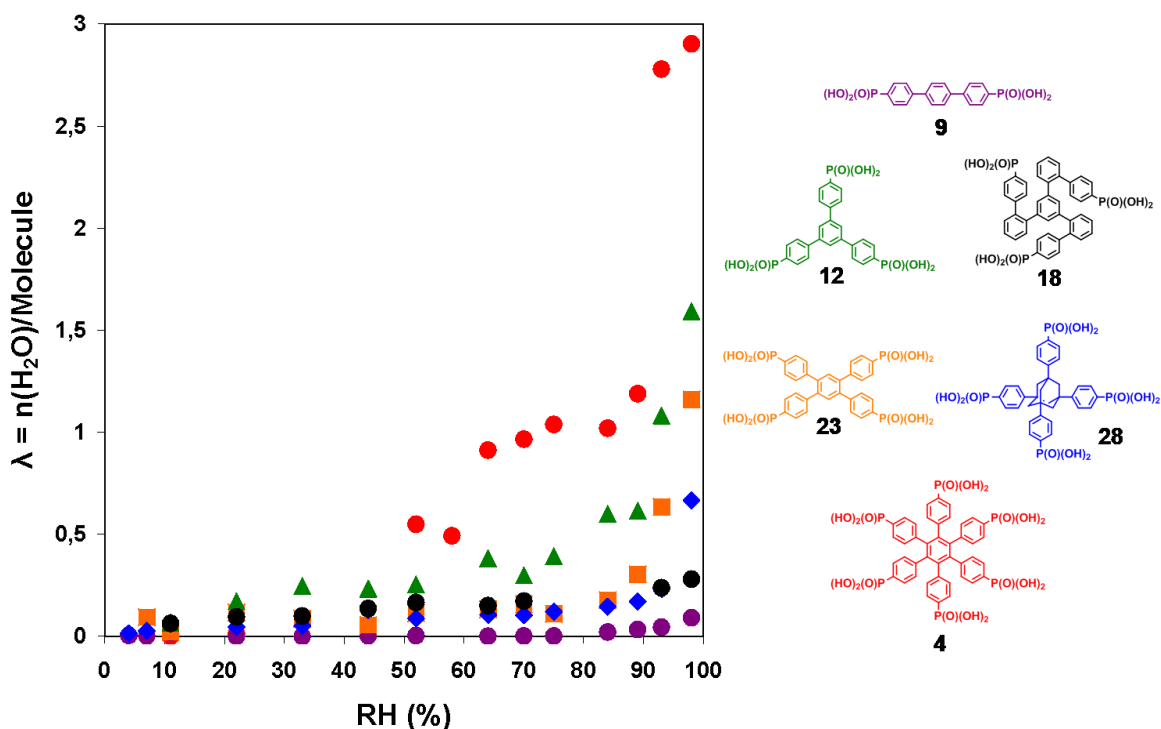


Fig. 3.43: Lambda of the phosphonic acid containing materials as a function of the RH at RT. Each compound is depicted with a color: (p,p' -terphenyl-4,4''-diyl)bisphosphonic acid (**9**) in violet; 1,3,5-tris(p -phosphonatophenyl)benzene (**12**) in green; 1,3,5-tris[4''-(phosphonato)-2'-biphenyl]ylbenzene (**18**) in black; 1,2,4,5-tetrakis(p -phosphonatophenyl)benzene (**23**) in orange; 1,3,5,7-tetrakis(p -phosphonatophenyl)adamantane (**28**) in blue; hexakis(p -phosphonatophenyl)benzene (**4**) in red.

As can be seen in Table 3.6, all compounds except the propeller-like molecule **18** have almost the same number of P atoms per C atoms and per phenyl rings. However, they present completely different maximum water uptake and λ_{max} values. It can be concluded that the self-organization and the geometry are more important than the ratio P/C.

It is obvious that when the number of phosphonic acid groups is increased, an increase of the maximum water uptake is not observed. Compounds **12** and **4** both present the highest maximum water uptake but they have different λ_{max} . This is due to the fact that **4** encloses twice the number of water molecules than **2** in its crystalline structure. This corresponds to 0.5 water molecules per phosphonic acid group for the two molecules.

3.3 The Influence of Geometry and the Number of Acidic Functions

Table 3.6: Physical data of the phosphonic acid-based compounds.

Compound	n(-P(O)(OH) ₂)	P/C	Water uptake max. (wt %) ^[a]	λ_{\max}	n(H ₂ O)/P(O)(OH) ₂ ^[c]	σ at 150 °C and 21 % RH (S/cm)
9	2	0.11	0.42	0.09	0.045	$1.4 \cdot 10^{-6}$
12	3	0.13	5.3	1.6	0.53	$5.2 \cdot 10^{-3}$
18	3	0.07	0.65	0.28	0.09	$1.6 \cdot 10^{-5}$
23	4	0.13	3.0	1.2	0.29	$6.5 \cdot 10^{-5}$
28	4	0.12	1.6	0.67	0.17	$9.1 \cdot 10^{-5}$
4	6	0.14	5.2	2.9	0.48	$2.8 \cdot 10^{-3}$

[a] the adamantane is counted as one phenyl ring

[b] the maximum water uptake is at 98 % RH for all materials

[c] at 98 % RH

3.3.5 Crystallinity

To correlate the proton conductivity to the supramolecular ordering of the molecules, different crystallinity studies have been carried out. WAXS measurements have been performed at 10, 30 and 60 % RH and at different temperatures. No significant modifications of the X-ray patterns are observed when temperature and RH are changed. Figure 3.44 displays the X-ray diffractograms of compounds **9**, **18** and **23** recorded at 10 % RH as an example.

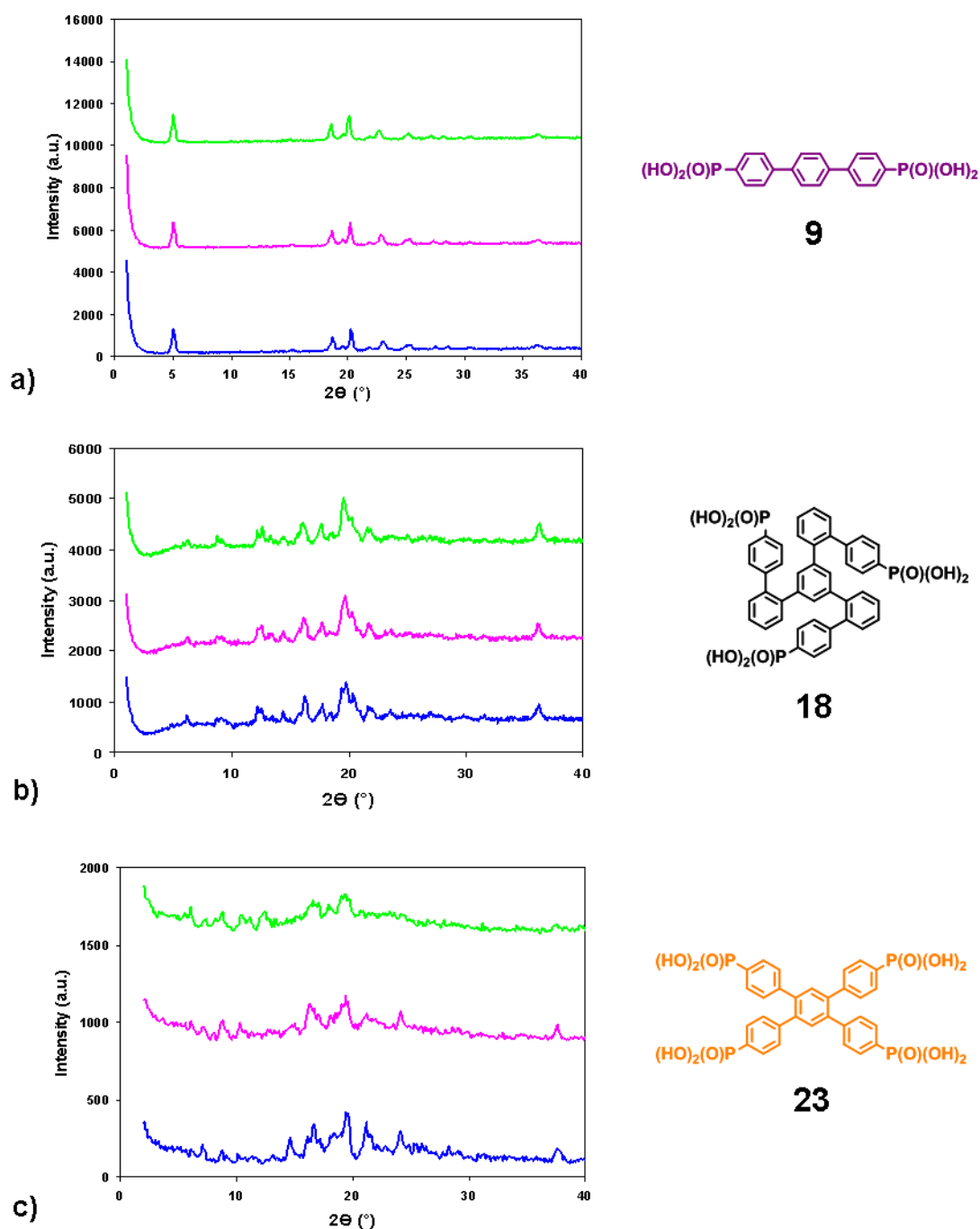


Fig. 3.44: X-ray diffractogram recorded at 10 % RH at 25, 100 and 200 °C (blue, pink and green respectively) of a) (p,p' -terphenyl-4,4''-diyl)bisphosphonic acid (**9**), b) 1,3,5-tris[4''-(phosphonato)-2'-biphenyl]ylbenzene (**18**) and 1,2,4,5-tetrakis(p -phosphonatophenyl)benzene (**23**).

The degree of crystallinity of the different samples is determined by calculating the ratio of the integrated peak area to total area for the experiments performed at 25 °C and 10 % RH. The values are presented in Table 3.7. From these data it can be

deduced that compounds **9**, **18**, **23** and **4** possess crystalline regions in which, like in a crystal, atoms or molecules are arranged in a periodic manner over long distances and amorphous regions in which the molecules have only order over short distances (a few atomic or molecular spacings). The absence of crystallinity of compounds **12** and **28** means that these materials lack long-range order although this does not exclude that they present some short-range one.

Table 3.7: Degree of crystallinity calculated at 25 °C and 10 % RH and proton conductivity at 150 °C and 21 % RH for the different compounds.

Compound	Degree of crystallinity at 25 °C and 10 % RH (%)	Proton conductivity at 150 °C and 21 % RH (S/cm)
9	7	$1.4 \cdot 10^{-6}$
12	0	$5.2 \cdot 10^{-3}$
18	10	$1.6 \cdot 10^{-5}$
23	24	$6.5 \cdot 10^{-5}$
28	0	$9.1 \cdot 10^{-5}$
4	93	$2.8 \cdot 10^{-3}$

The effect the degree of crystallinity of the material has on proton conductivity is not yet fully understood. It can be observed that proton conductivity may be in some way correlated to crystallinity degree since the molecules presenting a higher degree of crystallinity show higher proton conductivity. However this statement is not valid for compound **12** which does not present crystalline regions but shows very high bulk proton conductivity.

Since the crystallinity degree on its own does not give information about how molecules are ordered in a measured sample, which is a crucial issue to explain the differences in proton conductivity, crystals suitable for conventional X-ray crystallography needed to be grown.

With an understanding of how molecules pack, one gains insight into how well protons are able to flow through a material and thereby can develop design rules for more optimized molecular entities. Therefore it is necessary to obtain the single crystal structure of the different compounds. As mentioned in Section 3.2.5, little information

exists about the structure and properties of organic phosphonic acids and due to their poor solubility and strong hydrogen bonds the compounds are difficult to crystallize.

Among the synthesized molecules, the crystal structures of **12**^[48] and **28**^[50] have previously been reported in the literature. Single-crystalline salts of the triangular molecules **12** with DMAP were obtained as methanol solvate. The individual molecules of the cocrystals are associated by π -stacking and hydrogen bonding. The packing order in the lattice seems to be dominated by columnar organic domains composed of staples of eclipsed pairs of **12** as shown in Figure 3.45a.

Single crystals of tetragonal compound **28** were obtained without the help of any salt addition. The molecules self-assemble by hydrogen bonds into a diamondoid network as shown in Figure 3.45b. There are two tetrahedral nodes in the network: the first one is represented by the adamantane core and the second results from a tetrahedral assembly of four phosphonic acid groups with water molecules.

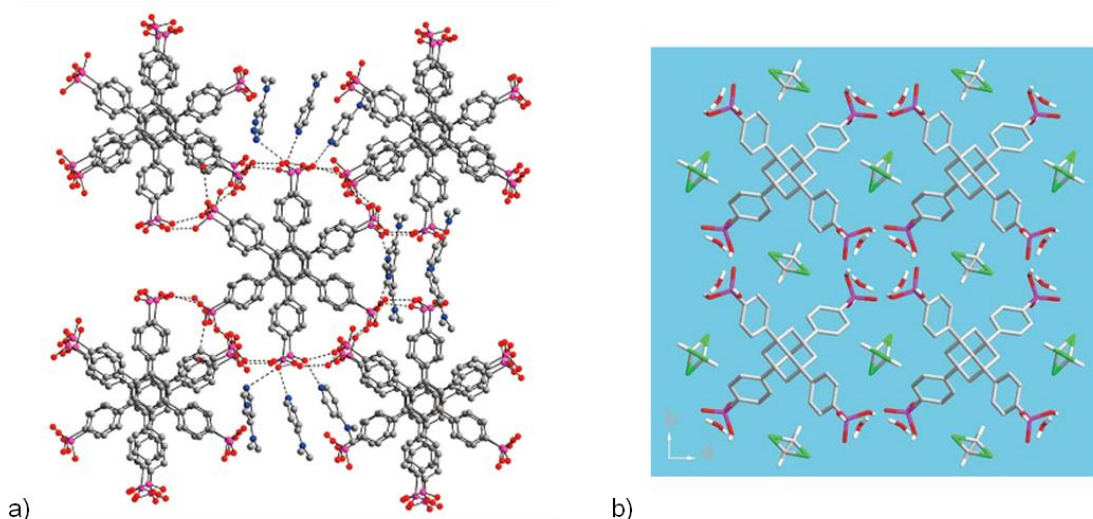


Fig. 3.45: a) Perspective view of the supramolecular motif of 1,3,5-tris(p-phosphonatophenyl)benzene (methanol molecules are omitted for clarity)^[48] and b) view of the crystal structure of **28** down the c-axis. Channels are shown with included water molecules and disordered CHCl₃ guests. H atoms on the organic core of **28** are removed for clarity.^[50]

Among the remaining four molecules, it has been possible to obtain the crystal structure of (*p,p'*-terphenyl-4,4''-diyl)bisphosphonic acid (**9**). The linear compound **9** is crystallized from NMP. The crystals obtained are suitable for diffraction; it is found that the molecules crystallize in the trigonal P 3₁ space group and the cell parameters are $a = 19.6890(2)$ Å, $b = 19.6890(2)$ Å and $c = 18.5040(2)$ Å. No continuous regions of phosphonic acid groups are detected in this crystal structure (see Figure 3.46).

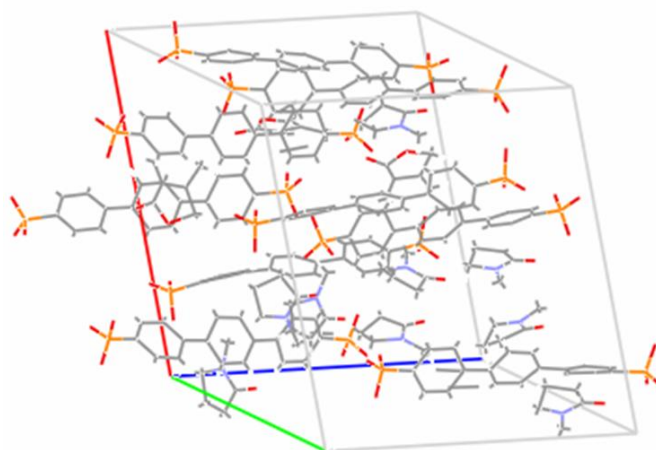


Fig. 3.46: Crystal structure of (*p,p'*-terphenyl-4,4''-diyl)bisphosphonic acid (**9**), H atoms are omitted for clarity.

All attempts to obtain single crystals of compounds **18** and **23** have failed. This is due to the low crystallization propensity of the molecules promoted by the strong hydrogen bonds and the low solubility of the materials in all types of solvents.

3.3.6 Solid-State NMR Investigations

High-resolution ^1H MAS NMR is a versatile tool to reveal information about supramolecular interactions, such as hydrogen bonding.^[81] The proton chemical shift value is highly sensitive to structural changes and can therefore display the strength of bonds and dynamics in the system. A correlation between the proton chemical shifts (δ_{iso}) and the strength of the hydrogen bonding has been reported by *Harris et al.*^[71, 82] Since the hydrogen bond strength depends on distances between oxygen atoms participating in hydrogen bonds it will also affect the chemical shift.^[82]

For example, ^1H chemical shifts of 10 to 17 ppm were reported for different phosphonic acid-containing materials, including benzene phosphonic acid. It was claimed that the shorter the distance between the oxygen atoms, the higher the chemical shift. In other words, when increasing the hydrogen bond strength, it is observed that the proton resonance frequency of the phosphonic acid signal is shifted towards lower field.^[83]

Tentatively, one would expect similar NMR spectra for all samples as they contain the same functional group added to the similar moiety. Therefore, it is of interest to compare the chemical shifts of the corresponding phosphonic acid signals for different geometrical shapes, as illustrated in Figure 3.47 and Table 3.8.

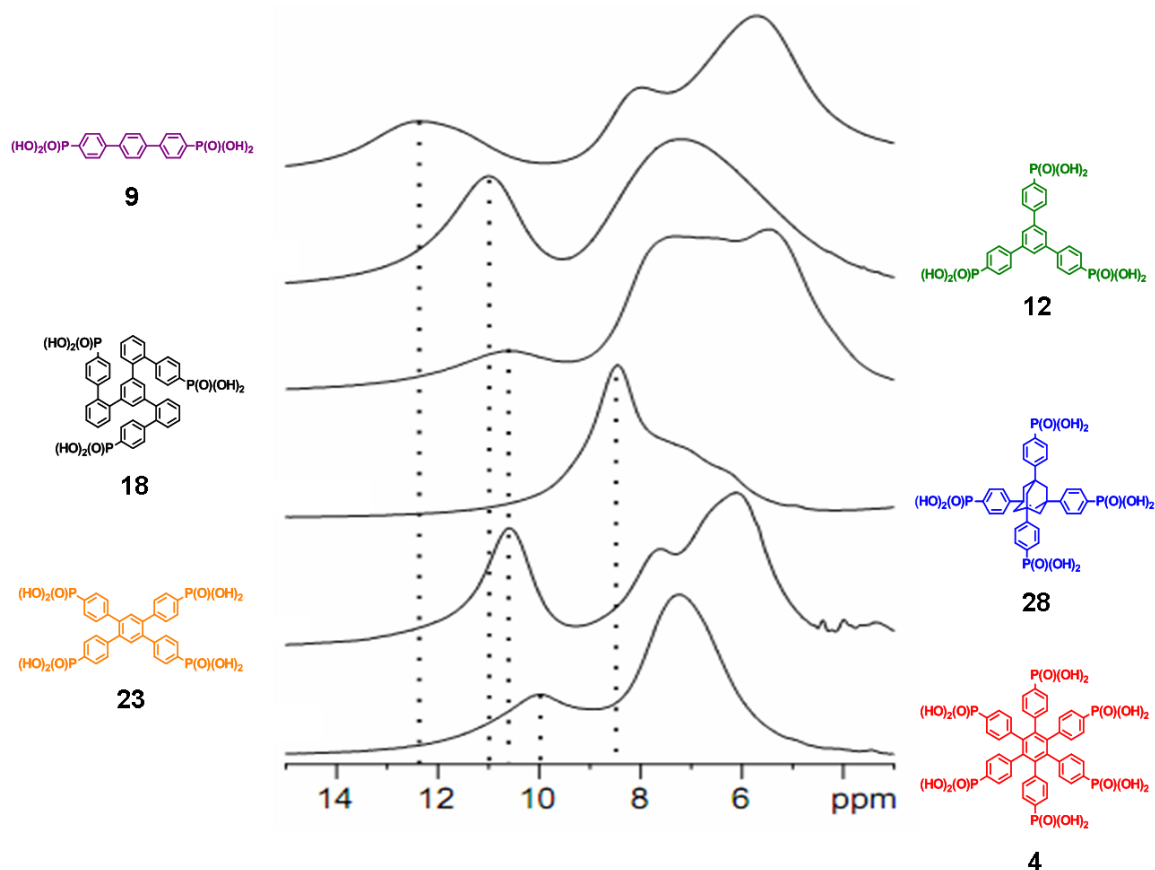


Fig. 3.47: Comparison of ^1H MAS NMR spectra recorded at 700 MHz for the different geometrical shapes at ambient conditions. Plotted from the top to the bottom with increasing number of phosphonic acid groups: (*p,p'*-terphenyl-4,4''-diyl)bisphosphonic acid (**9**), 1,3,5-tris(*p*-phosphonatophenyl)benzene (**12**), 1,3,5-tris[4''-(phosphonato)-2'-biphenyl]ylbenzene (**19**), 1,3,5,7-tetrakis(*p*-phosphonatophenyl)adamantane (**28**), 1,2,4,5-tetrakis(*p*-phosphonatophenyl)benzene (**23**), hexakis(*p*-phosphonatophenyl)benzene (**4**).

The phosphonic acid resonances range from 8.5 ppm to 12.3 ppm reflecting rather moderate hydrogen bond strength between phosphonic acid groups.^[84] The phosphonic acid resonances of (*p,p'*-terphenyl-4,4''-diyl)bisphosphonic acid (**9**) represent the highest chemical shift, i.e. from these measurements it can be stated that for compound **9** the distance between the oxygen atoms involved in hydrogen bonding is shorter than in the case of the other materials. Additionally, this material shows a relative broad line width of approximately 1800 Hz (4 ppm) compared to 1,2,4,5-tetrakis(*p*-phosphonatophenyl)benzene (**23**) with 675 Hz (1.5 ppm), indicating that the phosphonic acid groups in this compound are organized in a better ordered microstructure.

On the contrary, hexakis(*p*-phosphonatophenyl)benzene (**4**) presents a ^1H chemical shift of 9.9 ppm for the phosphonic acid signal which indicates a rather moderate hydrogen bond strength between the acidic groups and a relative large distance between them.^[84] However, it is also probable that the phosphonic acid groups of the ionomers form hydrogen bonds with residual or incorporated water contained in the system. In the case of for example compound **4**, it has been proven in Section 3.2 that the material is a crystal hydrate and comprises therefore bonded water. It can be supposed that if there is fast proton exchange between the phosphonic acid groups and the water, the chemical shift will be averaged. Thus taking into account that liquid water itself gives rise to a resonance at 4.8 ppm, a gradual shift towards lower frequencies is predicted when the content of the water increases. A resonance representing a highly ordered water based hydrogen bonded network is "standard" ice where the chemical shift in the ^1H MAS NMR spectrum is approximately at 5.8 ppm.^[85, 86] Thus from these data it can be concluded that small chemical shift values could also represent fast proton exchange between the phosphonic acid groups and incorporated water which results in an averaged resonance between the extremities.

Table 3.8: Chemical shifts from the ^1H MAS NMR spectra of the materials recorded at ambient conditions.

Compounds	δ_{iso} (ppm)
(<i>p,p'</i> -Terphenyl-4,4''-diyl)bisphosphonic acid (9)	12.3
1,3,5-Tris(<i>p</i> -phosphonatophenyl)benzene (12)	10.9
1,3,5-Tris[4''-(phosphonato)-2'-biphenyl]ylbenzene (18)	10.6
1,2,4,5-Tetrakis(<i>p</i> -phosphonatophenyl)benzene (23)	10.6
1,3,5,7-Tetrakis(<i>p</i> -phosphonatophenyl)adamantane (28)	8.5
Hexakis(<i>p</i> -phosphonatophenyl)benzene (4)	9.9

Figure 3.48 presents the changes in the chemical shifts of the hydrogen bonded phosphonic acid groups of compound **4** as a function of the amount of water present in the sample. Three different plots from top to bottom are shown in this Figure: a dried sample obtained after the synthesis (measured at 51 and 127 °C), the sample after being stored during one week at 100 % RH (measured at 51, 108 and 51 °C) and

finally this sample dried again (measured at 51 °C). It can be observed that the ^1H MAS NMR spectrum depends critically on the sample history since the release of water after exposing it at 100 % RH is inhibited. This observation is in agreement with the water uptake curve indicated in Figure 3.15 in Section 3.2.4.

Moreover, the ^1H MAS NMR spectrum of the freshly obtained compound (light grey line in Figure 3.48) shows that the phosphonic acid resonance is located at 10.0 ppm and upon water uptake (dark grey line in Figure 3.48) shifts towards 8.2 ppm. This fact supports the above mentioned assumption of an interaction between the incorporated water molecules and the acidic groups which results in an average resonance between extremities and also indicates a fast proton exchange between the phosphonic acid groups and the incorporated water.

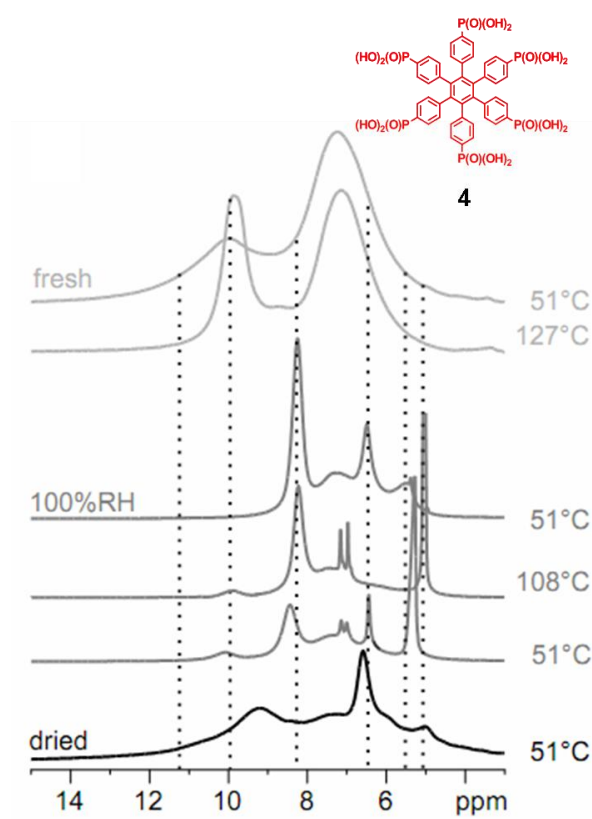


Fig. 3.48: ^1H MAS NMR spectra of hexakis(*p*-phosphonatophenyl)benzene (**4**) recorded at 700 MHz from the top: freshly obtained sample measured at 324 and 400 K (light grey); sample stored at 100 % RH and measured at 324, 381 and 324 K (dark grey); sample stored at 100 % RH and afterwards dried at 423 K under nitrogen flux and measured at 324 K (black).

In addition, the dried sample (black line in Figure 3.48) exhibits two relatively broad peaks located at 6.5 and 5.4 ppm. The presence of these signals indicates that most

probably phosphonic acid-water interaction sites are present in the sample after its storage at 100 % RH. Notably, for "wet" PVPA a ^1H chemical shift of 6.5 ppm is also observed and assigned to a phosphonic acid-water interaction, while the signal at 5.4 ppm may reflect water-water interaction.^[87, 88] It has to be pointed out that the dried sample (black line in Figure 3.48) shows a broad peak at around 9 ppm which is in between the phosphonic acid resonance of the fresh sample located at 10.0 ppm and the resonance of the "wet" sample at 8.2 ppm. This means that still some water interacting with the phosphonic acid groups which has been incorporated during the storage at 100 % RH is present in the sample even after drying. Thus the water uptake in case of **4** is not completely reversible.

As it has been pointed out in Chapter 3.2.7, the mobility of protons can be investigated by variable temperature solid-state NMR studies (VT ^1H MAS NMR). If there is a mobile proton, a change in temperature results in a continuous and significant narrowing of the line width.^[69, 70] In most cases, such local molecular dynamics lead to characteristic line broadening or narrowing of the ^1H signal characteristic of the acidic protons, sometimes associated with a shift of the line. Figure 3.49 presents the VT ^1H MAS NMR spectra of the six phosphonated molecules.

Hexakis(*p*-phosphonatophenyl)benzene, 1,3,5-tris[4''-(phosphonato)-2'-biphenyl]ylbenzene, 1,3,5-tris(*p*-phosphonatophenyl)benzene and 1,3,5,7-tetrakis(*p*-phosphonatophenyl)adamantane present a rather strong effect while increasing the temperature (Figures 3.49f, c, b and e respectively). The two first ones show a complex temperature dependency for the ^1H signal assigned to the hydrogen bonded protons since in addition to line narrowing a change of the chemical shift is also observed.

The ^1H MAS NMR spectrum of compound **4** has been described in detail in Chapter 3.2.7.

Two facts can be observed in the ^1H MAS NMR spectra of 1,3,5-tris[4''-phosphonato-2'-biphenyl]ylbenzene (**18**) shown in Figure 3.49c:

- The two broad peaks in the -6 °C spectrum become one narrow peak in the 146 °C spectrum;
- The peak at 13 ppm vanishes while increasing temperature while the peak at 11 ppm appears.

The first observation is a behavior which is commonly known and can be explained by an averaged equilibrium of different sites.^[58] On the other hand, the change in the chemical shift is rather a stepwise transition in the temperature range from 26 to 46 °C. This observation has already been reported for poly(vinyl triazole) derivates (PVTz).^[89] In contrast to PVTz, compound **18** does not impose a continuous shift toward lower ppm values. In the PVTz most of those characteristics are explained by a chemical exchange processes between the hydrogen bonded (NH...N) and the non-hydrogen bonded states. Thus, in analogy this material might also reflect a formation and breaking of hydrogen bonds.

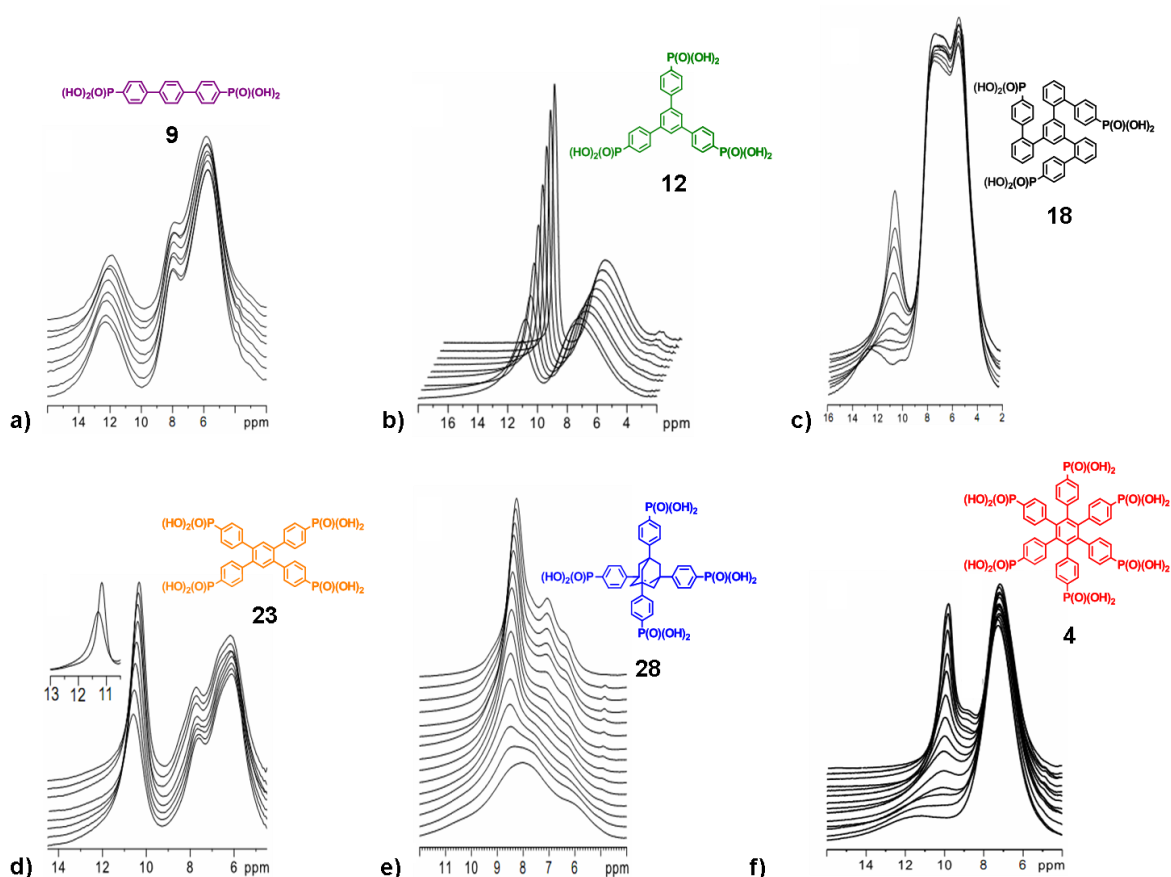


Fig. 3.49: VT ^1H MAS NMR spectra at 700 MHz measured at raising temperatures from bottom to top in 10 K steps: a) (*p,p'*-terphenyl-4,4''-diyl)bisphosphonic acid (**9**) (from 46 to 136 °C); b) 1,3,5-tris(*p*-phosphonatophenyl)benzene (**12**) (from 267 to 409 K); c) 1,3,5-tris[4''-(phosphonato)-2'-biphenyl]ylbenzene (**18**) (from 267 to 409 K); d) 1,2,4,5-tetrakis(*p*-phosphonatophenyl)benzene (**23**) (from 319 to 409 K); e) 1,3,5,7-tetrakis(*p*-phosphonatophenyl)adamantane (**28**) (from 267 to 409 K); f) hexakis(*p*-phosphonatophenyl)benzene (**4**) (from 267 to 409 K).

The fact that ^1H MAS NMR line widths are almost constant while the temperature is increased suggests an absence of fast ^1H mobility on the NMR timescale. This behavior is observed for compounds **9** and **23**, see Figures 3.49a and d.

Figure 3.50 shows the *Arrhenius* plots of the six compounds. From the slope of the plots, the apparent activation energy can be calculated (see Section 3.2.7). The values are listed in Table 3.9 which also contains the activation energy values derived from the IS measurements. In Figure 3.50, the slopes of compounds **18** and **4** superimpose, suggesting similar mobilities of the phosphonic acid groups. However this is in contradiction with the proton conductivity measurements performed under anhydrous conditions (see Figure 3.41 in Section 3.3.3) which clearly show that these two materials present different conductivity plots.

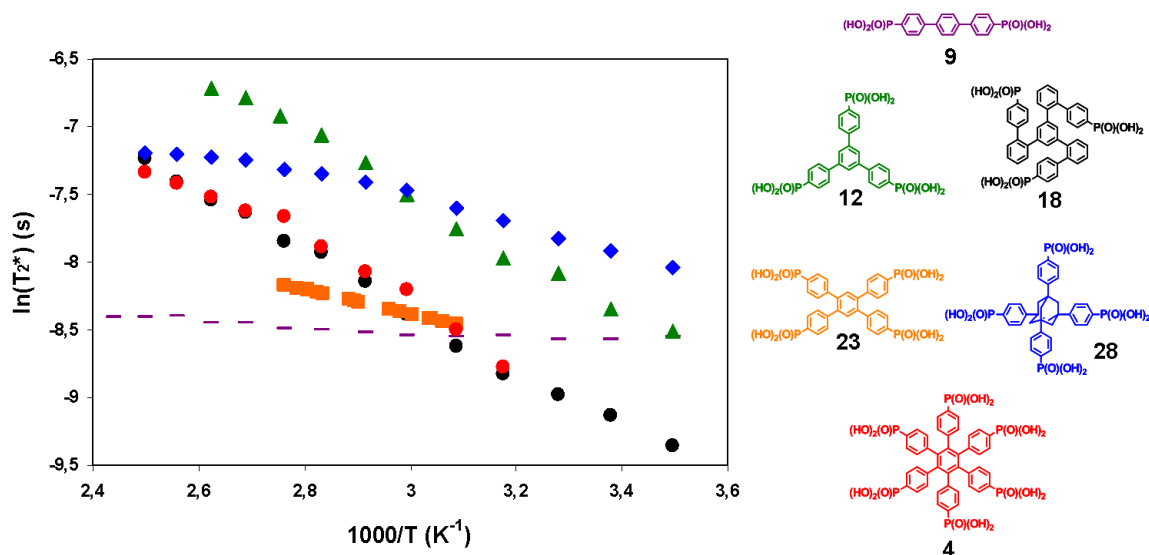


Fig. 3.50: The *Arrhenius* plots from the VT ^1H MAS NMR measurements of the different compounds. Each compound is depicted with a color: **9**: violet, **12**: green, **18**: black, **23**: orange, **28**: blue, **4**: red.

Intuitively one would assume that higher activation energies are found for protons among strongly hydrogen bonded positions. However, in case of phosphonic acid-containing polymers, such a simple relation of hydrogen-bond strengths and local proton mobility was not observed.^[90]

A comparison of the apparent activation energy derived from VT ^1H MAS NMR of the molecules reveals two different classes of compounds (see Table 3.9) which cannot be derived from the activation energies calculated from the IS data:

- Materials with an activation energy lower than 5 kJ/mol: (*p,p'*-Terphenyl-4,4''-diyl)bisphosphonic acid (**9**), 1,2,4,5-tetrakis(*p*-phosphonatophenyl)benzene (**23**) and 1,3,5,7-tetrakis(*p*-phosphonatophenyl)adamantane (**28**);
- Materials with an activation energy between 15 and 18 kJ/mol: 1,3,5-Tris(*p*-phosphonatophenyl)benzene (**12**), 1,3,5-tris[4''-(phosphonato)-2'-biphenyl]ylbenzene (**18**) and hexakis(*p*-phosphonatophenyl)benzene (**4**).

The first class of compounds shows activation energy values lower than 5 kJ/mol that are indicative of a rotational or tumbling motion. Interestingly, these molecules present an even number of acidic functions whereas the ones belonging to the second class have an odd number of phosphonic acid groups.

Since activation energies of temperature-activated motional processes involving hydrogen bonds are generally in the range of 120 kJ/mol,^[58] the obtained apparent activation energies cannot be attributed to a single thermally activated process. Notably, in rather ideal cases, where the NMR data reflect the proton motions responsible for observable bulk proton conductivity, the activation energy obtained from both the VT ¹H MAS NMR and IS are similar.^[70]

Table 3.9: Activation energies of the different materials calculated from the IS and NMR data.

Compounds	Ea (IS) (± 5 %) (kJ/mol)	Ea (NMR) (kJ/mol)
(<i>p,p'</i> -Terphenyl-4,4''-diyl)bisphosphonic acid (9)	71	2
1,3,5-Tris(<i>p</i> -phosphonatophenyl)benzene (12)	68	18
1,3,5-Tris[4''-phosphonato-2'-biphenyl]ylbenzene (18)	66	19
1,2,4,5-Tetrakis(<i>p</i> -phosphonatophenyl)benzene (23)	71	2
1,3,5,7-Tetrakis(<i>p</i> -phosphonatophenyl)adamantane (28)	87	4
Hexakis(<i>p</i> -phosphonatophenyl)benzene (4)	65	15

However in the case of these phosphonated molecules there is a discrepancy between the activation energy values calculated from IS and from NMR data. The

apparent activation energy values calculated from the NMR data are almost 60 times lower than the values obtained from the IS experiments. As explained for compound **4**, this discrepancy is attributed to the fact that the conductivity data represent charge transport on a macroscopic scale, while NMR detects the proton mobility on a microscopic scale.

^{31}P MAS NMR is an additional helpful tool to obtain structural information regarding the chemical structure and its surroundings.^[71] Figure 3.51 presents the liquid-state proton decoupling ^{31}P NMR spectra of the different compounds. It can be observed that the different geometrical shapes yield a range of 2.5 ppm from 1,2,4,5-tetrakis(*p*-phosphonatophenyl)benzene (**23**) (11.7 ppm) to 1,3,5,7-tetrakis(*p*-phosphonatophenyl)adamantane (**28**) (14.0 ppm). Notably, (*p,p'*-terphenyl-4,4''-diyl)bisphosphonic acid (**9**) and 1,3,5-tris(*p*-phosphonatophenyl)benzene (**12**) have exactly the same chemical shift (13.5 ppm).

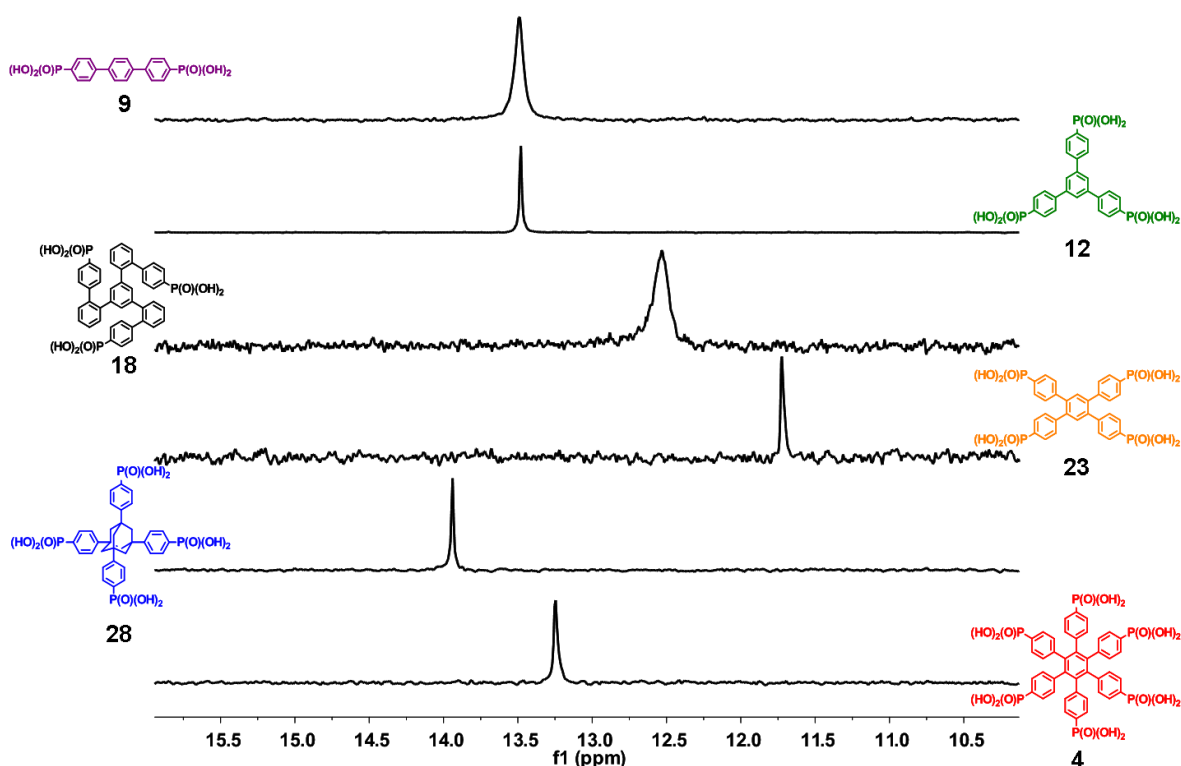


Fig. 3.51: Liquid-state ^{31}P -NMR spectra recorded at 202.5 MHz in DMSO- d_6 at 373 K. From bottom to top: (*p,p'*-Terphenyl-4,4''-diyl)bisphosphonic acid (**9**), 1,3,5-tris(*p*-phosphonatophenyl)benzene (**12**); 1,3,5-tris(4''-phosphonato-2'-biphenyl)yl)benzene (**18**); 1,2,4,5-tetrakis(*p*-phosphonatophenyl)benzene (**23**); 1,3,5,7-tetrakis(*p*-phosphonatophenyl)adamantane (**28**); hexakis(*p*-phosphonatophenyl)benzene (**4**).

Since the solubility of the samples is rather poor one can assume that there is no packing effect in the solution. Furthermore, the poor solubility results in different effective concentrations which might also affect the chemical shift. Additionally, the central aromatic ring connecting the phenylphosphonic acids might influence the electronic shielding of the ^{31}P nucleus and the chemical shift variations are possibly due to the chemical structure differences.

Similarly to the ^1H MAS NMR detailed above, the ^{31}P MAS NMR spectra show more differences than expected (c.f. Figure 3.52). A variation of the chemical shifts over 5 ppm is found even if all samples contain a phosphonic acid group attached to a phenyl ring which seems to indicate that the phosphonic acid groups of the investigated compounds orient in different macromolecular structures and are thus located in different local fields of the aromatic systems.

The ionomers are small molecules and can arrange in a more or less crystalline structure. If the surrounding of the phosphorus atoms is not completely identical the ^{31}P nucleus experiences different chemical shieldings resulting in a broad NMR signal. On the other hand, when the ^{31}P nucleus is present in a well-defined environment it gives rise to a sharp signal. As can be seen in Figure 3.52, 1,3,5-tris(*p*-phosphonatophenyl)benzene (**12**), 1,3,5-tris[4''-(phosphonato)-2'-biphenyl]ylbenzene (**18**), 1,3,5,7-tetrakis(*p*-phosphonatophenyl)adamantane (**28**) and hexakis(*p*-phosphonatophenyl)benzene (**4**) display a relatively broad chemical shift distribution. On the contrary, (*p,p'*-terphenyl-4,4''-diyl)bisphosphonic acid (**9**) and 1,2,4,5-tetrakis(*p*-phosphonatophenyl)benzene (**23**) show quite narrow line widths of 460 Hz and 370 Hz located at 21 and 17 ppm respectively. Interestingly these two molecules are not crystalline as it has been shown in Section 3.3.5 but the line widths of the solid-state spectra suggest that the phosphonic acid groups in the samples are highly ordered such that the ^{31}P nuclei are located in a well defined environment. Notably, these two materials do not show significant bulk proton conductivity or a microscopic mobility (see Section 3.3.3). Hence, this strongly suggests that a high degree of local ordering or crystallinity of the phosphonic acid sites does not favor proton conduction in these systems.

In the case of compound **9**, the narrow line width of the solid-state ^{31}P signal is somehow contrary to the broad peak observed in the ^1H MAS NMR (see Figure 3.47). This might be explained by the larger homonuclear dipolar coupling which broadens the ^1H signal. In addition, the ^{31}P MAS NMR spectrum of **9** shows an additional peak at 15 ppm which most probably corresponds to the phosphonic acid anhydride. This

assumption is supported by various ^{31}P MAS NMR spectra of phosphonic acid and anhydride containing samples.^[4, 67]

1,3,5-Tris[4''-(phosphonato)-2'-biphenyl]ylbenzene (**18**) presents an unusual ^{31}P MAS NMR spectrum, where the structure appears more complicated but highly ordered. In fact, the spectrum shows a clear separation of at least six peaks instead of one broad peak and the chemical shift distribution is quite broad and ranges from 30 to 15 ppm (7500 Hz). This interesting result might be due to the fact that the sample contains six different phosphorous species located in well-defined environments.

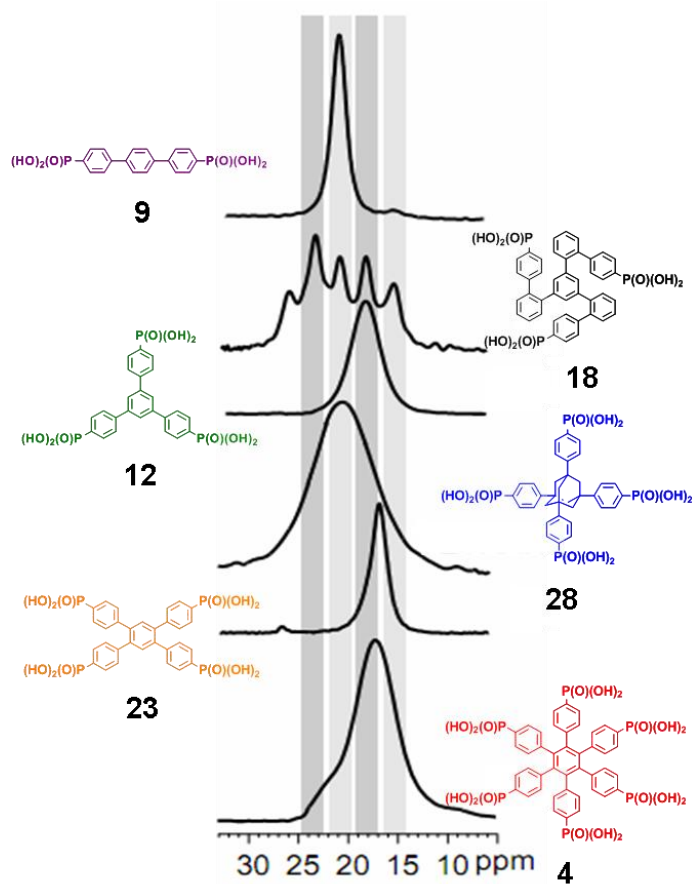


Fig. 3.52: ^{31}P MAS NMR spectra of the ionomers at 202 MHz at 303 K. Plotted from the top to the bottom with increasing number of phosphonic acid groups: (*p,p'*-terphenyl-4,4''-diyl)bisphosphonic acid (**9**), 1,3,5-tris[4''-(phosphonato)-2'-biphenyl]ylbenzene (**18**), 1,3,5-tris(*p*-phosphonatophenyl)benzene (**12**), 1,3,5,7-tetrakis(*p*-phosphonatophenyl)adamantane (**28**), 1,2,4,5-tetrakis(*p*-phosphonatophenyl)benzene (**23**), hexakis(*p*-phosphonatophenyl)benzene (**4**).

The ^{31}P MAS NMR spectra of a hexakis(*p*-phosphonatophenyl)benzene (**4**) sample which has been treated in the way described for Figure 3.48 are displayed in Figure

3.53. The signal at 18 ppm shown by the freshly obtained sample (light grey in Figure 3.53) presents a splitting into two signals when the sample has been exposed to 100 % RH (dark grey in Figure 3.53) supporting the presence of distinct phosphonic acid sites which are most probably due to the incorporation of water (different water hydration shells).

On the other hand, the spectrum of the sample dried after being exposed to 100 % RH (black line in Figure 3.53) displays a line width even smaller than in the "wet" state and at slightly higher ^{31}P chemical shift values. This observation suggests that higher chemical shifts might correspond to phosphonic acid groups which do not interact with water molecules and that the sample contains less water than the freshly obtained one.

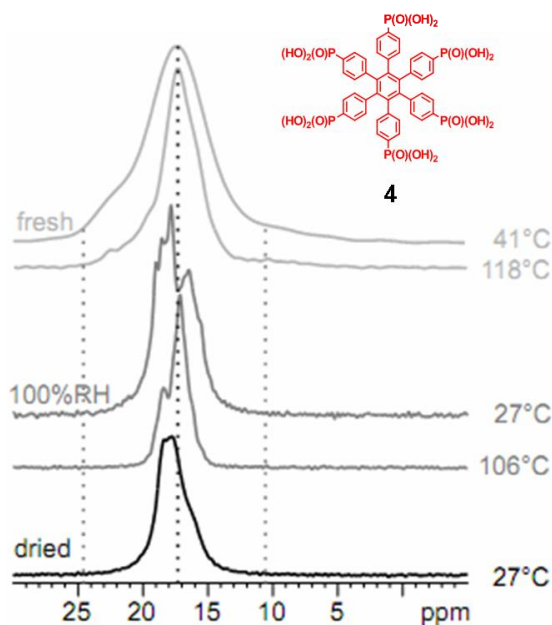


Fig. 3.53: ^{31}P MAS NMR spectra of hexakis(*p*-phosphonatophenyl)benzene (**4**) recorded at 284 MHz from the top: freshly obtained sample measured at 314 and 391 K (light grey); sample stored at 100% RH measured at 300 and 379 K (dark grey); sample stored at 100 % RH and afterwards dried at 2 h at 423 K under nitrogen flux and measured at 300 K (black).

3.3.7 Discussion

It has been reported in the literature that a high concentration of phosphonic acid groups is required to have intrinsic proton conductivity.^[4] In the case of the studied phosphonated materials, supramolecular ordering plays a crucial role since it determines whether the small molecules will be arranged in such ways that phosphonic acid groups can aggregate, i.e. whether regions of a high concentration of phosphonic

acid groups can be present, and proton-conducting pathways can be formed. The self-assembly of the molecules must lead to a morphology with a continuous phase of phosphonic acid groups to have high proton conductivity. In addition, as has been pointed out in Section 3.3.4, the proton conductivity of the different materials seems to correlate to the degree of crystallinity so that the molecules presenting a higher degree of crystallinity show higher proton conductivity (excepting compound **12**).

Compounds **12** and **4**, which self-assemble into columns and possess regions of high concentration of phosphonic acid moieties, provide high proton conductivity values ($8 \cdot 10^{-3}$ and $6 \cdot 10^{-3}$ S \cdot cm $^{-1}$ respectively), which moreover remain constant over temperature. In addition, the degree of crystallinity of **4** is 90 % which means that the crystalline repeating unit is present over a long range in 90 % of the sample. This fact is assumed to also be a reason for the high conductivity value observed for the compound.

Triangular molecule **12** is water soluble, which hinders its application as separator material in PEM. To render any application possible, the material would have to be embedded in a matrix ensuring mechanical stability. Moreover, it can be deduced that the flat temperature response of the proton conductivity by decreasing temperature under 1 bar H₂O atmosphere (Figure 3.39) for both compounds **12** and **4** is most likely due to the hysteresis of the water uptake (Figure 3.42).

Compound **28**, with tetragonal geometry, presents a proton conductivity which remains constant when the temperature is increased. However, the proton conductivity value is two orders of magnitude lower than in the previous case. This is due to the diamond-like structure which prevents the phosphonic acid groups from building up a continuous acidic phase necessary for proton conduction. The hysteresis of the water uptake of **28** is the most likely reason for the flat temperature response of the material above 120 °C where the RH decreases from 50 to 20 % (Figure 3.42).

Compound **18**, with propeller-like geometry, displays a proton conductivity which increases when the temperature is increased above 120 °C. This uncommon trend can be attributed to a *Grotthuss*-type mechanism for proton conduction. The proton conductivity reaches a value of $3 \cdot 10^{-4}$ S \cdot cm $^{-1}$ at 180 °C under humidified conditions. Even if this value is well below the one required for a separator material, the compound presents a conductivity which increases when the temperature is increased, a trend not typically observed in the literature. In this case, the supramolecular structure responsible for the *Grotthuss*-type mechanism is unknown but it can be stated that the structure should comprise regions of aggregated acidic moieties. However, the crystalline repeating unit is present over a higher length scale in only 9.5 % of the

material; this might also be a cause for the lower proton conductivity of the compound compared to **12** and **4**.

Compound **23**, with square planar geometry, exhibits a proton conductivity which decreases at higher temperature and which can be associated with a vehicle mechanism. The value of the conductivity at 180 °C is $6 \cdot 10^{-5} \text{ S} \cdot \text{cm}^{-1}$, lower than in the case of molecules associating into columns (compounds **12** and **4**) or into diamondoid networks (compound **28**). For this reason, regions of high concentration of phosphonic acid groups are not expected to be part of the supramolecular structure of the compound.

Linear compound **9** shows very low proton conductivity values ($2 \cdot 10^{-6} \text{ S} \cdot \text{cm}^{-1}$). This is due to the fact that according to the crystal structure the phosphonic acid groups do not form a continuous acidic phase and also to the degree of crystallinity at only 7 %. However, the conductivity value remains constant by increasing the temperature. This can be attributed to the low but constant hysteresis of the water uptake which could not be resolved in the water uptake measurements (Figure 3.42).

Similar to conductivity, water uptake is controlled by the supramolecular structure since this latter determines the amount of water molecules a compound can adsorb.

The solid-state NMR investigations conducted on these phosphonated small molecules show that there is a discrepancy between the activation energy values calculated from IS and from NMR data. The apparent activation energy values calculated from the NMR data are almost 60 times lower than the values obtained from the IS experiments. This discrepancy is attributed to the fact that the conductivity data represent charge transport on a macroscopic scale, while NMR detects the proton mobility on a microscopic scale

3.3.8 Summary

In contrast to state-of-the-art polymeric membranes, a series of phosphonic acid-containing organic molecules is proposed as alternative separator materials for FCs working at intermediate temperatures. Proton conductivity and water uptake measurements as well as crystallinity studies have been performed. The proton-conducting properties of the compounds are very different. It is obvious that conductivity is dominated by the supramolecular long-range ordering and the geometry of the compounds and not by the mobility of small molecules or by the dynamic of a polymer backbone. Therefore, we deduce that to have phosphonic acid-containing

organic molecules of high proton conductivity the molecules must organize in such a way that a nanophase separation between the hydrophobic and hydrophilic domains leading to a continuous acidic phase is formed. Moreover, from the WAXS studies described in Section 3.3.5 it can be deduced that materials which also present a high crystallinity degree (long range order) are suitable candidates as solid state separator materials even. However crystallinity is an important but not determining factor to have high proton conductivity since triangular compound **12** is amorphous but shows high conductivity values.

The supramolecular organization of the molecules also controls the water uptake: the number of adsorbed water molecules (which can help the proton transport by giving and taking protons) is a function of the supramolecular structure of the compound. Therefore, since compounds with a higher water uptake present a higher conductivity, it can be stated that molecules with structures which enhance water uptake lead to higher conductivity.

The study presented in this chapter provides a straightforward route towards reaching high proton conductivity in the solid state by the use of small molecules. It can be concluded that crystalline molecules which are able to self-assemble into columns are the best candidates as proton-conducting materials since a nanophase separation providing a continuous acidic phase outside the columns is formed. Compound **4** proved the most promising as it combines high and constant conductivity, providing excellent performance, with water insolubility.

Since high proton conductivity and water insolubility are essential requirements for novel proton conductors for fuel cell applications, these organic crystalline molecules can be considered a new type of separator material. Moreover, these molecules can be used either as main electrolytes or as additives in a PEM.

3.4 Substituted Hexaphenylbenzene Molecules

3.4.1 General Remarks

It has been demonstrated in Chapter 3.3 that among all the proposed systems crystalline molecules which are able to self-assemble into columns are the best proton-conducting materials since a nanophase separation providing a continuous acidic phase outside the columns is formed. Compound **4** proved the most promising as it combines high and constant conductivity exhibiting excellent performance, with water insolubility.

In Chapter 3.4 the synthesis and proton-conducting properties of HPB derivatives are examined to appraise into detail the effects of substitution in the aromatic core of the HPB. Three cases make up this chapter: the change of the phosphonic acid groups from the *para* to the *meta* position, the introduction of alkyl chains into the system and the replacement of phosphonic acid functions by sulfonic acid ones (see Figure 3.54). Proton conductivity, water uptake and crystallinity of the materials are compared to these of the model compound **4** treated in Chapter 3.2.

Another interesting aspect to consider is the increase of the number of phosphonic acid groups in the periphery of the HPB core since by raising the density of the acidic functions an enhancement of the conductivity is expected. The attempts made to synthesize this molecule are described in Section 3.4.5.

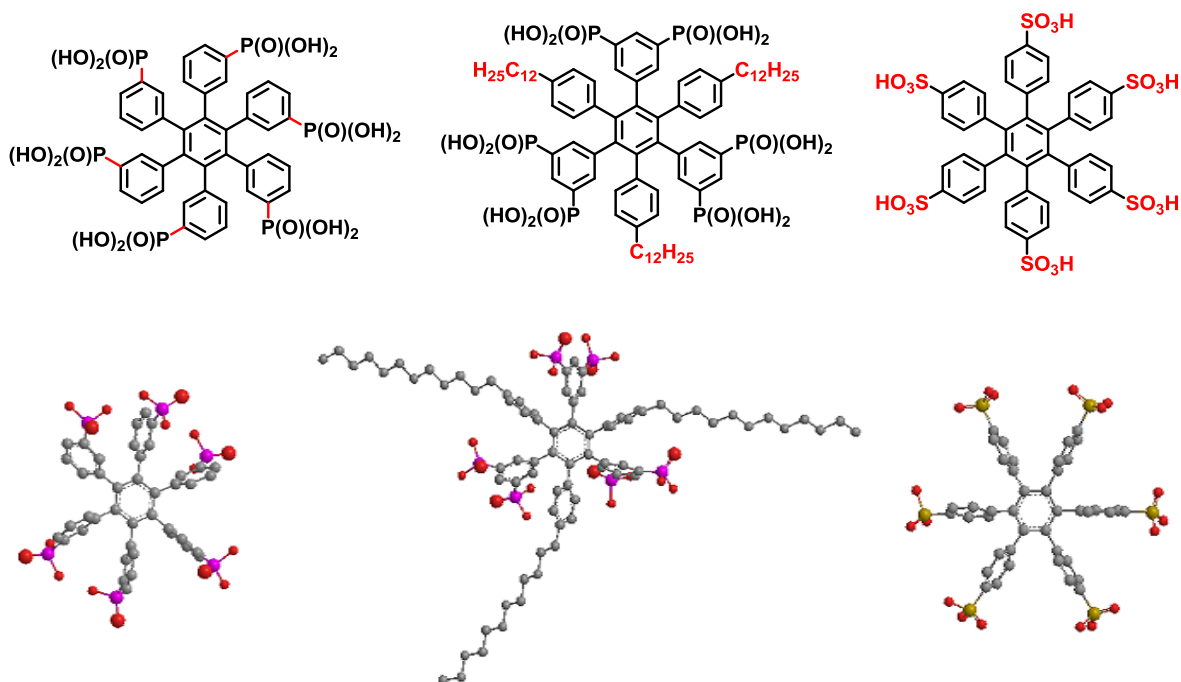


Fig. 3.54: Substituted HPB molecules proposed as solid state separator materials and their structures in the gas phase obtained from ChemDraw 3D molecular-mechanics force field calculations (MMFF94) energy minimization. H atoms are omitted for clarity.

3.4.2 Hexakis(*m*-phosphonatophenyl)benzene

Hexakis(*p*-phosphonatophenyl)benzene (**4**) has been proposed as a solid state proton conductor in Chapter 3.2 and it has been proved in Chapter 3.3 that it is the best candidate as separator material among other small molecules which also possess phosphonic acid functions. Therefore, it is of interest to study what effects the change of the position of the acidic groups have on proton conductivity as well as on the other properties of the initial compound **4**. At this point two options appear: the introduction of the acidic groups in the *ortho* or in the *meta* position of the HPB core. Since the *ortho* position is very hindered, it is decided to synthesize the other alternative hexakis(*m*-phosphonatophenyl)benzene.

Figure 3.55 shows the synthetic strategy applied to obtain the desired material. In principle, the synthesis of this molecule is similar to that described for its homologous compound **4** and instead of cyclotrimerizing bis(4-diethylphosphonatophenyl)acetylene (**2**) one has to use 1,2-bis(3-diethylphosphonatophenyl)ethyne (**33**). **33** is synthesized in four steps and can be obtained in gram scale. The cyclotrimerization of **33** proceeds with moderate yield (62 %) and the obtained compound can be subsequently hydrolyzed under mild conditions to get hexakis(*m*-phosphonatophenyl)benzene (**35**).

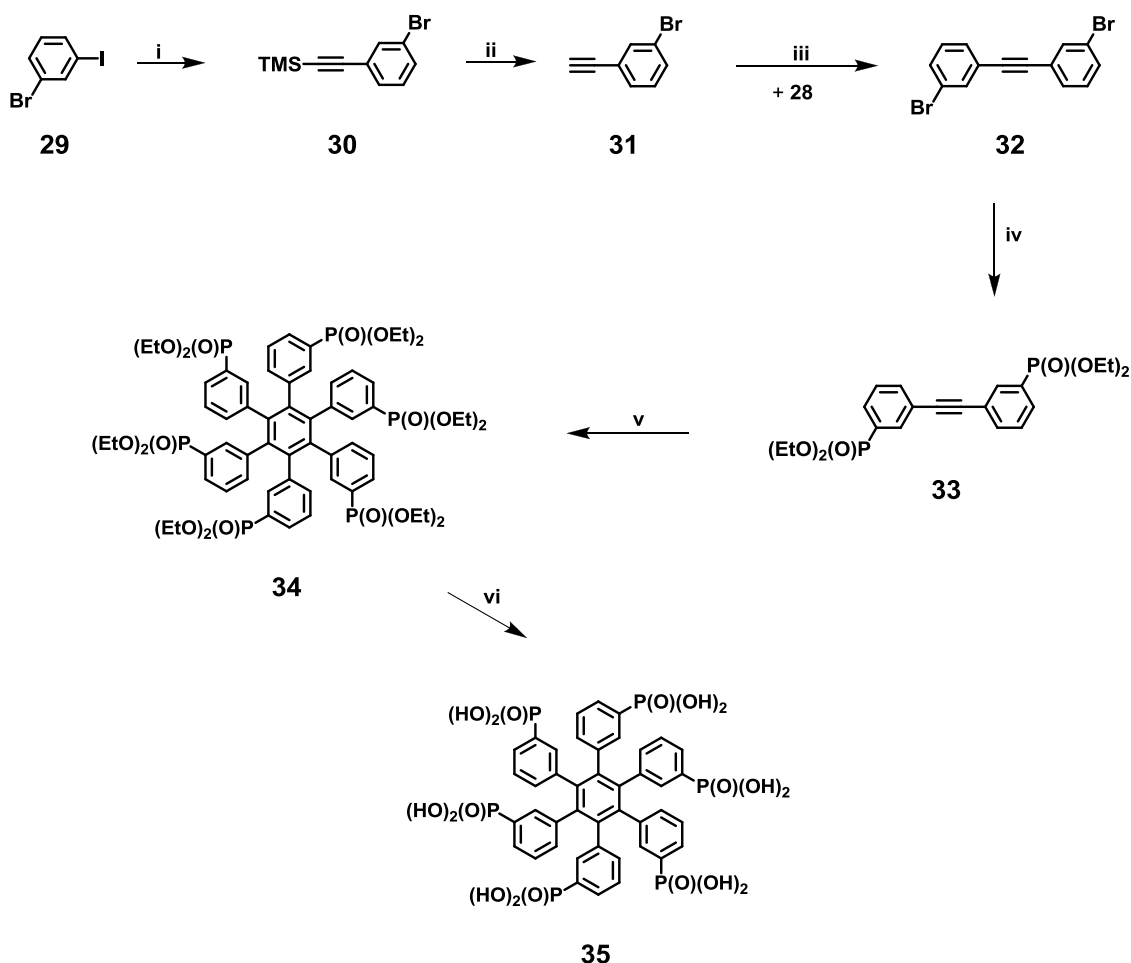


Fig. 3.55: Synthetic route toward hexakis(*m*-phosphonatophenyl)benzene (**35**): i) trimethylsilylacetylene, CuI, Pd(PPh₃)₂Cl₂, diisopropylamine, toluene, RT, 1 h, 87 %; ii) TBAF, THF, RT, 15 min, 78 %; iii) CuI, Pd(PPh₃)₂Cl₂, NEt₃, toluene, 60 °C, 12 h, 87 %; iv) HP(O)(OEt)₂, Pd(PPh₃)₄, NEt₃, toluene, 75 °C, 12 h, 68 %; v) Co₂(CO)₈, dioxane, reflux, 12 h, 62 %; vi) a. TMS-Br, DCM, RT, 48 h; b. MeOH, RT, 48 h, 87 %.

Like its homologous compound hexakis(*p*-phosphonatophenyl)benzene, **35** is poorly soluble in water, water/alcohol mixtures and all kind of organic solvents at RT and only slightly soluble in DMSO at elevated temperatures.

The ¹H-NMR spectrum of **35** recorded in deuterated DMSO at 373 K is shown in Figure 3.56. In the aromatic region, three peaks can be observed with a ratio 1:1:2. At 7.74 - 7.37 and 7.13 ppm there are a multiplet and a singlet respectively which can be assigned to the two protons which are direct neighbors of the C-P bond (H1 and H2 in Figure 3.56). The third peak in the aromatic region is found at 6.91 ppm. This signal corresponds to the two remaining protons of the phosphonic acid-containing aromatic ring. The fourth peak at about 5.9 ppm is caused by the free protons coming from the acidic groups and the residual water present in the deuterated DMSO.

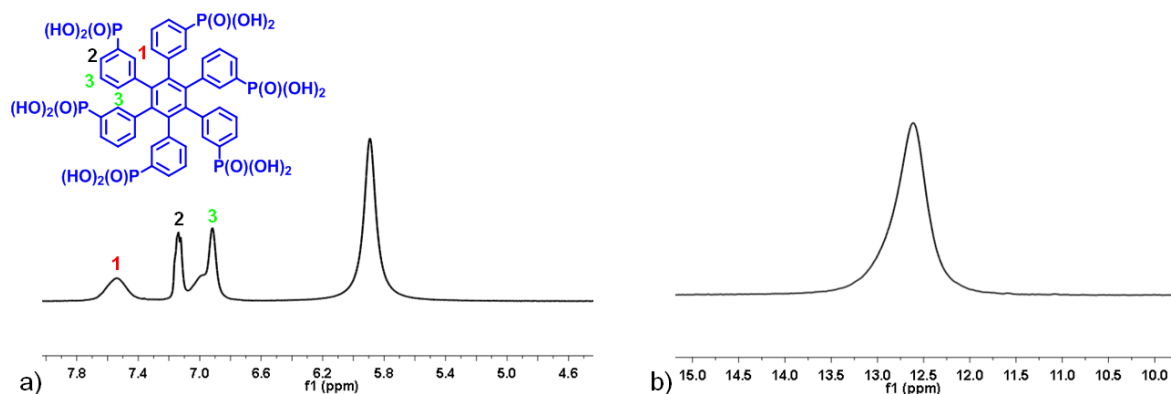


Fig. 3.56: ^1H - and ^{31}P -NMR spectra of hexakis(*m*-phosphonatophenyl)benzene (**35**) recorded in DMSO- d_6 at 373 K and 500 MHz.

The ^{31}P -NMR spectrum of the compound recorded at 373 K in deuterated DMSO shows only one peak corresponding to one kind of phosphorous species. Therefore from these NMR data it is assumed that even if the formation of an isomeric mixture as shown in Figure 3.57 is possible, this is not the case for the studied material. It is presumed that the obtained product is the atropisomer A since it possesses the most favorable structure which prevents two neighboring phosphonic acid groups to meet and thus to possibly react to give an anhydride.

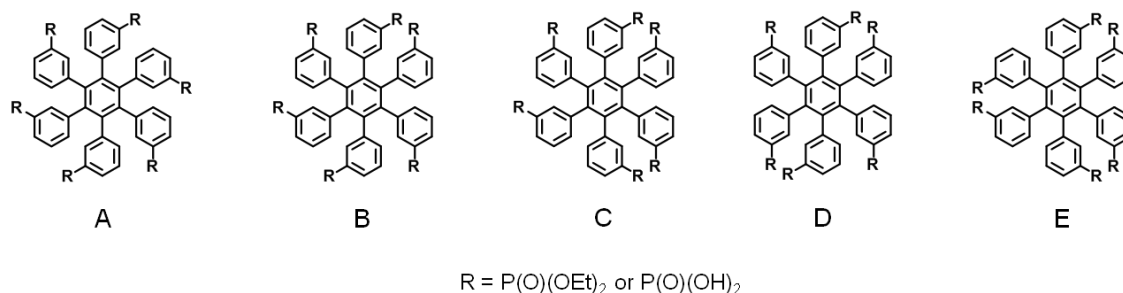


Fig. 3.57: Possible atropisomers of **34** and **35**.

Subsequently to the liquid-state NMR characterization and structure proof, proton conductivity measurements under 1 bar H_2O atmosphere have been carried out on a 100 mg pellet of the material and the results compared to the values obtained for Nafion® 117 and compound **4**. Figure 3.58 displays the corresponding curves for the three materials. As seen, the conductivity of hexakis(*m*-phosphonatophenyl)benzene is lower than the one of Nafion® 117 and the model compound **4**. Interestingly, in the interval between 110 and 150 °C the conductivity is found to decrease whereas above 150 °C it is stable so that the curve of the *meta* substituted HPB derivative is above this

temperature parallel to this of **4**. At around 175 °C, the proton conductivity value is $5.5 \cdot 10^{-5}$ S/cm, i.e. two orders of magnitude lower than the value found for **4** ($3.4 \cdot 10^{-3}$ S/cm).

Since above a certain temperature the sample exhibits a temperature independent proton conductivity, it seems that the evaporation of water, i.e. the vehicle mechanism, is most likely not the only reason for the conductivity decrease from 110 to 150 °C.

During the proton conductivity measurements, to obtain each point it is waited since the material has reached equilibrium. In the case of material **35**, for each measured point a waiting time of 24 h is allowed in order to calculate the conductivity value. However it has been observed that the sample needs more time to reach the equilibrium between the temperature range of 110 to 150 °C so that the corresponding conductivity values presented in Figure 3.58 are not completely equilibrated. This means that most probably the system needs more time to reach the equilibrium in this interval of temperature and that if one would wait more time then the sample should provide a temperature independent proton conductivity also below 150 °C.

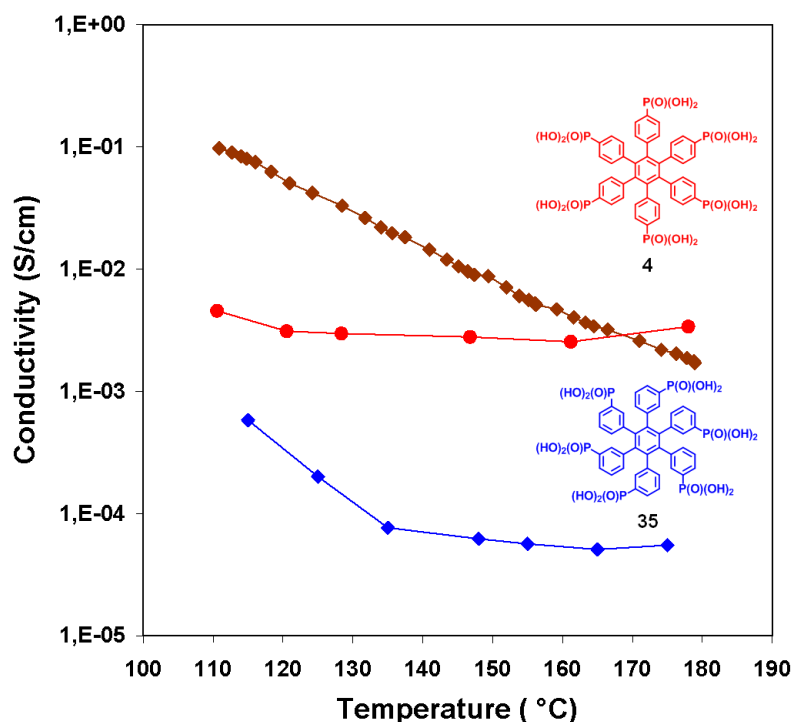


Fig. 3.58: Proton conductivity as a function of temperature measured under 1 bar H₂O atmosphere for hexakis(*m*-phosphonatophenyl)benzene (**35**) (blue curve). The curves of Nafion® 117 and compound **4** are shown for comparison (brown and red curves respectively).

From these measurements it can be concluded that like hexakis(*p*-phosphonatophenyl)benzene (**4**), compound **35** presents a proton conductivity which is temperature independent, however it exhibits lower conductivity values than **4**. One can assume that like its homologous *para* substituted HPB, material **35** stacks into columns. In this case, due to the substitution of the HPB in the *meta* position the acidic moieties can be placed either above or below the plane of the phenyl ring thus leading to regions of lower concentration of phosphonic acid groups, i.e. of lower proton conductivity values. Further investigations like TGA, water uptake and crystallinity studies need to be performed to elucidate whether **4** and **35** present a similar self-organization and thus to be sure that the above mentioned explanation can be considered as possible.

Compound **35** is subjected to TGA experiments to determine the thermal stability of the material. Figure 3.59 displays the TGA curve of both hexakis(*p*-phosphonatophenyl)benzene **4** and hexakis(*m*-phosphonatophenyl)benzene **35**. The TGA results reveal that both materials present a progressive mass loss, that of the *para* being more pronounced than that of the *meta* substituted HPB. Furthermore it can be observed that whereas **4** experiments an abrupt mass loss of 32 wt % at around 450 °C (which has been previously correlated to the decomposition of the hydrophobic core), **35** is stable until around 600 °C and shows from this temperature a progressively mass loss of 44 wt % until 800 °C.

Like **4**, **35** presents a mass loss at around 100 °C and another at around 200 °C which can be attributed to water released during the measurement. From 25 to 400 °C the mass loss is 7.8 wt %, which corresponds to ~ 4.4 water molecules per **35**. It has been explained in Section 1.3.3 that the maximum weight loss due to self-condensation of the acidic groups is limited to 3 water molecules per compound which corresponds to a weight loss of around 5 wt %. Thus like in the case of hexakis(*p*-phosphonatophenyl)benzene **4**, the weight loss of **35** from 25 to 400 °C cannot only be explained by condensation of the phosphonic acid groups and might be also due to water “coordinative” bonded in the structure of the material.^[37] To ascertain this statement, it is necessary to do other investigations like water uptake and crystallinity studies.

Very surprisingly, the material shows higher thermal stability than **4**, a crystalline compound very similar to **35**.

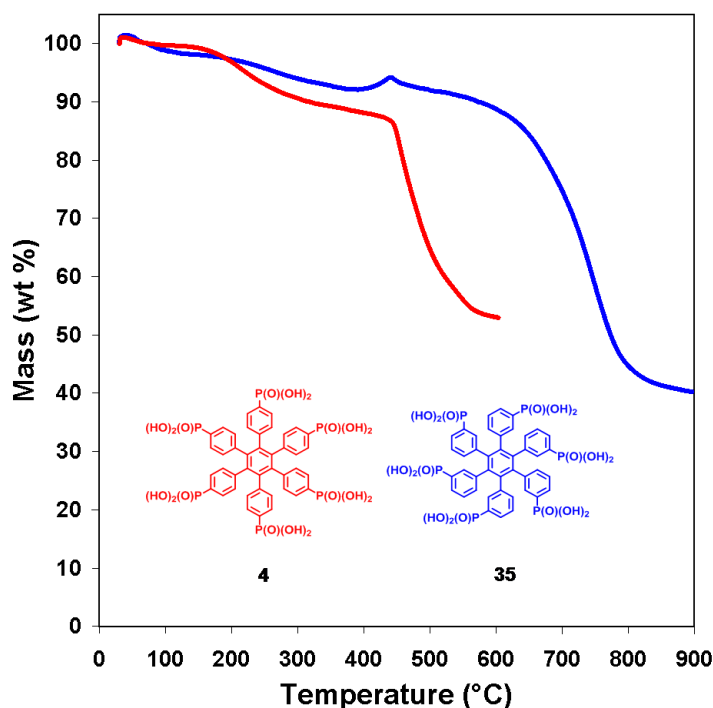


Fig. 3.59: Curves of the TGA experiments performed under N_2 at 10 K/min of hexakis(*p*-phosphonatophenyl)benzene (**4**) and hexakis(*m*-phosphonatophenyl)benzene (**35**) depicted in red and blue respectively.

Water uptake measurements at RT have been conducted to try to determine whether compound **35** is a hydrated crystal. During the storage of the sample at different RH no morphology changes with increasing RH have been noticed.

The water sorption isotherm at RT of hexakis(*m*-phosphonatophenyl)benzene (**35**) is depicted in Figure 3.60, which also shows the adsorption curve of hexakis(*p*-phosphonatophenyl)benzene (**4**) for comparison. Like in the case of **4**, a stepwise hydration and hysteresis also called type VI *van der Waals* isotherm^[38] is observed for compound **35**. In contrast to **4**, **35** begins to adsorb water at low RH (11 %) and from 11 to almost 60 % RH the hydration step is close to 0.5 water molecules per hexakis(*m*-phosphonatophenyl)benzene. The devolution of the curve of **35** is from 60 % RH similar to the one of **4**, however the maximum water uptake is higher. At 100 % RH, **4** can take up 3 water molecules whereas in the case of **35** the number is 3.5. Like for **4**, a pronounced hysteresis is expected for the desorption curve of hexakis(*m*-phosphonatophenyl)benzene.

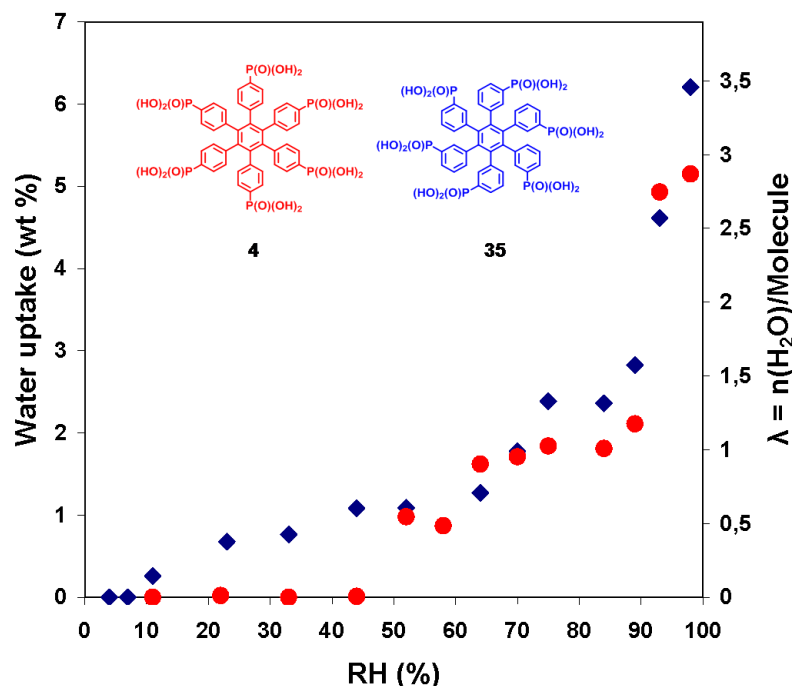


Fig. 3.60: Water sorption isotherm and lambda at RT of hexakis(*p*-phosphonatophenyl)benzene (**4**) and hexakis(*m*-phosphonatophenyl)benzene (**35**) depicted with ● and ◆ respectively.

From this water sorption studies it can be concluded that hexakis(*m*-phosphonatophenyl)benzene (**35**) and hexakis(*p*-phosphonatophenyl)benzene (**4**) are very similar and that both of them present the characteristics of crystal hydrates. Indeed since the proton conducting features of **35** are different than that of **4**, it is of interest to explore whether the crystallinity properties of compound **35** are the reason for this behavior.

Therefore WAXS studies have been performed at different temperatures and RH. The X-ray diffraction patterns of hexakis(*m*-phosphonatophenyl)benzene (**35**) at 33 % RH and different temperatures and at RT at different RH are displayed Figure 3.61a and b respectively. All patterns are composed of a broad peak between 4.3 and 3.9 Å and two narrow peaks at 3.3 and 2.3 Å respectively, indicated with blue and orange bands in Figures 3.61a and b. By maintaining the RH constant at 33 %, an increase of the temperature diminishes the intensity of the two narrow peaks. The same effect is observed by increasing the RH at a constant temperature (RT). In this case in the diffractogram recorded at 90 % RH the peak at 2.3 Å has disappeared whereas the intensity of the peak at 3.3 Å has considerably decreased. Thus it can be stated that both the loss and gain of water in the system prompted by a temperature and RH

increase respectively imply a decrease of the crystallinity of the material affecting proton conductivity.

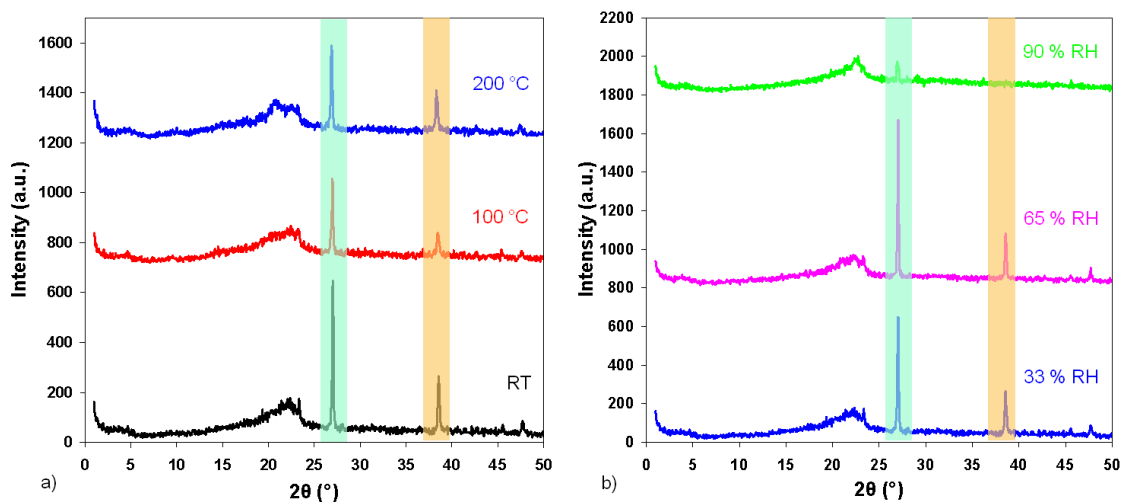


Fig. 3.61: X-ray diffractograms of hexakis(*m*-phosphonatophenyl)benzene (**35**) a) at 33 % RH and RT, 100 and 200 °C (black, red and blue lines respectively) and b) at RT and 33%, 65 % and 90 % RH (blue, pink and green lines respectively).

A comparison between the X-ray diffraction patterns of hexakis(*p*-phosphonatophenyl)benzene (**4**) and hexakis(*m*-phosphonatophenyl)benzene (**35**) is shown in Figure 3.62. It can be noticed that the reflections characteristic of a columnar arrangement corresponding to the inter- and intracolumnar distances and which have been observed in the case of compound **4** are absent in the diffractions pattern of compound **35**. Furthermore the *para* substituted compound presents more reflection peaks which most probably connote a higher crystallinity degree.

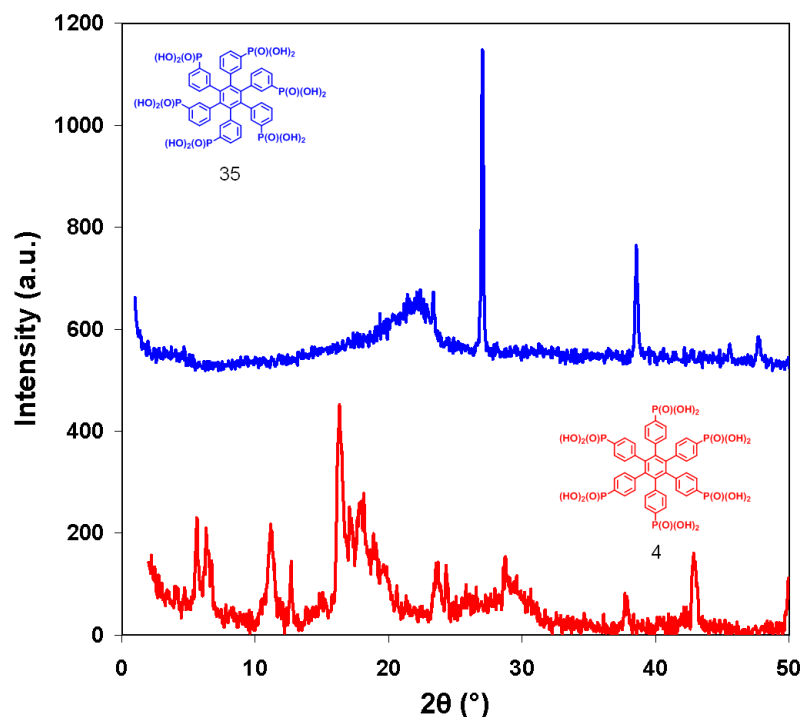


Fig. 3.62: X-ray diffractogram of hexakis(*p*-phosphonatophenyl)benzene (**4**) (red line) and hexakis(*m*-phosphonatophenyl)benzene (**35**) (blue line) recorded at RT and 33 % RH.

In this sub-section the proton-conducting properties of hexakis(*m*-phosphonatophenyl)benzene have been studied and compared to these of its homologous compound **4**. Since the proton conductivity curve of both materials exhibit a similar trend while increasing the temperature under 1 bar H₂O atmosphere it is assumed that the two compounds present similar proton transport mechanisms. From TGA and water uptake studies it has been elucidated that the material, like **4**, presents the characteristics of a crystal hydrate. Unfortunately the X-ray diffractogram of the compound does not provide information about the packing of the molecules since the sample is amorphous. To elucidate whether a columnar stacking is also present in the case of **35**, 2D WAXS measurements should be performed. If one supposes that both compounds **4** and **35** present a similar self-organization, then the lower conductivity values presented by **35** might be explained by the fact that the acidic moieties at the meta position can arrange either above or below the phenyl ring so that in some regions a lower proton concentration of protons deriving in a lower conductivity might be present.

3.4.3 1,3,5-Tris(3,5-biphosphonatophenyl)-2,4,6-tris(4-dodecylphenyl)-benzene

In the study of solid state proton conductors based on HPB molecules containing phosphonic acid functionalities, rather than exploring the effects of the *para* and *meta* positions on the proton transport properties of the compounds, one can focus on studying the impact of the introduction of alkyl chains. In principle, it is expected that the alkyl chains will affect the crystallinity since disorder is introduced into the system. However on the other hand it is also reckoned that the alkyl chains will increase the solubility of the material so that films can be cast from a solution of the molecule in a solvent so that in-plane instead of through-plane conductivity can be measured.

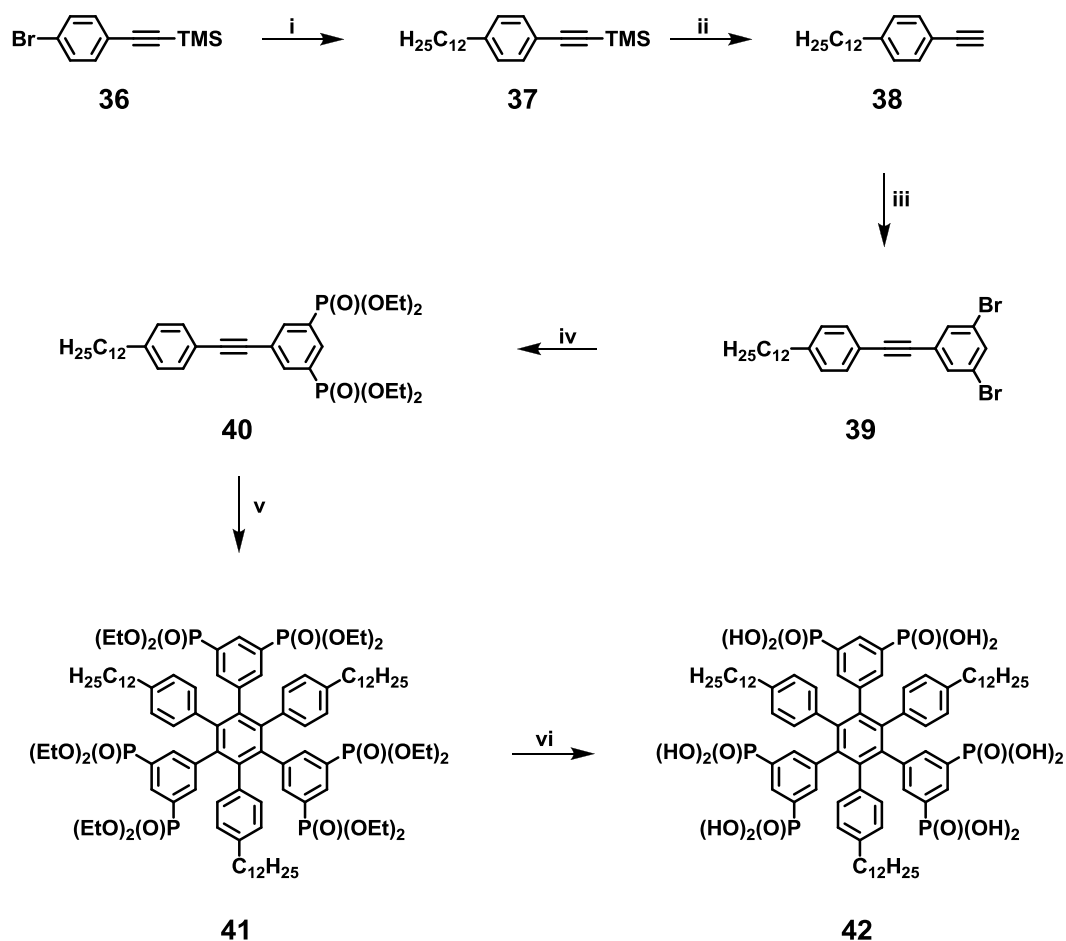


Fig. 3.63: Synthetic route toward 1,3,5-tris(3,5-biphosphonatophenyl)-2,4,6-tris(4-dodecylphenyl)-benzene (**42**): i) $C_{12}H_{25}MgBr$, $Pd(dppf)Cl_2$, THF, 60 °C, 12 h, 90 %; ii) TBAF, THF, RT, 15 min, 89 %; iii) CuI , $Pd(PPh_3)_2Cl_2$, NEt_3 , toluene, 60 °C, 12 h, 74 %; iv) $HP(O)(OEt)_2$, $Pd(PPh_3)_4$, NEt_3 , toluene, 75 °C, 12 h, 70 %; v) $Co_2(CO)_8$, reflux, 12 h, 61 %; vi) a. TMS-Br, DCM, RT, 48 h; b. MeOH, RT, 48 h, 97 %.

Therefore, 1,3,5-tris(3,5-biphosphonatophenyl)-2,4,6-tris(4-dodecylphenyl)-benzene (**42**) is proposed as the next case to focus on. The material is obtained using the synthetic route described in Figure 3.63. Tetraethyl 5-((4-dodecylphenyl)ethynyl)-1,3-phenylenediphosphonate (**40**) is synthesized in gram scale via a four-step procedure. The subsequent trimerization yields a mixture of regioisomers which cannot be separated by silica gel or gel permeation chromatography. After hydrolysis under mild conditions, the product is obtained as a mixture of regioisomers: 1,3,5-tris(3,5-biphosphonatophenyl)-2,4,6-tris(4-dodecylphenyl)-benzene (**42a**) and 1,2,3-tris(3,5-biphosphonatophenyl)-4,5,6-tris(4-dodecylphenyl)-benzene (**42b**) as shown in Figure 3.64. At this point it is important to clarify that for the purpose of this work it is not crucial to separate the two isomers since it is assumed that crystallinity, an important but not determining factor to obtain materials of high proton conductivity (see Chapter 3.3), is anyway decreased with respect to the model compound **4** due to the introduction of the alkyl chains.

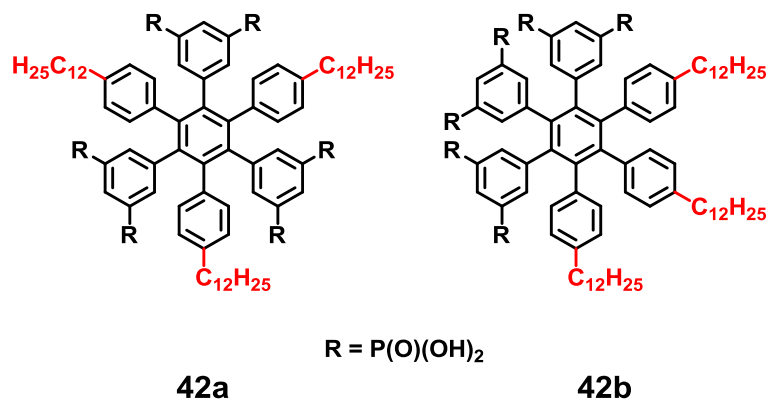


Fig. 3.64: Possible isomers obtained from the synthesis, from left to right: 1,3,5-tris(3,5-biphosphonatophenyl)-2,4,6-tris(4-dodecylphenyl)-benzene (**42a**) and 1,2,3-tris(3,5-biphosphonatophenyl)-4,5,6-tris(4-dodecylphenyl)-benzene (**42b**).

The final material is obtained as a white solid which is partially soluble in DMSO and methanol and poorly soluble in water and polar organic solvents like THF. To characterize the compound liquid-state NMR has been used. In Figure 3.65, the ^{31}P -NMR spectrum of the material is compared to that of model compound **4**.

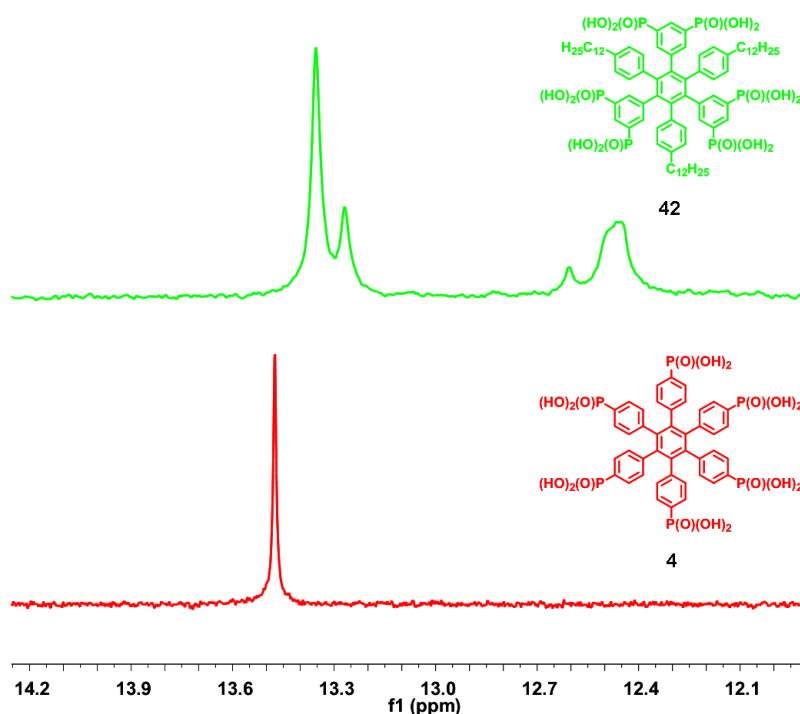


Fig. 3.65: ^{31}P -NMR spectra of hexakis(*p*-phosphonatophenyl)benzene (**4**) (red) and 1,3,5-tris(3,5-biphosphonatophenyl)-2,4,6-tris(4-dodecylphenyl)-benzene (**42**) (green) recorded in DMSO at 373 K and 121 MHz and RT and 284 MHz respectively.

It can be observed that only one peak corresponding to one sort of phosphorous is present in the spectrum of hexakis(*p*-phosphonatophenyl)benzene (**4**) whereas in the case of the material studied in this section two doublets at 13.31 and 12.53 ppm are obtained (with corresponding *J* coupling constant of 24.1 and 39.5 Hz) fitting to two phosphorous species. The integration of the peaks shows that the sort of phosphorous giving the doublet at 13.3 ppm represents 61.4 % of the total phosphorous species whereas the signal at 12.5 ppm corresponds to 38.7 % of the phosphorous species present in the material.

Since molecule **42a** is completely symmetric, there is only one kind of phosphorous species and thus only one peak in the phosphorous spectrum is expected (Figure 3.66). In the case of **42b**, there are two types of phosphorous species which are depicted in yellow and green in Figure 3.65. The sort of phosphorous depicted in green is present in 66.7 % whereas the species in blue is present in 33.3 %. To simplify the interpretation of the ^{31}P -NMR spectra, they are often recorded decoupled of the proton signals, i.e. spin-spin couplings are seldom observed. Moreover, integration is inaccurate (almost useless when there is one-bond coupling to ^1H) in a regular

decoupled ^{31}P NMR spectrum because of uneven NOE (Nuclear *Overhauser* effect) enhancement of the signals by decoupling and long longitudinal relaxation times (T_1 's).

As it has been seen in Section 3.3.6, it is very difficult to predict the position of the phosphorous peak in the spectrum and for the molecules studied in Chapter 3.3 (in which the phosphorous species present all a similar environment) there is a spread of 2.5 ppm (from 14.0 to 11.7 ppm) in the ^{31}P spectra. Therefore the position of the peak corresponding to the green phosphorous in **42b** with respect to the position of the yellow phosphorous cannot be predicted.

From the ^{31}P -NMR spectrum obtained for material **42** it can only be said that two phosphorous species are present and thus that the spectrum corresponds to a material which is an isomeric mixture of **42a** and **42b**.

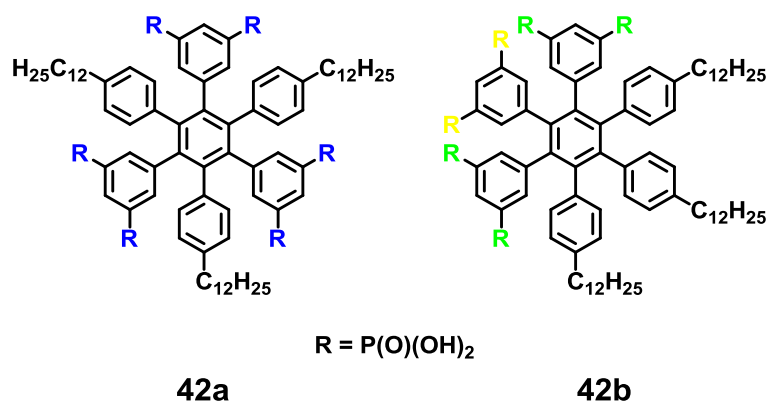


Fig. 3.66: Type of phosphorous species present in 1,3,5-tris(3,5-biphosphonatophenyl)-2,4,6-tris(4-dodecylphenyl)-benzene (**42a**) (blue) and 1,2,3-tris(3,5-biphosphonatophenyl)-4,5,6-tris(4-dodecylphenyl)-benzene (**42b**) (yellow and green).

In the figures of the following sections, the material is depicted as being **42a** for simplicity reasons but it has to be kept in mind that it is actually a mixture of isomers and that the number **42** means **42a** + **42b**.

This section concentrates on the proton conductivity measurements performed for material **42** under three different types of conditions: under 1 bar H_2O atmosphere by increasing the temperature, at RT by decreasing the RH and under anhydrous conditions. Since the material is soluble in methanol, two types of methods to measure the conductivity are available: one can cast a film and measures the in-plane conductivity and one can press a pellet and records the through-plane conductivity.

Around 2 mm thick films of compound **42** have been cast from methanol. However, the films are brittle and therefore the compound is not appropriate to be used as PEM in this morphological state. No proton conductivity measurements have been performed for this material in the form of a film since during the experiment the film cracked at several positions. Therefore the conductivity measurements under the three types of conditions above described are measured on a hand-pressed pellet (100 mg, 5.4 mm diameter, 2.0 mm thickness).

Firstly, the proton conductivity of 1,3,5-tris(3,5-biphosphonatophenyl)-2,4,6-tris(4-dodecylphenyl)-benzene is measured under 1 bar H₂O atmosphere. As it is shown in Figure 3.67, **42** has a lower conductivity than the phosphonated HPB. The proton conductivity of **42** is at 170 °C three orders of magnitude lower than this of **4** ($6.0 \cdot 10^{-6}$ and $2.5 \cdot 10^{-3}$ S/cm respectively).

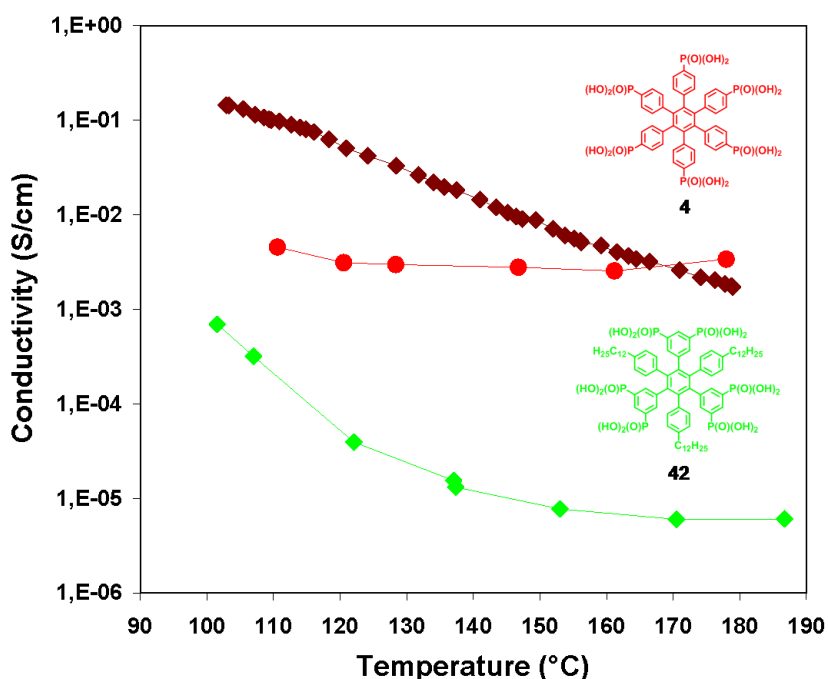


Fig. 3.67: Proton conductivity under 1 bar H₂O atmosphere of hexakis(*p*-phosphonatophenyl)benzene (**4**) and 1,3,5-tris(3,5-biphosphonatophenyl)-2,4,6-tris(4-dodecylphenyl)-benzene/**42** depicted with ● and ◆ respectively. The curve of Nafion® 117 is shown as comparison (◆).

Moreover, it can be observed that the curve of 1,3,5-tris(3,5-biphosphonatophenyl)-2,4,6-tris(4-dodecylphenyl)-benzene decreases while the temperature is increased

from 100 to around 160 °C and then remains constant until 190 °C. The behavior of the conductivity curve of the compound below 160 °C is typical of materials in which the vehicle mechanism is responsible for proton transport. The decay of the proton conductivity in this temperature region is similar to the decay that shows Nafion® 117.

Proton conductivity measurements at 25 °C by decreasing RH have been conducted to study the behavior of compound **42** only by changing one parameter, the RH (in the previous experiments, both the temperature and the RH are varied). It is expected to gain a deep knowledge of the proton transport mechanism taking place through the material. The sample is stored at an atmosphere of 100 % RH during 24 h to let it equilibrate before starting the measurements. The results are presented in Figure 3.68 which also shows the curve of Nafion® 117 as comparison.

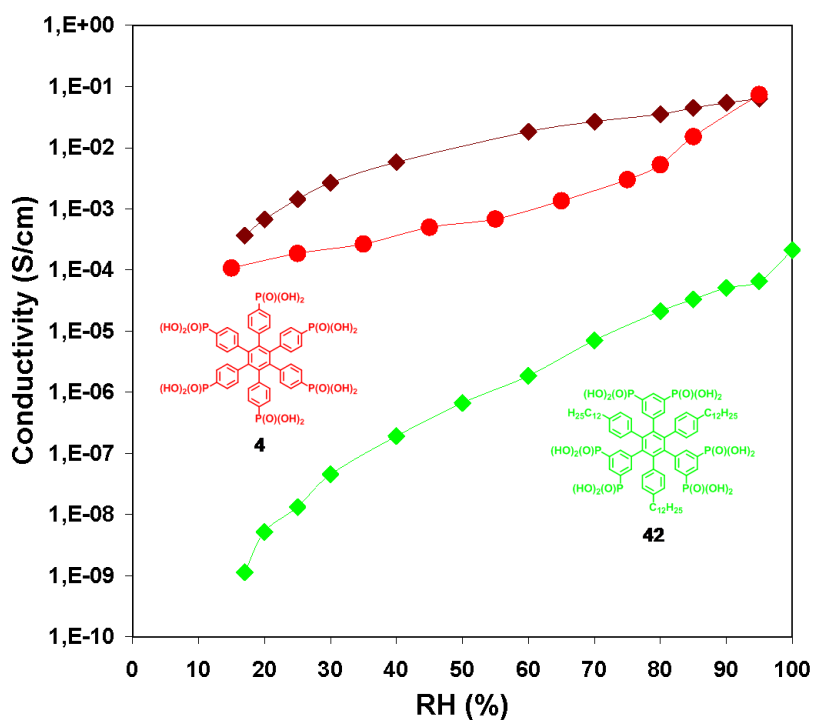


Fig. 3.68: Proton conductivity at RT measured by decreasing the RH for hexakis(*p*-phosphonatophenyl)benzene (**4**) and 1,3,5-tris(3,5-biphosphonatophenyl)-2,4,6-tris(4-dodecylphenyl)-benzene/**42** depicted with ● and ◆ respectively. The curve of Nafion® 117 is shown as comparison (◆).

A constant decrease of conductivity by decreasing the RH is observed. The conductivity of the compound is at 100 % RH of two orders of magnitude less than this

of **4** ($2.1 \cdot 10^{-4}$ and $7.4 \cdot 10^{-2}$). However this difference becomes larger while the RH is decreased, in particular to RH below 40 %. As it has been explained in Chapter 3.2, a non-water based mechanism is responsible for the proton transport of **4** and explains why the conductivity drop below 40 % RH is less pronounced than the one of Nafion® 117. This is not the case for **42** which presents a curve very similar to this of Nafion® 117, in particular at RH below 40 % the conductivity drops in a very pronounced way which can be attributed to a vehicle mechanism for proton transport. Because **4** and **42** present two types of mechanism for the transport of protons, the difference of conductivity becomes larger by decreasing RH.

These conductivity measurements demonstrate that the introduction of alkyl chains into the HPB core does not help in making a material with better proton conducting properties than **4**. Even if films of **35** can be cast from methanol, they are brittle and cannot be used as PEM in FC applications. Moreover, 1,3,5-tris(3,5-biphosphonatophenyl)-2,4,6-tris(4-dodecylphenyl)-benzene (**42**) possesses lower proton conducting properties than **4** either under 1 bar H₂O atmosphere and at RT. In addition, the conductivity curves of **35** under the measured conditions are similar to that of materials in which the vehicle mechanism is responsible for the proton transport mechanism. For these three reasons it can be concluded that hexakis(*p*-phosphonatophenyl)benzene is a better candidate to be used as separator material in FC compared to 1,3,5-tris(3,5-biphosphonatophenyl)-2,4,6-tris(4-dodecylphenyl)-benzene.

The reasons for the low performance of the material compared to the model compound **4** need to be investigated. Therefore, the thermal stability of the material has been studied and water uptake measurements and crystallinity studies have been performed.

Figure 3.69 displays the TGA curves of material **42** and hexakis(*p*-phosphonatophenyl)benzene. The two materials present very similar trends for the curves which means that their thermal stability is akin. Compound **4** exhibits a mass loss of 32 wt % at 450 °C whereas material **42** of 37 wt % which is assumed to be due to the degradation of the hydrophobic core. The continuous mass losses from 25 to 400 °C are much lower in the case of material **42** than of compound **4** (7.4 wt % instead of 12 wt %). However 7.4 wt % correspond to ~ 6.2 water molecules per **42**. Since the maximum weight loss due to condensation of the phosphonic acid groups is 3.6 wt % which corresponds to 3 water molecules, condensation alone cannot explain

the weight losses below 400 °C. In the case of compound **4** it has been determined that it is a crystal hydrate and that the water molecules enclosed in the structure are responsible for the weight losses. It is therefore necessary to investigate whether this is also the case for **42**, i.e. whether the material is a crystal hydrate. Therefore, water uptake as well as crystallinity studies have been performed.

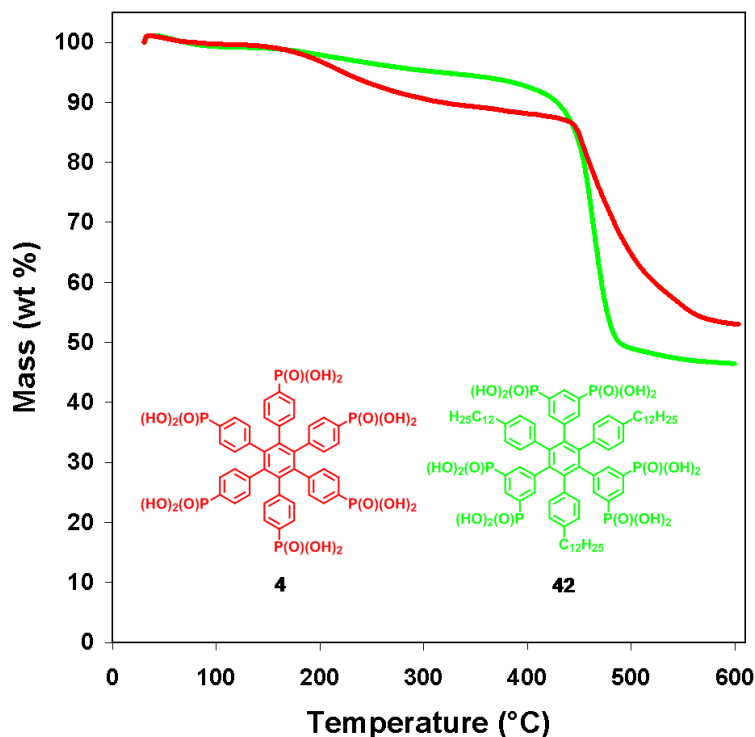


Fig. 3.69: Curves of the TGA experiments performed under N₂ at 10 K/min of hexakis(*p*-phosphonatophenyl)benzene (**4**) and 1,3,5-tris(3,5-biphosphonatophenyl)-2,4,6-tris(4-dodecylphenyl)-benzene/1,2,3-tris(3,5-biphosphonatophenyl)-4,5,6-tris(4-dodecylphenyl)-benzene (**42**) depicted in red and green respectively.

Water sorption measurements have been performed at RT for material **42**. Figure 3.70 shows the adsorption isotherms of this compound and of hexakis(*p*-phosphonatophenyl)benzene for comparison.

It has been deduced from the proton conductivity experiments that a vehicle mechanism must be responsible for the transport of protons through the material. Usually compounds which show a water-based proton transport process display very high water uptake and λ .^[28, 39, 42] Surprisingly, this is not the case for **42** which presents a maximum water uptake (at 100 % RH) of 1.5 wt % and a maximum λ of about 1.3.

The adsorption isotherm can be either classified as Type V *van der Waals* adsorption isotherm, an isotherm which is related to the Type III in that the adsorbent-adsorbate interaction is weak,^[38] or as Type VI since it can be considered that the material presents two steps during the water adsorption: below 44 % RH the water uptake is 0 wt % and from 64 to 93 % RH it is around 1 wt %. This stepwise water adsorption isotherm characteristic of crystal hydrates fits nicely with the above described TGA curve.

As can be seen in Figure 3.70, both water uptake and lambda values of material **42** are lower than those of **4**. Since the latter shows higher conductivity values under the various experimental conditions applied, it can be deduced that water plays a crucial role in the transport of protons through the materials so that a higher water uptake implies a higher conductivity. This does not mean that water has to participate in the form of mobile molecules in the proton transport mechanism since as deduced in Chapter 1.3 hexakis(*p*-phosphonatophenyl)benzene presents a non-water based proton transport mechanism whereas as demonstrated above material **42** needs the mobility of water molecules to transport protons.

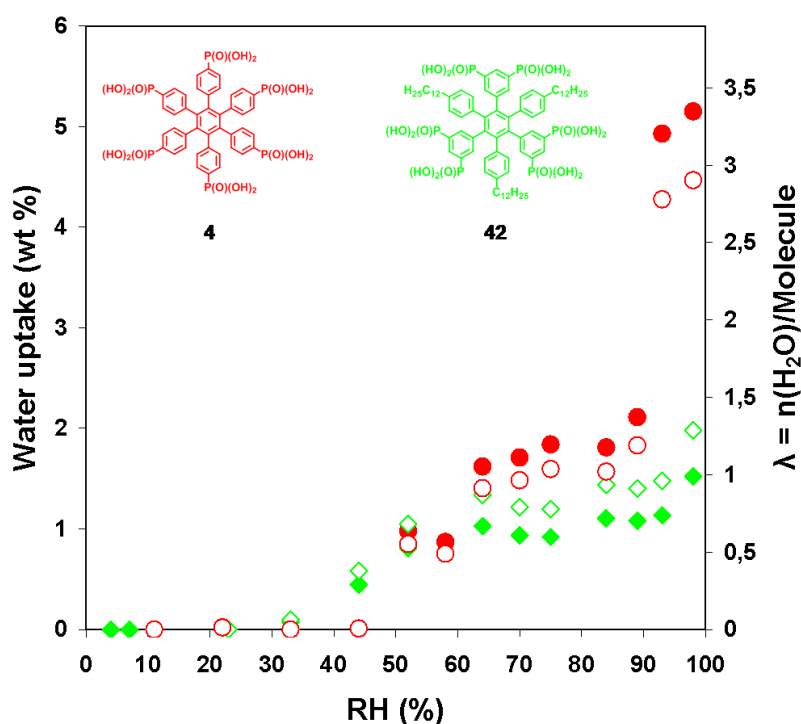


Fig. 3.70: Water sorption isotherm (● and ◆) and lambda (○ and ◇) at RT of hexakis(*p*-phosphonatophenyl)benzene (**4**) and 1,3,5-tris(3,5-biphosphonatophenyl)-2,4,6-tris(4-dodecylphenyl)-benzene/1,2,3-tris(3,5-biphosphonatophenyl)-4,5,6-tris(4-dodecylphenyl)-benzene (**42**) and depicted in red and green respectively.

Since both thermal stability and water adsorption studies performed on compound **42** indicate that the material possesses characteristics of crystal hydrates, crystallinity investigations have been performed.

2D WAXS measurements have not been successful since it has not been possible to extrude the material. On the other hand, WAXS measurements have been performed at different temperatures and RH and are depicted in Figure 3.71. As seen, the sample presents two sharp reflection peaks at low angle which correspond to ~ 38 and 22 \AA and one broad peak at 4.4 \AA . No variations are observed by increasing the temperature or the RH.

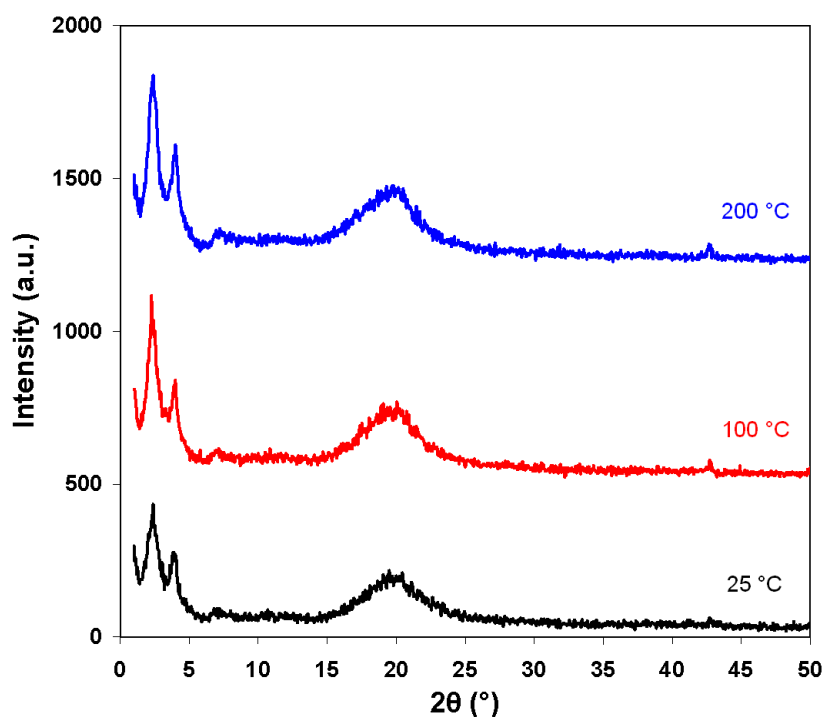


Fig. 3.71: X-ray diffractogram recorded at 33% RH at 25, 100 and 200 °C (black, red and blue respectively) of 1,3,5-tris(3,5-biphosphonatophenyl)-2,4,6-tris(4-dodecylphenyl)-benzene/1,2,3-tris(3,5-biphosphonatophenyl)-4,5,6-tris(4-dodecylphenyl)-benzene (**42**).

Figure 3.72 shows the X-ray diffractogram of **42** compared to the one of the model compound **4**. It can be observed that the compound presenting the alkyl chains shows a less number of diffraction peaks indicating a lower crystallinity. Moreover, it can be noticed that the reflections characteristic of a columnar arrangement corresponding to the inter- and intracolumnar distances and which have been observed in the case of compound **4** are absent in the diffractions pattern of compound **42**.

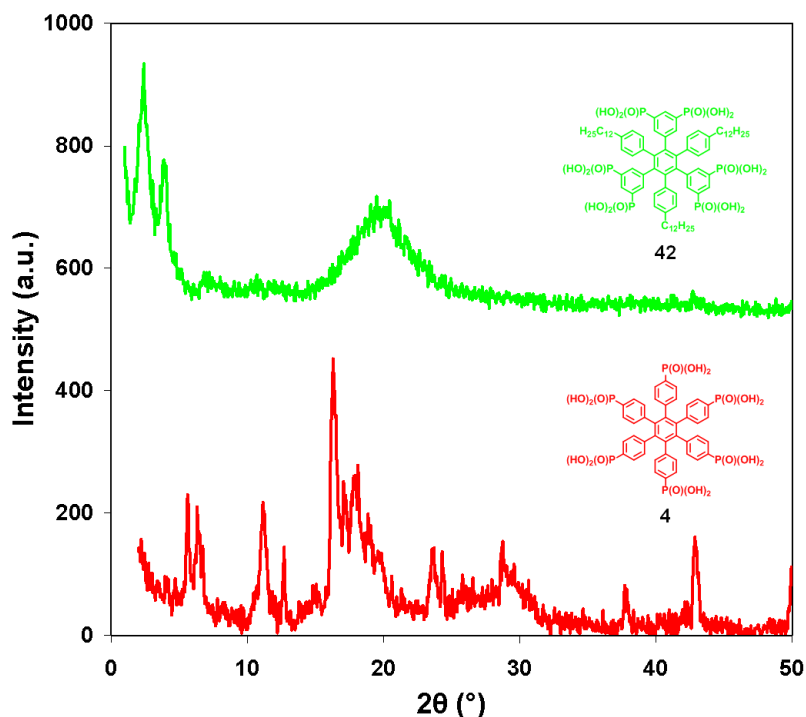


Fig. 3.72: X-ray diffractograms of hexakis(*p*-phosphonatophenyl)benzene **4** (red line) and 1,3,5-tris(3,5-biphosphonatophenyl)-2,4,6-tris(4-dodecylphenyl)-benzene/1,2,3-tris(3,5-biphosphonatophenyl)-4,5,6-tris(4-dodecylphenyl)-benzene (**42**) (green line) recorded at RT and 33 % RH.

The introduction of alkyl chains at the periphery of the HPB core has a profound impact on the proton-conducting and the crystallinity properties of the material. The diverse proton conductivity studies performed on the compound allow concluding that in contrast to hexakis(*p*-phosphonatophenyl)benzene the proton-conducting mechanism taking place through the material is based on the motion of protonated water molecules (vehicle mechanism). Even if both TGA and water uptake studies suggest that the material is a crystal hydrate, the phosphonated HPB containing alkyl chains presents a lower degree of crystallinity than **4**. Interestingly, this compound adsorbs less water than hexakis(*p*-phosphonatophenyl)benzene and thus exhibits a lower conductivity. The presence of the alkyl chains in the HPB core induces a lower degree of order in the system affecting the proton transport mechanism and making it water-dependent.

3.4.4 Hexakis(*p*-sulfonatophenyl)benzene

Hexakis(*p*-sulfonatophenyl)benzene is the equivalent of compound **4** with sulfonic instead of phosphonic acid functions. The aromatic core provides high hydrophobicity whereas the sulfonic acid groups the capacity to be solvated by water. The aim of this section is to see what effects the sulfonic acid groups have on the proton transport properties of the material and what differences are present between the phosphonic and sulfonic acid analogues.

Hexakis(*p*-sulfonatophenyl)benzene (**45**) is synthesized by aromatic sulfonation of the HPB core with chlorosulfonic acid and subsequent hydrolysis with NaOH (see Figure 3.73). The obtained molecule is very hygroscopic and soluble in all kind of polar solvents.

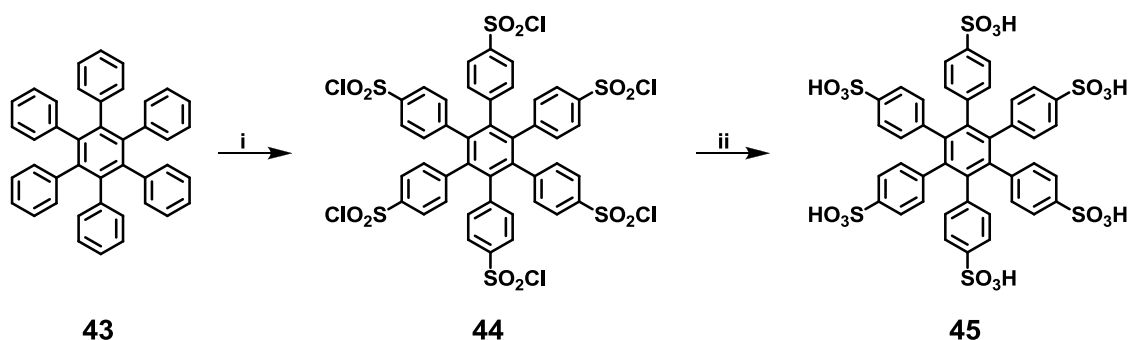


Fig. 3.73: Synthetic route toward hexakis(*p*-sulfonatophenyl)benzene (**45**): i) chlorosulfonic acid, CH₂Cl₂, RT, 24 h, 97 %; ii) NaOH, 50 °C, 36 h, 95 %.

Due to the hygroscopic nature of the material, it is not possible to measure its proton conductivity in any of the conditions described in the previous sections for compounds **35** and **42**. In contact with the water present in the atmosphere, the material takes up weight and becomes fluid. Therefore, even if the formation of a pellet is possible by fast pressing, by sandwiching it between the two electrodes the pellet collapses and the electrodes touch each other.

From the point of view of fuel cells working at intermediate temperatures, this molecule does not have any application since water is always present in the environment of a PEM. If there is any possibility of making a pellet of the compound and measuring it under very low humidity conditions, high conductivity values may be obtained.

An increase of the hydrophobicity will most probably yield a molecule with a lower water affinity than **45** but with most probably a water-based transport mechanism.

Figure 3.74 displays the TGA curves of the two *para* substituted HPB derivatives: compounds **4** and **45**. In the curve of the sulfonated HPB, six degradation steps can be recognized that give a total mass loss of 58.4 wt %:

- From 100 to 210 °C: 5.7 wt %;
- From 210 to 300 °C: 15.6 wt %;
- From 300 to 358 °C: 6.8 wt %;
- From 358 to 420 °C: 19.2 wt %;
- From 420 to 530 °C: 6.4 wt %;
- From 530 to 587 °C: 4.7 wt %.

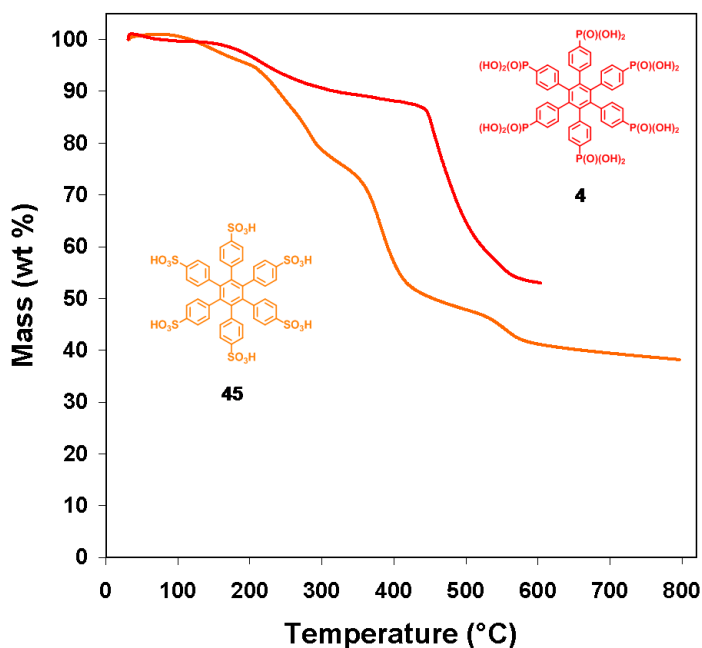


Fig. 3.74: Curves of the TGA experiments performed under N_2 at 10 K/min of hexakis(*p*-phosphonatophenyl)benzene (**4**) and hexakis(*p*-sulfonatophenyl)benzene (**45**) depicted in red and orange respectively.

This is most probably due to the hygroscopic character of the material. The measurements have been performed under N_2 flux to avoid the contact with the water present in the atmosphere however water is present in the sample since during its preparation which usually takes some seconds the material is in contact with the atmospheric air. This TGA curve indicates that the compound is not suitable to be used

as separator material since in a FC working at intermediate temperatures gaseous and liquid water is always present.

Like in the former case of hexakis(*p*-phosphonatophenyl)benzene, titration measurements have been performed on the hexa sulfonated HPB. Figure 3.75 presents the corresponding titration curve and its derivative plot. The measurements have been carried out as described in Chapter 1.3.6, 20.8 mg of compound **45** are allowed to agitate during 48 h at RT in 50 mL of a 3 M KCl solution. Subsequently, the suspension is titrated against a 0.01 M NaOH solution during 52 h.

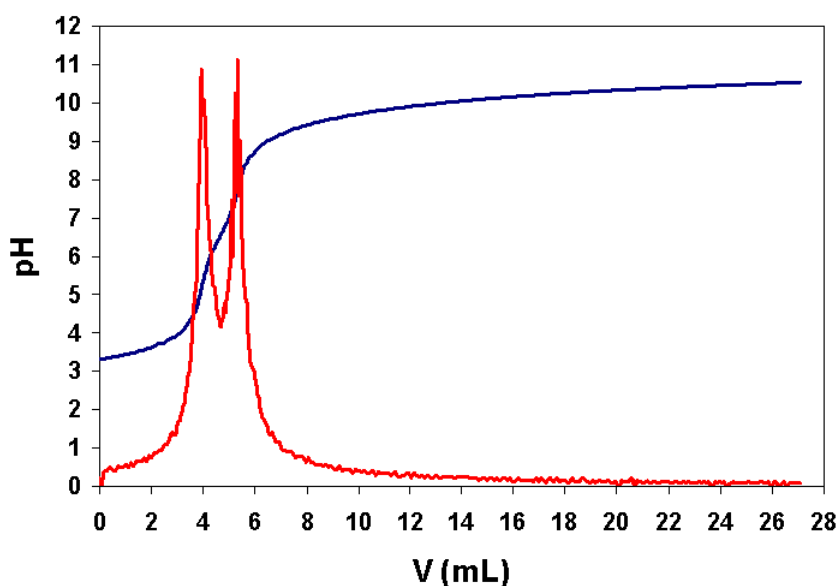
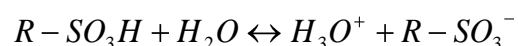


Fig. 3.75: Titration curve of hexakis(*p*-sulfonatophenyl)benzene (**45**) (blue line) and its derivative plot (red line).

Every maximum in the derivate plot represents a specific type of protons or acidic centers with different acidity. Since sulfonic acid is a monoprotic acid, only one maximum in the derivative plot is expected.



Interestingly, contrary to what one might anticipate, hexakis(*p*-sulfonatophenyl)benzene behaves like a diprotic acid since two maxima are observed in the derivative plot. This means that two dissociation processes take place during

titration with pKa values of 5.15 and 7.76, i.e. that compound **45** gives progressively its protons.

In the literature, phosphonic acid based polymers have been described as being mono-^[91] and diprotic^[55] acids whereas, excepting compound **4**, phosphonic acid-containing small molecules are diprotic.^[53, 54] As expected, sulfonic acid based compounds are found to be monoprotic^[92] since the sulfonic acid group contains only one ionizable hydrogen atom. In the case of the studied material, an elevated negative charge density is present while the first protons react with the hydroxyl groups so that only after the addition of more NaOH the second portion of protons can be subtracted from the molecule.

The ion-exchange capacity of compound **45** is calculated from the titration data and compared to theoretical value by using the following formula:

$$IEC = \frac{n(H)}{m(\text{compound } 45)} = \frac{n(SO_3H)}{m(\text{compound } 45)} \text{ mmol / g}$$

In the case of these measurements, 20.8 mg of hexakis(*p*-sulfonatophenyl)benzene have been used. This gives a theoretical value for the IEC of 5.91 mmol/g. The experimental values for the IEC obtained from the titration experiments are of 1.89 and 2.56 for the two maxima and 4.45 for the sum of both. This value indicates that almost 75 % of the protons have reacted with the NaOH during the titration. The theoretical IEC value of hexakis(*p*-sulfonatophenyl)benzene is inferior to the one of compound **4** whereas the experimental value is higher (11.8 and 3.5 for **4** respectively). This indicates that even if the phosphonated HPB possesses a higher number of protons than its sulfonated homologous, it has a lower capacity to exchange them than **45**. This is most probably due to the high density of acidic groups in **4** (see Chapter 3.2.6).

3.4.5 Hexakis(3,5-biphosphonatophenyl)benzene

Alternatively to the above described systems possessing all six times either phosphonic or sulfonic acid groups, one can think about raising the number of acidic moieties at the periphery of the HPB. It is expected than an increase of the density of the phosphonic acid groups would also mean an increase of the proton conductivity values. Thus hexakis(3,5-biphosphonatophenyl)benzene is proposed as next step to follow in the study of small molecules which can be proton conductors in the solid state.

In principle, this molecule might be synthesized by following the synthetic pathway proposed in Figure 3.76. Bis(3,5-bisdiethylphosphonatophenyl)acetylene (**50**) is obtained via a four step synthetic route in gram scale. Unfortunately, the cyclotrimerization reaction which would lead to the corresponding hexakis(3,5-bisdiethylphosphonatophenyl)benzene (**51**) is not successful.

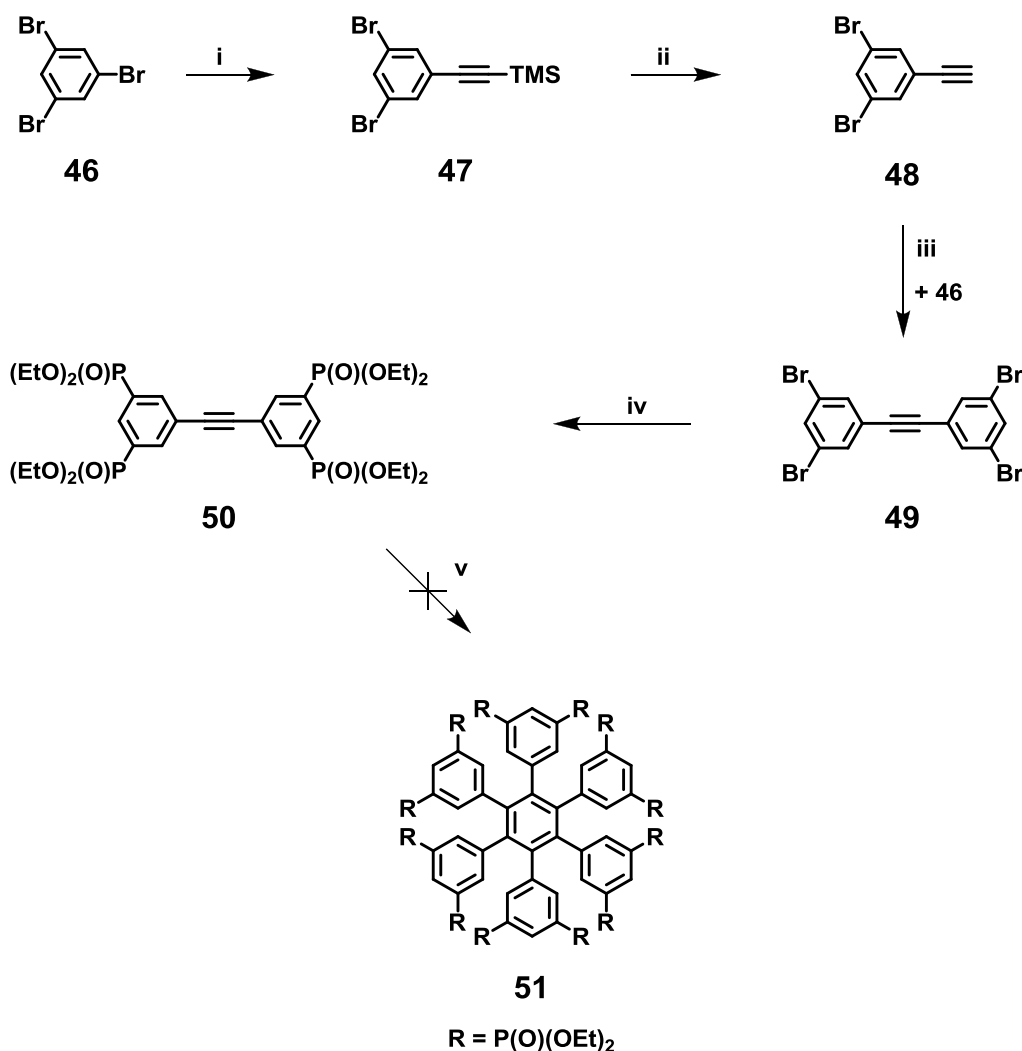


Fig. 3.76: Synthetic route toward hexakis(3,5-bisdiethylphosphonatophenyl)benzene (**51**): i) trimethylsilylacetylene, CuI, Pd(PPh₃)₂Cl₂, diisopropylamine, toluene, RT, 1 h, 57 %; ii) TBAF, THF, RT, 15 min, 89 %; iii) CuI, Pd(PPh₃)₂Cl₂, NEt₃, toluene, 60 °C, 12 h, 73 %; iv) HP(O)(OEt)₂, Pd(PPh₃)₄, NEt₃, toluene, 75 °C, 12 h, 63 %; v) Co₂(CO)₈, dioxane, reflux, 12 h.

Since the first reported example of cyclotrimerization of acetylene leading to benzene by *Berthelot* in 1866 (thermal trimerization), seventeen transition metals have proven to be effective catalyst to obtain substituted benzenes.^[93-95] Most often the cyclotrimerization of phenylacetylenes is done by using simple cobalt complexes like

cyclopentadienylcobalt or carbonylcobalt.^[96-100] However recently other catalytic systems which use Zn or Mg as reducing agents have been developed to obtain dihydroaromatic compounds under mild reaction conditions in good to excellent yields.^[101-106]

The most common mechanism for the cyclotrimerization of acetylenes was proposed by *N.E. Schore* and begins with the formation of a metallocyclopentadiene complex (see Figure 3.77).^[107] As an 18-electron complex, ML_{n+3} (**1**), undergoes a pair of ligand-substitution reactions resulting in the formation of a bisacetylene complex **3**, the catalytically active species. Oxidative cyclization of two coordinated alkyne units produces either metallocycle **4** or **5**.^[108] After dissociation of a third ligand and coordination of a third alkyne (species **6**), two pathways are possible. Either alkyne insertion generates metallocycloheptatriene **7**, or [4 + 2] cycloaddition generates bridged bicycle **8**. Since reductive elimination from a metallocycloheptatriene to form an arene is symmetry forbidden, the former pathway is questionable.^[109] In both cases after ligand dissociation the substituted benzene **10** is obtained. A third route proposed for ruthenium catalysts involves formal [2 + 2] cycloaddition of the alkyne followed by rearrangement (species **9**), reductive elimination (species **7**), and arene decomplexation (species **10**).^[110]

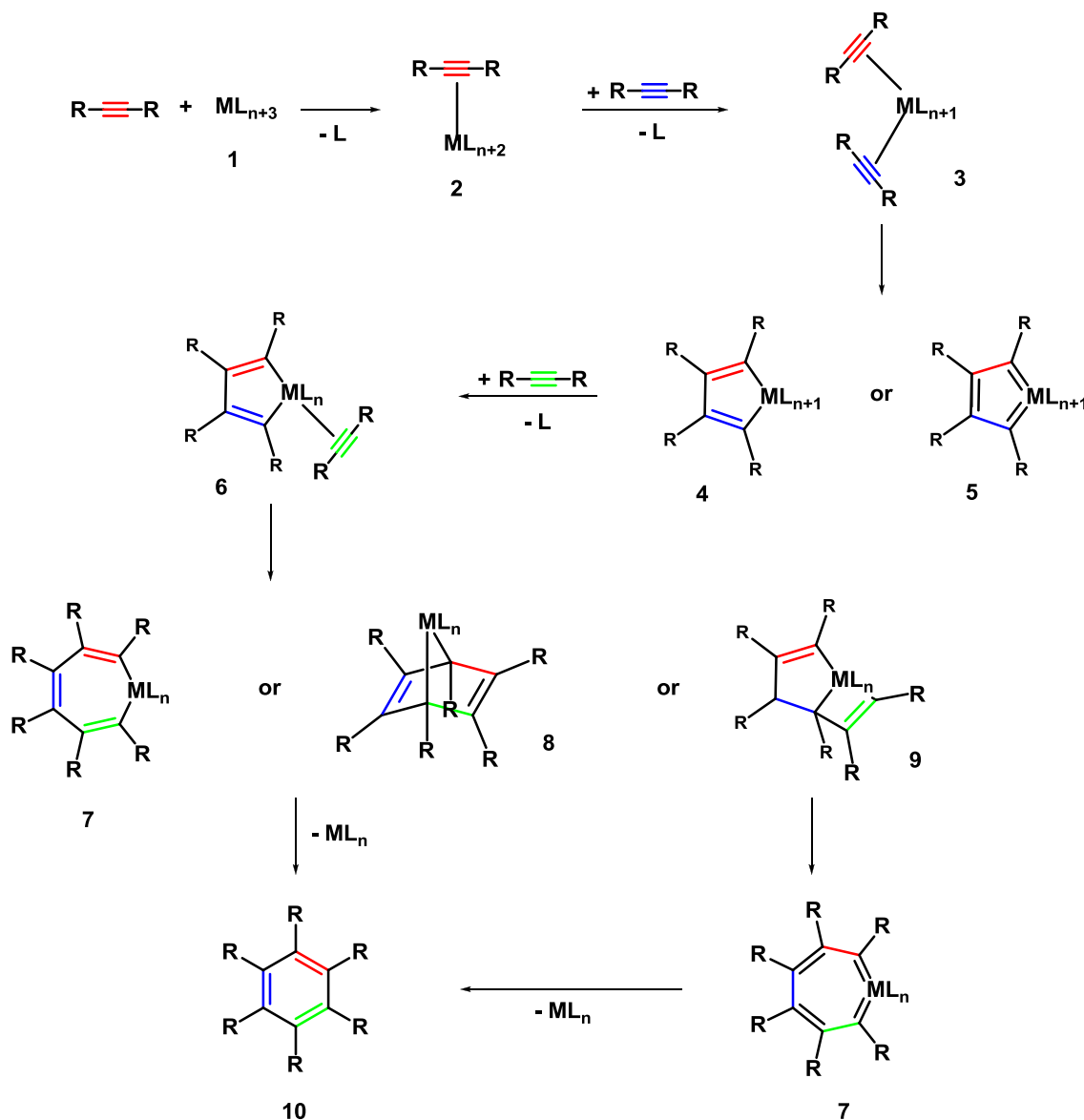


Fig. 3.77: Representation of the cyclotrimerization mechanism.

The [2 + 2 + 2] cyclization reaction has first been tried in dioxane using $Co_2(CO)_8$ as catalyst. These reaction conditions have been used by the *Müllen* group for the cyclotrimerization of substituted (bisphenyl)acetylenes.^[111] Since no product is obtained, other cobalt-based catalytic systems which have been described in the literature for the cycloaddition reactions of substituted alkynes have been used.^[105, 106, 112-115] The experimental conditions applied as well as the molecules obtained are summarized in Table 3.10. Unfortunately, in all cases the trimerization reaction does not conduct to the obtainment of the desired product.

Table 3.10: Experimental conditions and molecules obtained for the cyclotrimerization of bis(3,5-bisdiethylphosphonatophenyl)acetylene **50**.

Catalytic system/Solvent	Temperature	Obtained compounds
CoI ₂ dppe + Zn/CH ₃ CN ^[112]	RT	Educt
	80 °C	Educt
CoBr ₂ (dppe)/CH ₃ CN	RT	Educt
	50 °C	Educt
CoBr ₂ /CH ₃ CN	RT	Educt
	50 °C	Educt
CoBr ₂ (dppe) + Zn +	RT	No educt, no product
ZnI ₂ /CH ₃ CN ^[106]	50 °C	No educt, no product

Cyclotrimerization reactions carried out with substituents in the *meta*- positions have been already reported in the literature using Co₂(CO)₈ as catalyst^[116, 117] and have proven to succeed for the synthesis of 1,3,5-tris(3,5-biphosphonatophenyl)-2,4,6-tris(4-dodecylphenyl)-benzene (**42**). In the present case, two explanations are offered to explain why the trimerization of **50** is not successful:

- The steric crowding caused by the bulky substituents in the *meta* positions;
- The electron-withdrawing effect of the phosphonic ester groups.

At this point it has to be cleared up that the synthetic route to obtain **42** involved the cyclotrimerization of tetraethyl 5-((4-dodecylphenyl)ethynyl)-1,3-phenylenediphosphonate (**40**). This molecule carries also two electron-withdrawing groups in the *meta* position however the difference with **50** is that **40** is asymmetric, i.e. the phosphonic ester groups are only on one side of the triple bond whereas in the case of **50** the ester functionalities are present on both sides (see Figure 3.78). The substitution of the ligand by **50** to obtain a stable metallocyclopentadiene complex (**4** or **5** in Figure 3.77) which can further dissociate a third ligand and coordinate a third alkyne might be unfavorable. The combination of the nine atomic orbitals of the metal with alkyne orbitals give rise to nine molecular orbitals which might not contain 18 valence electrons due to the electron deficiency of the alkyne caused by the phosphonic ester moieties. This fact can explain why it is not possible to cyclotrimerize **50**.

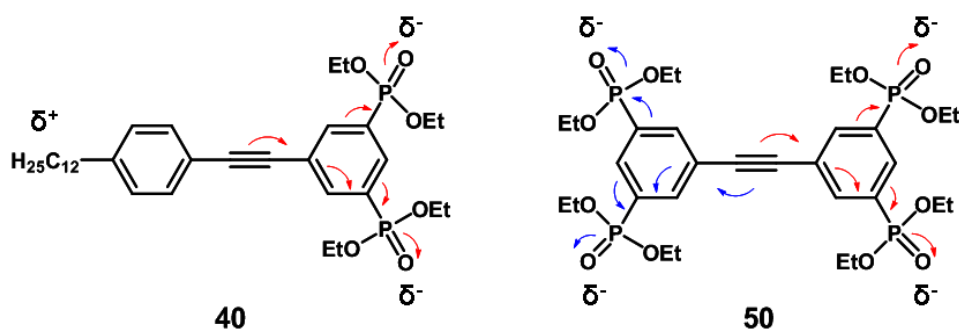


Fig. 3.78: Schematic representation of the possible charge distribution in the substituted (bisphenyl)acetylene molecules **40** and **50** due to the phosphonic ester functionalities.

3.4.6 Summary

The work presented in this chapter is an exploration of the impact that the change from the *para* to the *meta* position, the introduction of alkyl chains and the replacement of phosphonic by sulfonic acid groups have on the proton conducting properties of solid state proton-conducting HPB molecules. All three modifications of the model compound **4** yield products of lower conductivity. Possible explanations for the decrease of proton mobility have been proposed in the corresponding sections. It has been demonstrated in Section 3.4.3 that the change of the position of the phosphonic acid functionalities from *para* to *meta* results in a decrease of the conductivity values but the conductivity still remains temperature-independent. The *meta* substituted compound is a crystal hydrate and the reason for the lower conductivity compared to model compound **4** might be the possibility that the acidic moieties have to arrange either above or below the plane of the phenyl ring. This creates regions with a lower concentration of phosphonic acid groups and thus lower conductivities.

On the other hand, the introduction of alkyl chains is proven to have also a negative impact on the proton-conducting properties of the material since by decreasing the crystallinity compared to the model compound **4**, the conductivity also decreases. Moreover in this case the transport mechanism seems to be water-based. Interestingly, the compound presents lower adsorption values than hexakis(*p*-phosphonatophenyl)benzene but since the vehicle mechanism is responsible for the proton transport the conductivity values are lower.

The replacement of phosphonic by sulfonic acid groups leads to a compound of high IEC which however cannot be used as separator material due to its extreme affinity to

water. The extension of the hydrophobic core might yield a material with lower water solubility but most probably with a water-based proton transport mechanism.

In addition in this chapter the increase of the density of phosphonic acid groups on the periphery of the HPB has been also explored. Different cyclotrimerization methods have been proposed to obtain hexakis(3,5-bisdiethylphosphonatophenyl)benzene (**51**) but all of them have failed.

3.5 Expanding the Periphery of the Hexaphenylbenzene

3.5.1 General remarks

Section 3.5 focuses on studying the impact the expansion of the HPB core has on the proton conductivity of phosphonic acid-containing solid state proton conductors. For this purpose, two HPB derivatives have been synthesized and characterized and their proton conductivities have been compared to the one of their respective analogues.

Keeping in mind that hexakis(*p*-phosphonatophenyl)benzene (**4**) is of all the presented compounds momentarily the one showing the highest proton conductivity in the solid state, its hydrophobic core is increased to determine the concrete effects hydrophobicity and phosphonic acid density have on proton transport properties (see Figure 3.79). In addition, an analogue of hexakis(*m*-phosphonatophenyl)benzene (**35**) is synthesized and characterized. It is expected to gain a deeply insight into the proton conducting characteristic of phosphonic acid based expanded HPB compounds.

Another interesting aspect which is explored in this chapter is the increase of the phosphonic acid functionalities from six to twelve. It is of interest to know whether adopting the same synthetic procedure as used to obtain the compounds depicted in Figure 3.79 the synthesis of a HPB-based molecule with twelve phosphonic acid functions is possible.

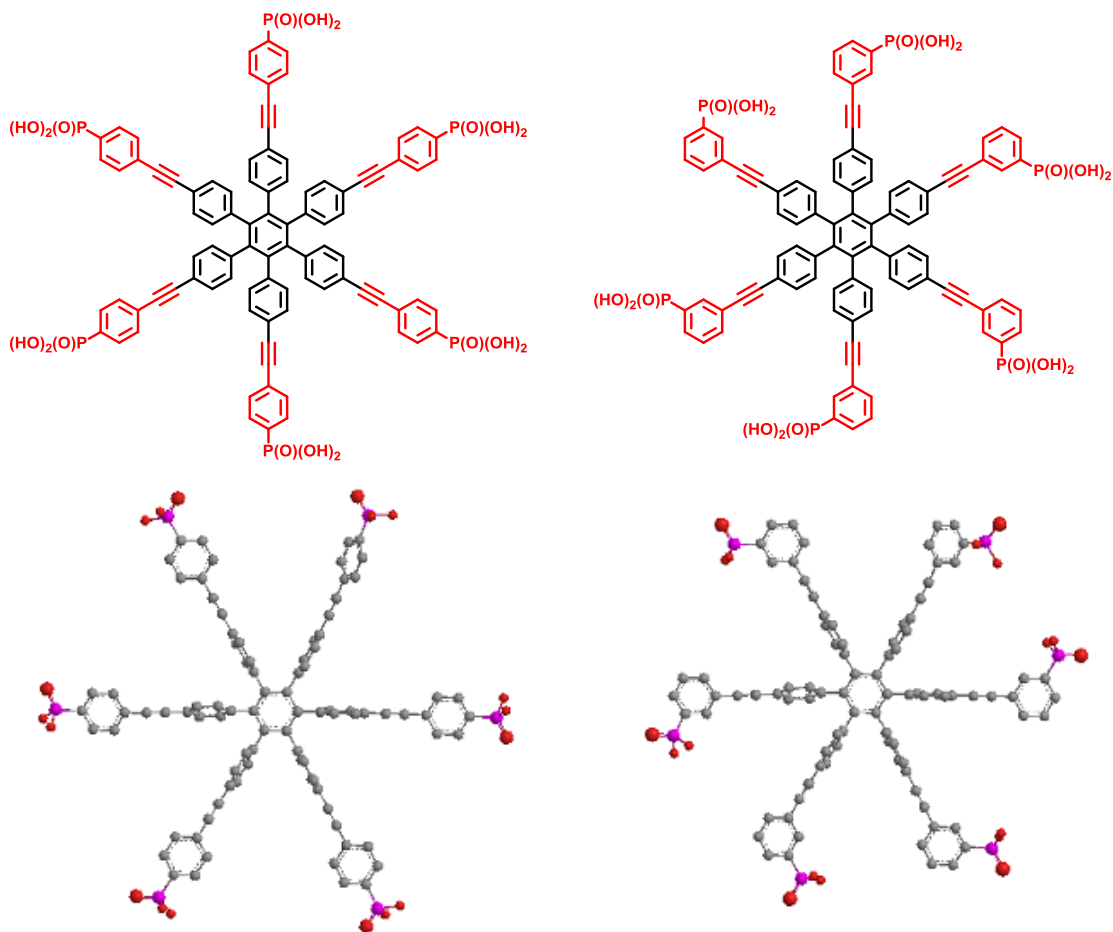


Fig. 3.79: HPB derivatives proposed as solid state separator materials and their structures in the gas phase obtained from ChemDraw 3D molecular-mechanics force field calculations (MMFF94) energy minimization. H atoms are omitted for clarity.

3.5.2 Para and Meta substituted Molecules

The *Sonogashira-Hagihara* coupling reaction^[118] of terminal alkynes with hexaiodohexaphenylbenzene is applied for the synthesis of the desired compounds. Firstly, two terminal alkynes diethyl (4-ethynylphenyl)phosphonate (**54**) and diethyl (3-ethynylphenyl)phosphonate (**56**) need to be synthesized. **54** is obtained in gram scale via a two step reaction consisting of the replacement of bromine by diethylphosphonate groups in [(4-bromophenyl)ethynyl]trimethylsilane (**52**) followed by deprotection with tetra-*n*-butylammonium fluoride (Figure 3.80).

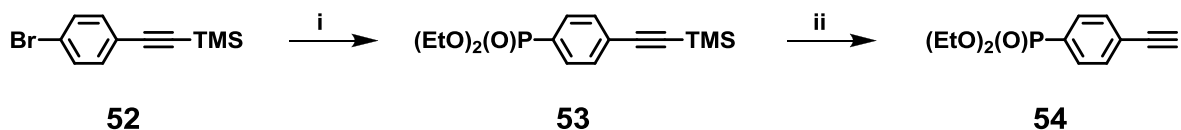


Fig. 3.80: Synthetic route toward diethyl (4-ethynylphenyl)phosphonate (**54**): i) HP(O)(OEt)_2 , $\text{Pd(PPh}_3)_4$, NEt_3 , toluene, 75°C , 12 h, 60 %; ii) TBAF, THF, RT, 40 min, 83%.

In the case of diethyl (3-ethynylphenyl)phosphonate (**56**), [(3-bromophenyl)ethynyl]trimethylsilane (**30**) has first to be obtained as described in Section 3.4.2. The phosphonic ester group is subsequently introduced by using a palladium catalyzed cross-coupling reaction and the molecule deprotected with tetra-*n*-butylammonium fluoride (Figure 3.81).

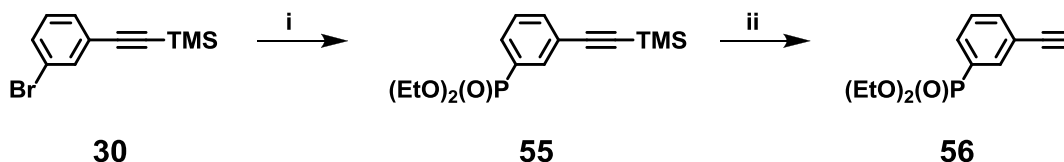


Fig. 3.81: Synthetic route toward diethyl (3-ethynylphenyl)phosphonate (**56**): i) HP(O)(OEt)_2 , $\text{Pd(PPh}_3)_4$, NEt_3 , toluene, 75°C , 12 h, 67 %; ii) TBAF, THF, RT, 15 min, 91 %.

The esters of the desired expanded HPB compounds are obtained by coupling the above described terminal alkynes **54** and **56** with hexaiodohexaphenylbenzene in toluene by 60°C using $\text{Pd(PPh}_3)_4$ as catalyst and triethylamine as base. The use of diisopropylamine as base did not conduct to the wanted product, most probably because it is a weaker base than triethylamine. The *para* and *meta* substituted hexakis[(phenylethynyl)phenyl]benzene **58** and **60** are purified by column chromatography and hydrolyzed under mild conditions to afford hexakis[*p*-(*p*-phosphonatophenylethynyl)phenyl]benzene (**59**) and hexakis[*p*-(*m*-phosphonatophenylethynyl)phenyl]benzene (**61**) respectively.

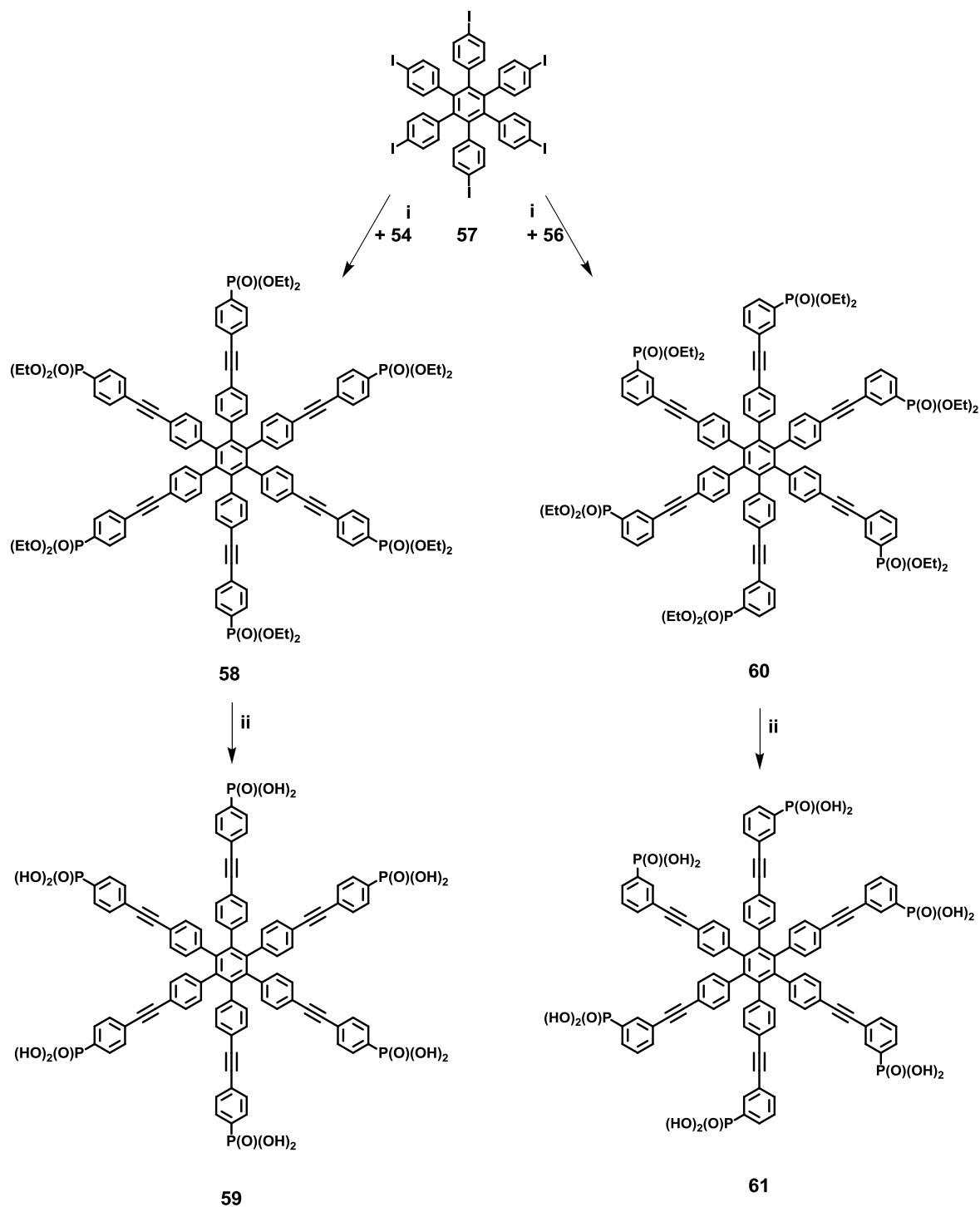


Fig. 3.82: Synthetic route toward hexakis[*p*-(*p*-phosphonatophenylethynyl)phenyl]benzene (**59**) and hexakis[*p*-(*m*-phosphonatophenylethynyl)phenyl]benzene (**61**): i) Pd(PPh₃)₄, CuI, NEt₃, toluene, 60 °C, 12 h, 43 %; ii) a. TMS-Br, DCM, RT, 48 h; b. MeOH, RT, 48 h, 98 %.

Both phosphonic acid containing molecules are poorly soluble in water, water alcohol mixtures and non-polar organic solvents. The solubility of **59** in polar organic

solvents like DMSO is higher than the one of compound **61**. The latter is only slightly soluble in DMSO at elevated temperatures and therefore no resolved liquid-state ^{13}C -NMR spectrum could be obtained.

Figure 3.83 displays the ^{31}P -NMR spectra recorded in deuterated DMSO for compounds **59** and **61** as well as for hexakis(*p*-phosphonatophenyl)benzene (**4**) and hexakis(*m*-phosphonatophenyl)benzene (**35**) for comparison. The spectrum of **59** shows only one peak at 12.4 ppm which corresponds to the only type of phosphorous atoms present in the molecule. The peak is shifted toward higher fields compared to the homologous compound **4**.

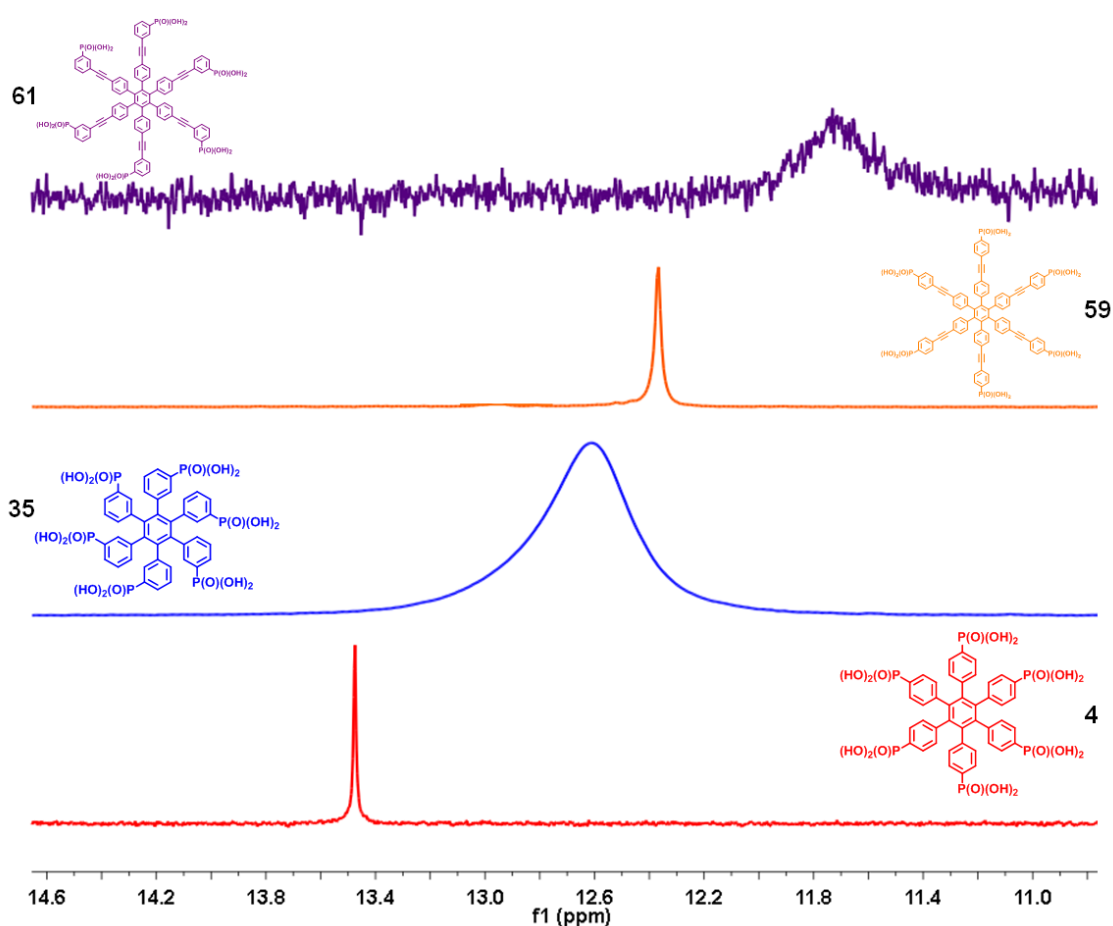


Fig. 3.83: ^{31}P -NMR spectra of hexakis(*p*-phosphonatophenyl)benzene (**4**) (red) and hexakis(*m*-phosphonatophenyl)benzene (**35**) (blue), hexakis[*p*-(*p*-phosphonatophenylethynyl)phenyl]benzene (**59**) (orange) and hexakis[*p*-(*m*-phosphonatophenylethynyl)phenyl]benzene (**61**) (violet) recorded in DMSO at: 373 K - 121 MHz, 373 - 121 MHz, RT - 202 MHz and RT - 202 MHz respectively.

In the case of compound **61**, the NMR signal obtained is also shifted toward higher fields as compared to **35**. Due to the poor solubility of the material in all kinds of solvents, the resolution of the spectrum is not good enough to identify whether the ^{31}P -NMR signal splits into a multiplet corresponding to the different types of phosphorous species (i.e. that a isomeric mixture is obtained) or whether only one peak attributed to one kind of phosphorous species is present like in the case **35**.

The proton conductivity properties of the two materials have been checked under different conditions. Like in case of the other compounds, first of all the proton transport has been measured under 1 bar H_2O atmosphere by increasing the temperature, i.e. by decreasing the RH. Figure 3.84 displays the conductivity curves of **59** and **61** and also of model compound **4**, Nafion® 117 and (*p,p'*-terphenyl-4,4'-diyl)bisphosphonic acid **9** as comparison. This latter has been chosen since it presents the lowest conductivity of all materials studied in Section 3.3.

Compound **59** presents a conductivity which slightly decreases upon increasing temperature. At 160 °C, the proton conductivity value of **59** is two orders of magnitude lower than the one of **4** ($7.7 \cdot 10^{-5}$ S/cm). The initial conductivity decay of proton conductivity (from 100 until 130 °C) is most probably due to the loss of water and is in accordance with a vehicle mechanism. Above 160 °C the conductivity curve could be considered to present a plateau like model compound **4**. For this reason it is not clear from these conductivity measurements whether a water based diffusion process is responsible for the proton transport through compound **59** or whether like in the case of **4** the proton conductivity is not based on the diffusion of water molecules.

Hexakis[*p*-(*m*-phosphonatophenylethynyl)phenyl]benzene (**61**) exhibits a tremendous/huge conductivity decay from 110 to 155 °C. Within these temperatures the conductivity value decreases by six orders of magnitude from $1.9 \cdot 10^{-2}$ to $1.3 \cdot 10^{-8}$ S/cm. At 155 °C the conductivity of **61** is even two orders of magnitude lower than that of compound **9** studied in Chapter 3.3 showing the lowest conductivity. This pronounced conductivity drop can be attributed to a material in which like Nafion® the proton transport is based on the vehicle mechanism.

It has also to be considered that the density of phosphonic acid functions of **59** and **61** is 0.43 and this of **4** and **35** 0.92, i.e. by increasing the size of the aromatic core the density is decreased by half. This is an expected fact contrary to the above described evolution of the conductivity curves for compounds **59** and **61**, specially for the latter.

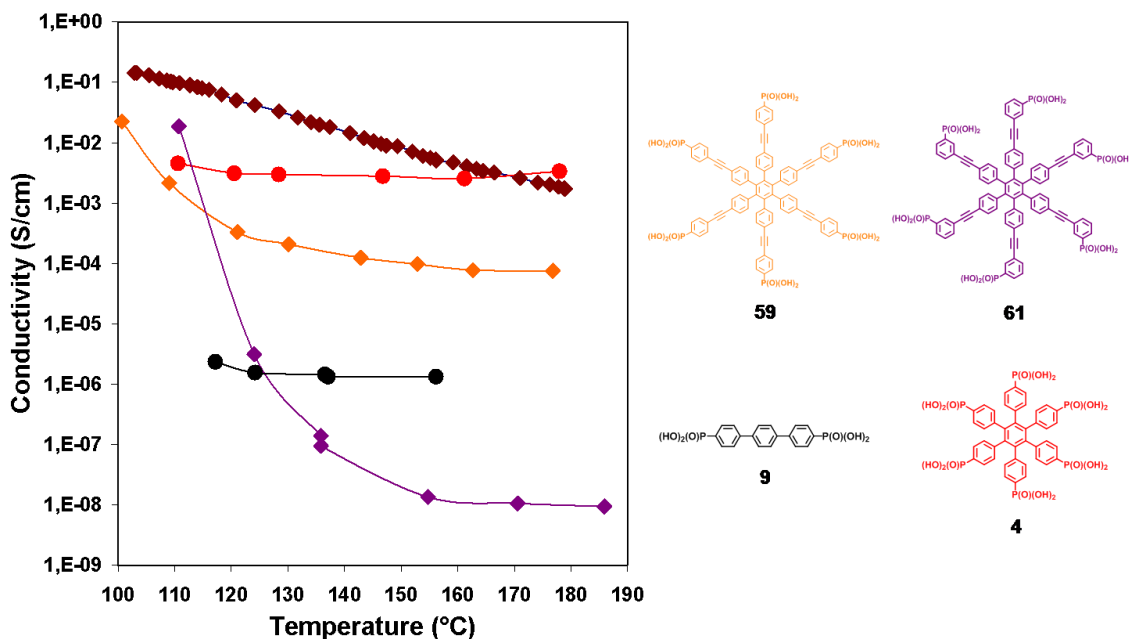


Fig.3.84: Plots of the proton conductivity under 1 bar H₂O atmosphere for hexakis[*p*-(*p*-phosphonatophenylethynyl)phenyl]benzene (**59**) (♦) and hexakis[*p*-(*m*-phosphonatophenylethynyl)phenyl]benzene (**61**) (◆). The curves of Nafion® 117 (◆), hexakis(*p*-phosphonatophenyl)benzene (**4**) (●) and (*p,p'*-terphenyl-4,4'-diyl)bisphosphonic acid (**9**) (●) are shown for comparison.

Another relevant experiment is to measure the proton conductivity by decreasing the RH at a fixed temperature. Contrary to the above mentioned case in which both temperature and RH are modified, in this experiment only one parameter (the RH) is changed. This has been done for compounds **59** and **61** at two temperatures: 25 and 55 °C.

Conductivity measurements at 25 °C by decreasing RH have been performed for compound **59** to try to assess the type of proton transport mechanism since this could not be determined only by using the experiment done under 1 bar H₂O atmosphere. Figure 3.85 shows the evolution of the conductivity curves of hexakis[*p*-(*p*-phosphonatophenylethynyl)phenyl]benzene (**59**) as well as of Nafion® 117, model compound **4** and compound **9** as comparison. Firstly, it can be observed that the conductivity of **59** is in between this of **4** and **9** (like it was in Figure 3.84). However, whereas for compounds **4** and **9** the conductivity decreases continuously by decreasing RH, Nafion® 117 and compound **59** experiment a pronounced conductivity drop below 40 % RH which is due to the lower presence of water in the system. Thus it can be concluded that in hexakis[*p*-(*p*-phosphonatophenylethynyl)phenyl]benzene like in Nafion® 117 the transport of protons is based on the diffusion of water molecules

whereas this is not the case for model compound **4** and (*p,p'*-terphenyl-4,4'-diyl)bisphosphonic acid (**9**).

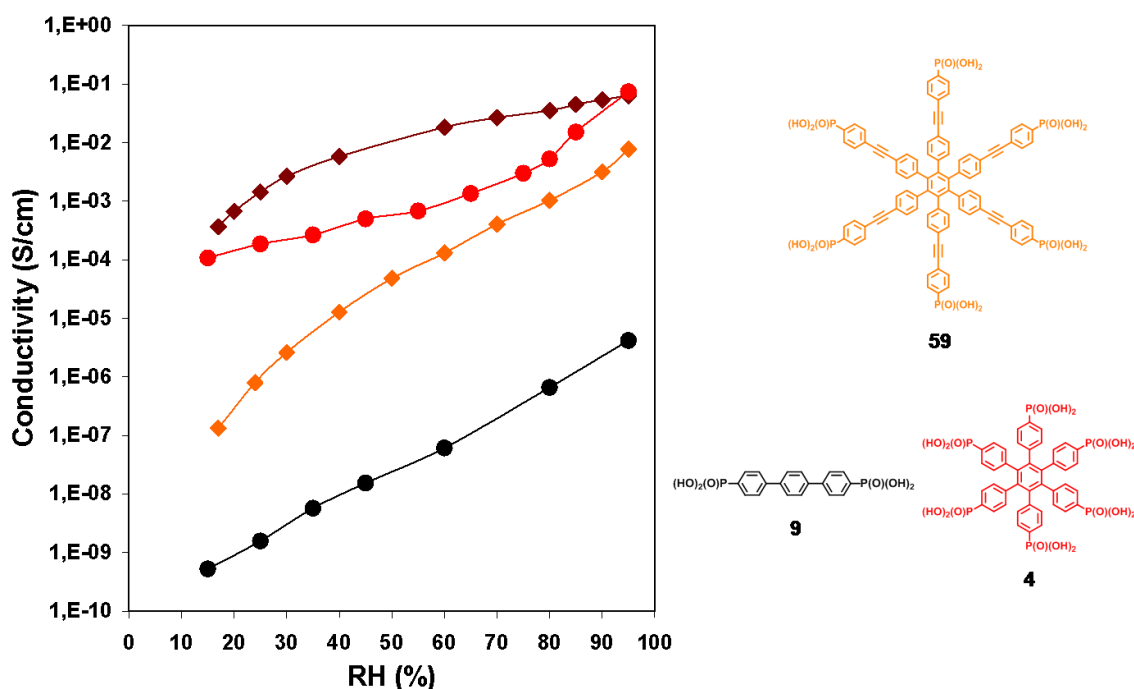


Fig. 3.85: Plots of the proton conductivity at 25 °C as a function of RH for hexakis[*p*-(*p*-phosphonatophenylethynyl)phenyl]benzene (**59**) (◆). The curves of Nafion® 117 (♦), hexakis(*p*-phosphonatophenyl)benzene (**4**) (●) and (*p,p'*-terphenyl-4,4'-diyl)bisphosphonic acid (**9**) (●) are shown for comparison.

Measurements performed at 55 °C by decreasing RH for **59** and **61** are shown in Figure 3.86. Surprisingly the conductivity of **61** is over the whole RH range higher than that of **59**, especially at high humidity. High values are obtained for both compounds at 95 % RH ($7.2 \cdot 10^{-2}$ and $1.4 \cdot 10^{-2}$ S/cm respectively). The evolution of the curve of compound **61** is very similar to the one of **59**. The conductivity decay of **61** becomes more pronounced below 40 % RH. This is an indication that sums up to those gained from the measurements performed under 1 bar H₂O atmosphere to conclude that the vehicle mechanism is responsible for the transport of protons through the material.

The conductivity of **59** is slightly increased by performing the measurements at 55 °C with respect to 25 °C. The curve at 55 °C corroborates the impact that water has on the proton transport mechanism of the compound.

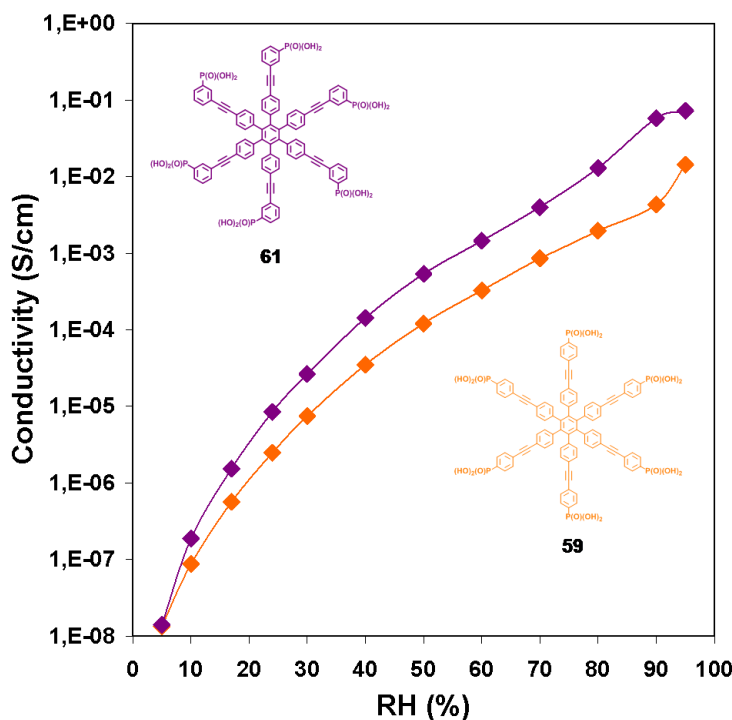


Fig. 3.86: Plots of the proton conductivity at 55 °C as a function of RH for hexakis[*p*-(*p*-phosphonatophenylethynyl)phenyl]benzene (**59**) (◆) and hexakis[*p*-(*m*-phosphonatophenylethynyl)phenyl]benzene (**61**) (♦).

Conductivity measurements performed at a fixed RH by increasing the temperature are of relevance since from the conductivity data Arrhenius plots can be drawn and from the slope of the natural logarithmic plots the activation energies can be calculated (see Section 3.2.2).

The proton conductivity of compound **59** under dry N₂ flux (0 % RH) is plotted in Figure 3.87. The pellet is first heated from RT to 160 °C, then cooled to RT and heated again. This is done in order to get rid of the possible water present in the sample. Proton conductivity is recorded during the three temperature cycles; however Figure 3.87 only reports the third cycle which corresponds to the intrinsic proton conductivity. The *Arrhenius* plot is almost linear in the experimental temperature ranges (proton conductivity increasing with temperature), indicating that one dominant proton conducting mechanism, with constant activation energy, is present in the material. From the slope of the Arrhenius plot, an activation energy of 128 kJ/mol is calculated. This value is almost the double than the value obtained for model compound **4** and PVPA. Thus it can be stated that in compound **59** protons have to attain higher energy levels than ions in **4** and PVPA have to do.

The maximum value of the proton conductivity for **59** is $5.3 \cdot 10^{-8}$ S/cm at 160 °C. This value is four orders of magnitude lower than that observed for **4** ($1.10^{-4.3}$ S \cdot cm $^{-1}$) and three orders of magnitude lower than this of an annealed PVPA sample ($\sim 1.10^{-5.5}$ S \cdot cm $^{-1}$).

It is known that compounds possessing low activation energy will present a fast proton transport and high conductivity. Hexakis[*p*-(*p*-phosphonatophenylethynyl)phenyl]benzene (**59**) presents an activation energy higher than hexakis(*p*-phosphonatophenyl)benzene (**4**), thus a slower proton transport yielding lower conductivity values.

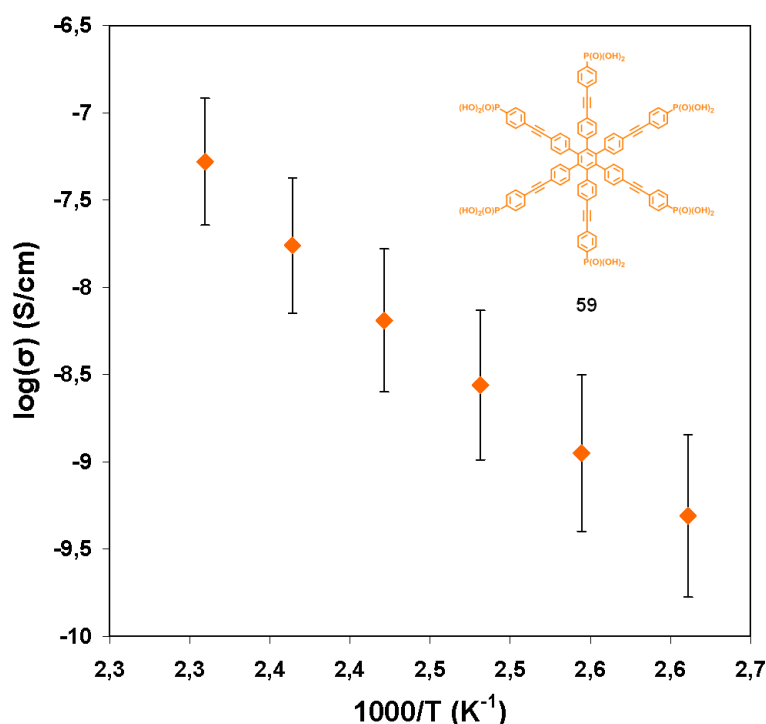


Fig. 3.87: *Arrhenius* plot of hexakis[*p*-(*p*-phosphonatophenylethynyl)phenyl]benzene (**59**) at 0 % RH (N₂ flux) and its corresponding error bar.

Proton conductivity measurements have also been performed at 15, 50 and 75 % RH and the corresponding activation energies have been calculated from the slope of the *Arrhenius* plots using the formula described in Section 3.2.2. Figure 3.88 displays the *Arrhenius* plots of compound **59** at the different RH and the corresponding error bars. It can be observed that the higher the humidity conditions applied, the higher the conductivity values obtained and the smaller the slope of the corresponding *Arrhenius* plot.

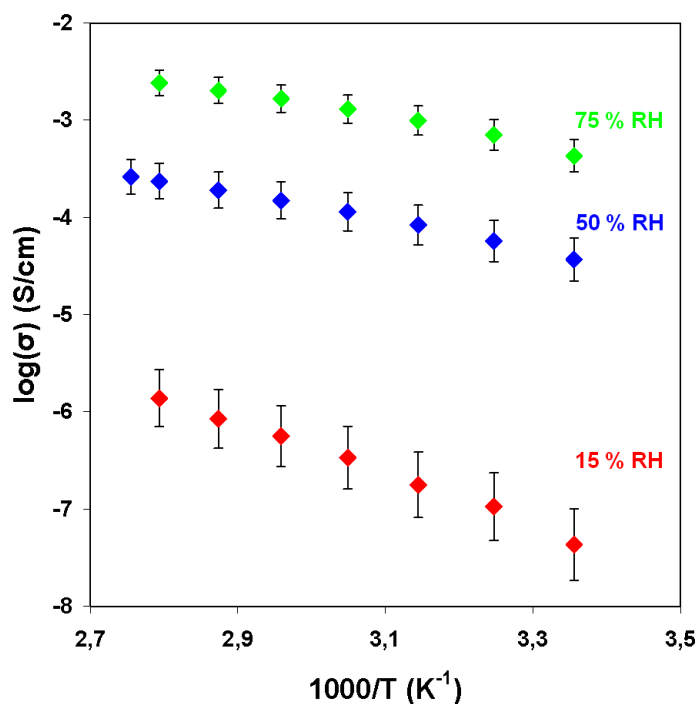


Fig. 3.88: *Arrhenius* plots of hexakis[*p*-(*p*-phosphonatophenylethynyl)phenyl]benzene (**59**) at 15, 50 and 75 % RH depicted in red, blue and green respectively and the corresponding error bars.

The *Arrhenius* plots calculated at the four different humidity conditions for compound **59** are presented in Table 3.11. By increasing the RH, the activation energy diminishes. The drop is very severe when passing from 0 to 15 % RH since the apparent activation energy decays from 128 to 50 kJ/mol. This indicates that when increasing the RH from 0 to 15 %, the energy barrier for the proton hopping highly decreases. At 15 % RH, the apparent activation energy of **59** is even lower than this of **4** (64.9 kJ/mol). A further increase of the RH from 15 to 50 % implies a decrease of the apparent activation energy however less pronounced than in the previous case. By increasing again the RH from 50 to 75 %, the apparent activation energy does not appreciably changes.

Thus it can be concluded that water plays an important role in the transport of protons through **59** since the energy barrier for proton hopping considerably decreases by placing the sample in a water-containing atmosphere. Contrary to model compound **4**, the effect is remarkable at low RH (15 %) since the activation energy decreases more than the half of its value at 0 % RH.

Table 3.11: Activation energies of hexakis[*p*-(*p*-phosphonatophenylethynyl)phenyl]benzene (**59**) at different humidity conditions.

RH (%)	Ea (± 5 %) (kJ/mol)
0	128
15	50
50	27
75	25

The effect of the RH on the proton transport properties of **59** has also been studied. As shown in Table 3.12, the proton conductivity is increased in three orders of magnitude upon increasing the RH from 15 to 50 %. A further increase of the RH to 75 % implies an increase of the conductivity in one order of magnitude.

Table 3.12: Proton conductivity of hexakis[*p*-(*p*-phosphonatophenylethynyl)phenyl]benzene (**59**) at 55 °C and different humidity conditions.

RH (%)	Proton conductivity (± 5 %) (S/cm)
15	$3.4 \cdot 10^{-7}$
50	$1.2 \cdot 10^{-4}$
75	$1.3 \cdot 10^{-3}$

From these impedance spectroscopy investigations on hexakis[*p*-(*p*-phosphonatophenylethynyl)phenyl]benzene (**59**) and hexakis[*p*-(*m*-phosphonatophenylethynyl)phenyl]benzene (**61**) it can be concluded that:

- Compounds **59** and **61** present a vehicle mechanism for proton transport;
- Under 1 bar H₂O atmosphere the low proton conductivity of **61** cannot only be explained by means of the decrease of the phosphonic acid density of the material compared to its homologous hexakis(*m*-phosphonatophenyl)benzene (**35**);

- The apparent activation energy of compound **59** is strongly affected by the water content of the atmosphere: by increasing the RH, the activation energy strongly decreases and the proton conductivity increases.

Water seems to play a decisive role in controlling the proton conducting properties of both compounds. Therefore, TGA, water uptake and crystallinity studies have been performed to elucidate the function and relevance of water molecules in the proton transport mechanism.

Both materials have been subjected to TGA experiments to determine their thermal stability. The TGA results presented in Figure 3.89 reveal that contrary to model compound **4** and sample **35**, both materials show a continuous mass loss until 900 °C. From 25 to 180 °C **59** presents a plateau and then starts to lose mass progressively, its mass loss at 900 °C being 56.2 wt %. On the contrary, **61** shows a shorter plateau from 25 to 120 °C and a smaller mass loss at 900 °C (45.2 wt %). In both cases, no unique degradation temperature can be determined since the decomposition is progressive.

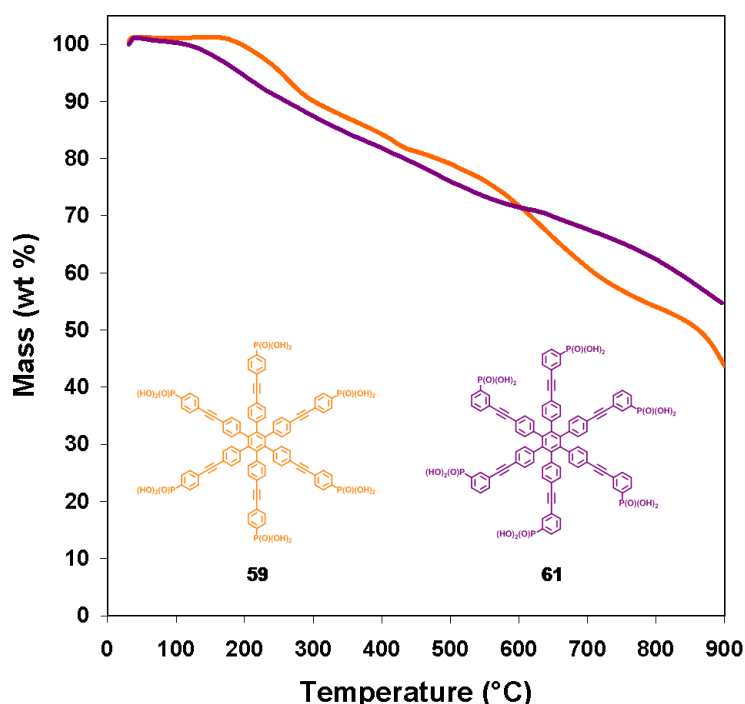


Fig. 3.89: TGA curves recorded at 10 K/min in N₂ of hexakis[*p*-(*p*-phosphonatophenylethynyl)phenyl]benzene (**59**) and hexakis[*p*-(*m*-phosphonatophenylethynyl)phenyl]benzene (**61**), depicted with orange and violet lines respectively.

For compounds **4** and **35**, there is a clear decomposition temperature which is attributed to the hydrophobic core and therefore the mass losses before this temperature can be correlated to water. On the contrary, this cannot be done for **59** and **61** due to the absence of degradation temperature.

Water uptake measurements have been performed at RT for hexakis[*p*-(*p*-phosphonatophenylethynyl)phenyl]benzene (**59**) and hexakis[*p*-(*m*-phosphonatophenylethynyl)phenyl]benzene (**61**). Figure 3.90 presents the water adsorption isotherms and the lambdas as a function of RH.

Surprisingly, the two compounds show very high water adsorption values as well as very high lambdas compared to their homologous materials **4** and **35**. The maximum water uptake of compound **59** is 50 wt % whereas this of **61** is slightly higher (56 wt %). **59** can take up a maximum of 45 water molecules whereas hexakis[*p*-(*m*-phosphonatophenylethynyl)phenyl]benzene 51.

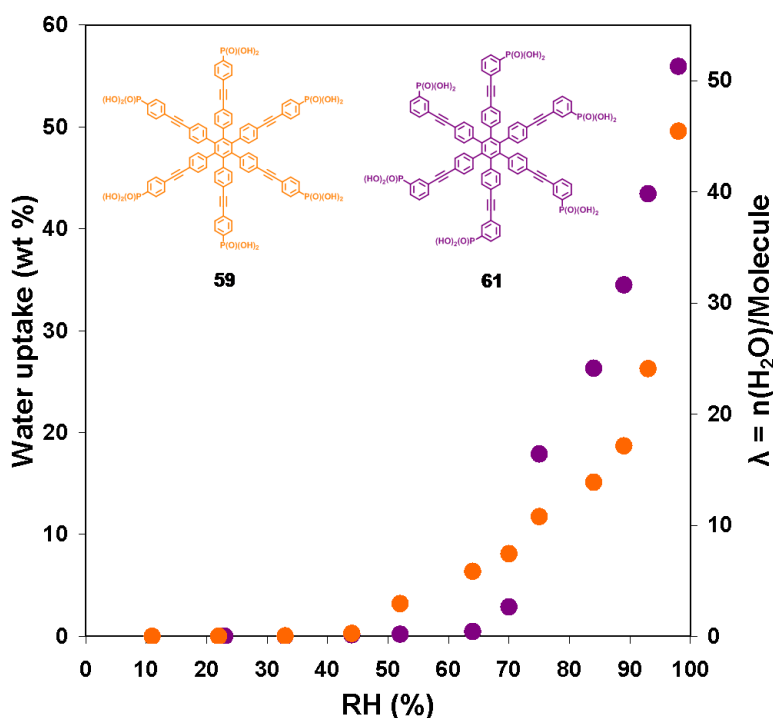


Fig. 3.90: Water adsorption isotherms and lambdas at RT of hexakis[*p*-(*p*-phosphonatophenylethynyl)phenyl]benzene (**59**) and hexakis[*p*-(*m*-phosphonatophenylethynyl)phenyl]benzene (**61**).

Like hexakis(*p*-phosphonatophenyl)benzene (**4**), compound **59** starts to take up water above 50 % RH. Its water adsorption curve is similar to a type III *van der Waals*

adsorption isotherm which is reversible and has an unlimited uptake.^[38] This unlimited uptake in this case does not indicate that the compounds are water soluble.

On the other hand hexakis[*p*-(*m*-phosphonatophenylethynyl)phenyl]benzene (**61**) first starts to adsorb water molecules at RH above 65 % and its adsorption curve, also of type III, is much steeper than this of **59**.

The water adsorption isotherms of these two compounds are similar to this of Nafion® 117, PVPA and phosphoric acid doped polybenzimidazole (PBI) membranes.^[28, 42] At 100 % RH, the water uptake values of **59** and **61** are ten times higher than these of the homologous compounds **4** and **35** and around five times higher than the value obtained for Nafion® 117 under the same experimental conditions.^[42]

Table 3.13: Water uptake at 100 % RH of different proton-conducting materials.

Compound	Water uptake at 100 % RH
Nafion® 117 ^[42]	~ 16
PVPA ^[28]	100
PBI-5.7H ₃ PO ₄ ^{[42]*}	n.a.
Hexakis(<i>p</i> -phosphonatophenyl)benzene 4	5.2
Hexakis(<i>m</i> -phosphonatophenyl)benzene 35	6.2
Hexakis[<i>p</i> -(<i>p</i> -phosphonatophenylethynyl)phenyl]benzene 59	50
Hexakis[<i>p</i> -(<i>m</i> -phosphonatophenylethynyl)phenyl]benzene 61	56

*5.7 mol H₃PO₄ per PBI unit

These water uptake experiments can be correlated to the above described proton conductivity measurements. Above 45 % RH, **59** starts to absorb water which is translated into a decrease of the activation energy and into an increase of the proton conductivity. In the case of **61**, a steep increase of the water uptake is observed above 70 % RH which can be correlated to a very pronounced decrease of the conductivity.

Interestingly, a higher water uptake in the case of phosphonic acid-containing small molecules is not equivalent to higher proton conductivity since **61** is the compound

which possesses both the higher water uptake and the lower proton conductivity under 1 bar H₂O atmosphere.

From these water uptake studies it can be concluded that both **59** and **61** must possess a structure in which the incorporation of water molecules is easier than in the case of **4** and **35**. Since the packing of **59** and **61** is unknown and can help to understand the role of water in the proton transport mechanism, crystallinity studies have been performed.

WAXS studies have been carried out at different temperatures and RH. Figure 3.91a displays the X-rays diffractograms of compound **59** recorded at 33 % RH at different temperatures. The material presents two narrow peaks at 3.4 and 2.9 Å and a broader peak at 2.1 Å. The absence of sharp reflection peaks more particularly in the region of low angles which could be attributed, as for compound **4**, to a columnar arrangement as well as the absence of peaks at other interatomic distances allow to deduct that on one side the material is less crystalline than compound **4** and on the other hand it doesn't stack into columns.

Figure 3.91b shows the X-ray diffractogram of hexakis[*p*-(*m*-phosphonatophenylethynyl)phenyl]benzene (**61**) recorded at 33 % RH and various temperatures. No sharp reflection peaks as for compound **59** can be noticed so it can be concluded that the material must be amorphous.

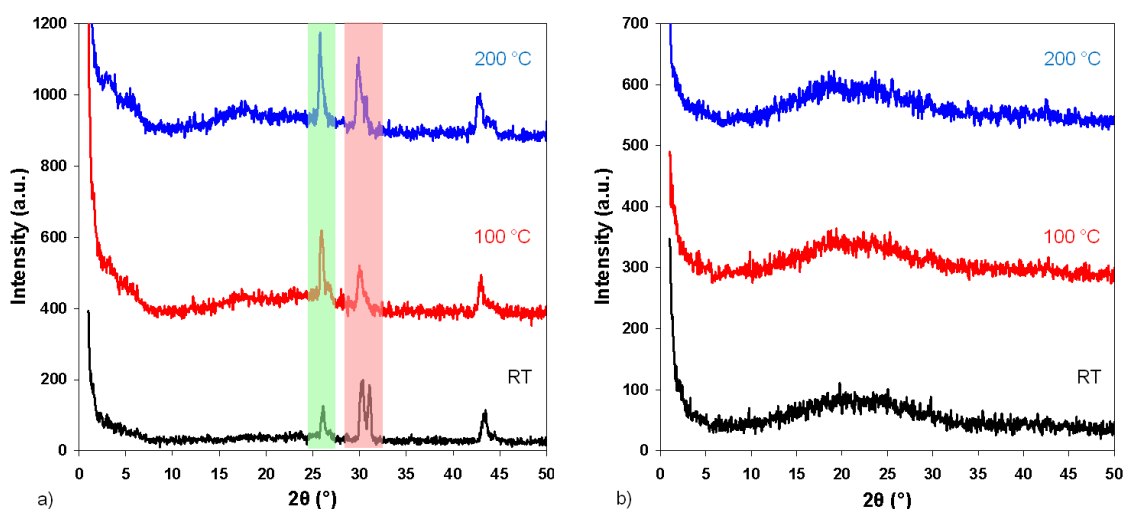


Fig. 3.91: X-ray diffractogram recorded at 33% RH at 25, 100 and 200 °C (black, red and blue respectively) of a) hexakis[*p*-(*p*-phosphonatophenylethynyl)phenyl]benzene (**59**) and b) hexakis[*p*-(*m*-phosphonatophenylethynyl)phenyl]benzene (**61**).

It has been tried to grow single crystals of compound **59** and **61** however all attempts have failed so far most probably due to the poor solubility of the materials in organic solvents which are volatile. Since the esters of the phosphonic acid-containing molecules are very well soluble in all kind of solvents, the crystallization procedure has been applied to compounds **58** and **60**. Of course, the crystal structure of the ester and the acid would not be the same but comparable since the benzene units have a strong tendency to pack and thus to segregate from the polar acid or ester functions. Moreover, in the case of hexakis(*p*-phosphonatophenyl)benzene (**4**) and its ester it was found that the ester also arranges into columns, the intracolumnar distance being identical to that of the acid (axis a: 0.8 nm) and the intercolumnar distances being bigger (axis b: 1.5 nm (ester) instead of 1.3 nm (acid) and axis c: 1.6 nm (ester) instead of 1.4 nm (acid)). Therefore, it is expected that a comparable result will be observed in the case of compound **59** and its ester.

Crystals of hexakis[*p*-(*p*-diethylphosphonatophenylethynyl)phenyl]benzene (**58**) suitable for X-ray diffraction analysis have been obtained from DCM. The molecules crystallize in the monoclinic space group $C 2/c$ and the cell parameters are $a = 40.259(2) \text{ \AA}$, $b = 24.1310(14) \text{ \AA}$ and $c = 21.4220(13) \text{ \AA}$. As can be seen in Figure 3.92b, the molecules organize into layers (axis a and b) which pack in a staggered fashion in the c axis direction. The distance between layers is 2.14 nm (axis c) as shown in Figure 3.92a whereas the intralayer distance is $\sim 2.5 \text{ nm}$.

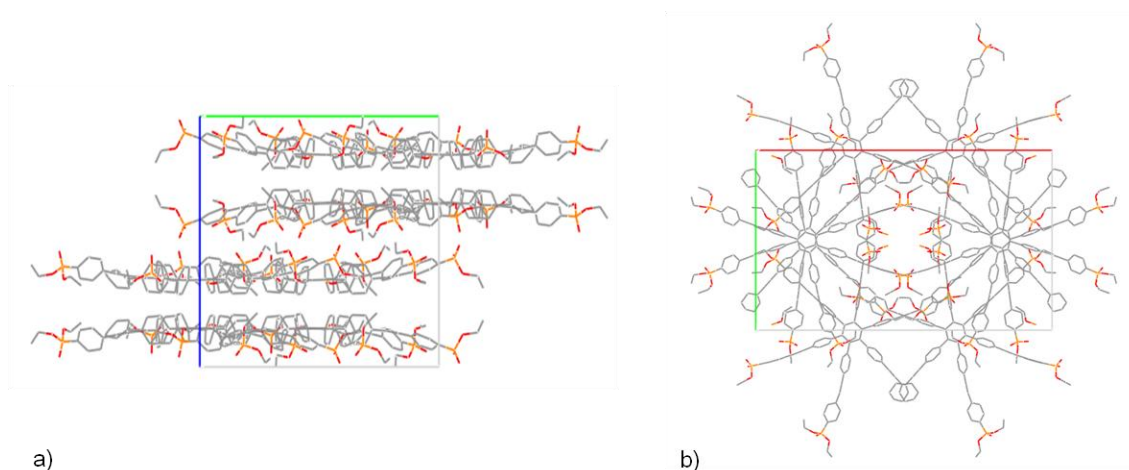


Fig. 3.92: Crystal structure of hexakis[*p*-(*p*-diethylphosphonatophenylethynyl)phenyl]benzene (**58**): a) view along axis a; b) view along axis c. H atoms are omitted for clarity.

It is expected that the crystal structure of **59** is similar to that of its ester, which is known. If this is true, then the molecules arrange into layers and both intra- and

interlayer distance should be around 2 nm. It has been demonstrated that the intercolumnar distance is around 1.4 nm in the case of **4** whereas for **59** the intralayer distance should be at least 2 nm. Figure 3.93b shows a schematic representation of the top view of the columns and the layers in case of compounds **4** and **59** respectively where the effect of the size expansion of the HPB periphery can be observed. The local concentration of protons in the system is decreased by increasing the size of the molecule which explains the lower conductivity of **59** with respect to **4**.

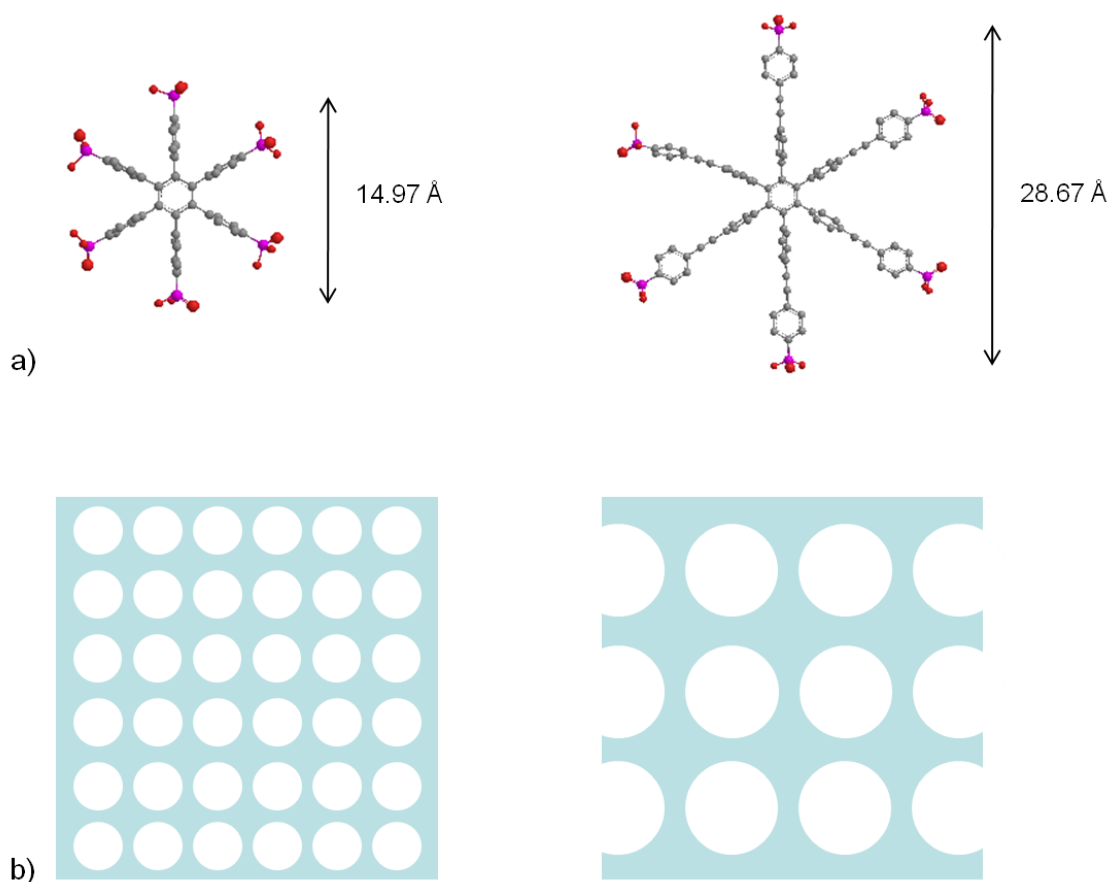


Fig. 3.93: a) Chemical structures of hexakis(*p*-phosphonatophenyl)benzene (**4**) and hexakis[*p*-(*p*-diethylphosphonatophenylethynyl)phenyl]benzene (**59**) in the gas phase obtained from ChemDraw 3D molecular-mechanics force field calculations (MMFF94) energy minimization. H atoms are omitted for clarity. The distance indicated is this between two opposite P atoms. b) Simplified schematic representation of the top view of the columns for compound **4** (left scheme) and of the top view of the layers for compound **59** (right scheme). The white circles represent the molecules.

The same argumentation can be used to explain the low conductivity of hexakis[*p*-(*m*-phosphonatophenylethynyl)phenyl]benzene (**61**) compared to hexakis(*m*-

phosphonatophenyl)benzene (**35**). Furthermore it has to be denoted that in contrast to its homologous compound **35**, **61** is completely amorphous which might have an influence on the proton transport properties of the material.

3.5.3 Hexakis[*p*-(3,5-bisphosphonatophenylethynyl)phenyl]benzene

In section 3.4.5 it has been explained that all attempts to obtain hexakis(3,5-bisdiethylphosphonatophenyl)benzene failed. Since the synthetic route above described to obtain **59** and **61** is successful, it is believed that it is possible to synthesize a molecule with a HPB-based hydrophobic core and twelve phosphonic acid functionalities via a *Sonogashira-Hagihara* coupling between tetraethyl 5-ethynyl-1,3-phenylenediphosphonate and hexaiodohexaphenylbenzene. Figure 3.93 describes the proposed synthetic procedure.

Tetraethyl 5-ethynyl-1,3-phenylenediphosphonate (**63**) is generated via a three synthetic route. Firstly, a protected acetylene group is introduced into the 3,5-dibromophenyl moiety by a *Sonogashira-Hagihara* coupling reaction between 1,3,5-tribromobenzene and trimethylsilylacetylene. Afterwards, the bromine groups in the obtained [(3,5-dibromophenyl)ethynyl]trimethylsilane (**47**) have to be replaced by phosphonic acid ester groups. In this case, the commonly applied palladium catalyzed cross-coupling reaction using diethyl phosphite and triethylamine is not successful and alternatively one has to use a nickel catalyzed *Michaelis-Arbusow* rearrangement. This is done using mesitylene as solvent, triethyl phosphite as reagent and NiBr₂ as catalyst. The desired product is obtained in 71 % yield. Subsequently, tetraethyl 5-[(trimethylsilyl)ethynyl]-1,3-phenylenediphosphonate (**62**) is deprotected using tetra-*n*-butylammonium fluoride to afford the acetylene that has to be coupled to hexaiodohexaphenylbenzene (**55**).

Unfortunately, the *Sonogashira-Hagihara* coupling reaction between tetraethyl 5-ethynyl-1,3-phenylenediphosphonate (**63**) and **55** is not successful. Firstly, it is tried to use the same synthetic conditions than for hexakis[*p*-(*p*-diethylphosphonatophenylethynyl)phenyl]benzene (**58**) and hexakis[*p*-(*m*-diethylphosphonatophenylethynyl)phenyl]benzene (**60**): Pd(PPh₃)₄, CuI, NEt₃, toluene, 60 °C, 12 h. Since these conditions do not afford the desired product, other bases like e.g. diisopropylamine have been used. Unfortunately, any attempts to introduce tetraethyl 5-ethynyl-1,3-phenylenediphosphonate (**63**) in the HPB-based hydrophobic core are unsuccessful.

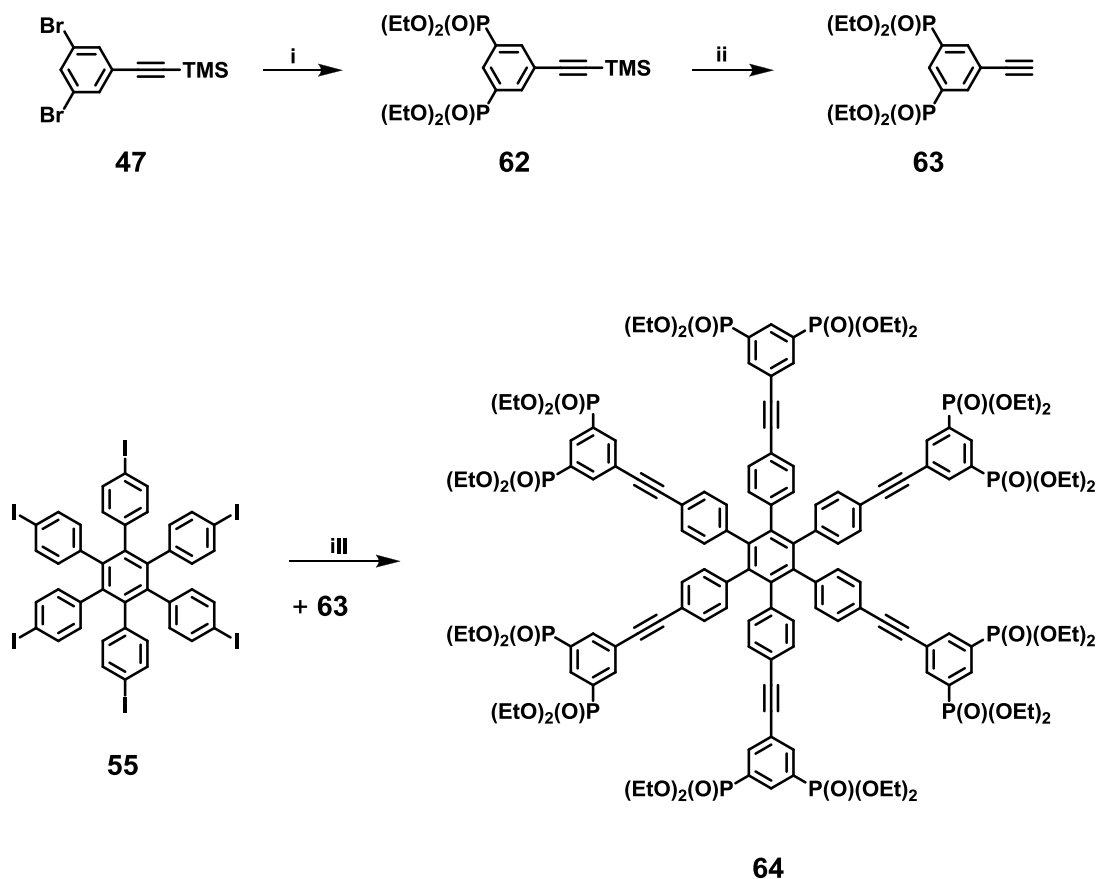


Fig. 3.94: Proposed synthetic route toward hexakis(*p*-(3,5-bisphosphonatophenylethynyl)phenyl)benzene (**64**): i) $\text{P}(\text{O})(\text{OEt})_3$, NiBr_2 , mesitylene, 160°C , 12 h, 71 %; ii) TBAF, RT, 15 min, 83 %; iii) $\text{Pd}(\text{PPh}_3)_4$, CuI , NEt_3 , toluene, 60°C , 12 h.

3.5.4 Summary

In this section, the impact of the extension of the size of the hydrophobic core on the proton transport properties of phosphonic acid based HPB derivatives has been studied. Therefore, hexakis[*p*-(*p*-phosphonatophenylethynyl)phenyl]benzene (**59**) and hexakis[*p*-(*m*-phosphonatophenylethynyl)phenyl]benzene (**61**) have been synthesized and characterized. Both compounds present a mechanism for proton transport which seems to be based on the diffusion of water molecules through the systems. From proton conductivity as well as water uptake studies it can be deduced that water plays an important role in proton transport.

Interestingly crystallinity studies have proved that **59** is semi-crystalline and that it most probably organizes into staggered layers whereas **61** is amorphous. On account of the bigger distance between molecules in a layer of compound **59** with respect to the intercolumnar distance of hexakis(*p*-phosphonatophenyl)benzene (**4**), there is a lower

positive charge concentration which might explain the differences in proton conductivity between the two systems.

Unfortunately, all attempts to obtain a HPB based molecule with twelve phosphonic acid functions have failed.

3.6 Conclusions

In this chapter it has been vividly demonstrated that phosphonic acid-containing small molecules can be used as solid state proton conductors in FC working at intermediate temperatures. The key point to reach high proton conductivity values is to have a self-organization of the molecules providing a continuous acidic phase for the transport of protons.

In particular, it is found that hexakis(*p*-phosphonatophenyl)benzene satisfies all critical requirements for a separator material:

- It exhibits high and constant proton conductivity (constant performance);
- It is stable during operation;
- It can be synthesized in gram-scale.

The material can be seen as an inverse proton-conducting cable since it is composed of a hydrophobic core and periphery consisting of the phosphonic acid functions contributing to the proton conductivity. In addition, it exhibits constant proton conductivity from 120 to 180 °C. This absence of any significant temperature dependence has been only observed before for a phosphonated fully aromatic polymer,^[31] which presents however slightly inferior proton conductivity values.

A comparative study of a series of compounds which possess various geometries and number of acidic moieties reveals that molecules which self-assemble into columns are the best candidates since a 3D continuous acidic phase is formed outside the columnar hydrophobic core. Furthermore from this study it is suggested that crystallinity is an important but not determining factor to achieve high proton conductivity values.

Focus then turned to ascertain the impact that the change from the *para* to the *meta* position, the introduction of alkyl chains and the replacement of phosphonic by sulfonic acid groups have on the proton conducting properties of solid state proton conducting-HPB molecules. The two first modifications conduct to products of lower conductivity. The *meta* substituted compound presents like hexakis(*p*-phosphonatophenyl)benzene

a constant proton conductivity above 150 °C . This is most probably due to the similar self-organization of the *meta* and *para* substituted molecules into columnar structures. The lower proton conductivity values of hexakis(*m*-phosphonatophenyl)benzene is a consequence of the possibilities that the acidic functions have to organize either above or below the plane of the phenyl ring thus creating areas of a lower concentration of phosphonic acid groups exhibiting lower conductivity. In the case of the HPB containing alkyl chains, it has been observed that in contrast to model compound **4** the vehicle mechanism is responsible for the transport of protons. It is also demonstrated in this study that the introduction of sulfonic acid groups produces a compound which due to its extreme hydrophilic character cannot be used as separator material in FC systems.

The impact the extension of the periphery of the HPB core has on proton conductivity has been explored in the last section of this chapter. It has been demonstrated that the obtained molecules present lower crystallinities than their homologous materials **4** and **35** and that the increase of the size of the periphery has a profound effect on proton conductivity. Compound **59** is semi-crystalline and most probably the molecules form layers with an intralayer distance higher than the intercolumnar distance found for compound **4**. Thus the local proton concentration is diminished which conducts to lower proton conductivity values. Material **61** is found to be completely amorphous and it is supposed that it organizes in the same way than **59**. The diminishment of the proton concentration might be the reason for its lower conductivity compared to **4** and **35** whereas the fact that it is amorphous might explain its lower conductivity with respect to **59**.

The motivation of this body of work has been to increase proton mobility by a novel concept consisting of the self-assembly and preorganization of phosphonic acid based small molecules. From the extensive study presented in this chapter, it can be deduced that the best candidate to be used as separator material for FC working at intermediate temperatures is hexakis(*p*-phosphonatophenyl)benzene. On the one hand, this material presents the appropriate self-assembly properties so that channels for the transport of protons can be created assuring a constant proton conductivity. On the other hand, it possesses the adequate concentration of phosphonic acid groups which provide high conductivity values.

3.7 Bibliography

- [1] M. Winter, R. J. Brodd, *Chem. Rev.* **2004**, *104*, 4245
- [2] K. D. Kreuer, *J. Membr. Sci.* **2001**, *185*, 29.
- [3] M. Schuster, T. Rager, A. Noda, K. D. Kreuer, J. Maier, *Fuel Cells* **2005**, *5*, 355
- [4] H. Steininger, M. Schuster, K. D. Kreuer, A. Kaltbeitzel, B. Bingöl, W. H. Meyer, S. Schauff, G. Brunklaus, J. Maier, H. W. Spiess, *Phys. Chem. Chem. Phys.* **2007**, *9*, 1764
- [5] B. Lafitte, P. Jannasch, *Advances in Fuel Cells* **2007**, *1*, 119
- [6] Y. Yang, S. Holdcroft, *Fuel Cells* **2005**, *5*, 171
- [7] J. Ding, C. Chuy, S. Holdcroft, *Adv. Funct. Mater.* **2002**, *12*, 389
- [8] Z. Shi, S. Holdcroft, *Macromolecules* **2005**, *38*, 4193
- [9] L. Rubatat, Z. Shi, O. Diat, S. Holdcroft, B. J. Frisken, *Macromolecules* **2006**, *39*, 720
- [10] T. B. Norsten, M. D. Guiver, J. Murphy, T. Astill, T. Navessin, S. Holdcroft, B. L. Frankamp, V. M. Rotello, J. Ding, *Adv. Funct. Mater.* **2006**, *16*, 1814
- [11] B. Lafitte, P. Jannasch, *Advanced Functional Materials* **2007**, *17*, 2823
- [12] J. C. J. Bart, *Acta Crysta.* **1968**, *B24*, 1277
- [13] M. D. Watson, A. Fechtenkotter, K. Müllen, *Chem. Rev.* **2001**, *101*, 1267
- [14] K. Kobayashi, T. Shirasaka, A. Sato, E. Horn, N. Furukawa, *Angew. Chem. Int. Ed.* **1999**, *38*, 3483
- [15] K. Kobayashi, T. Shirasaka, E. Horn, N. Furukawa, *Tetrahedron Lett.* **2000**, *41*, 89
- [16] K. Kobayashi, A. Sato, S. Sakamoto, K. Yamaguchis, *J. Am. Chem. Soc.* **2003**, *125*, 3035
- [17] K. E. Maly, E. Gagnon, T. Maris, J. D. Wuest, *J. Am. Chem. Soc.* **2007**, *129*, 4306
- [18] A. L. Schwan, *Chem. Soc. Rev.* **2004**, *33*, 218
- [19] A. K. Bhattacharya, G. Thyagarajan, *Chem. Rev.* **1981**, *81*, 415
- [20] M. Kastler, W. Pisula, R. J. Davies, T. Gorelik, U. Kolb, K. Müllen, *small* **2007**, *3* 1438
- [21] C. E. McKenna, M. T. Higa, N. H. Cheung, M. C. McKenna, *Tetrahedron Lett.* **1977**, *18*, 155
- [22] C. Carbonneau, R. Frantz, J. O. Durand, M. Granier, G. F. Lanneau, R. J. P. Corriu, *J. Mater. Chem.* **2002**, *12*, 540
- [23] R. E. Engel, *CRC Press, Inc., Boca Raton*, **1988**, 21.
- [24] S. M. Haile, C. R. I. Chisholm, K. Sasaki, D. A. Boysen, T. Uda, *Faraday Discussions* **2007**, *134*, 17.
- [25] K. D. Kreuer, S. J. Paddison, E. Spohr, M. Schuster, *Chem. Rev.* **2004**, *104*, 4637
- [26] N. Agmon, *Chem. Phys. Lett.* **1995**, *244*, 456
- [27] S. Hara, S. Takano, M. Miyayama, *J. Phys. Chem. B* **2004**, *108*, 5634
- [28] A. Kaltbeitzel, S. Schauff, H. Steininger, B. Bingöl, G. Brunklaus, W. H. Meyer, H. W. Spiess, *Solid State Ionics* **2007**, *178*, 469
- [29] A. L. Rusanov, D. Yu Likhatchev, K. Müllen, *Russ. Chem. Rev.* **2002**, *71*, 761
- [30] M. A. Hickner, H. Ghassemi, Y. S. Kim, B. R. Einsla, J. E. McGrath, *Chem. Rev.* **2004**, *104*, 4587
- [31] T. Rager, M. Schuster, H. Steininger, K. D. Kreuer, *Adv. Mater.* **2007**, *19*, 3317
- [32] T. Uma, M. Nogami, *Anal. Chem.* **2008**, *80*, 506
- [33] K. Funke, *Solid State Ionics* **1986**, *18*, 183
- [34] K. Funke, R. Hoppe, *Solid State Ionics* **1990**, *40*, 200
- [35] B. Bingöl, *Dissertation, Mainz* **2007**.
- [36] K. D. Kreuer, *Chem. Mater.* **1996**, *8*, 610
- [37] R. Büll, *Angew. Chem.* **1936**, *49*, 145
- [38] K. S. W. Sing, D. H. Everett, R. A. W. Haul, L. Moscou, R. A. Pierotti, J. Rouquerol, T. Siemieniewska, *Pure Appl. Chem.* **1985**, *57*, 603
- [39] T. A. Zawodzinski Jr, C. Derouin, S. Radzinski, R. J. Sherman, V. T. Smith, T. E. Springer, S. Gottesfeld, *J. Electrochem. Soc.* **1993**, *140*, 1041
- [40] C. C. Araujo, K. D. Kreuer, M. Schuster, G. Portale, H. Mendil-Jakani, G. Gebel, J. Maier, *Phys. Chem. Chem. Phys.* **2009**, *11*, 3305
- [41] M. Schuster, C. C. de Araujo, V. Atanasov, H. T. Andersen, K. D. Kreuer, J. Maier, *Macromolecules* **2009**, *42*, 3129

- [42] Q. Li, R. He, R. W. Berg, H. A. Hjuler, N. J. Bjerrum, *Solid State Ionics* **2004**, 168, 177.
- [43] A. J. Ryan, W. Bras, G. R. Mant, G. E. Derbyshire, *Polymer* **1994**, 35, 4537
- [44] D. Wasserfallen, *Dissertation, Mainz* **2006**.
- [45] M. Kastler, *Dissertation, Mainz* **2006**.
- [46] X. Feng, W. Pisula, L. Zhi, M. Takase, K. Müllen, *Angew. Chem. Int. Ed.* **2008**, 47, 1703
- [47] G. M. Sheldrick, *Acta Crystallogr., Sect. A: Found. Crystallogr.* **2007**, 64, 112
- [48] J. Beckmann, R. Rüttinger, T. Schwich, *Cryst. Growth Des.* **2008**, 8, 3271
- [49] G. B. Hix, V. Caignaert, J. M. Rueff, L. Le Pluart, J. E. Warren, P. A. Jaffres, *Cryst. Growth Des.* **2007**, 7, 208.
- [50] K. M. E. Jones, A. H. Mahmoudkhani, B. D. Chandler, G. K. H. Shimizu, *CrystEngComm* **2006**, 8, 303
- [51] M. Mehring, M. Schurmann, R. Ludwig, *Chem. Eur. J.* **2003**, 9, 837
- [52] M. Mehring, *Eur. J. Inorg. Chem.* **2004**, 2004, 3240.
- [53] P. C. Crofts, G. M. Kosolapoff, *J. Am. Chem. Soc.* **1953**, 75, 3379
- [54] P. C. Crofts, G. M. Kosolapoff, *J. Am. Chem. Soc.* **1953**, 75, 5738
- [55] T. Rager, M. Schuster, H. Steininger, K. D. Kreuer, *Adv. Mater.* **2007**, 19, 3317
- [56] M. Klapper, C. Hamciuc, R. Dyllick-Brenzinger, K. Müllen, *Angew. Chem. Int. Ed.* **2003**, 115, 4835
- [57] <http://www.britannica.com/EBchecked/topic/292789/ion-exchange-capacity>.
- [58] G. R. Goward, M. F. H. Schuster, D. Sebastiani, I. Schnell, H. W. Spiess, *J. Phys. Chem. B* **2002**, 106, 9322
- [59] B. S. Hickman, M. Mascal, J. J. Titman, I. G. Wood, *J. Am. Chem. Soc.* **1999**, 121, 11486
- [60] B. Faßbender, *Dissertation, Mainz* **2010**.
- [61] D. D. Laws, H. M. L. Bitter, A. Jerschow, *Angew. Chem. Int. Ed.* **2002**, 41, 3096
- [62] A. R. Grimmer, B. Blümich, *Solid State NMR I: Methods*. Springer Verlag: Heidelberg, Germany **1994**.
- [63] P. Lazzaretti, *Prog. Nuc. Mag. Reson. Spec.* **2000**, 36, 1
- [64] J. Gomes, R. B. Mallion, *Chem. Rev.* **2001**, 101, 1349
- [65] E. Brunner, U. Sternberg, *J. Phys. Chem. B* **1998**, 32, 21
- [66] C. G. Densmore, P. G. Rasmussen, G. R. Goward, *Macromolecules* **2005**, 38, 416
- [67] Y. J. Lee, B. Bingöl, T. Murakhtina, D. Sebastiani, W. H. Meyer, G. Wegner, H. W. Spiess, *J. Phys. Chem. B* **2007**, 111, 9711
- [68] H. W. Spiess, *Adv. Polym. Sci.* **1985**, 66, 23
- [69] M. Schuster, T. Rager, A. Noda, K. D. Kreuer, J. Maier, *Fuel Cells* **2005**, 5, 355
- [70] G. Ye, N. Janzen, G. R. Goward, *Macromolecules* **2006**, 39, 3283
- [71] R. K. Harris, L. H. Merwin, G. Hägele, *J. Chem. Soc., Faraday Trans. 1* **1989**, 85, 1409
- [72] S. A. Taylor, J. L. White, N. C. Elbaum, R. C. Crosby, G. C. Campbell, J. F. Haw, G. R. Hatfield, *Macromolecules* **1992**, 25, 3369
- [73] N. Yoza, N. Ueda, S. Nakashima, *Fresenius J. Anal. Chem.* **1994**, 348, 633
- [74] J. Zauhar, A. D. Bandrauk, K. D. Truong, A. Michel, *Synthesis* **1995**, 703
- [75] X. Feng, J. Wu, V. Enkelmann, K. Müllen, *Org. Lett.* **2006**, 8, 1145
- [76] V. R. Reichert, L. J. Mathias, *Macromolecules* **1994**, 27, 7015
- [77] M. V. Vasylyev, D. Astruc, R. Neumann, *Adv. Synth. Catal.* **2005**, 347, 39
- [78] S. R. Narayanan, S. P. Yen, L. Liu, S. G. Greenbaum, *J. Phys. Chem. B* **2006**, 110, 3942
- [79] H. Chihara, K. Nakatsu, *Bull. Chem. Soc. Jpn.* **1959**, 32, 903
- [80] A. J. Hailwood, S. Horrobin, *Trans. Faraday Soc.* **1946**, 42, 84.
- [81] S. P. Brown, *Prog. Nucl. Magn. Reson. Spectrosc.* **2007**, 50, 199
- [82] R. K. Harris, P. Jackson, H. M. Lawrence, B. S. Say, G. Hägele, *J. Chem. Soc., Faraday Trans. 1* **1988**, 84, 3649
- [83] C. Gervais, M. Profeta, V. Lafond, C. Bonhomme, T. Azais, H. Mutin, C. J. Pickard, F. Mauri, F. Babonneau, *Magn. Reson. Chem.* **2004**, 42, 445
- [84] P. A. Frey, *Magn. Reson. Chem.* **2001**, 39, S190
- [85] W. K. Rhim, D. P. Burum, D. D. Elleman, *J. Chem. Phys.* **1979**, 71, 3139
- [86] B. G. Pfrommer, F. Mauri, S. G. Louie, *J. Am. Chem. Soc.* **2000**, 122, 123
- [87] F. Jiang, A. Kaltbeitzel, W. H. Meyer, H. Pu, G. Wegner, *Macromolecules* **2008**, 41, 3081

-
- [88] F. Jiang, A. Kaltbeitzel, B. Fassbender, G. Brunklaus, H. Pu, W. H. Meyer, H. W. Spiess, G. Wegner, *Macromol. Chem. Phys.* **2008**, *209*, 2494
- [89] U. Akbey, S. Granados-Focil, E. B. Coughlin, R. Graf, H. W. Spiess, *J. Phys. Chem. B* **2009**, *113*, 9151
- [90] G. Brunklaus, S. Schauff, D. Markova, M. Klapper, K. Müllen, H. W. Spiess, *J. Phys. Chem. B* **2009**, *113*, 6674
- [91] B. Bingöl, W. H. Meyer, M. Wagner, G. Wegner, *Macromol. Rapid Commun.* **2006**, *27*, 1719
- [92] Q. Yang, M. P. Kapoor, S. Inagaki, *J. Am. Chem. Soc.* **2002**, *124*, 9694
- [93] J. G. Rodriguez, R. Martín-Villamil, I. Fonseca, *J. Chem. Soc., Perkin Trans. 1* **1997**, 1997, 945
- [94] H. Sakurai, Y. Nakadaira, A. Hosomi, Y. Eriyama, K. Hirama, C. Kabuto, *J. Am. Chem. Soc.* **1984**, *106*, 8315
- [95] W. Reppe, W. Schweckendiek, *J. Liebigs Ann.Chem.* **1948**, *560*, 104
- [96] D. H. Wu, B. H. Xu, Y. Z. Li, H. Yan, *Organometallics* **2007**, *26*, 4344
- [97] L. D. Field, A. J. Ward, *J. Organomet. Chem.* **2003**, *681*, 91
- [98] L. Yong, H. Butenschön, *Chemical communications* **2002**, *2002*, 2852
- [99] F. Montilla, T. Avilés, T. Casimiro, A. A. Ricardo, M. Nunes da Ponte, *J. Organomet. Chem.* **2001**, *632*, 113
- [100] M. S. Sigman, A. W. Fatland, B. E. Eaton, *J. Am. Chem. Soc.* **1998**, *120*, 5130
- [101] G. Hilt, S. Lueers, K. I. Smolko, *Org. Lett* **2005**, *7*, 251
- [102] G. Hilt, S. Lueers, K. Harms, *J. Org. Chem.* **2004**, *69*, 624
- [103] G. Hilt, K. I. Smolko, *Angew. Chem.* **2003**, *115*, 2901
- [104] G. Hilt, K. I. Smolko, *Angew. Chem. Int. Ed.* **2003**, *42*, 2795
- [105] G. Hilt, T. Vogler, W. Hess, F. Galbiati, *Chem. Commun.* **2005**, *2005*, 1474
- [106] G. Hilt, W. Hess, T. Vogler, C. Hengst, *J. Organomet. Chem.* **2005**, *690*, 5170
- [107] N. E. Schore, *Chem. Rev.* **1988**, *88*, 1081
- [108] J. P. Collman, J. W. Kang, W. F. Little, M. F. Sullivan, *Inorg. Chem.* **1968**, *7*, 1298
- [109] J. H. Hardesty, J. B. Koerner, T. A. Albright, G. Y. Lee, *J. Am. Chem. Soc.* **1999**, *121*, 6055
- [110] K. Kirchner, M. J. Calhorda, R. Schmid, L. F. Veiros, *J. Am. Chem. Soc.* **2003**, *125*, 11721
- [111] M. D. Watson, A. Fechtenkotter, K. Mullen, *Chem. Rev.* **2001**, *101*, 1267
- [112] H.-T. Chang, M. Jeganmohan, C.-H. Cheng, *Chem. Commun.* **2005**, 4955
- [113] V. Gandon, C. Aubert, M. Malacria, *Chem. Commun.* **2006**, 2209
- [114] G. Chouraqui, M. Petit, C. Aubert, M. Malacria, *Org. Lett.* **2004**, *6*, 1519
- [115] G. Hilt, C. Hengst, W. Hess, *Eur. J. Org. Chem.* **2008**, *2008*, 2293
- [116] Q. Zhang, P. Prins, S. C. Jones, S. Barlow, T. Kondo, Z. An, L. D. A. Siebbeles, S. R. Marder, *Org. Lett.* **2005**, *7*, 5019
- [117] Z. Wang, F. Dötz, V. Enkelmann, K. Müllen, *Angew. Chem. Int. Ed.* **2005**, *44*, 1247
- [118] R. Chinchilla, C. Nájera, *Chem. Rev.* **2007**, *107*, 874

4 Phosphonic Acid based Organic-Inorganic Hybrid Materials

4.1 Introduction

In contrast to the previous chapter in which the proton transport properties of hydrogen bonded networks of phosphonic acid groups have been investigated, this body of work focuses on exploring the use of phosphonated molecules and metal cations to obtain ionic networks with porous and crystalline properties. The objective of the present study is to produce highly microporous phosphonated open-framework structures which moreover present crystallinity (so that the regularity of the pore size is assured through the entire ionic network) since the combination of these two properties in phosphonated ionic networks still remains an open issue. In addition at the same time it is aimed to investigate whether a trisphosphonated organic molecule can be used as linker to obtain porous hybrid materials.

Commonly mesoporous metal phosphonates are produced by adapting the methodology employed for obtaining MCM-41^[1] and therefore using organic surfactant molecules as templates (MCM-type approach). An alternative procedure to obtain porous materials has been developed by *Dines et al.*^[2] It consists of forming inorganic layers of the metal and PO₃ groups and then cross-linking these layers with the alkyl or aryl groups and spacing these pillars with small phosphonate or phosphate ions.^[3-6] Among all known metal phosphonates, layered structures are predominant wherein aryl- or alkylphosphonate molecules are coordinated to the metal oxide layers.^[5, 7-9] Efforts have been made to prevent the formation of simple layers and create open-framework structures. *Vasylyev et al.* have prepared a mesoporous material constructed from a dendritic tetraphosphonate.^[10] The compound presents a surface area of 118 m²/g but is amorphous. In contrast, *Taylor et al.* have obtained a

crystalline copper based tetrahedral organophosphonate which exhibits low microporosity ($198 \text{ m}^2/\text{g}$).^[11] However, the combination of crystallinity and high microporosity in phosphonated open-framework structures still remains an open issue. Crystallinity is a very important property since it assures the regularity of the pore size through the entire ionic network.

Moreover, organic-inorganic hybrid materials are most exclusively composed of mono- and bisphosphonates linkers and the use of organic molecules possessing a higher number of phosphonic acid functions remains unexplored.

In this chapter it is dealt with these two concerns. In this body of work the concept of using a multi-functionalized phosphonic acid based molecule (1,3,5-tris(*p*-phosphonatophenyl)benzene) and tri- and tetravalent metal cations to produce by a non MCM-type approach (i.e., in the absence of surfactant) crystalline and microporous organic-inorganic hybrid materials of high specific surface areas is explored.

Firstly, the synthesis and characterization of the different phosphonated organic-inorganic hybrid materials are presented followed by a discussion in which models for pore formation are proposed (Section 4.7) and a conclusion. The characterization is divided into three parts:

- Structural characterization (Section 4.3): it comprises infrared spectroscopy, thermal analysis and solid-state NMR. The objective of this section is to prove the formation of the phosphonated hybrid materials and to elucidate their composition.
- Morphological characterization (Section 4.4): X-ray powder diffraction and electron microscopy allow the study of the degree of structural order and the microstructure of the solids respectively.
- Textural characterization (Section 4.5 and 4.6): the textural properties of porous materials such as surface area, total pore volume, microporosity and hydrophobicity are key factors for their application. The textural analysis is usually based on the investigation of physical adsorption of inert gases like nitrogen or krypton at 77K or argon at 87 K.^[12-14] In this work, nitrogen sorption at 77 K is used to determine the specific surface area, micropore volume and pore size distribution of the compounds. Moreover hydrogen sorption analyses have been performed to study the hydrogen storage capacity of the materials.

4.2 Synthesis

It has been tried to obtain organic-inorganic hybrid materials based on 1,3,5-tris(*p*-phosphonatophenyl)benzene using di- (copper and zinc), tri- (aluminum) and tetravalent (zirconium and tin) metals. The effect that the variation of several synthetic parameters has on the porous properties of the materials has been studied. The reaction time has been maintained identical in all experiments (3 days). Firstly, the role of the solvent has been determined. This has been done by using different solvents (DMSO or water) as well as solvent mixtures (DMSO/water mixtures) and afterwards studying their influences on the yield of the reaction and the porous properties of the obtained materials. Secondly, the influence of the temperature has been investigated by performing the reactions at 90, 150 and 200 °C. In addition, in the case of the materials synthesized using trivalent metals two different salts have been used ($\text{Al}(\text{NO}_3)_3 \cdot 9\text{H}_2\text{O}$ and $\text{Al}(\text{NO}_3)_3 \cdot 1\text{H}_2\text{O}$) whereas in the case of the other metals the same salt has been utilized for all the syntheses.

Solvothermal synthesis in Ace Glass pressure tubes has been used to produce all the desired materials. It has been reported in the literature^[15] that the washing procedure affects the textural properties of the materials. Thus for all samples the solvents have been eliminated by using the same procedure which consists on washing the sample three times with water and centrifugating it in order to remove the trapped solvent and then heating it in a vacuum oven during 12 h at 120 °C.

All attempts to synthesize organic-inorganic hybrid materials based on 1,3,5-tris(*p*-phosphonatophenyl)benzene in any of the test conditions described in Tables 4.1 to 4.3 have yielded to the obtainment of solid products. However, the yields of the reactions are very low (from 3 to 60 %) compared to the ones described in the literature.^[15] This is particularly true for the materials synthesized at 200 °C which present a very low yield and a dark color. Yields have been calculated by using the following formula:

$$\text{Yield } (\%) = \frac{\text{mass of the solid obtained}}{(\text{mass of the linker} + \text{mass of the salt})} \cdot 100$$

In order to determine the chemical stoichiometries of the compounds, elemental chemical analysis has been used. Unfortunately by this analytical technique only the amounts of C, H, S and N present in the sample can be obtained but the amounts of

metal and P remain unknown. Thus it is decided to use inductively coupled plasma mass spectrometry (ICP-MS). This analytical technique is highly sensitive and capable of the determination of a range of metals and several non-metals at concentrations below one part in 10^{12} (part per trillion). However, due to the insolubility of the organic-inorganic hybrid materials in aqueous as well as non-aqueous solutions, the amount of P and metal cannot be successfully determined by using ICP-MS.

All prepared compounds are reported in Tables 4.1 to 4.3.

Table 4.1: Synthetic conditions and resulting compounds for trivalent metal 1,3,5-tris(*p*-phosphonatophenyl)benzene.

Sample	Salt	Metal/R11 Metal/P(O)(OH) ₂	Solvent	T (°C)	Yield (%)	Chemical analysis (wt %)
M5-R11	Al(NO ₃) ₃ ·9H ₂ O	3.99/1 1.33/1	DMSO/H ₂ O 1/1	150	15	C = 46.58 H = 2.93 S = 0.00 N = 0.00
M6-R11	Al(NO ₃) ₃ ·9H ₂ O	3.99/1 1.33/1	DMSO/H ₂ O 1/1	200	23	C = 49.19 H = 2.85 S = 0.99 N = 0.00
M13-R11	Al(NO ₃) ₃ ·1H ₂ O	3.99/1 1.33/1	DMSO/H ₂ O 1/1	150	25	C = 46.24 H = 2.99 S = 1.57 N = 0.00
M14-R11	Al(NO ₃) ₃ ·9H ₂ O	3.99/1 1.33/1	H ₂ O	90	12	C = 43.94 H = 3.93 S = 0.00 N = 0.00

Table 4.2: Synthetic conditions and resulting compounds for divalent metal 1,3,5-tris(*p*-phosphonatophenyl)benzene.

Sample	Salt	Metal/R11 Metal/P(O)(OH) ₂	Solvent	T (°C)	Yield (%)	Chemical analysis (wt %)
M9-R11	Cu(NO ₃) ₂ ·3H ₂ O	6/1 2/1	H ₂ O	150	34	C = 24.66 H = 1.53 S = 0.00 N = 4.20
M22-R11	Cu(NO ₃) ₂ ·3H ₂ O	6/1 2/1	DMSO	150	13	C = 53.24 H = 4.245 S = 3.765 N = 0.00
M28-R11	Cu(NO ₃) ₂ ·3H ₂ O	6/1 2/1	DMSO/H ₂ O 1/1	200	26	C = 39.78 H = 2.53 S = 8.88 N = 0.00
M31-R11	Cu(NO ₃) ₂ ·3H ₂ O	6/1 2/1	H ₂ O	90	42	C = 37.82 H = 2.47 S = 7.29 N = 0.00
M10-R11	ZnCl ₂	6/1 2/1	H ₂ O	90	32	C = 44.63 H = 2.76 S = 0.00
M24-R11	ZnCl ₂	6/1 2/1	DMSO	150	34	C = 46.23 H = 3.23 S = 2.55
M25-R11	ZnCl ₂	6/1 2/1	DMSO/H ₂ O 1/1	150	27	C = 45.96 H = 1.96 S = 2.23
M29-R11	ZnCl ₂	6/1 2/1	DMSO/H ₂ O 1/1	200	18	C = 61.26 H = 3.69 S = 4.04
M32-R11	ZnCl ₂	6/1 2/1	H ₂ O	3/150	33	C = 63.61 H = 3.42 S = 3.27

Table 4.3: Synthetic conditions and resulting compounds for tetravalent metal 1,3,5-tris(*p*-phosphonatophenyl)benzene.

Sample	Salt	Metal/R11 Metal/P(O)(OH) ₂	Solvent	T (°C)	Yield (%)	Chemical analysis (wt %)
M11-R11	ZrOCl ₂ .8H ₂ O	3/1 1/1	DMSO	90	7	C = 27.48 H = 2.14 S = 0.00
M12-R11	ZrOCl ₂ .8H ₂ O	3/1 1/1	DMSO	150	5	C = 27.88 H = 2.73 S = 4.23
M15-R11	ZrOCl ₂ .8H ₂ O	3/1 1/1	H ₂ O	90	26	C = 28.36 H = 2.75 S = 0.00
M16-R11	ZrOCl ₂ .8H ₂ O	3/1 1/1	DMSO/H ₂ O 1/1	90	46	C = 28.02 H = 2.22 S = 0.58
M17-R11	ZrOCl ₂ .8H ₂ O	3/1 1/1	DMSO/H ₂ O 1/1	150	43	C = 31.79 H = 2.74 S = 0.71
M26-R11	ZrOCl ₂ .8H ₂ O	3/1 1/1	DMSO/H ₂ O 1/1	200	50	C = 32.11 H = 1.56 S = 9.05
M30-R11	ZrOCl ₂ .8H ₂ O	3/1 1/1	DMSO	200	79	C = 33.07 H = 3.34 S = 12.17
M7-R11	SnCl ₄ .5H ₂ O	6/1 2/1	H ₂ O/BuOH 1/1	150	41	C = 19.84 H = 1.43 S = 0.00
M8-R11	SnCl ₄ .5H ₂ O	6/1 2/1	DMSO/H ₂ O 1/1	150	3	C = 21.89 H = 1.86 S = 1.48
M20-R11	SnCl ₄ .5H ₂ O	6/1 2/1	DMSO	150	60	C = 18.99 H = 2.38 S = 4.77
M27-R11	SnCl ₄ .5H ₂ O	6/1 2/1	DMSO/H ₂ O 1/1	200	8	C = 34.52 H = 2.81 S = 4.18

4.3 Structural Characterization

In this section it is aimed to prove the formation of various non-covalent ionic networks composed of a trisphosphonated organic molecule and different metal cations. Therefore infrared spectroscopy and solid-state NMR techniques have been used. In addition, thermal analysis has also been employed since the thermal stability of the hybrid materials is also an important issue.

4.3.1 Infrared Spectroscopy

The *Fourier* transform infrared spectroscopy (FTIR) spectra have been recorded in transmission mode between 4000 and 500 cm^{-1} and are shown in Figures 4.1 to 4.3. The characteristic bands of organophosphorous compounds are shown in Table 4.4. It is expected that the bands corresponding to the OH groups as well as to P=O vibrations are not present in the organic-inorganic hybrid materials due to the ionic interactions between the phosphonic acid group and the different metals.

Table 4.4: Characteristic bands of organophosphorous compounds.^[16]

Group	Wavenumber (cm^{-1})
P-Phenyl	1440 (sharp)
P-O-P	970 – 910 (broad)
P(O)(OH)	2700 – 2560 (O-H in H bonds) (broad)
	1300 – 1180 (P=O) (sharp)

A typical FTIR spectrum of an organic-inorganic hybrid material comprising 1,3,5-tris(*p*-phosphonatophenyl)benzene as linker and aluminum as connector along with the spectrum of the starting material are shown in Figure 4.2. The spectrum of the product is consistent with the formation of a hydrated aluminum complex of phenylphosphonic acid. A significant change in the spectrum of the product is the disappearance of the typical frequency pattern of the phosphonic acid in the region of the OH stretching vibrations ($\sim 2700 \text{ cm}^{-1}$) indicated in green in Figure 4.2. The characteristic stretching of the P-Phenyl linkage is present at 1389 cm^{-1} along with other multiple modes involving the PO_3 group in both spectra. So it

may be concluded that the phenyl-PO₃ entity is retained in the new compound. However, the band located at 1138 cm⁻¹ in the spectrum of the starting material is missing in that of the product. This is strong evidence for the absence of the P=O double bond in the structure of the product.

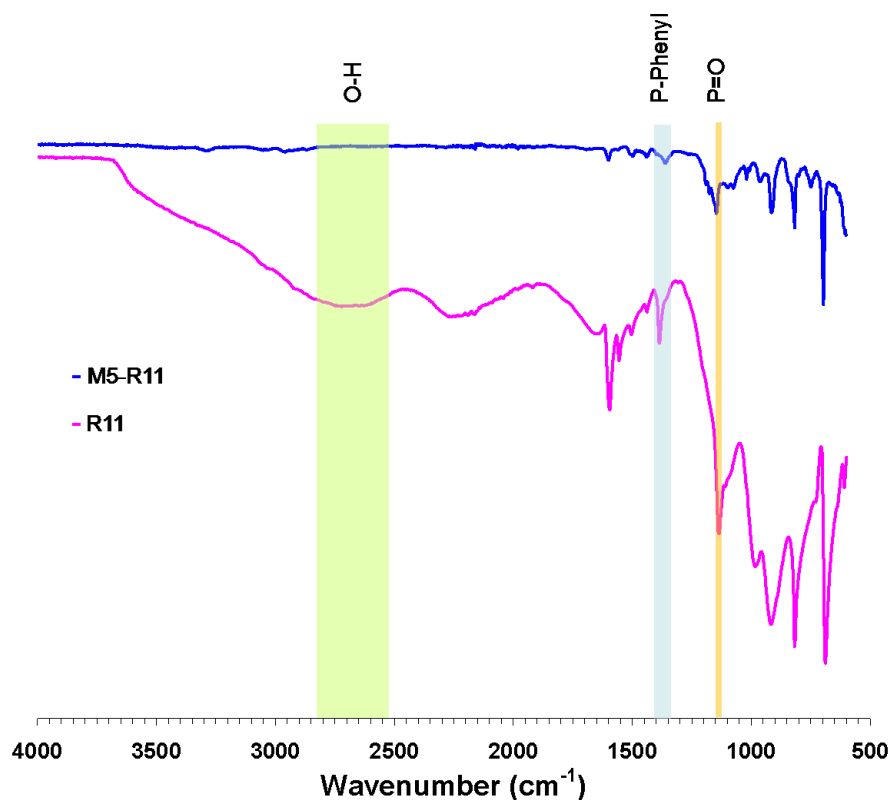


Fig. 4.2: FTIR spectra of R11 and M5-R11 (pink and blue lines respectively).

Figure 4.3 displays the IR spectra of aluminum trisphosphonates M5-R11 and M6-R11 synthesized in DMSO/H₂O at 150 and 200 °C respectively. In both spectra the bands characteristics of the phosphonic acid groups (O-H and P=O) are not present, indicating that in the materials a new bond between the metal and the acidic moiety has been formed. Significant differences can be observed between the two spectra. The characteristic stretching of the P-Phenyl linkage is present at 1388 cm⁻¹ in both spectra however the intensity is much lower in the case of M6-R11. Moreover, the P-O-P vibration characteristic of substances containing anhydride moieties can be observed in the case of M6-R11 as a broad peak (918 - 970 cm⁻¹). However, the case of M5-R11 two sharp peaks at 917 and 968 cm⁻¹ are observed. Thus it may be stated that the increase of the temperature from 150 to 200 °C conducts to a material which differs significantly from the one made at 150 °C.

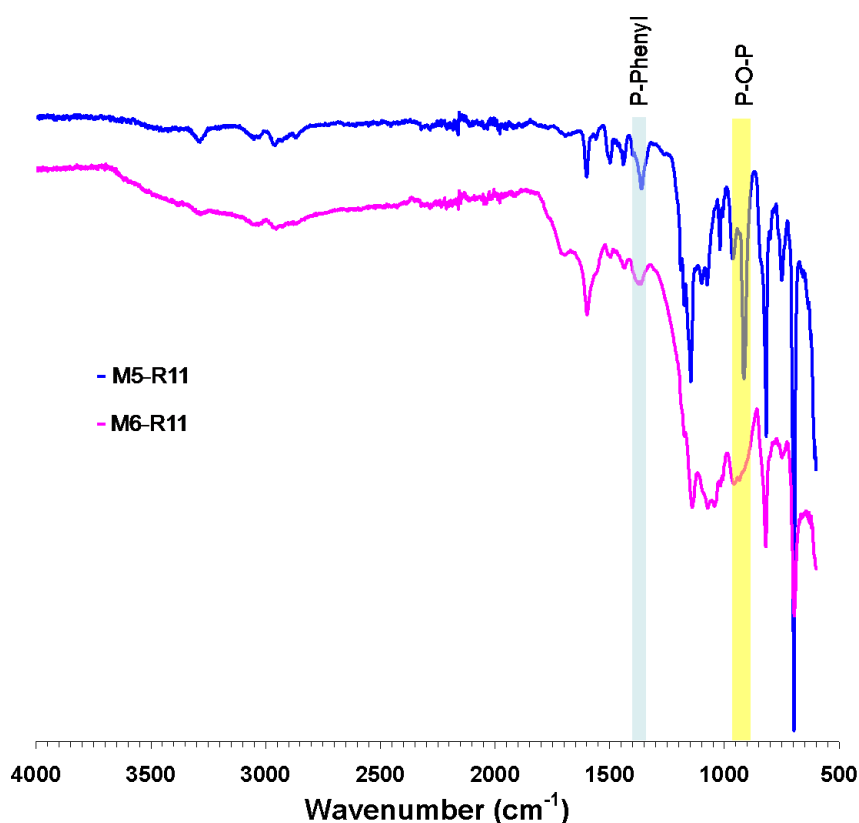


Fig. 4.3: FTIR spectra of M5-R11 and M6-R11: aluminum based compounds obtained under different synthetic conditions (blue and pink lines respectively).

Typical spectra of hybrid materials synthesized using 1,3,5-tris(*p*-phosphonatophenyl)benzene as linker and Cu, Zn, Al, Zr and Sn as connectors are shown in Figure 4.4. A common feature of the spectra is the absence of the typical frequency pattern of the phosphonic acid in the region of the OH and the P=O stretching vibrations (~ 2700 and 1140 cm^{-1} respectively) indicating that no free acidic moieties are present in the final compounds. The P-Phenyl stretching bands are range from 1350 to 1393 cm^{-1} . It may be concluded that the phenyl-PO₃ entity is retained in the new compounds.

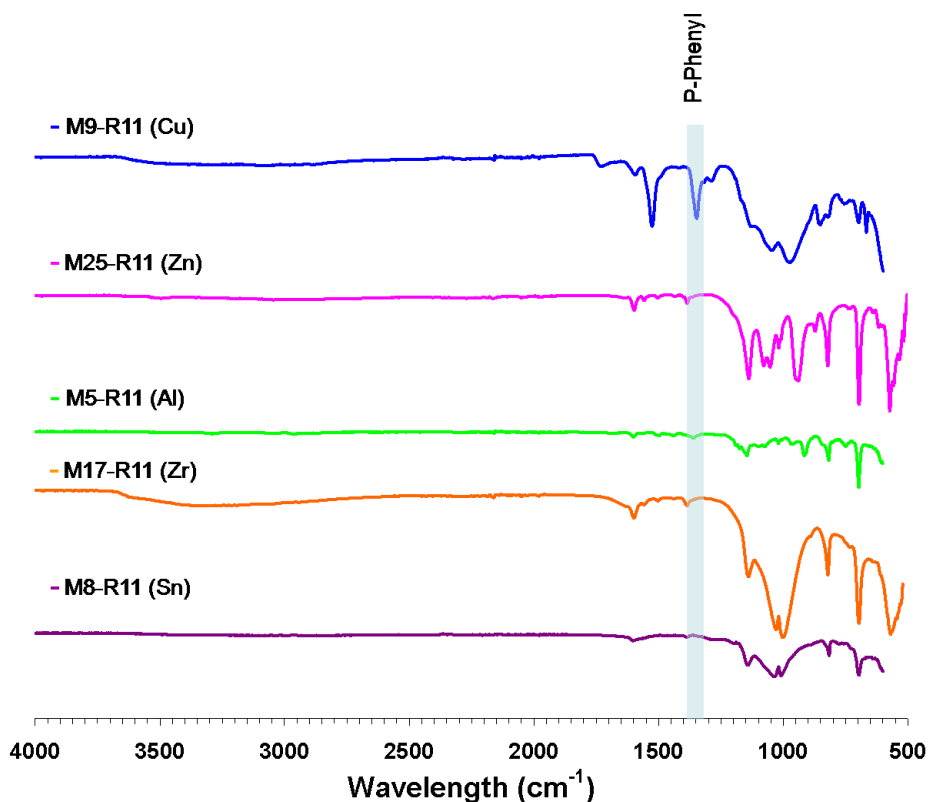


Fig. 4.4: FTIR spectra of organic-inorganic hybrid materials synthesized using Cu (M9-R11), Zn (M25-R11), Al (M5-R11), Zr (M17-R11) and Sn (M8-R11) as connectors under the same conditions depicted with blue, pink, green, orange and violet lines respectively.

4.3.2 Thermal Analysis

TGA experiments have been performed for all samples from RT to 900 °C to study the thermal properties of the compounds. For the sake of consistency, Figure 4.5 gives the TGA curves of the samples which are representative of each metal used as connector, i.e. five curves are represented. All samples exhibit more or less pronounced weight losses below 300 °C which correspond to trapped species such as H₂O, DMSO or EtOH. Moreover at these low temperatures some condensation water which comes from the hydroxyl groups of the linker is also lost. The weight loss which can be attributed to the combustion of the organic moieties ranges from 400 to 550 °C. Only M17-R11, the sample which has been made with zirconium, presents a continuous weight loss from 100 to 900 °C and no degradation temperature can be given. Generally speaking, these samples are thermally stable below 400 °C as only water and DMSO are lost below that temperature.

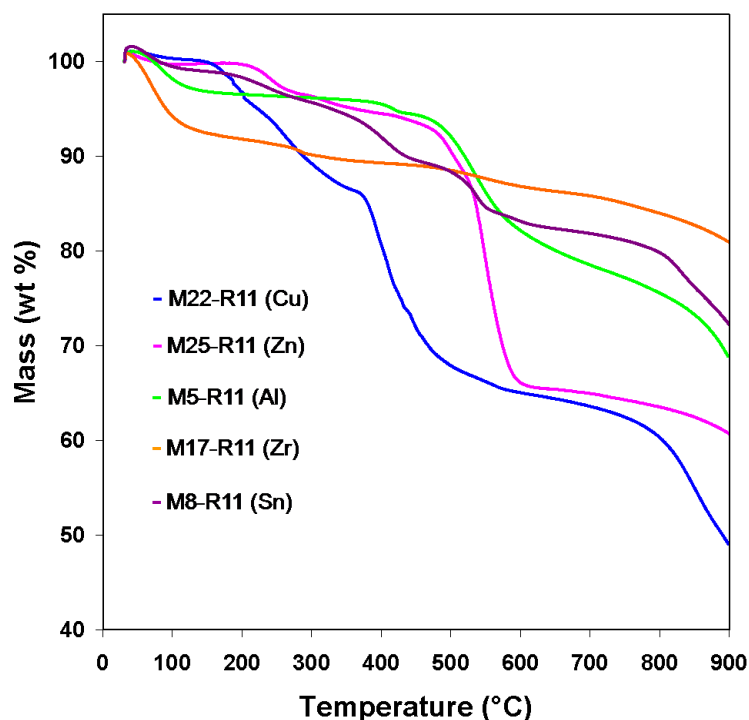


Fig. 4.5: TGA curves for M22-R11, M25-R11, M5-R11, M17-R11 and M8-R11 corresponding to Cu, Zn, Al, Zr and Sn-containing organic-inorganic hybrid materials depicted in blue, pink, green, orange and violet respectively.

4.3.3 Solid-State NMR

Solid-state NMR measurements have been performed in order to try to understand the structure of the metal trisphosphate solids obtained. Figure 4.6a shows the ^1H single pulse excitation (SPE) spectra of 1,3,5-tris(*p*-phosphonatophenyl)benzene (**12**) and M5-R11. In the spectrum of 1,3,5-tris(*p*-phosphonatophenyl)benzene, the two peaks at 10.0 and 7.0 ppm are assigned to hydroxyl and phenyl protons respectively. Since in the ^1H SPE spectrum of M5-R11 there is no signal around 10.0 ppm, it can be concluded that the hydroxyl units in the ionic network are deprotonated. The new signal at 4.3 ppm can be assigned to mobile residual water in the ionic network, since the signal vanishes in the ^1H double quantum spectrum (see Figure 4.7a). The ^1H NMR signal of the aromatic protons at 7.0 ppm shows significantly reduced chemical shift dispersion in M5-R11, indicating a more regular packing arrangement on the molecular level. The line shape of the much better resolved signal even suggests a splitting of signal into two peaks at 6.6 ppm and 7.1. Consistently, the ^{31}P $\{^1\text{H}\}$ CP MAS NMR of M5-R11 is significantly better resolved than the spectrum of compound **12** as can be seen in Figure 4.6b. Moreover, the broad ^{31}P signal at 18.2 ppm in the ^{31}P MAS

spectrum of 1,3,5-tris(*p*-phosphonatophenyl)benzene is shifted to 11.5 ppm in the spectrum of M5-R11.

The $^{13}\text{C}\{^1\text{H}\}$ CP NMR spectra confirm the trend indicated by the ^1H and ^{31}P spectra. As shown in Figure 4.6c, all carbon sites of M5-R11 are well resolved in the $^{13}\text{C}\{^1\text{H}\}$ CP-MAS spectrum and can be assigned according to the labeling given in Figure 4.6d in contrast to the broad and unspecific signals observed in the $^{13}\text{C}\{^1\text{H}\}$ CP-MAS spectrum of compound **12**.

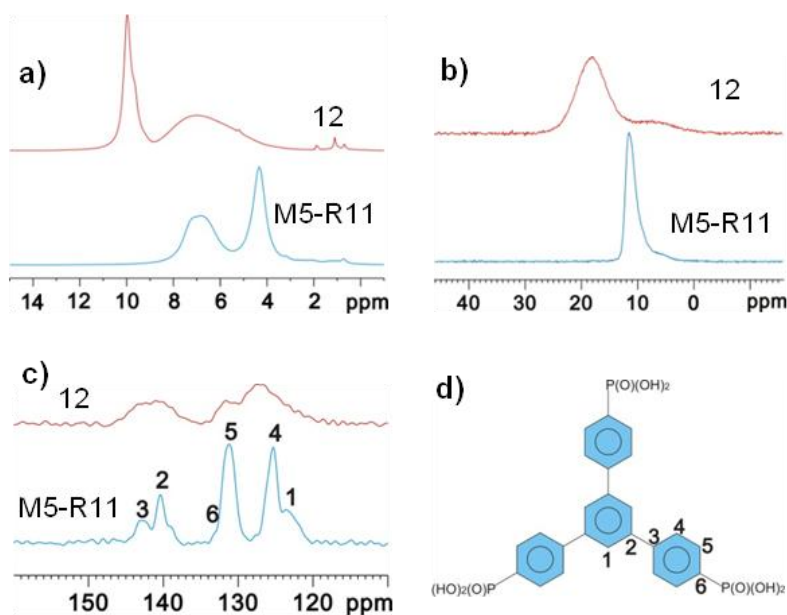


Fig. 4.6: a) ^1H SPE spectra of **12** and M5-R11 (red and blue curves respectively). b) $^{31}\text{P}\{^1\text{H}\}$ CP spectra of **12** and M5-R11 using 3ms contact time (red and blue curves respectively). c) $^{13}\text{C}\{^1\text{H}\}$ CP spectra of **12** and M5-R11 with contact time of 2ms (red and blue curves respectively). The nutation frequencies for all nuclei were set to 100 kHz. d) Molecular structure of **12**.

In conclusion, M5-R11 shows notably better resolution in all three different NMR experiments compared to TPB. These findings reveal that a well ordered material is formed after introducing Al^{3+} to 1,3,5-tris(*p*-phosphonatophenyl)benzene. In order to preliminarily demonstrate the structure of the aluminum sites in M5-R11, a ^{27}Al MAS spectrum has been recorded (see Figure 4.7a). The spectrum shows a single sharp peak at -10.7 ppm which is characteristic for aluminum sites with an octahedral oxygen environment.^[17-19]

The other ionic networks composed of aluminum have been also investigated by solid-state NMR spectra. Identical information has been obtained for all samples. Notably, the spectra of M14-R11 show better resolution due to its higher ordered structure.

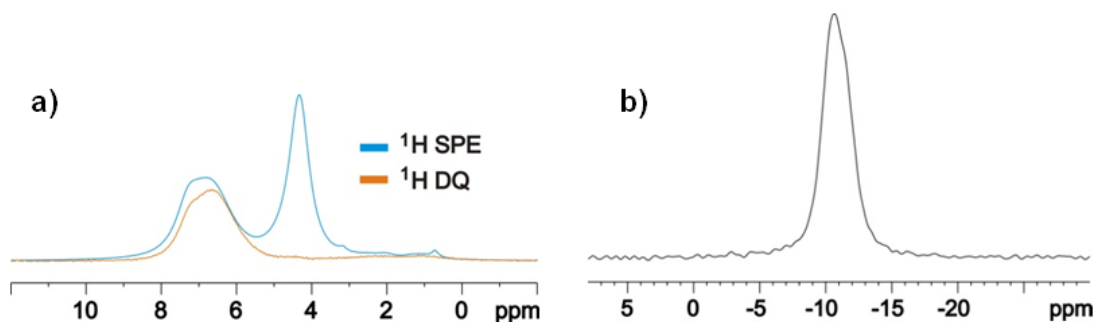


Fig. 4.7: a) ^1H SPE spectrum and ^1H BaBa DQ spectrum for M5-R11. The nutation frequency was set to 100 kHz. b) ^{27}Al MAS spectrum of M5-R11.

Figure 4.8 displays the ^1H MAS and the back-to-back (BaBa) ^1H 1D MAS NMR spectra of M12-R11 and M8-R11, examples of zirconium and tin based trisphosphonates respectively. The peak corresponding to the acidic protons observed in the spectrum of 1,3,5-tris(*p*-phosphonatophenyl)benzene at around 11 ppm shown in Figure 4.6a is not present in the case of M12-R11 and M8-R11, thus it can be stated that the samples do not contain free acidic protons. In the BaBa ^1H 1D MAS NMR spectra of the solids, the signal at around 6 ppm for M12-R11 and M8-R11 has disappeared. These signals can be assigned to water present in the samples which contains mobile protons that do not interact with others.

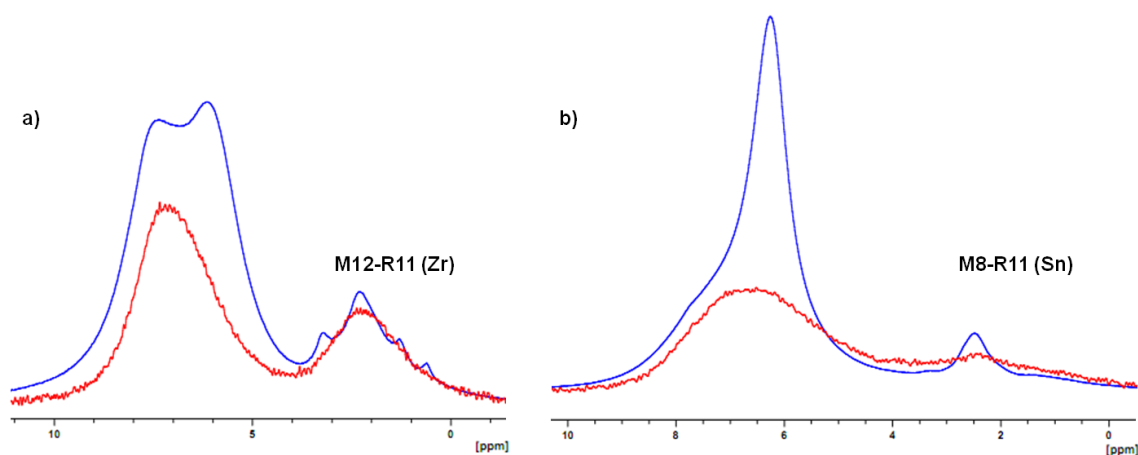


Fig. 4.8: Solid state ^1H MAS spectra (blue line) and BaBa ^1H 1D MAS spectra (red line) recorded at 25 KHz of a) M12-R11 (Zr) and b) M8-R11 (Sn).

4.4 Morphology Characterization

The study of the degree of structural order of the materials is a very important issue since it is aimed to obtain crystalline solids so that in the case they also present porous properties, the regularity of the pores can be assured. X-ray powder diffraction has been used to analyze the different samples and to determine whether they are amorphous or crystalline. Moreover, electron microscopy has been applied to characterize the microstructure of the samples including some insights about the particle sizes and shapes.

4.4.1 X-Ray Analysis

Since no single crystals are formed during the solvothermal reaction, X-ray powder diffraction patterns have been recorded for all samples in order to identify whether the ionic networks are crystalline or amorphous and whether the type of metal plays a role in obtaining a crystalline solid. The distance d between atomic layers (in Angstroms Å) in a crystal can be calculated using *Bragg's law* described in Section 3.2.5.

Figure 4.9a shows the X-ray powder diffraction pattern of copper based organic-inorganic hybrid materials. All compounds are amorphous since no diffraction peaks are observed in the pattern. Only in the case of M31-R11 a reflection at 17.8 Å is present.

The X-ray powder diffraction patterns corresponding to zinc based hybrid materials are displayed in Figure 4.9b. The diffraction pattern of ZnCl_2 is shown as comparison. From the five synthesized materials, three can be considered as amorphous due to the absence of diffraction peaks: M10-R11, M29-R11 and M32-R11. The other two materials are semicrystalline since they present peaks in the region of 20.1 to 8.1 Å and at higher angles, i.e. smaller distances. The peaks due not correspond to the reflections observed for ZnCl_2 , so it can be deduced that the salt has been completely washed out during the preparation of the compounds and that it does not contribute to the diffraction patterns of M24-R11 and M25-R11.

Interestingly, these two compounds have been synthesized at 150 °C during three days in DMSO and DMSO/H₂O for M24-R11 and M25-R11 respectively. M32-R11, which is amorphous, has also been obtained at 150 °C but using H₂O as solvent. It can therefore be deduced that the temperature and the solvent play an important role and that the use of DMSO and 150 °C might be decisive to obtain a crystalline material.

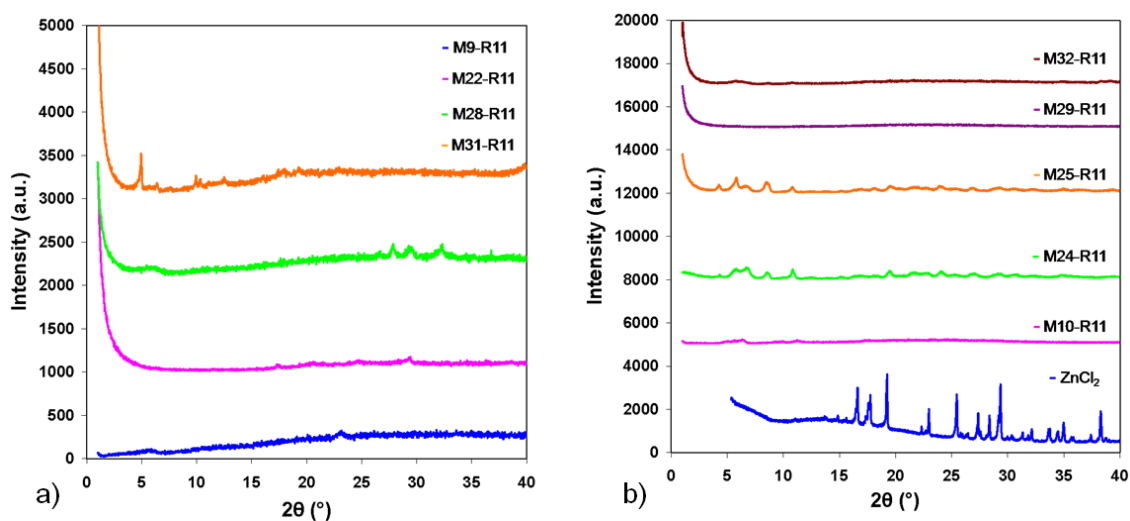


Fig. 4.9: a) X-Ray powder diffraction patterns of copper based organic-inorganic hybrid materials having 1,3,5-tris(*p*-phosphonatophenyl)benzene as linker. From the bottom to the top: M9-R11, M22-R11, M28-R11 and M31-R11. b) X-Ray powder diffraction patterns of zinc based organic-inorganic hybrid materials having 1,3,5-tris(*p*-phosphonatophenyl)benzene as linker. From the bottom to the top: ZnCl₂, M10-R11, M24-R11, M25-R11, M29-R11 and M32-R11.

The X-ray powder diffraction patterns of the aluminum based hybrid materials are shown in Figure 4.10. The diffraction patterns of R11 and Al(NO₃)₃·9H₂O are shown as comparison. Excepting M6-R11, all Al based compounds display two narrow diffraction peaks in the small angle region. M13-R11 and M14-R11 show more narrow peaks at higher angles indicating higher crystallinities and a semicrystalline nature of the products. Notably in the case of M14-R11 the two peaks at low angle are split. In all cases, the diffraction peaks do not correspond to the characteristic peaks of the salt used during the synthesis thus the latter has been completely washed out and does not contribute to the diffraction pattern of the hybrid materials. It seems that products obtained at lower reaction temperature (M14-R11) are more crystalline than those obtained at higher reaction temperatures (M6-R11).

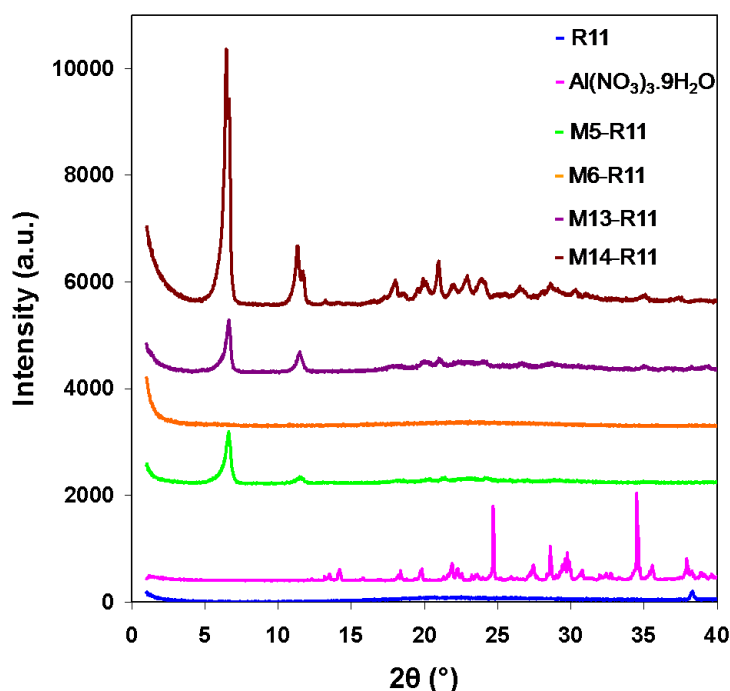


Fig. 4.10: X-Ray powder diffraction patterns of aluminum based organic-inorganic hybrid materials having 1,3,5-tris(*p*-phosphonatophenyl)benzene as linker. From the bottom to the top: 1,3,5-tris(*p*-phosphonatophenyl)benzene (**12**), $\text{Al}(\text{NO}_3)_3 \cdot 9\text{H}_2\text{O}$, M5-R11, M6-R11, M13-R11 and M14-R11.

The two characteristic distances at low angle of the aluminum-containing solids are reported in Table 4.5. The first diffraction peak ranges between 13.3 and 13.6 Å whereas the second between 7.5 and 7.8 Å.

Table 4.5: Characteristic distances at low angles of the aluminum based compounds from the X-ray powder diffraction patterns. M6-R11 is omitted because no reflections are observed.

Compound	First distance (Å)	Second distance (Å)
M5-R11	13.3	7.5
M13-R11	13.3	7.6
M14-R11	13.6	7.8

As reported in the literature,^[9, 20-24] the general trend for zirconium and aluminum bisphenyldiphosphonates is the formation of two-dimensional pillared structures with the organobisphosphonate unit linking adjacent inorganic sheets (see Figure 4.12). The

porosity found in these materials can be explained by a model derived from that earlier proposed by *Clearfield* et al. for zirconium bisphenyldiphosphonates.^[4, 9] According to this model, schematically depicted in Figure 4.11, parallel inorganic $M(\text{PO}_3)_2$ -layers would be connected/cross-linked by the bisphenyldiphosphonate groups. However, some phosphonate groups could remain protonated and so they do not participate in the bonding to adjacent inorganic layers. This linkage would result in layers of unequal length crosslinked by the organic groups, with some biphenyl moieties and fluoride anions which are only bonded to a single layer.

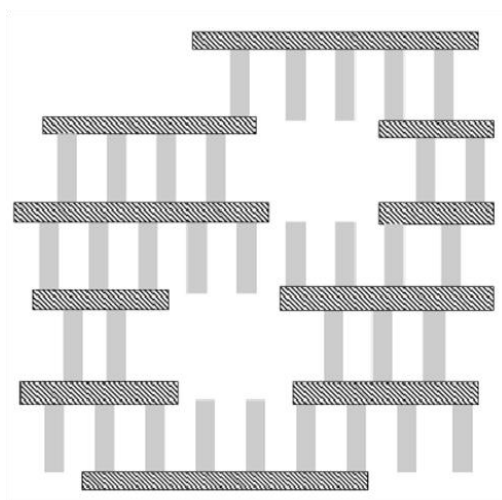


Fig. 4.11: Schematic drawing of how micropores may be formed in the zirconium and aluminum bisphenyldiphosphonates. The gray rectangles represent the biphenyl pillars and the horizontal striped bars are the inorganic layers. The biphenyl groups bounding the pore are bonded to the layers through only one phosphonate group.^[9]

In the case of zirconium based materials, if biphenyl is used as pillar then an interlayer spacing of $\sim 14 \text{ \AA}$ is found in the X-ray powder diffraction pattern whereas if terphenyl is used as linker the interlayer distance is found to be $\sim 18 \text{ \AA}$.^[9] Therefore it is expected that if 1,3,5-tris(*p*-phosphonatophenyl)benzene is a pillar and Al forms the inorganic layers the interlayer distance would be between 14 and 18 \AA since the height of the molecule is between this of biphenyl-4,4'-diyldiphosphonic acid and (*p,p'*-terphenyl-4,4''-diyl)bisphosphonic acid as shown in Figure 4.12.

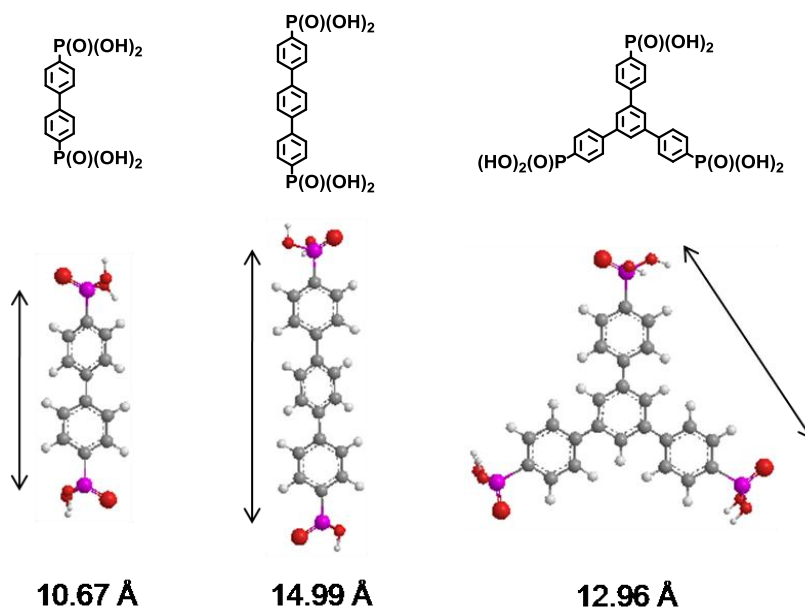


Fig. 4.12: Chemical structures of biphenyl-4,4'-diylbisphosphonic acid, (*p,p'*-terphenyl-4,4''-diyl)bisphosphonic acid and 1,3,5-tris(*p*-phosphonatophenyl)benzene (top) and their structures in the gas phase obtained from ChemDraw 3D molecular-mechanics force field calculations (MMFF94) energy minimization. The distance indicated is this between two opposite P atoms.

However the values obtained for the aluminum trisphenyltrisphosphonates M5-R11, M13-R11 and M14-R11 (between 13.3 and 13.6 Å) are slightly lower than those found for aluminum bisphenyldiphosphonates (between 13.8 and 14 Å) indicating that a layered structure in which the trisphenylbenzene cores are the pillars between the $\text{Al}(\text{PO}_3)_2$ -layers is not a model that fits with the X-ray powder diffraction pattern. Moreover in the X-ray diffraction pattern of layered structures the second diffraction peak usually corresponds to the half of the interlayer distance.^[25] Since this is not the case for the aluminum based trisphosphonate materials, it can therefore be stated that a layered structure cannot be proposed in this case.

An alternative model, schematically depicted in Figure 4.13, can be proposed to explain the X-ray powder diffraction pattern of the aluminum based organic-inorganic hybrid materials which contain 1,3,5-tris(*p*-phosphonatophenyl)benzene as linker. It corresponds to the formation of a crystalline open-framework with a hexagonal packing of pores. Two trivalent cation Al^{3+} are coordinated to three phosphonic acid groups to assure electroneutrality so that a hexagonal lattice is formed (Figure 4.13b). This is possible on the one side due to the trivalent character of the metal and on the other side to the trivalent functionality of the linker and its triangular geometry.

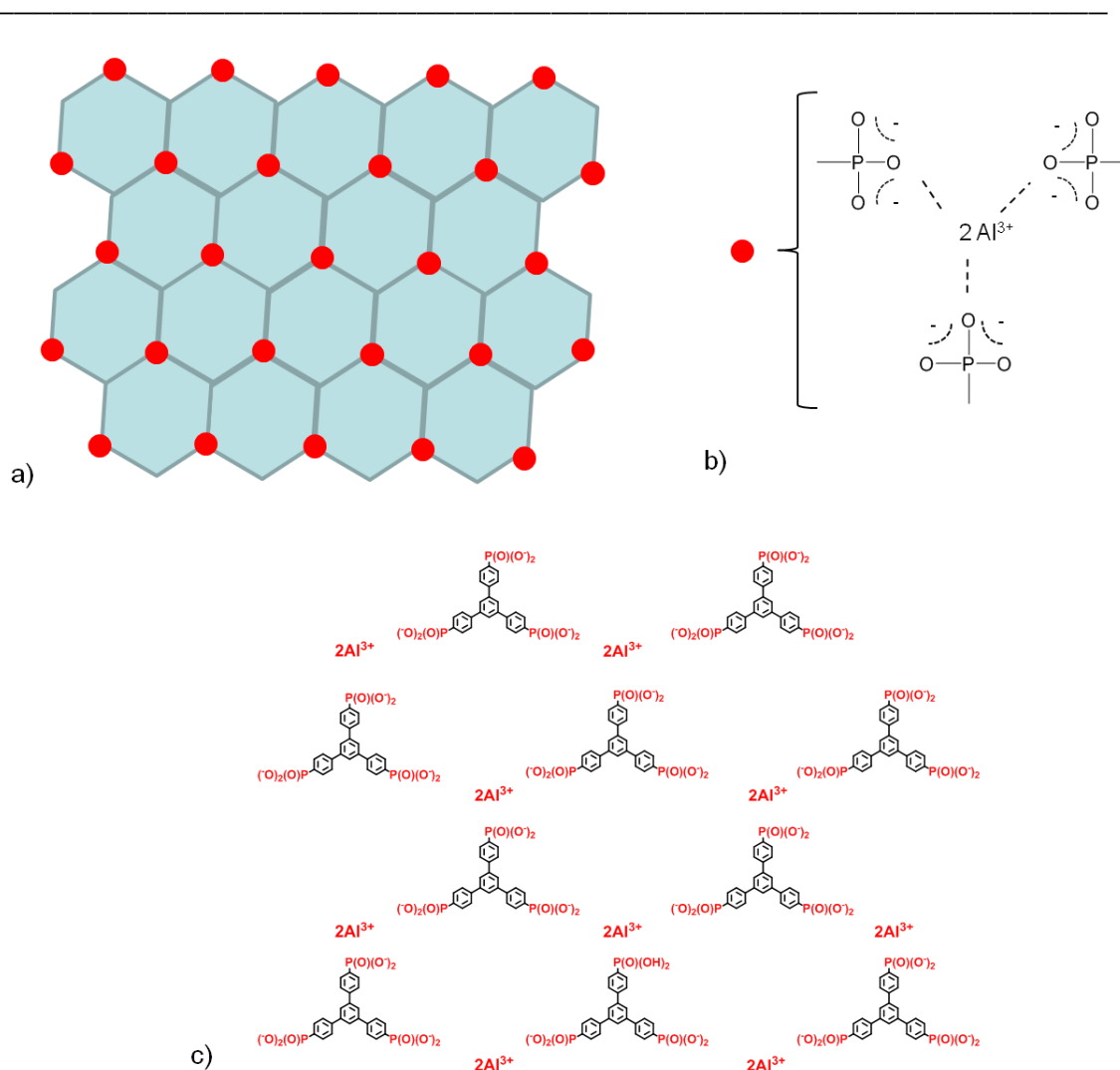


Fig. 4.13: a) Schematic representation of the hexagonal lattice composed of 1,3,5-tris(*p*-phosphonatophenyl)benzene and aluminum, the red dots represent the Al-phosphonic acid interactions b) and the grey bars the trisphenylbenzene core. c) Chemical representation of the model.

A geometry optimization of the proposed sheet-like structure has been carried out by Dr. Enkelmann, MPI-P in Mainz/Germany, to try to index the X-ray pattern which is shown in Figure 4.14b. For simplification the model has been made with only one of the two Al³⁺ cations needed to have electroneutrality and phosphonate groups with two instead of three O atoms. The resulting periodicities (for example, the void-to-void distance) has been used to assemble a hexagonal unit cell ($a = 17.93 \text{ \AA}$, $b = 31.05 \text{ \AA}$), while the layer distance between the sheets has been fixed at 3.6 \AA (axis *c*). An eclipsed AAA structure, in which the atoms of each layer are placed above their analogues in the next layer with P6/mmm symmetry, is found to be very close to the experimental structure (see Figure 4.14a). Excepting an adjustment of the lattice

parameters, the pattern of the simplified model corresponds almost perfectly with this of M14-R11 suggesting that the aluminum based trisphosphonate compounds organize in hexagonal lattice.

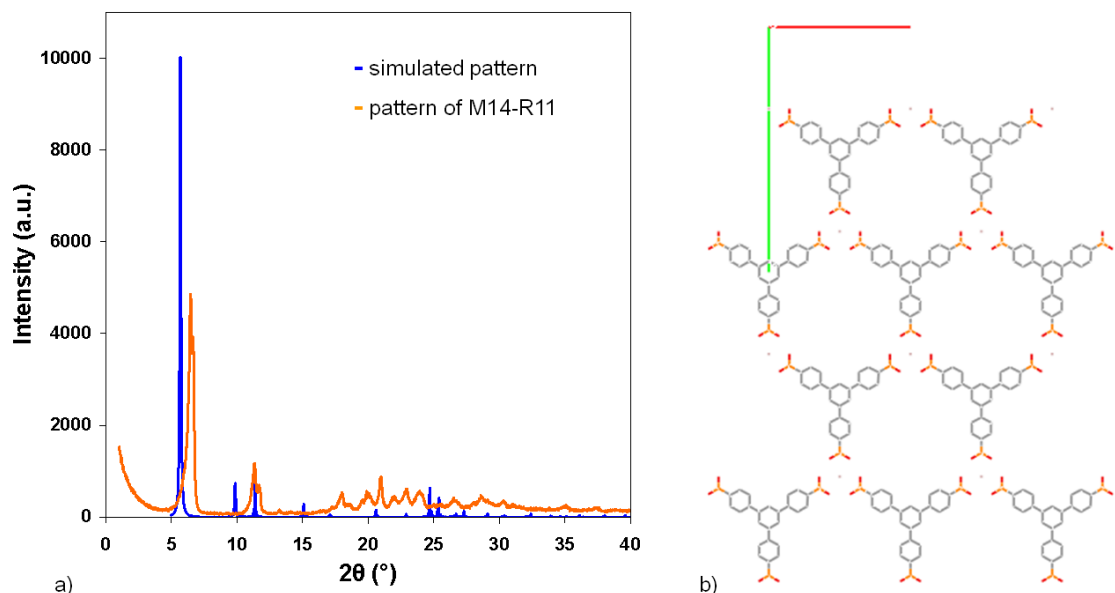


Fig. 4.14: a) X-Ray diffraction patterns of M14-R11 and the model (orange and blue lines respectively) and b) view along axis c of the model structure of the aluminum trisphosphonate compound; for simplification the model has been calculated with only one of the two Al³⁺ cations needed to have electroneutrality and phosphonate groups with two instead of three O atoms.

Figure 4.15a displays the X-ray powder diffraction patterns of the zirconium based organic-inorganic hybrid materials. The diffraction pattern of ZrOCl₂ is shown as comparison. The curve of M11-R11 is identical to this of M12-R11 and has therefore been omitted. It can be observed that all compounds except M16-R11 and M17-R11 present a broad diffraction peak at low angles which corresponds to distances ranging from 13.5 to 17.3 Å. Moreover M26-R11 and M30-R11 show sharp diffraction peaks at higher angles indicating a higher degree of crystallinity. In all cases, the diffraction peaks do not correspond to the characteristic peaks of the salt used during the synthesis thus this later has been completely washed out and does not contribute to the diffraction pattern of the hybrid materials.

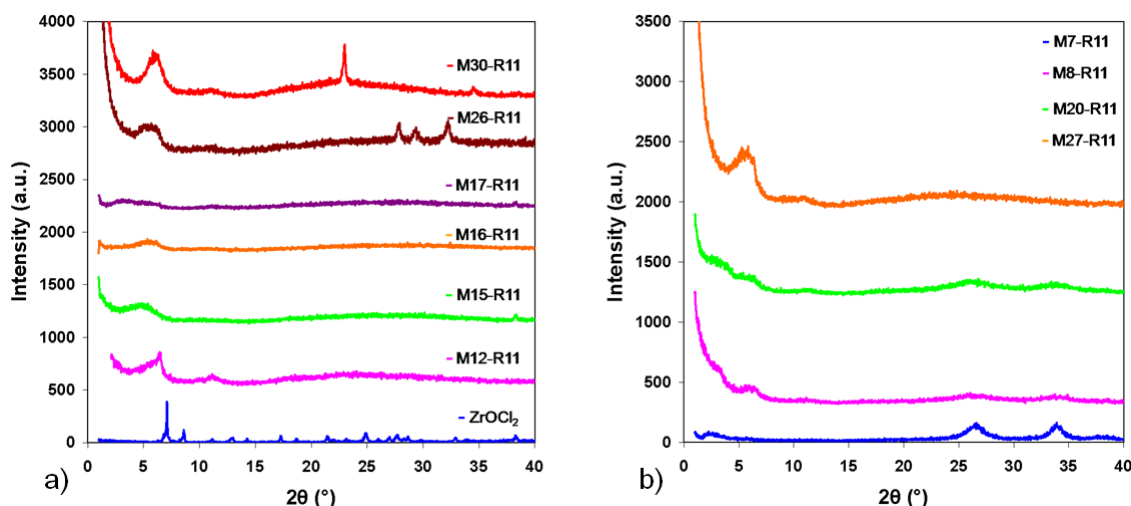


Fig. 4.15: a) X-Ray powder diffraction patterns of zirconium based organic-inorganic hybrid materials having 1,3,5-tris(*p*-phosphonatophenyl)benzene as linker. From the bottom to the top: ZrOCl_2 , M12-R11, M15-R11, M16-R11, M17-R11, M26-R11 and M30-R11. b) X-Ray powder diffraction patterns of tin based organic-inorganic hybrid materials having 1,3,5-tris(*p*-phosphonatophenyl)benzene as linker. From the bottom to the top: M7-R11, M8-R11, M20-R11 and M27-R11

The most probable model to describe the structure of zirconium based hybrid materials containing a triangular molecule as linker is the one used by Clearfield et al. for zirconium based bi- and terphenyl bisphosphonates^[25] in which the trisphenylbenzene units are the pillars and the inorganic layers are formed by $\text{Zr}(\text{PO}_3)_2$ -groups (see Figure 4.8 and 4.10). Since zirconium is a tetravalent element, no hexagonal lattice like in the previous case is expected to be formed. As indicated above, the interlayer distance in the case of layered materials which contain trisphenylbenzene units as pillars would be between 14 and 18 Å since the height of 1,3,5-tris(*p*-phosphonatophenyl)benzene is between this of biphenyl-4,4'-diylidiphosphonic acid and (*p,p'*-terphenyl-4,4''-diyl)bisphosphonic acid as shown in Figure 4.12. This corresponds to the found values which are reported in Table 4.6.

Table 4.6: Characteristic distances at low angles of the zirconium based compounds from the X-ray powder diffraction patterns. M16-R11 and M17-R11 are omitted because no reflections are observed.

Compound	Distance (Å)
M11-R11	13.7
M12-R11	13.5
M15-R11	17.3
M26-R11	15.2
M30-R11	14.0

The X-ray powder diffraction patterns of the tin based materials are shown in Figure 4.15b. Except for M20-R11, which is completely amorphous, the other prepared samples present broad diffraction peaks at low (M8-R11 and M27-R11) or at high angles (M7-R11). The corresponding distances can be calculated using the *Bragg's* law and give values of 13.9 and 15.1 Å for M8-R11 and M27-R11 respectively and of 3.3 and 2.6 Å for M7-R11.

The use of tin as connector to produce hybrid materials has been studied by the group of *A. Clearfield*.^[8, 26-30] It has been demonstrated that amorphous or semi-crystalline compounds are porous whereas the crystalline materials do not have porosity. The porous materials form layered structures. In the case of the present materials containing a trisphosphonate linker a layered structure like for the zirconium based compounds is expected. The distance of 13.9 and 15.1 Å found for M8-R11 and M27-R11 would corroborate these assumptions and would correspond to the interlayer distance.

4.4.2 Electron Microscopy

Electron microscopy allows characterizing the microstructure of the samples including some insights about the particle sizes and shapes therefore scanning electron microscopy (SEM) has been performed.

Figure 4.16 shows the SEM micrographs for two representative samples of divalent organic-inorganic hybrid materials M9-R11 and M25-R11, containing Cu and Zn respectively. In the case of M9-R11, the obtained pictures indicate particle aggregates

of irregular shapes and sizes ranging between 0.1 and 2 μm . Surprisingly, triangles equilateral of 2 μm and 0.8 μm of thickness are encountered through the material. Platelike particles with flat surfaces with sizes from 2 to 30 μm can be observed in Figure 4.16b.

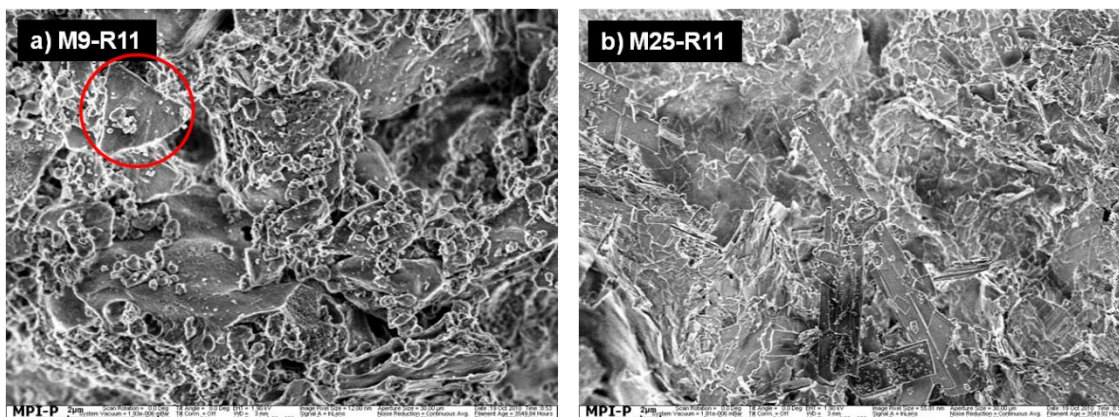


Fig. 4.16: SEM micrographs of a) M9-R11 (Cu) and b) M25-R11 (Zn).

Figure 4.17 displays the SEM micrographs for the aluminum based trisphosphonate materials. The micrograph of M5-R11 shows mainly two types of particles: needles of $\sim 0.5 \mu\text{m}$ width and platelets of 0.3 μm diameter. In the case of M13-R11, the micrograph reveals that there are heterogeneous particles of 150 - 200 nm width and also triangles equilateral with edges of $\sim 200 \text{ nm}$. Surprisingly, in the micrograph of M14-R11 one can observe hexagonal columns that have a width above 1 μm and a diameter of $\sim 1.5 \mu\text{m}$ (between corners). These hexagons observed in Figure 4.20d exhibit regular crystalline shapes. It can be noticed that within the crystallites the distance between the corners of the hexagon is larger than the height of the column. Therefore it can be deduced that the crystal growth is faster in this plane.

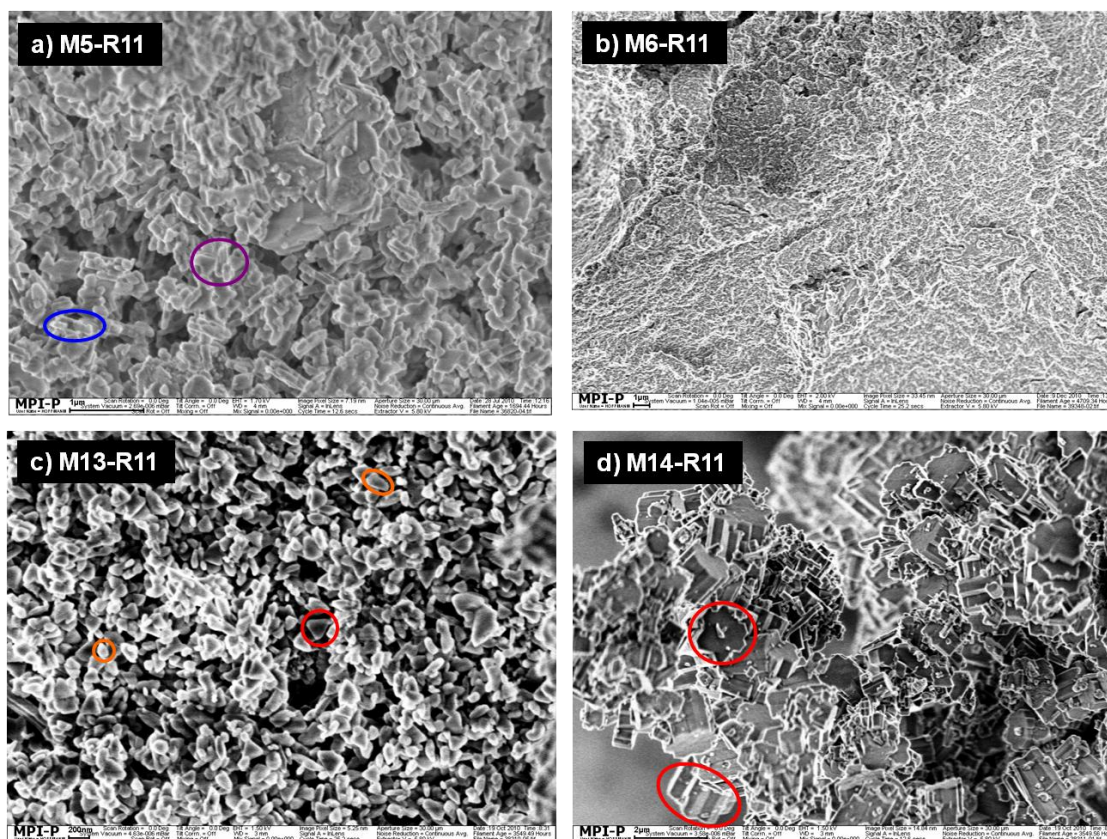


Fig. 4.17: SEM micrographs of a) M5-R11, b) M6-R11, c) M13-R11 and d) M14-R11

The SEM micrographs of two representative samples of tetravalent hybrid materials are displayed in Figure 4.21. The left picture shows the SEM micrograph of M12-R11 containing zirconium whereas the right one shows the micrograph of M8-R11 containing tin. The micrograph of M12-R11 reveals that the compound is composed of particles of heterogeneous sizes and shapes. However triangles equilateral of $0.3 \mu\text{m}$ (sides) are irregularly encountered through the material. In the case of using 4,4'-biphenyl and 4,4'-terphenylbis(phosphonic acid) as linkers in the synthesis of hybrid materials containing zirconium, layered structures are obtained in which biphenyl and terphenyl units are pillars between the $\text{Zr}(\text{PO}_3)_2^-$ layers.^[24] The obtained SEM micrographs reveal particles in the 10 to 100 μm range and a host of fragments of submicron sizes. The particles exhibit no regular crystalline shape.^[9]

M8-R11 displays a homogeneous spongelike topology of the surface with holes of about $1 \mu\text{m}$ at the surface. This type of topology has been already observed for tin phenylphosphonates, which show also micro-sized spheres.^[26]

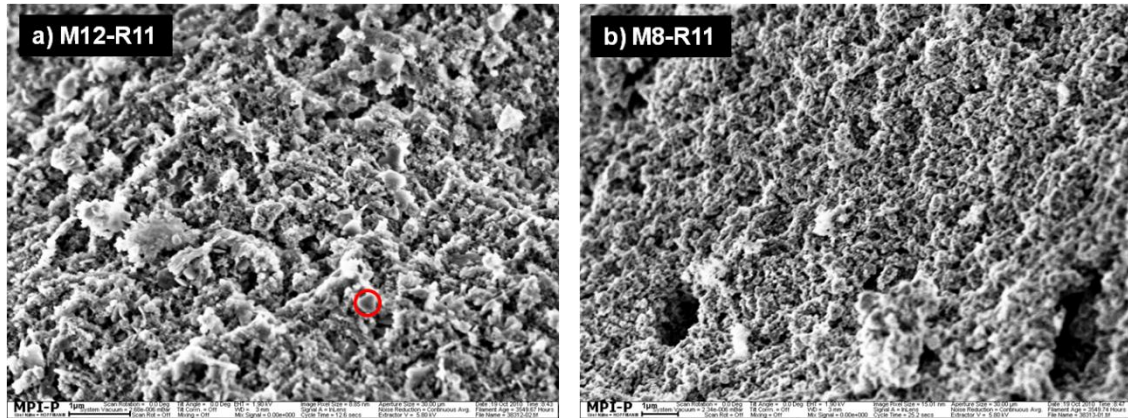


Fig. 4.18: SEM micrographs of a) M12-R11 (Zr) and b) M8-R11 (Sn).

4.5 Textural Characterization

The textural properties of porous materials such as surface area, total pore volume, microporosity and hydrophobicity are key factors for their applications. The porous properties of the materials have been analyzed by nitrogen physisorption at 77 K and the textural parameters obtained from the corresponding nitrogen adsorption-desorption isotherms are given in Tables 4.5 to 4.7. In order to empty the pores prior to the analysis, 20 - 30 mg samples of the materials have been heated to 100 °C for 24 h under high vacuum. For each sample, the sorption analysis has been performed directly after this activation procedure.

4.5.1 Divalent Metals as Connectors

The sorption isotherms for the divalent metal series are shown in Figure 4.19. For these compounds the isotherms show a nearly flat course at low and intermediate relative pressures corresponding to non-porous materials. Upon approaching the saturation pressure at $p/p_0 = 1.0$ a strong gas uptake is again observed which is due to the condensation of nitrogen in large macropores, interparticular voids and the external surface of the material.

Table 4.7 presents the textural parameters calculated for the divalent trisphosphonates compounds. None of the compounds presents porosity which corresponds to the results published in the literature.^[23]

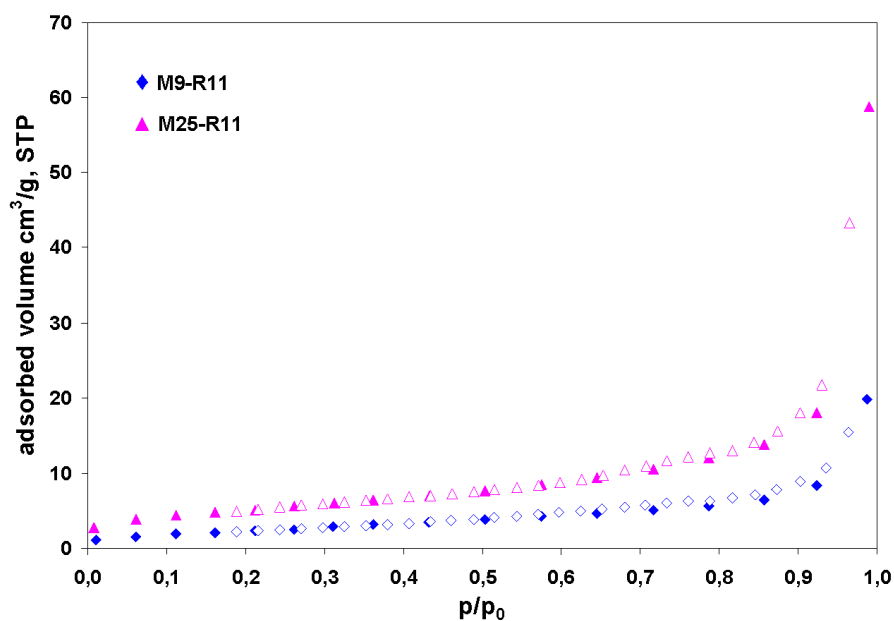


Fig. 4.19: Nitrogen sorption isotherms of Cu and Zn based compounds: M9-R11 (blue diamonds) and M25-R11 (pink triangles). Adsorption and desorption are represented with filled and unfilled symbols respectively.

Table 4.7: Textural parameters calculated for the Cu and Zn based compounds.

Sample	S_{BET} (m ² /g)	MPV _{0.1} (cm ³ /g)	PV _{0.8} (cm ³ /g)
M9-R11	9	0.003	0.008
M22-R11	5	0.001	0.007
M28-R11	11	0.004	0.011
M31-R11	9	0.002	0.01
M10-R11	11	0.002	0.011
M24-R11	15	0.006	0.012
M25-R11	19	0.007	0.019
M29-R11	7	0.002	0.006
M32-R11	21	0.008	0.021

4.5.2 Trivalent Metal as Connector

As seen in Figure 4.20, the adsorption isotherms for all aluminum based compounds excepting M6-R11 show a steep gas uptake at low relative pressures and a flat course in the intermediate section, thus reflecting the microporous nature of the materials. Since no hysteresis is observed, the isotherms can be classified as belonging to Type I. This shape is typically noticed for microporous materials or which the pore diameter is below 2.0 nm.^[31]

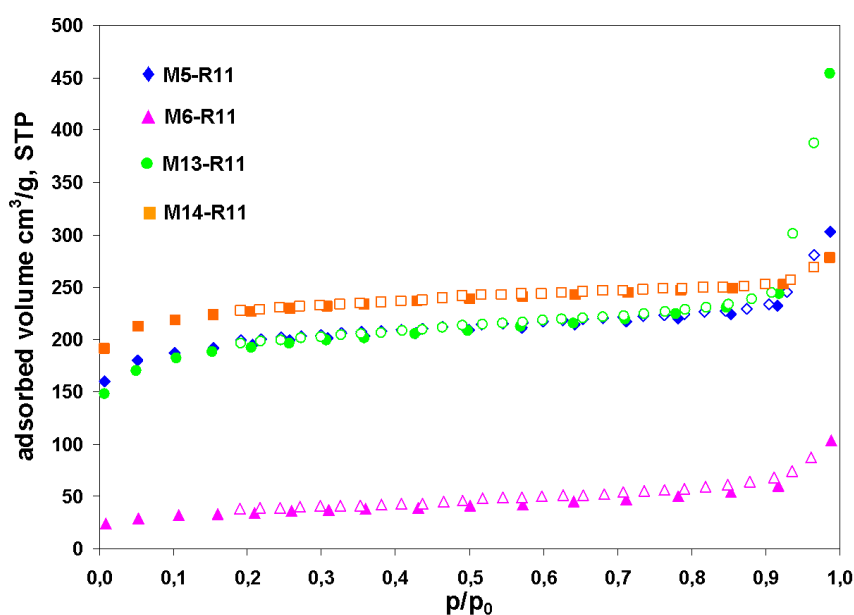


Fig. 4.20: Nitrogen sorption isotherms of Al based compounds: M5-R11 (blue diamonds), M6-R11 (pink triangles), M13-R11 (green circles) and M14-R11 (orange squares). Adsorption and desorption are represented with filled and unfilled symbols respectively.

Concerning the filling of the pores in microporous materials, the following mechanism has been suggested. The adsorption starts within the smallest micropores of the material called “ultramicropores” (diameters below 1.0 nm) at very low relative pressures of $p/p_0 = 10^{-6} - 10^{-5}$. During this filling, such pores are the preferential sites for gas molecules due to the overlap of the adsorption potentials from opposite pore walls.^[32] Subsequently, in the pressure regime from $p/p_0 = 10^{-4} - 10^{-2}$ monolayer adsorption in the remaining larger micropores with diameters up to 2.0 nm is progressively completed (secondary filling).^[33] At a relative pressure of $p/p_0 = 0.1$ all micropores are considered to be occupied by the gas molecules. For this reason the adsorbed gas volume is converted into the corresponding liquid volume which equals

the overall micropore volume (MPV) of the sample. For M14-R11 a high MPV of $0.34 \text{ cm}^3/\text{g}$ is found (see Table 4.8).

When increasing the relative pressure, only minor gas amounts are adsorbed by the sample resulting in a weak slope of the isotherm (plateau). The filling of mesopores and macropores takes place in this pressure range. Upon approaching the saturation pressure at $p/p_0 = 1.0$ a strong gas uptake is observed for many microporous samples which is due to the condensation of nitrogen in large macropores, interparticular voids and the external surface of the material. In order to suppress this effect, the total pore volume of the sample is usually calculated at a relative pressure of $p/p_0 = 0.8$ as described above. For M14-R11 a PV of $0.38 \text{ cm}^3/\text{g}$ is found by this method (see Table 4.8). In agreement with the classification of M14-R11 as a microporous material no hysteresis is found upon desorption. The isotherm exhibits full reversibility.

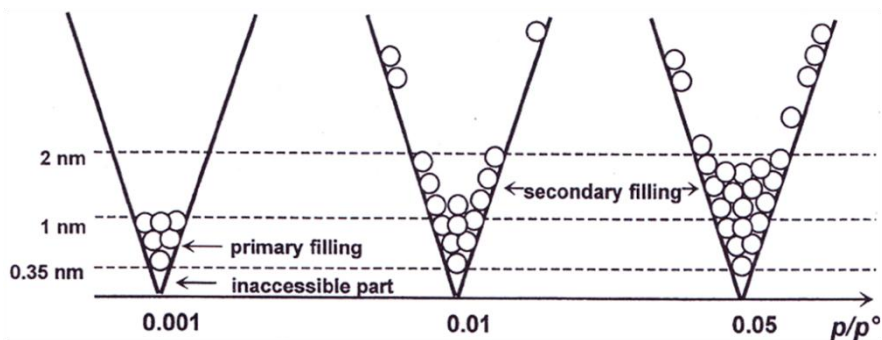


Fig. 4.21: Main steps of the successive filling of micropores during adsorption as seen for Al based trisphosphonate materials.^[32]

All the synthesized organic-inorganic hybrid materials using Al as connector are porous. The surface area of the sample is calculated using the *Brunauer-Emmett-Teller* (BET) model which was developed in 1938 and takes multilayer adsorption into account.^[32, 34] This is in contrast to the classical *Langmuir* theory which is based on the assumption of pure monolayer adsorption.^[32, 35] However, it has to be considered that at preferential sites such as narrow pores, edges and grooves multilayer adsorption sets in prior to the completion of a closed monolayer. In the BET model the adsorbed model is thus not considered to be of uniform thickness but rather to be made of random stacks of gas molecules.

The BET model can be described with the help of the following equation:

$$\frac{1}{W \cdot [(p/p_0) - 1]} = \frac{1}{W_m + C} + \frac{C - 1}{W_m \cdot C} \cdot (p/p_0)$$

where W is the weight of gas adsorbed at a given relative pressure p/p_0 , W_m is the weight of adsorbate constituting a monolayer of surface coverage and C is the BET constant.

The BET equation requires a linear plot which for most solids, using nitrogen as the analysis gas, is restricted to a limited region of the adsorption isotherm which is usually found in the p/p_0 range of 0.05 to 0.35. The BET constant is related to the energy of adsorption in the first adsorbed layer.

Thus, from the slope s and the intercept i of the BET plot the weight of the monolayer can be calculated:

$$s = \frac{C - 1}{W_m \cdot C}$$

$$i = \frac{1}{W_m + C}$$

Combining both equations yields the desired equation for W_m :

$$W_m = \frac{1}{s + 1}$$

From this value, the total surface area S_T can be derived using the molecular cross-sectional area A_{CS} of nitrogen (16.2 \AA^2):

$$S_T = \frac{W_m \cdot A_{CS} \cdot N_A}{M}$$

In this equation N_A is *Avogadro's* number and M is the molecular weight of the adsorbate. In order to compare the surface area of different samples, the value of the specific surface area S_{BET} is usually given, which is obtained by division of S_T by the weight w of the sample:

$$S_{BET} = \frac{S_T}{W}$$

The BET plot of M14-R11 is shown in Figure 4.22 as example. It reveals a virtually linear fit to the experimental data. The surface area S_{BET} calculated as described above is $662 \text{ m}^2/\text{g}$ for this sample.

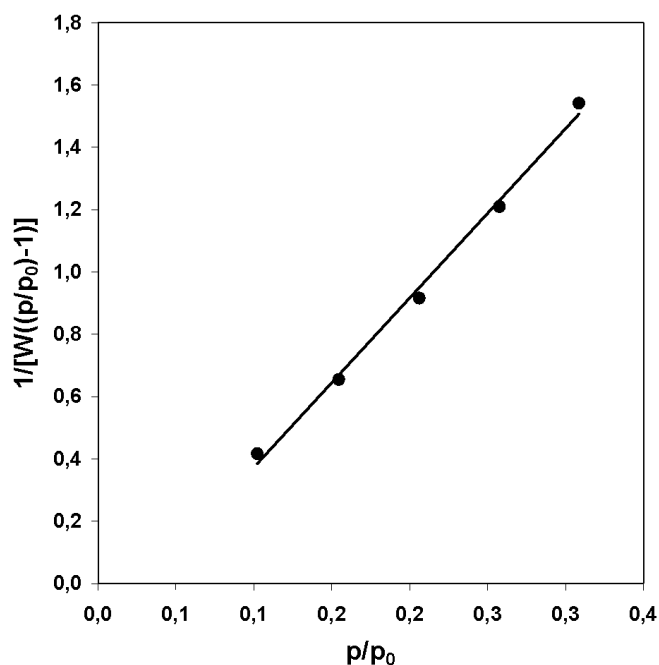


Fig. 4.22: BET plot of M14-R11.

Table 4.8 presents the BET surface area (S_{BET}) and the calculated micropore volumes at $p/p_0 = 0.1$ and 0.8 for all the aluminum based trisphosphonate compounds. Remarkably, the highest BET surface areas of 662 and $576 \text{ m}^2/\text{g}$ have been obtained in the case of M14-R11 and M5-R11 respectively and the compound with the lowest BET surface area is M6-R11 ($108 \text{ m}^2/\text{g}$) (see Table 4.8). These maximum values obtained are higher than these of aluminum biphosphonates synthesized by a non MCM-type approach^[15] and in the same range than these of aluminum phosphonates and diphosphonates synthesized by a surfactant-assisted procedure (MCM-type approach in which surfactant molecules are used as templates) which are however mesoporous.^[18, 36]

On the one hand, the effect of the temperature can be estimated. It can be deduced that the higher the temperature the lower the surface area. The rise of the temperature affects dramatically the porous properties of the materials when the temperature is increased from 150 to $200 \text{ }^\circ\text{C}$ since the BET surface area is decreased by five (M5-R11 and M6-R11). In addition it can be observed that the use of $\text{Al}(\text{NO}_3)_3 \cdot 1\text{H}_2\text{O}$ instead of

$\text{Al}(\text{NO}_3)_3 \cdot 9\text{H}_2\text{O}$ under the same synthetic conditions doesn't affect the textural properties of the obtained materials M13-R11 and M5-R11 respectively.

Furthermore, it can be observed that in contrast to the published aluminum bisphenyldiphosphonates which synthesized in H_2O are not microporous and develop microporosity due to the inclusion of DMSO molecules,^[15] in the present case the sample synthesized in H_2O presents the highest microporosity suggesting that another type of mechanism is responsible for the porosity in the material. The micropores in the aluminum bisphenyldiphosphonates are formed by the coming together of layers of unequal length around the DMSO molecules. The washings of the samples remove the trapped DMSO developing microporosity, resulting in voids which are schematically represented in Figure 4.11.

Table 4.8: Textural parameters calculated for the aluminum based compounds.

Sample	S_{BET} (m^2/g)	$\text{MPV}_{0.1}$ (cm^3/g)	$\text{PV}_{0.8}$ (cm^3/g)
M5-R11	576	0.29	0.34
M6-R11	108	0.049	0.078
M13-R11	573	0.28	0.35
M14-R11	662	0.34	0.38

The pore size distribution has been calculated for all aluminum based compounds by using the Density Functional Theory (DFT) method which is applicable to the entire range of pore sizes accessible by the adsorptive molecule.^[37, 38] The corresponding curves are depicted in Figure 4.23. The calculated pore size distribution shows mean pore diameters below 1.2 nm for M5-R11 whereas the solid synthesized at 200 °C (M6-R11) presents micropore size distribution below 2 nm. Like for M5-R11, the mean pore diameter of the material synthesized in water (M14-R11) is smaller/lower than 1.2 nm whereas for M13-R11 it is 0.9 nm.

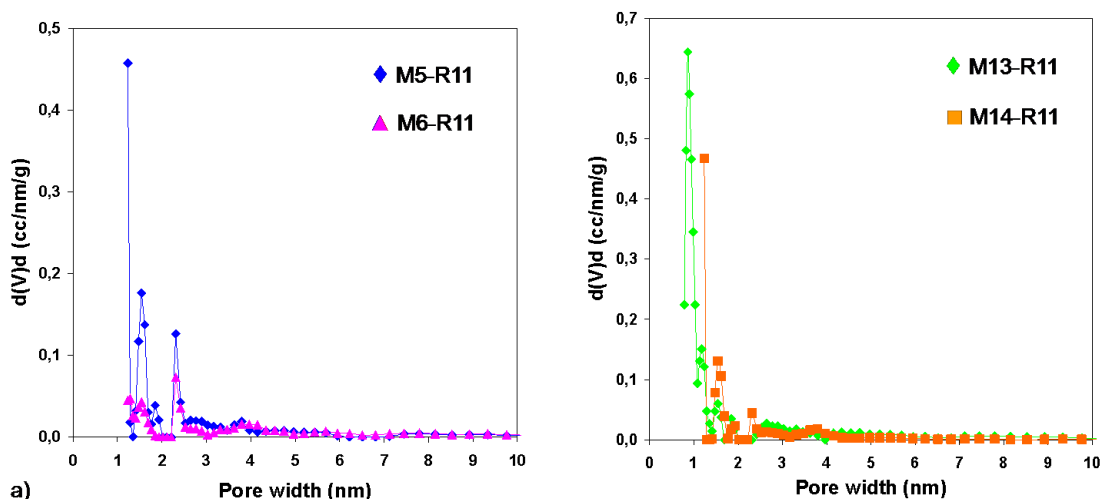


Fig. 4.23: Pore size distribution obtained by the DFT method for a) M5-R11 and M6-R11 (blue diamonds and pink triangles respectively) and b) M13-R11 and M14-R11 (green diamonds and orange squares respectively).

Thus it can be concluded that excepting the solid synthesized at 200 °C (M6-R11), all aluminum trisphenyltrisphosphonates are microporous and that the pore diameter are below ~ 1 nm.

4.5.3 Tetravalent Metals as Connectors

Two N_2 sorption isotherms for representative samples of the tetravalent series are shown in Figure 4.24. Figure 4.24a displays the sorption isotherm of M12-R11 (zirconium based trisphosphonate) and M8-R11 (tin based trisphosphonate) as an example for the tetravalent series of materials. Due to the evolution of the curves, the compounds can be classified as microporous.

The porosity of M20-R11 and M27-R11, both tin based compounds, differs significantly from the previous case. The most notable feature of the isotherm which is depicted in Figure 4.24b is the irreversible sorption behavior resulting in the presence of a pronounced hysteresis loop upon desorption. Only at a relative pressure of $p/p_0 = 0.42$ for M27-R11 and 0.44 for M20-R11 both branches of the isotherm meet again. The isotherms of both materials can thus be classified as type IV.^[31]

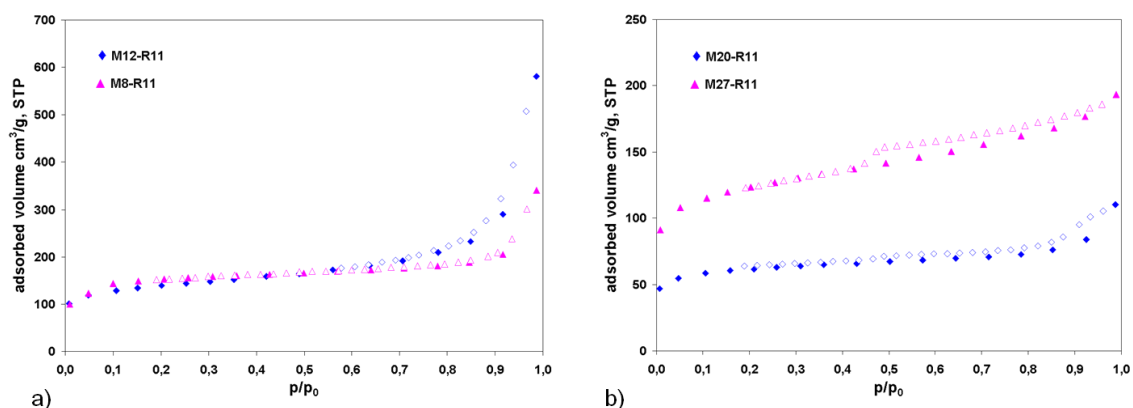


Fig. 4.24: a) Nitrogen sorption isotherms of Zr and Sn based compounds M12-R11 (blue diamonds) and M8-R11 (pink triangles). Adsorption and desorption are represented with filled and unfilled symbols respectively. b) Nitrogen sorption isotherms of tin based compounds M20-R11 (blue diamonds) and M27-R11 (pink triangles). Adsorption and desorption are represented with filled and unfilled symbols respectively

The observed hysteresis is typical of mesoporous materials and related to the capillary effect that occurs upon condensation in the multilayer regime. Typically, pores with diameters between 3.0 and 7.0 nm are affected by this phenomenon.^[32] The appearance of partial irreversibility during the sorption analysis is related to metastable states which cause the adsorbate to be entrapped upon desorption. The exact assessment of the hysteresis behavior of mesoporous materials remains however under discussion.

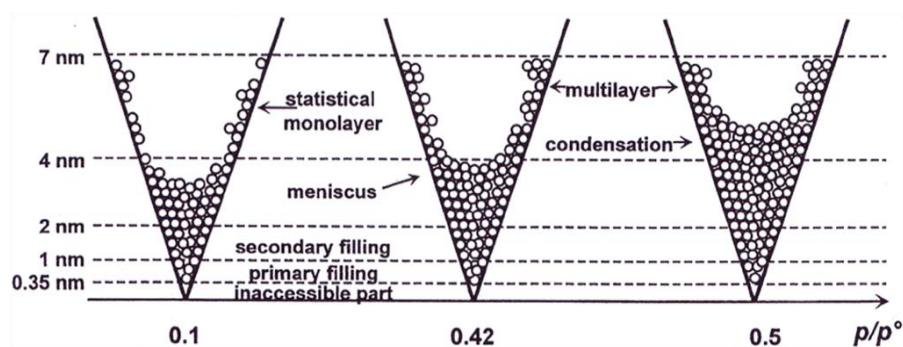


Fig. 4.25: Main steps of the successive filling of mesopores during adsorption as seen for M20-R11 and M27-R11.^[32]

The textural parameters calculated for the zirconium and tin based hybrid materials are shown in Table 4.7. M12-R11 is of all the zirconium based compounds the one with the highest BET surface area whereas M8-R11 presents the highest porosity of all the

tin based materials. These two solids possess similar porous properties since their respective BET surface areas are 435 and 457 m²/g and their N₂-sorption curves are similar. The values obtained for the BET surface area are inferior to the one reported above for aluminum based organic-inorganic hybrid materials.

In contrast to the microporous aluminum trisphosphonates, the solids synthesized with tetravalent elements zirconium and tin do not show a change of the porous properties at elevated temperatures, thus temperature does not play a role for these materials.

However contrary to the microporous aluminum trisphosphonates, the choice of the solvent seems to be important to obtain microporous zirconium based solids since at 90 °C, while changing the solvent from DMSO (M11-R11) to water (M15-R11) passing by DMSO/H₂O (M16-R11), the specific surface area decreases from 394 to 87 m²/g. In the case of tin based hybrid materials, it is observed that the compound produced in pure DMSO (M20-R11) presents a lower porosity than its analogues in DMSO/H₂O (M8-R11) and DMSO/BuOH (M7-R11) indicating that also in this case the choice of the solvent can alter the porous properties of the material. These results have been also observed for group IV bisphenyldiphosphonate compounds.^[25]

The observed lower specific BET surface areas of M20-R11 compared to M8-R11 is in accordance with the predominance of mesopores in the material. Interestingly, M27-R11 possesses a lower surface area than M8-R11 but comparable to that of other microporous tin based trisphosphonate solids most probably due to the presence of micropores in the material.

The calculated specific surface area of the obtained zirconium and tin trisphenyltrisphosphonates is in the range of the published values for mono- and biphosphonates tin compounds.^[6, 9, 27, 29] The presence of mesoporosity in tin phosphonates compounds is a well known phenomenon in amorphous tin phosphonates.^[27]

Table 4.7: Textural parameters calculated for the zirconium and tin based compounds.

Sample	S_{BET} (m^2/g)	$\text{MPV}_{0.1}$ (cm^3/g)	$\text{PV}_{0.8}$ (cm^3/g)
M11-R11	394	0.18	0.28
M12-R11	435	0.20	0.32
M15-R11	87	0.035	0.078
M16-R11	247	0.11	0.19
M17-R11	328	0.15	0.23
M26-R11	333	0.15	0.23
M30-R11	346	0.15	0.26
M7-R11	372	0.17	0.25
M8-R11	457	0.22	0.28
M20-R11	184	0.09	0.11
M27-R11	379	0.18	0.25

Figure 4.26 displays the pore size distribution calculated by the DFT method of zirconium and tin based trisphosphonate materials. Figure 4.26a shows mean pore diameters below 1.5 nm for M12-R11 whereas in the case of M8-R11 the mean pore diameters range from 1.3 to 1.9 nm. These values are in accordance with the trend of the curves for these compounds (see Figure 4.24a) which indicate that they were microporous. In the case of the solids M20-R11 and M27-R11 (see Figure 4.26b), both tin based trisphosphonates, the mean pore diameters range from 1.2 to 2.3 nm and from 1.2 to 3.8 nm respectively indicating that the materials are mesoporous but present a contribution of microporosity. This can be also observed in Figure 4.28 since at relative pressures below 0.4 the desorption curve corresponds to the adsorption one meaning that there is no more hysteresis.

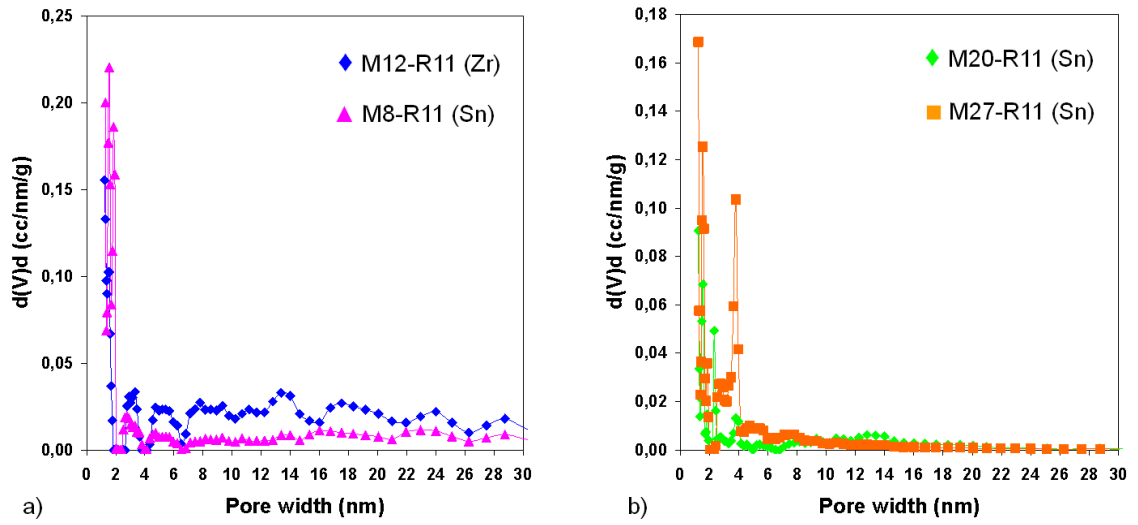


Fig. 4.26: Pore size distribution obtained by the DFT method for a) M12-R11 (Zr) and M8-R11 (Sn) (blue diamonds and pink triangles respectively) and b) M20-R11 (Sn) and M27-R11 (Sn) (green diamonds and orange squares respectively).

4.6 Hydrogen Storage

4.6.1 Hydrogen as a Future Energy Carrier

Hydrogen is the lightest and most abundant chemical element, constituting 90 % of the atoms in the universe. Two-thirds of the hydrogen atoms are present in water whereas the rest in living organisms and fossil fuels (hydrocarbons).^[39, 40] Hydrogen atoms are highly electronegative (2.20 in the Pauling scale) and therefore eager to bond, releasing energy when doing so. This characteristic makes them potentially useful. However, since the amount of unattached hydrogen on earth is very low, this atom must then be liberated by breaking chemical bonds, a process which requires energy. When they are released from the large molecules they are part of, they paired up into a diatomic gas H₂ which at standard temperature and pressure is colorless, odorless, tasteless, non toxic and highly combustible. Hydrogen gas can only be liquefied at - 252.9 °C.^[39]

Hydrogen is seen as the clean fuel of the future due to two reasons: when it is burned or oxidized into a fuel, no pollutions (greenhouse gases) are emitted and it releases per mass unit more energy than any other fuel.^[41] However, the use of hydrogen in our everyday life presents different challenges since it is hard to store, transport, liquefy, and handle safely; and capable of releasing only as much energy as human beings first pump into it.

4.6.2 The Storage of Hydrogen

Hydrogen as energy carrier can be used either for stationary or mobile applications (e.g., hydrogen driven vehicles). The latter is the most compelling goals for hydrogen storage because the transportation sector is the largest consumer of oil, producing greenhouse gases.^[42] Thus building an infrastructure that allows for easy and cost-effective transportation and delivery of hydrogen energy is a critical step toward a future hydrogen economy.

The 2015 energy density targets for the hydrogen storage system (including container and necessary components) are 9.0 wt % and 81 kg H₂ per m³, which approach the expectations of the automotive industry. However hydrogen is the lightest element and at RT and pressure, it takes up roughly 3000 times as much space as gasoline containing the same amount of energy. If one considers that the mass density

of elemental hydrogen is only 70.8 kg/m^3 in its liquid state at 20 K (1 atm) and that 5 kg of hydrogen gas fills a volume of 56 m^3 under ambient conditions, the targets can be considered as daunting tasks. Furthermore, both of these insights ignore the contribution of the mass of the necessary container.^[41]

A hydrogen storage unit for mobility and transport applications should possess the following characteristics:^[43]

- Safety;
- Reversibility in the temperature range 0 - 100 °C;
- High hydrogen concentration.

Three different methods are currently available for the storage of hydrogen.^[43, 44]

- By increasing pressure and/or lowering temperatures (physical storage);
- By hydrides (chemical storage);
- By physisorption at surfaces (physical storage).

The most established method is the storage of hydrogen compressed or cryogenically liquefied. The two other procedures have been only most recently developed. The fastest way to charge and discharge a storage vessel with hydrogen is to maintain its molecular identity. Adsorption is a borderline situation between physical and chemical storage. However, it is most of the time considered as a physical storage technology since the interactions between the hydrogen and the adsorbents are weak and the hydrogen do not dissociate but is molecularly adsorbed.^[44] Since at RT and atmospheric pressure the current known adsorbents do not present storage capacities which are close to the targeted values, the use of cryogenic or pressure systems will be necessary. The difference between cryo-adsorption and chemical storage in a hydride is shown in Figure 4.27.

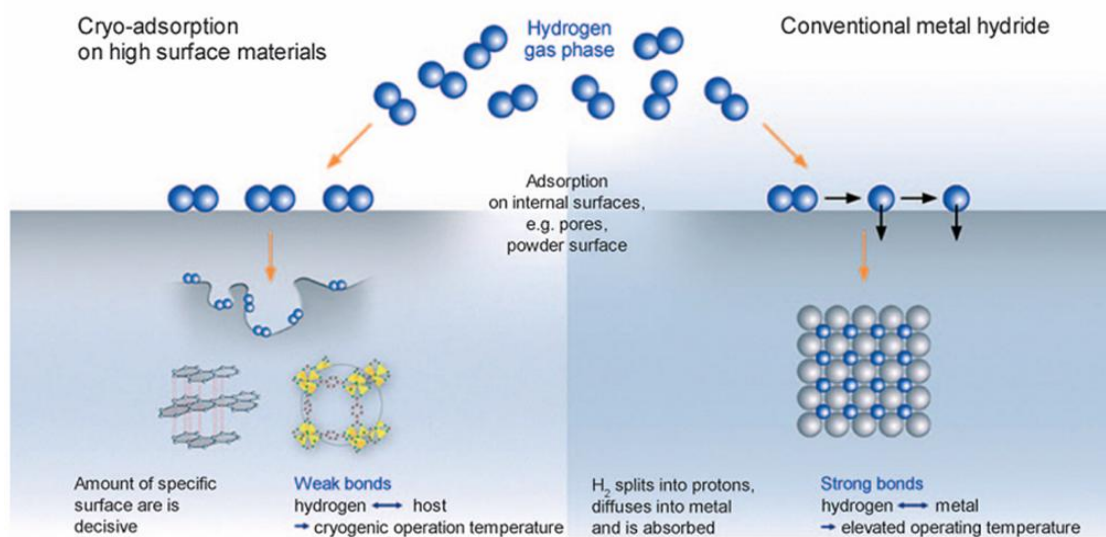


Fig. 4.27: Schematic representation of cryo-adsorption and chemical storage in a hydride.^[44]

Different classes of materials are potential candidates to store hydrogen due to their high porosity:

- Active carbon;^[45-47]
- Carbon nanotubes;^[48, 49]
- Zeolites and other silicate materials;^[50-52]
- Metal-organic frameworks (MOF);^[53, 54]
- Covalent organic frameworks (COF);^[55, 56]
- Hypercrosslinked polymers (HCP);^[57]
- Polymers of intrinsic microporosity (PIM).^[57]

Among those systems, carbon materials have been the most widely examined due to their low density, high surface area, good chemical stability and amenability to a wide range of processing conditions. Active carbons with optimized pore geometry yield values for the physisorbed H_2 at 70 bar of 45.0 g.^[45] Carbide-derived carbons present a storage capacity of 30 g H_2 /kg at 1 bar.^[47]

Since the first report of hydrogen adsorption by carbon nanotubes,^[48] a wide range of uptake values have been reported. Sample preparation and morphology seem to play an important role and adsorption values of approximately 5 wt % at 77 K and < 1 wt % at RT under high pressure have been reported.^[49, 58-61] Theoretical modeling studies of the interaction of hydrogen with carbon in systems of many geometries and

scales revealed that uptake of only a few wt % is achievable with this class of materials.^[62, 63] However, reports of improved uptake on changing the morphology have appeared recently.^[64]

Zeolites are aluminosilicates, however nowadays also aluminophosphates are also included in the definition. There are crystalline microporous materials with pores no larger than 10 Å. Hydrogen adsorption values of 18.1 g H₂/kg at 15 bar have been measured.^[52] Up-to-date, the zeolitic material with the highest micropore volume is ITQ-33 (0.37 cm³/g).^[65] However, the storage capacity of the material when filling it with hydrogen at liquid hydrogen density would only amount to about 2.5 wt %. It can be therefore stated that zeolite-based materials are not suitable compounds for hydrogen storage in case of technical applications.

Covalent organic frameworks are 3D crystalline solids entirely constructed from strong covalent bonds (C-C, C-O, C-B, and B-O). COFs present high surface areas (3472 and 4210 m²/g for COF-102 and COF-103, respectively) and extremely low densities (0.17 g/cm³).^[55]

Polymers such as HCP and PIM have recently appeared as alternative hydrogen storage materials.^[57] To date, the best PIMs based on a triptycene monomer and takes up 2.7 wt % H₂ at 10 bar and 77 K.^[57] It can be expected that in future polymers with higher storage capacity will appear.

4.6.3 Trisphosphonate Hybrid Materials for Hydrogen Storage

Carboxylic acid based MOFs have been proposed as hydrogen storage materials.^[66] However, the use of porous phosphonic acid based open frameworks has been centered on catalysis, proton-conducting FC membranes and ion-exchange and their potential applications for the storage of hydrogen remains unexplored.^[25] Thereof, there is an acute need to collect and analyze hydrogen uptake measurements on these materials to establish the favorable factors for its storage. In this section, such measurements are reported for two representative materials, M13-R11 and M12-R11, aluminum and zirconium based trisphosphonates respectively. With these results, the impact of internal surface area and the metal on the storage capacity are considered.

The hydrogen uptake measurements have been performed at the TU Dresden/Germany by Dr. I Senkovska. Figures 4.28a and b present the hydrogen

uptake for M13-R11 and M12-R11, aluminum and zirconium based trisphosphonates which have been chosen for their large surface areas (573 and 435 m²/g respectively). The chemical differences of the organic units manifest themselves in the hydrogen sorption behavior. The isotherms in Figures 4.28a and b display distinct initial slopes and curvatures as well as different desorption curves. Notably, a hysteresis is observed in the case of M13-R11.

At the highest pressure achieved in these experiments the maximum uptake varies considerably, from 0.01 wt % for M13-R11 to 0.45 wt % for M12-R11. This is surprising since actually the aluminum based compound presents a higher specific surface area than the zirconium hybrid material. Notable is the large value of the initial slope of the M12-R11 isotherm, indicating higher affinity for molecular hydrogen.

The obtained values are lower than these published for MOFs (between 0.9 and 1.6 wt %)^[66] and PIM (2.7 wt %).^[57] Thus it can be concluded that in the case of trisphosphonate organic-inorganic hybrid materials a high surface area doesn't imply a high hydrogen adsorption capacity and that zirconium based solids present higher hydrogen affinity and higher hydrogen storage capacity than aluminum based compounds.

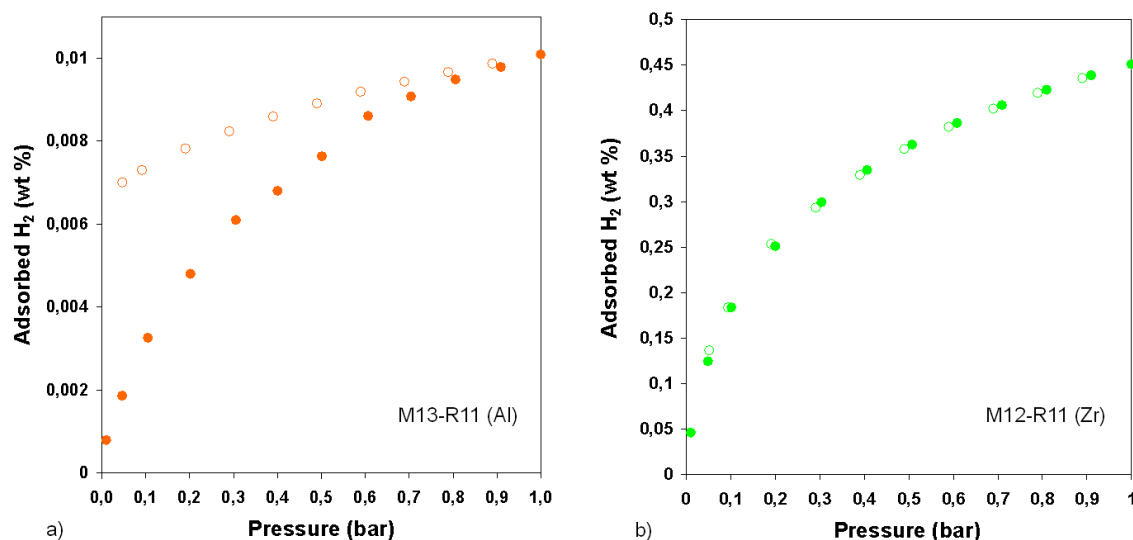


Fig. 4.28: Hydrogen isotherms measured gravimetrically at 77 K (adsorption, ●; desorption, ○) for a) aluminum based trisphosphonate M13-R11 and b) zirconium based trisphosphonate M12-R11.

4.7 Discussion

It has been demonstrated that porosity of pillared phosphonates arose from the special growth pattern of these materials.^[20, 25, 67, 68] As above explained the general method is to react a diphosphonic acid, $\text{H}_2\text{O}_3\text{P-R-PO}_3\text{H}_2$, with a suitable metallic cation to form inorganic layers of the metal and PO_3 groups and then to crosslink these layers with the alkyl or aryl groups (R) and space these pillars (which crosslink the layers) with phosphate (POH) or phosphite (PH) groups.

4.7.1 Divalent Metals as Connectors

A large number of divalent phosphonates have been prepared and afford fully determined isotype crystallographic structures.^[69] However their textural properties are usually not reported. One typical structure which is obtained with most divalent metals phosphonates is $\text{M}(\text{O}_3\text{PR})\cdot\text{H}_2\text{O}$.^[70, 71] This structure consists of quite compact layers of metals in an octahedral environment of oxygen atoms. Interestingly, the divalent materials prepared with 1,3,5-tris(*p*-phosphonatophenyl)benzene are amorphous and non-porous. It seems that Cu^{2+} and Zn^{2+} are not suitable metallic cations to afford solids with porous properties using 1,3,5-tris(*p*-phosphonatophenyl)benzene as linker.

4.7.2 Aluminum as Connector

The results obtained from the textural characterization carried out on the synthesized aluminum trisphenylphosphonates can be correlated to the crystallinity studies. It has been observed that the solid synthesized at 200 °C (M6-R11) has the lowest specific surface area and is the unique of this series to be amorphous. Thus it can be deduced that on the one side an increase of the temperature to 200 °C is disadvantageous for the porous properties of the aluminum trisphosphonates and that on the other side porosity and crystallinity are closely related. It appears evident from the obtained results that crystallinity is a key to obtain porous materials.

In the aluminum bisphenyldiphosphonate materials reported in the literature, the formation of microporosity is a consequence of the coming together of layers of unequal length around the DMSO molecules. These DMSO molecules act as template agents during the crystal growth and after their washings of the samples microporosity is developed (see Figure 4.12).

The mechanism of pore formation for aluminum trisphenylphosphonate solids is due to the crystalline structure formed by the tri-functionalized linker with triangular geometry and the trivalent nature of the metal. A hexagonal lattice is formed in which the nodes are composed of ionic interaction between the positively charged Al^{3+} and the negatively charged phosphonate groups (see Figure 4.29). Since no acidic hydrogen atoms have been observed by FTIR and solid-state NMR, it can be supposed that all the phosphonic acid functions have reacted with the Al^{3+} cations. The presence of two peaks in the ^{27}Al spectrum is due to the possible interaction of water molecules with the metal which affords then two types aluminum species, hydrated and a non-hydrated.

Pores below 2 nm of diameter are formed which fit to the results obtained from the DFT calculations. Therefore in this case water can be employed as solvent and replace DMSO since the solvent doesn't act as template agents during crystallization. Microporosity of aluminum trisphosphonate materials is induced by the crystalline structure of the compound and not by the solvent inclusions of solvent molecules or uneven growth of layers like in the case of aluminum and zirconium biphosphonates hybrid materials.^[15, 25] This is due to the combination of a trivalent metal and a tri-functional linker which on the one side provides the perfect stoichiometry and on the other side affords the hexagonal geometry.

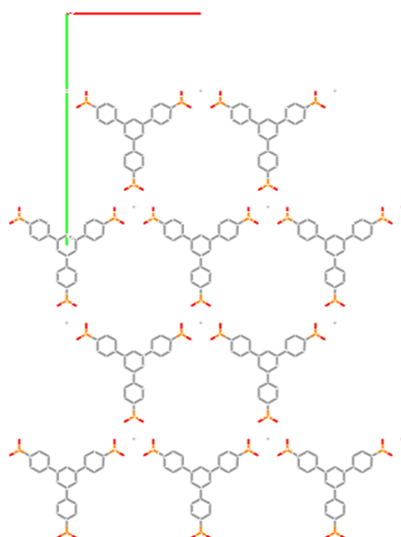


Fig. 4.29: Proposed model for the formation of porosity in aluminum trisphenyltrisphosphonate hybrid materials (view along the axis c). For simplification the model has been simulated with only one of the two Al^{3+} cations needed to have electroneutrality and phosphonate groups with two instead of three O atoms.

Thus it can be concluded that the hexagonal model for the structure of the aluminum trisphosphonates proposed in Section 4.4.1 supplies answers for the following observations:

- Al^{3+} , a light metal cation, can be successfully used as connector to produce microporous hybrid materials;
- The microporous compounds are crystalline and produce nanosized crystallites with a minimum of long range order;
- The choice of the solvent doesn't alter the pore size or regularity;
- The temperature influences the porous properties and temperatures above 200 °C conduct to amorphous solids with lower porosity and pore size regularity.

4.7.3 Tetravalent Metals as Connectors

To explain the porosity of group IV bisphenyldiphosphonates, *Clearfield et al.* proposed a model based on crystal growth.^[25] The central idea is that upon mixing the diphosphonic acid (biphenyl- or triphenyldiphosphonates) with the dissolved tetravalent metal, rapid precipitation of fine particles occurs. In this process both phosphonic acid groups bond to metals forming part of two layers. Statistically, it is expected that the growth rate of the layers would not be the same because much depends on how the second acid group attaches itself to a nascent layer after the first in the same molecule has become part of an adjacent growing layer. This uneven growth leads to gaps in the structure as shown in Figure 4.11.

In the case of zirconium and tin hybrid materials containing 1,3,5-tris(*p*-phosphonatophenyl)benzene as linker it has been shown that the obtained solids are mostly amorphous. An interlayer distance between 13.5 and 17.3 Å has been found for zirconium based compounds whereas the *d*-spacing lays between 13.9 and 15.1 Å for the tin based hybrid materials. It has been therefore deduced in Section 4.4.1 that also in the case of using a tri-functionalized linker the obtained materials form layers. Upon mixing the triangular linker and the metal, precipitation occurs and layers are formed. Since they have different growth rates gaps in the structure are formed as indicated in

Figure 4.30. These gaps are the pores which can incorporate gas molecules. Excepting two tin based compounds, all obtained solids are microporous.

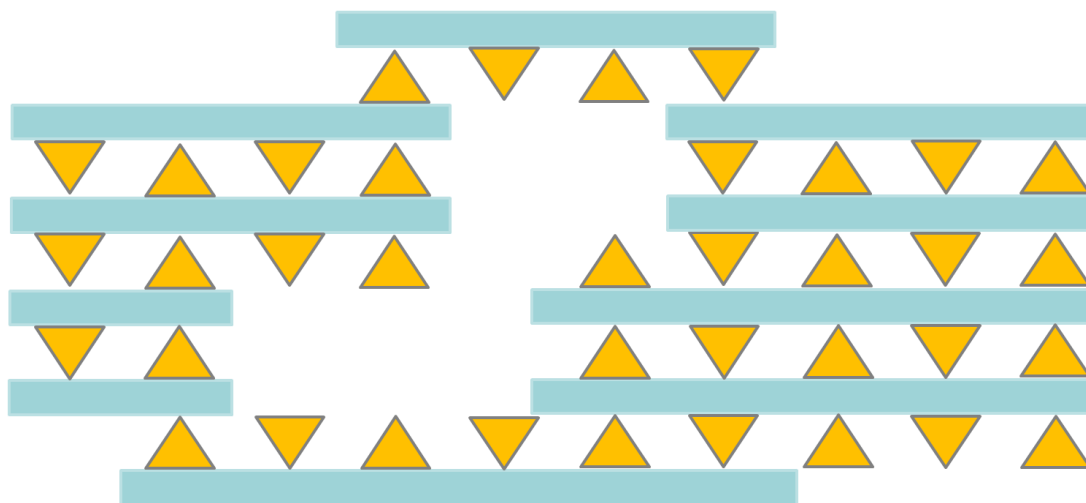


Fig. 4.30: Proposed model for the formation of porosity in the zirconium and tin trisphenyltrisphosphonate compounds. The orange triangles represent the trisphenylbenzene units and the grey bars the metal phosphonate layers.

Thus the proposed model based on this of *Clearfield* et al. gives answers to the following facts:

- The porous materials are amorphous and upon precipitation form layers;
- The choice of the solvent is crucial to obtain porous materials;
- Tin based compounds present mesoporosity.

In the case of zirconium trisphosphonates it has been observed that while carrying on the solvothermal reaction in aqueous media instead of in DMSO, materials with lower porosity are obtained. The reason for this behavior has not yet been found. *Clearfield* et al. have suggested for pillared zirconium aryldiphosphonates avoiding water to obtain microporous materials however no explanation has been given.^[4, 5]

Mesoporosity might be formed when the gaps between the layers are high enough to create pores of diameters above 2 nm. Since no acidic protons have been determined neither by FTIR nor by solid-state NMR it can be deduced that in the pores some metals must be present to ensure the electroneutrality of the material.

4.8 Conclusion

Organic-inorganic hybrid materials using 1,3,5-tris(*p*-phosphonatophenyl)benzene as linker have been prepared with Cu, Zn, Al, Zr and Sn as connectors. The two key results of this work are that:

1. 1,3,5-Tris(*p*-phosphonatophenyl)benzene can serve as linker to afford porous hybrid materials. It is the first time that a trisphosphonated organic molecule is applied to obtain microporous phosphonated open-frameworks.
2. Porosity arises from the special growth pattern of these materials. The combination of crystallinity and porosity is only possible by applying a metal and a linker of the same geometry and functionality. Crystallinity is a critical issue since it is desired to have phosphonated open-frameworks with regular pore sizes.

In the case of aluminum based trisphosphonates a hexagonal lattice is formed due to the perfect stoichiometry and geometry offered by the trivalent metal and the trivalent triangular linker. Microporous solids are produced which are furthermore crystalline, thus the regularity of the pores is maintained. High surface areas up to 662 m²/g have been obtained which are higher than the published results for phosphonated hybrid materials synthesized by a non-MCM-type approach.^[15] The materials presented in this section which contain aluminum as connector are the first example of phosphonated organic-inorganic hybrid materials which exhibit at the same time high microporosity and crystallinity. The regularity of the pores is then assured through the entire ionic network. However the tested aluminum based material does not show high affinity and storage capacity for hydrogen. For this reason even if the connector, Al³⁺, is a light metal cation which is a requirement to reduce the framework density to enhance gravimetric hydrogen capacity^[72] the materials are not an appropriate choice for the storage of hydrogen.

The use of tetravalent metals as connectors affords porous materials which are however amorphous since metal and linker have different functionalities and geometries. Porosity is due to the uneven growth rates of layers during particle formation. Heterogeneity of the pore size is obtained due to the non-crystalline nature of the materials and gives rise in some cases to mesoporosity. The zirconium based

solid tested presents a more elevated affinity for hydrogen as well as a higher hydrogen storage capacity than the aluminum based compound.

The trisphosphonate solids obtained using divalent metals as connectors are amorphous and non-porous. This might be due to the unfavorable divalent nature of the metal which avoids the formation of a hexagonal lattice like in the case of the aluminum based compounds and of layered structured like in the case of the zirconium and tin based materials.

4.9 Bibliography

- [1] C. T. Kresge, M. E. Leonowicz, W. J. Roth, J. C. Vartuli, J. S. Beck, *Nature* **1992**, 359, 710
- [2] M. D. Dines, P. M. Digiacomo, K. P. Callahan, P. C. Griffith, R. H. Lane, R. E. Cooksey, *Chemically Modified Surfaces in Catalysis and Electrocatalysis*, 192, ACS, Washington, DC **1982**, Edited by J.S. Miller, 223.
- [3] G. Alberti, U. Costantino, F. Marmottini, R. Vivani, P. Zappelli, *Angew. Chem. Int. Ed.* **1993**, 32, 1357
- [4] A. Clearfield, Z. Wang, *J. Chem. Soc., Dalton Trans.* **2002**, 2937
- [5] A. Clearfield, *Chem. Mater.* **1998**, 10, 2801
- [6] A. Clearfield, Z. Wang, P. Bellinghausen, *J. Solid State Chem.* **2002**, 167, 376
- [7] M. d. M. Gómez-Alcántara, A. Cabeza, M. Martínez-Lara, M. A. G. Aranda, R. Suau, N. Bhuvanesh, A. Clearfield, *Inorg. Chem.* **2004**, 43, 5283
- [8] M. d. M. Gómez-Alcántara, A. Cabeza, P. Olivera-Pastor, F. Fernández-Moreno, I. Sobrados, J. Sanz, R. E. Morris, A. Clearfield, M. A. G. Aranda, *Dalton Trans.* **2007**, 2394
- [9] Z. Wang, J. M. Heising, A. Clearfield, *J. Am. Chem. Soc.* **2003**, 125, 10375
- [10] M. Vasylyev, R. Neumann, *Chem. Mater.* **2006**, 18, 2781
- [11] J. M. Taylor, A. H. Mahmoudkhani, G. K. H. Shimizu, *Angew. Chem. Int. Ed.* **2007**, 46, 795
- [12] O. Solcova, H. Snajdaufova, V. Hejtmanek, P. Schneider, *Chem. Papers* **1999**, 53, 396
- [13] A. Feliczak, I. Nowak, *Materials Science-Poland* **2008**, 26, 237
- [14] M. Park, S. Komarneni, J. Choi, *J. Materials Science* **1998**, 33, 3817
- [15] M. d. M. Gómez-Alcántara, A. Cabeza, L. Moreno-Real, M. A. G. Aranda, A. Clearfield, *Microporous and Mesoporous Materials* **2006**, 88, 293
- [16] M. Hesse, M. Herbert, B. Zeeh, *Spektroskopische Methoden in der organischen Chemie, 7., überarbeitete Auflage*, Thieme.
- [17] A. Cabeza, M. A. G. Aranda, S. Bruque, D. M. Poojary, A. Clearfield, J. Sanz, *Inorg. Chem.* **1998**, 37, 4168
- [18] J. El Haskouri, C. Guillem, J. Latorre, A. Beltrán, D. Beltrán, P. Amorós, *Chem. Mater.* **2004**, 16, 4359
- [19] J. E. Haky, J. B. Brady, *Mater. Res. Bull.* **1997**, 32, 297
- [20] A. Clearfield, *Curr. Opin. Solid State Mater. Sci.* **2002**, 6, 495
- [21] D. M. Poojary, B. Zhang, P. Bellinghausen, A. Clearfield, *Inorg. Chem.* **1996**, 35, 4942
- [22] D. M. Poojary, B. Zhang, P. Bellinghausen, A. Clearfield, *Inorg. Chem.* **1996**, 35, 5254
- [23] B. Zhang, D. M. Poojary, A. Clearfield, *Inorg. Chem.* **1998**, 37, 1844
- [24] A. Clearfield, *Dalton Trans.* **2008**, 6089
- [25] A. Clearfield, *Dalton Trans.* **2008**, 44, 6089
- [26] A. Subbiah, D. Pyle, A. Rowland, J. Huang, R. A. Narayanan, P. Thiyagarajan, J. Zon, A. Clearfield, *J. Am. Chem. Soc.* **2005**, 127, 10826
- [27] A. Cabeza, M. d. M. Gómez-Alcántara, P. Olivera-Pastor, I. Sobrados, J. Sanz, B. Xiao, R. E. Morris, A. Clearfield, M. A. G. Aranda, *Microporous and Mesoporous Materials* **2008**, 114, 322
- [28] S. Kirumakki, S. Samarajeewa, R. Harwell, A. Mukherjee, R. H. Herber, A. Clearfield, *Chem. Commun.* **2008**, 5556
- [29] S. Kirumakki, J. Huang, S. Subbiah, J. Yao, A. Rowland, B. Smith, A. Mukherjee, S. Samarajeewa, A. Clearfield, *J. Mater. Chem.* **2009**, 19, 2593
- [30] J. Huang, A. Subbiah, D. Pyle, A. Rowland, B. Smith, A. Clearfield, *Chem. Mater.* **2006**, 18, 5213
- [31] K. S. W. Sing, D. H. Everett, R. A. W. Haul, L. Moscou, R. A. Pierotti, J. Rouquerol, T. Siemieniewska, *Pure Appl. Chem.* **1985**, 57, 603
- [32] F. Rouquerol, J. Rouquerol, K. Sing, *Adsorption by Powders and Porous Solids; Academic Press: London*, **1999**.
- [33] A. Ansón, M. Benham, J. Jagiello, M. A. Callejas, A. M. Benito, W. K. Maser, A. Züttel, P. Sudan, M. T. Martínez, *Nanotechnology* **2004**, 15, 1503

- [34] S. Brunauer, P. H. Emmett, E. Teller, *J. Am. Chem. Soc.* **1938**, *60*, 309
- [35] I. Langmuir, *J. Am. Chem. Soc.* **1916**, *38*, 2221
- [36] J. El Haskouri, C. Guillem, J. Latorre, A. Beltrán, D. Beltrán, P. Amorós, *Eur. J. Inorg. Chem.* **2004**, 1804
- [37] C. Lastoskie, K. E. Gubbins, N. Quirke, *J. Phys. Chem.* **1993**, *97*, 4786
- [38] C. Lastoskie, K. E. Gubbins, N. Quirke, *Langmuir* **1993**, *9*, 2693
- [39] R. Coontz, B. Hanson, *Science* **2004**, *305*, 957.
- [40] L. Schlapbach, A. Züttel, *Nature* **2001**, *414*, 353
- [41] R. F. Service, *Science* **2004**, *305*, 958
- [42] J. L. C. Rowsell, O. M. Yaghi, *Angew. Chem. Int. Ed.* **2005**, *44*, 4670
- [43] L. Schlapbach, *MRS Bull.* **2002**, *27*, 675
- [44] U. Eberle, M. Felderhoff, F. Schueth, *Angew. Chem. Int. Ed.* **2009**, *48*, 6608
- [45] B. Panella, M. Hirscher, S. Roth, *Carbon* **2005**, *43*, 2209
- [46] Y. Gogotsi, R. K. Dash, G. Yushin, T. Yildirim, G. Laudisio, J. E. Fischer, *J. Am. Chem. Soc.* **2005**, *127*, 16006
- [47] G. Yushin, R. Dash, J. Jagiello, J. E. Fischer, Y. Gogotsi, *Adv. Funct. Mater.* **2006**, *16*, 2288
- [48] A. C. Dillon, K. M. Jones, T. A. Bekkedahl, C. H. Kiang, D. S. Bethune, M. J. Heben, *Nature* **1997**, *386*, 377
- [49] H. G. Schimmel, G. J. Kearley, M. G. Nijkamp, C. T. Visser, K. P. de Jong, F. M. Mulder, *Chem. Eur. J.* **2003**, *9*, 4764
- [50] A. W. C. van den Berg, P. P. Pescarmona, J. Schoonman, J. C. Jansen, *Chem. Eur. J.* **2007**, *13*, 3590
- [51] A. Zecchina, S. Bordiga, J. G. Vitillo, G. Ricchiardi, C. Lamberti, G. Spoto, M. Bjoergen, K. P. Lillerud, *J. Am. Chem. Soc.* **2005**, *127*, 6361
- [52] H. W. Langmi, A. Walton, M. M. Al-Mamouri, S. R. Johnson, D. Book, J. D. Speight, P. P. Edwards, I. Gameson, P. A. Anderson, I. R. Harris, *J. Alloys Compd.* **2003**, *356* - 357.
- [53] J. L. C. Rowsell, O. M. Yaghi, *Microporous Mesoporous Mater.* **2004**, *73*, 3
- [54] U. Mueller, M. Schubert, F. Teich, H. Puetter, K. Schierle-Arndt, J. Pastré, *J. Mater. Chem.* **2006**, *16*, 626
- [55] H. M. El-Kaderi, J. R. Hunt, J. L. Mendoza-Cortes, A. P. Cote, R. E. Taylor, M. O'Keeffe, O. M. Yaghi, *Science* **2007**, *316*, 268
- [56] A. P. Côté, A. I. Benin, N. W. Ockwig, M. O'Keeffe, A. J. Matzger, O. M. Yaghi, *Science* **2005**, *310*, 1166
- [57] P. M. Budd, A. Butler, J. Selbie, K. Mahmood, N. B. McKeown, B. Ghanem, K. Msayib, D. Book, A. Walton, *Phys. Chem. Chem. Phys.* **2007**, *9*, 1802
- [58] P. Bénard, R. Chahine, *Langmuir* **2001**, *17*, 1950
- [59] G. G. Tibbetts, G. P. Meisner, C. H. Olk, *Carbon* **2001**, *39*, 2291
- [60] M. G. Nijkamp, J. Raaymakers, A. J. Van Dillen, K. P. De Jong, *Applied Physics A: Materials Science & Processing* **2001**, *72*, 619
- [61] M. Becher, M. Haluska, M. Hirscher, A. Quintel, V. Skakalova, U. Dettlaff-Weglikovska, X. Chen, M. Hulman, Y. Choi, S. Roth, *C.R. Phys.* **2003**, *4*, 1055
- [62] M. Rzepka, P. Lamp, M. A. De La Casa-Lillo, *J. Phys. Chem. B* **1998**, *102*, 10894
- [63] A. Züttel, P. Sudan, P. Mauron, T. Kiyobayashi, C. Emmenegger, L. Schlapbach, *Int. J. Hydrogen Energy* **2002**, *27*, 203
- [64] G. Gundiah, A. Govindaraj, N. Rajalakshmi, K. S. Dhathathreyan, C. N. R. Rao, *J. Mater. Chem.* **2003**, *13*, 209
- [65] A. Corma, M. J. Diaz-Cabanas, J. L. Jordá, C. Martinez, M. Moliner, *Nature* **2006**, *443*, 842
- [66] J. L. C. Rowsell, A. R. Millward, K. S. Park, O. M. Yaghi, *J. Am. Chem. Soc.* **2004**, *126*, 5666
- [67] A. Clearfield, *Curr. Opin. Solid State Mater. Sci.* **1996**, *1*, 268
- [68] K. Maeda, *Microporous Mesoporous Mater.* **2004**, *73*, 47
- [69] A. Vioux, J. Le Bideau, P. H. Mutin, D. Leclercq, *Top Curr. Chem.* **2004**, *232*, 145
- [70] J. Le Bideau, C. Payen, P. Palvadeau, B. Bujoli, *Inorg. Chem.* **1994**, *33*, 4885
- [71] S. Drumel, P. Janvier, P. Barboux, M. Bujoli-Doeuff, B. Bujoli, *Inorg. Chem.* **1995**, *34*, 148
- [72] J. L. C. Rowsell, O. M. Yaghi, *Angew. Chem. Int. Ed.* **2005**, *44*, 4670

5 Conclusions and Outlook

In this work, non-covalent networks of phosphonic acid-containing molecules have been obtained for different applications. On the one hand, hydrogen bonded networks of phosphonated small molecules have been prepared to be used as proton conductors for FC working at intermediate temperatures. On the other hand, crystalline and microporous ionic networks composed of metal cations and phosphonated molecules have been obtained and their porous properties have been studied. In addition, models for pore formation have been proposed.

5.1 Solid State Proton-Conducting Materials

The incorporation of phosphonic acid groups in small molecules opens up a wide field of new materials with promising proton transport properties. The study presented in the first part of the thesis provides a novel straightforward route towards reaching high proton conductivity in the solid state by the use of small molecules. With an understanding of how the molecules pack, insights into how well protons are able to flow through a material are gained and thereby one can develop design rules for more optimized molecular entities. From this work, the following points have been deduced:

1. Small molecules can replace polymeric membranes and be used as proton conductors in FCs working at intermediate temperatures. Hexakis(*p*-phosphonatophenyl)benzene is a crystalline 3D proton conductor. The compound can be seen as an inverse proton-conducting cable due to its columnar structure which provides a proton-conducting periphery. Under 1 bar H₂O atmosphere a constant value of $3.2 \cdot 10^{-3}$ S/cm is reached. These results suggest that this material tested in a MEA should give a good performance with respect to its proton conductivity and chemical and thermal stability.

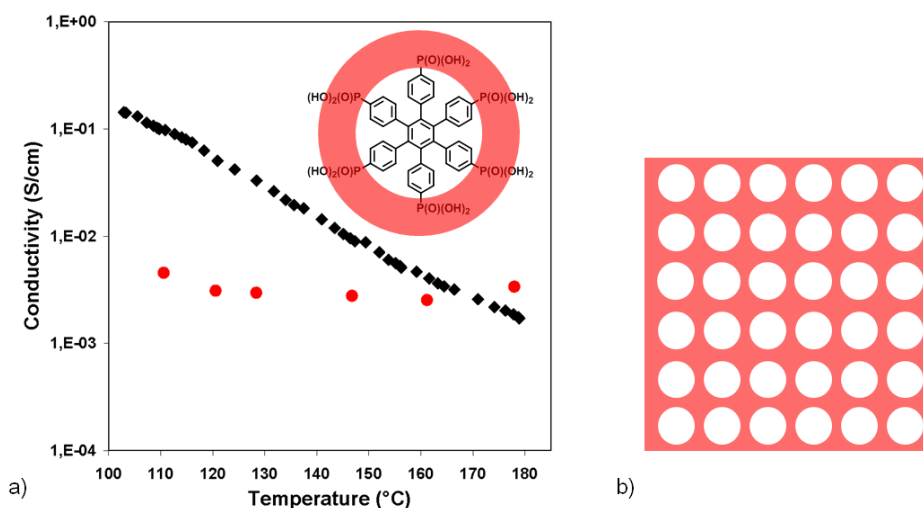


Fig. 5.1: a) Proton conductivity of hexakis(*p*-phosphonatophenyl)benzene under 1 bar H₂O atmosphere (●) and this of Nafion® 117 (◆) and b) schematic representation of the 3D proton-conducting phase in the material (in red).

2. To have phosphonic acid-containing organic molecules of high proton conductivity the molecules must organize in such a way that a nanophase separation between the hydrophobic and hydrophilic domains leading to a continuous acidic phase is formed. Therefore from all the synthesized compounds presented in Section 3.3, the ones which self-organize into columns are the best candidates as PEM since a high concentration of protons is built up around the hydrophobic cores providing high proton conductivity. Furthermore these systems exhibit a conductivity which is temperature independent. In addition, in this study it has been concluded that crystallinity is an important but not a determining factor to have high proton conductivity.
3. The modification of hexakis(*p*-phosphonatophenyl)benzene either by changing the phosphonic acid groups from the *para* to the *meta* positions or by introducing alkyl chains affords products of lower crystallinity and lower proton conductivity. On the one hand, the acidic moieties in the *meta* position can arrange either above or below the plane of the phenyl ring so that regions of a low concentration of phosphonic acid functions might form being the reason for the lower proton conductivity with respect to hexakis(*p*-phosphonatophenyl)benzene. On the other hand the introduction of alkyl

chains provides a material in which the transport of protons is based on the diffusion of water molecules.

4. Increasing the size of the hydrophobic periphery of the HPB has a profound impact on proton conductivity. Molecules of lower crystallinity are obtained which form layered structures. The concentration of protons is lower than the one found for hexakis(*p*-phosphonatophenyl)benzene due to the increased size of the hydrophobic core provoking lower conductivities.

The work presents an innovative and novel approach towards reaching high proton conductivity in the solid state consisting of using small molecules which by self-assembly provide a continuous proton-conducting phase. So far, hexakis(*p*-phosphonatophenyl)benzene is the first example of a crystalline proton conductor exhibiting high and constant performance in the solid state. However even higher proton conductivity values may be obtained by increasing the phosphonic acid density at the periphery of the HPB. Furthermore the introduction of phosphonic acid functions at the periphery of HBC molecules may conduce to molecules which possess at the same time proton- and electron-conducting properties due to the phosphonic acid moieties and the aromatic core respectively. The compounds could be deposited under vacuum at the electrodes so that they act as compatibilizers at the interface between the proton-conducting material and the electrodes (see Figure 5.2). It is expected that by applying these molecules as compatibilizers the problems deriving from the three-phase MEA system could be avoided.

In addition, the phosphonated small molecules presented in the first part of the thesis could be envisaged as additives in either sulfonated or phosphonated membranes to create organic-organic nanocomposites. They could be introduced in the membranes via dispersion in the form of ester and be subsequently hydrolyzed.

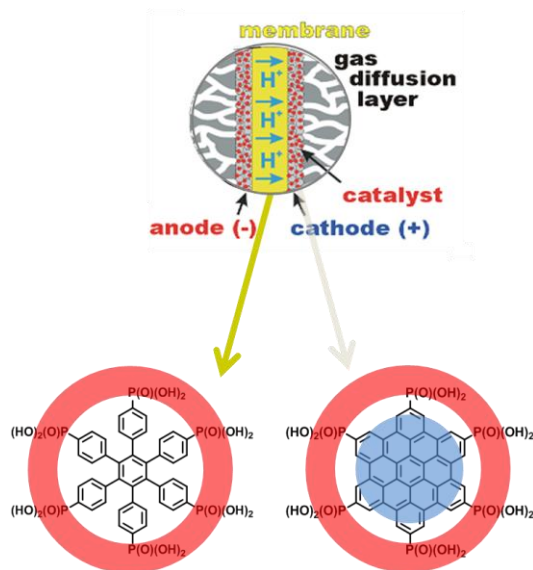


Fig. 5.2: Schematic representation of a MEA. The red circle represents the proton-conducting phase whereas the blue ones the electron-conducting part.

5.2 Linkers for Porous Hybrid Materials

In the second part, 1,3,5-tris(*p*-phosphonatophenyl)benzene has been used as linker in the synthesis of phosphonated open-frameworks. Robust solids are formed due to the ionic interactions between the positively charged metal cations and the negatively charged phosphonic acid groups. The key results of this work are that:

1. 1,3,5-Tris(*p*-phosphonatophenyl)benzene can be used as linker to obtain porous hybrid materials. It is the first time that a trisphosphonated organic molecule is applied to obtain microporous phosphonated open-frameworks.
2. Porosity arises from the special growth pattern of these materials. It is possible to obtain a microporous and at the same time crystalline ionic network of phosphonated molecules only by combining a linker and a connector of the same geometry and functionality.

It has been concluded that:

- The combination of a trivalent metal and a trivalent triangular linker offers the perfect stoichiometry and geometry, so that in the case of aluminum based

trisphosphonates a hexagonal lattice is formed (see Figure 5.3a). Microporous crystallites are produced as shown in Figure 5.3b. The regularity of the pores is assured due to the crystalline nature of the materials. Specific surface areas up to 662 m²/g have been obtained which are higher than the published results for trisphosphonated hybrid materials synthesized by a non-MCM-type approach. For the first time, a phosphonated organic-inorganic open-framework is produced which combines high microporosity and crystallinity.

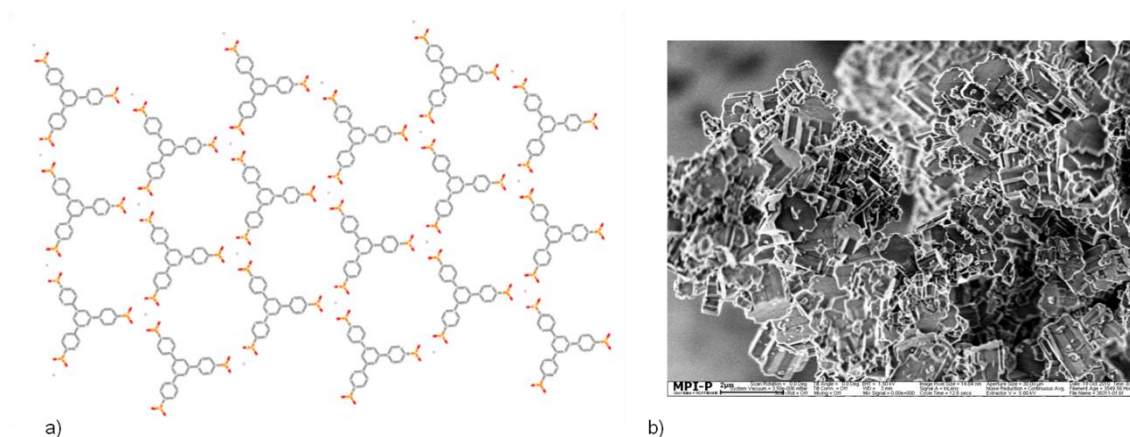


Fig. 5.3: a) Representation of the hexagonal lattice of aluminum based trisphosphonate solids; b) SEM micrograph of an aluminum based trisphosphonate compound (M14-R11).

- The use of tetravalent metals as connectors affords amorphous porous materials since metal and linker present different geometries and functionalities. Most probably porosity is due to the uneven growth rates of layers during particle formation. Heterogeneity of the pore size is obtained due to the non-crystalline nature of the materials and gives rise in the case of tin based solids to mesoporosity. The zirconium based material tested presents a more elevated affinity for hydrogen as well as a higher hydrogen storage capacity than the aluminum based compound.
- Amorphous and non-porous materials are obtained by using divalent metals as connectors. This might be due to the unfavorable divalent nature of the metal which avoids the formation of a hexagonal lattice like in the case of the aluminum based compounds and of layered structured like in the case of the zirconium and tin based materials.

In this study it has proven feasible to obtain a phosphonated open-framework which presents at the same time crystalline and porous properties. This is only possible by the combination of a linker and a connector which exhibit the same functionality and geometry. In the specific case of using 1,3,5-tris(*p*-phosphonatophenyl)benzene as linker, Al³⁺ has proven to be an adequate connector. These investigations are of relevance since they provide new information about the parameters which are needed to connect crystallinity and porosity in phosphonated hybrid materials. Therefore, they can help to develop design rules for more optimized molecular entities. Optimization of many parameters can afford phosphonated open-framework materials with higher surface areas or hydrogen storage capacities. Since the perfect stoichiometry and geometry have been reached by using aluminum as connector, the work could be extended to other trivalent metal cations like Fe³⁺. Furthermore, it would be of interest to analyze the impact the linker has on the porous properties of the final compounds by applying the other molecules which have been designed as proton conductors in this dissertation. Besides, the phosphonated open-framework materials presented in this dissertation could be envisaged as catalysts for the dehydration of ethanol into ethylene.

6 Experimental Part

6.1 General Methods

6.1.1 Chemicals and Solvents

All used chemicals and solvents were obtained from the companies ABCR, Acros, Aldrich, Alpha-Aesar, Fluka, Lancaster, Merck and Strem. Unless otherwise mentioned, they were used as obtained.

6.1.2 Chromatography

Preparative column chromatography was performed on silica gel from Merck with a grain size of 63 - 200 μm (silica gel) or 40 - 63 μm (flash silica gel, Geduran Si 60). For analytical thin layer chromatography (TLC), silica gel coated substrates "60 F254" from Merck were used. Compounds were detected by fluorescence quenching at 254 nm, self-fluorescence at 366 nm or staining in an iodine vapor chamber. For eluents, analytically pure solvents (p.a. or technical grade) were distilled prior to the use.

6.1.3 Inert Atmosphere

Oxygen or moisture sensitive reactions were carried out in an argon atmosphere (Westfalen AG). If not mentioned specifically, reactions were degassed by bubbling a stream of argon through the reaction mixture.

6.2 Analytical Techniques

6.2.1 Mass Spectrometry

Field-desorption mass spectra were obtained on a VG Instruments ZAB 2-SE-FPD spectrometer.

6.2.2 NMR Spectroscopy

^1H -NMR, ^{13}C -NMR, ^{31}P -NMR, H,H-COSY and C,H-COSY experiments were recorded in the listed deuterated solvents on a Bruker DPX 250, Bruker AMX 300, Bruker DRX 500 or a Bruker DRX 700 spectrometer. The deuterated solvent was used as an internal standard, CD_2Cl_2 was set to $\delta\text{H} = 5.32$ ppm and $\delta\text{C} = 54.00$ ppm, THF to $\delta\text{H} = 3.58$ ppm and $\delta\text{C} = 67.57$ ppm, DMSO to $\delta\text{H} = 2.50$ ppm and $\delta\text{C} = 39.51$ ppm, $\text{C}_2\text{D}_2\text{Cl}_4$ to $\delta\text{H} = 5.91$ ppm and $\delta\text{C} = 74.20$ ppm, $(\text{CD}_3)_2\text{CO}$ to $\delta\text{H} = 2.05$ ppm and $\delta\text{C} = 29.84$ and D_2O to $\delta\text{H} = 4.79$ ppm.^[1, 2]

6.2.3 Elemental Analysis

Elemental analysis of solid samples was carried out on a Foss Heraeus Vario EL as a service of the Institute for Organic Chemistry, Johannes Gutenberg-Universität of Mainz. Liquid compounds or oils were not analyzed because of the difficulties to remove residual solvents and atmospheric gases like CO_2 .

6.2.4 Infrared Spectroscopy

Infrared spectroscopy was measured on a Nicolet 730 FT-IR spectrometer in the evanescence field of a diamond. The sample was deposited as pristine material on the diamond crystal and pressed on it with a stamp. 64 measurements were recorded for each sample, the background was subtracted.

6.2.5 X-Ray Scatting

Powder X-ray diffraction measurements were performed on a using a Siemens D 500 Kristalloflex diffractometer with a graphite-monochromatized CuK α X-ray beam, emitted from a rotating Rigaku RU-300 anode.

6.2.6 Wide Angle X-Ray Scattering

The WAXS measurements were made with a standard copper anode (2.2 kW) source with a pinhole collimator equipped with an X-ray mirror (Osmic type CMF15-sCu6) and a Bruker detector (High-star) with 1024·1024 pixels.

Angular range: 2 - 30°

Resolution= 0.07°

Intensity: 2·10⁶ Counts/s

Beam divergence: $\Delta\theta = 0.4^\circ$

Suppression of the Cu-K β -radiation: $\Delta E/E < 0.04$

6.2.7 Two-Dimensional Wide Angle X-Ray Scattering

The two-dimensional wide-angle X-ray diffraction experiments were performed by means of a rotating anode (Rigaku 18 kW) X-ray beam with a pinhole collimation and a 2D Siemens detector with a beam diameter of ca 1 mm. A double graphite monochromator for the Cu-K α radiation ($\lambda = 0.154$ nm) was used.

6.2.8 Thermal Gravimetric Analysis

Thermal gravimetric analysis (TGA) data were acquired with Mettler instrument (TGA/SDTA 851e) at a heating rate of 10 K/min. The volatile products of the TGA experiments were analyzed at a heating rate of 10 K/min under Helium atmosphere using a Pfeiffer ThermoStar mass spectrometer.

6.2.9 Melting Points

Melting points were determined on a Büchi hot stage apparatus and were uncorrected.

6.2.10 Single Crystal Analysis

The single crystal analysis was performed on a Nonius-KCCD diffractometer with a Mo-K α ($\lambda = 0.71923$ Å, graphite monochromatized) at a temperature of 150 K. The structures were solved by direct methods (Shelxs) and refined on F with anisotropic temperature factors for all non-hydrogen atoms. The H atoms were refined with fixed isotropic temperature factors in the riding mode.

6.2.11 Impedance Spectroscopy

Through-plane as well as in-plane proton conductivity was measured by dielectric spectroscopy in a two-electrode geometry using an SI 1260 impedance/gain-phase analyzer. A 100 mg uniaxially pressed pellet of 5.5 mm diameter and 2.1 mm thickness was used. Conductivity measurements in pure water vapor ($p(\text{H}_2\text{O}) = 105$ Pa) above 100 °C were carried out in a double-wall temperature-controlled glass chamber with a water inlet and outlet, both heated by a small furnace. To constantly flush the sample with pure H₂O atmosphere, water was evaporated, the gas subsequently adjusted to the desired temperature and piped through the heated inlet of the glass oven. A pressure of 105 Pa adapts itself due to the small outlet of the oven against ambient. It should be noted that the RH, set by a H₂O atmosphere at 105 Pa, decreases with increasing temperature according to the table of vapor pressure. 120 °C corresponds to a RH of ~ 50 %, at 150 °C the RH is close to 20 %. In the case of proton conductivity measurements as a function of RH, the humidity of air during data acquisition was set by mixing dry nitrogen with humidity saturated nitrogen. The RH was measured using a Sensiron SHT15 sensor.

Nafion® 117 membrane was pre-treated by boiling in deionized water for 1 h, boiling in 3 % H₂O₂ for 1 h, rinsing in water repeatedly, boiling in 0.5 M H₂SO₄ for 1 h and rinsing again in water. The membrane was stored in deionized water.

6.2.12 Water Uptake

In order to determine the amount of water adsorption, the sample was stored under an atmosphere of fixed humidity and temperature for 3 days. The humidity was set by saturated salt solutions according to literature data.^[3] Water desorption was determined by storing the samples under 98 % RH for 3 weeks and then transferring them to atmospheres of lower fixed humidity for 3 days at constant temperature. Water sorption

was measured on a Mettler MX5 microbalance until constant weight was obtained; the water sorption was calculated from the following equation:

$$\text{Water sorption} = \frac{W_{\text{wet}} - W_{\text{dry}}}{W_{\text{dry}}} \times 100$$

6.2.13 Potentiometric Titration

Potentiometric titrations were conducted with a Metrohm Titranda 836 at 25 °C. The compound was allowed to agitate during 24 h in 50 mL of a 3 M KCl solution and was titrated during at least 48 h against a 0.01 M NaOH solution.

6.2.14 Nitrogen Sorption

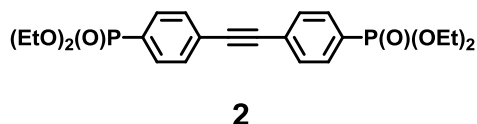
Nitrogen sorption experiments and micropore analysis were conducted at -195.8 °C using an Autosorb-1 from Quantachrome Instruments. Before sorption measurements, the samples were degassed in vacuum overnight at 150 °C. NLDFT pore-size distributions were determined using the carbon/slit-cylindrical pore model of the Quadrawin software. Pore volumes at $p/p_0 = 0.1$ and $p/p_0 = 0.8$ were converted into the corresponding liquid volumes using a nitrogen density of $1.25 \cdot 10^{-3} \text{ g/cm}^3$ (gaseous) and $8.10 \cdot 10^{-1} \text{ g/cm}^3$ (liquid).

6.2.15 Electron Microscopy

SEM measurements were performed on a LEO 1530 field emission scanning electron microscope.

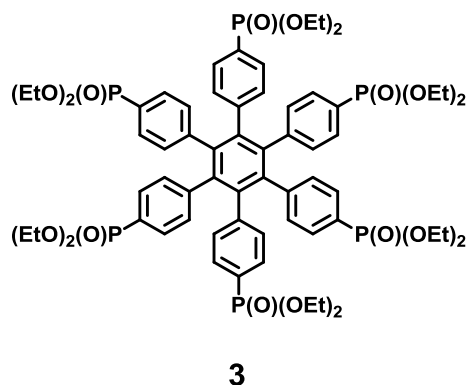
6.3 Hexakis(*p*-phosphonatophenyl)benzene

6.3.1 Bis(4-diethylphosphonatophenyl)acetylene



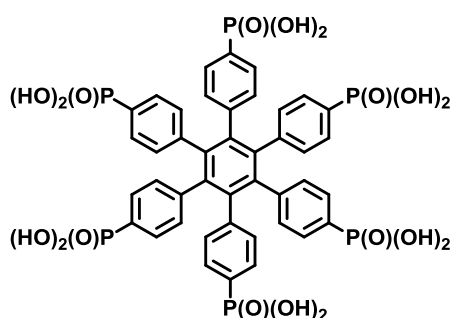
Bis(4-bromophenylacetylene) (**1**) (1.384 g, 4 mmol) was dissolved in anhydrous toluene (85 ml) and stirred under argon until it was dissolved. Diethyl phosphite (6.31 ml, 48 mmol) and triethylamine (4.92 ml, 48 mmol) were added and the mixture was degassed with Ar during 20 min; finally tetrakis(triphenylphosphine)palladium (0) (1.16 g, 1 mmol) was added with a high argon purge and the mixture heated at 75 °C overnight. After cooling to room temperature, diethyl ether was added to the reaction mixture to precipitate the triethylamine hydroiodide, which was removed by filtration. The filtrate was evaporated to give a yellowish oil. The crude product was purified by column chromatography on silica gel (ethyl acetate - methanol 10:1). 1.47 g (82 %) of a white solid was obtained. MS (FD, 8 kV) $m/z = 450.5$ g/mol - calculated: 450.4 g/mol for $C_{22}H_{28}O_6P_2$; 1H -NMR (250 MHz, CD_2Cl_2 , RT, δ in ppm) 7.85 - 7.71 (m, 4 H), 7.69 - 7.54 (m, 4 H), 4.21 - 3.91 (m, 8 H), 1.36 - 1.20 (m, 12 H); ^{13}C -NMR (75 MHz, CD_2Cl_2 , RT, δ in ppm) 132.26, 132.15, 132.13, 131.95, 130.98, 128.48, 127.19, 127.14, 91.17, 62.77, 62.70, 16.70, 16.62; ^{31}P NMR (202 MHz, RT, δ in ppm) 15.20 (s). EA found 58.81 % C, 6.30 % H – calculated 58.67 % C, 6.27 % H, 21.31 % O, 13.75 % P.

6.3.2 Hexakis(*p*-diethylphosphonatophenyl)benzene



Bis(4-diethylphosphonatophenyl)acetylene (**2**) (2.86 g, 6.341 mmol) and dioxane (39 ml) were introduced in a round flask and the solution was degassed with Ar during 10 min. $\text{Co}_2(\text{CO})_8$ (228.2 mg, 0.6341 mmol) was introduced and the mixture heated at 125 °C during the night under Ar atmosphere. The solvent was evaporated under vacuum. The dark blue oil was purified by column chromatography (ethyl acetate - methanol 7:3) to give 1.96 g (69 %) of an orange-like solid. MS (FD, 8 kV) $m/z = 1352.0$ g/mol - calculated: 1351.20 g/mol for $\text{C}_{66}\text{H}_{84}\text{O}_{18}\text{P}_6$; $^1\text{H-NMR}$ (75 MHz, CD_2Cl_2 , RT, δ in ppm) 7.29 (dd, $J = 8.2$ Hz, 13.0, 12 H), 6.98 - 6.91 (m, 12 H), 3.93 - 3.77 (m, 24 H), 1.16 (t, $J = 7.1$ Hz, 36 H); ^{13}C NMR (75 MHz, CD_2Cl_2 , RT, δ in ppm) 144.10, 140.26, 131.81, 131.69, 131.03, 130.95, 127.80, 126.31, 62.47, 62.42, 16.64, 16.60; ^{31}P NMR (284 MHz, CD_2Cl_2 , RT, δ in ppm) 17.31 (s). EA found 57.44 % C, 6.25 % H – calculated 58.67 % C, 6.27 % H, 21.31 % O, 13.75 % P.

6.3.3 Hexakis(*p*-phosphonatophenyl)benzene



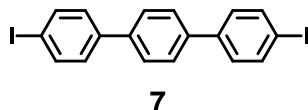
4

Hexakis(*p*-diethylphosphonatophenyl)benzene (**3**) (1.92 g, 1.418 mmol) was treated with trimethylsilylbromide (2.605 g, 2.364 mmol) in 150 ml of DCM for 48 h. Then, DCM was evaporated and the product of this first step dried under vacuum. The product of the first step was treated with MeOH (100 ml) for another 48 h. 1.4 g (97 % yield) of a yellowish powder were obtained. (Mp: 329 °C); ^1H NMR (75 MHz, DMSO, 100 °C, δ in ppm) 7.16 (dd, $J = 0.75$ and 3.0 Hz, 12 H), 7.01 (dd, $J = 0.75$ and 2.25 Hz, 12 H); ^{13}C NMR (126 MHz, 100 °C, δ in ppm) 141.49 (d, $J = 3.0$), 139.14 (s), 130.93 (d, $J = 183.3$), 129.99 (d, $J = 9.1$), 128.54 (d, $J = 10.0$); ^{31}P NMR (121 MHz, 100 °C, δ in ppm) 13.48 (s); EA found 47.89 % C, 3.1 % H - calculated: 49.72 % C, 3.58 % H, 28.39 % O, 18.32 % P.ⁱ

ⁱ Since the compound is a crystal hydrate, it is not possible to determine its exact composition.

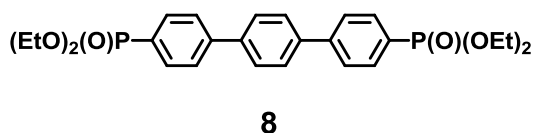
6.4 The Influence of Geometry and the Number of Acidic Functions

6.4.1 4,4'-Diiodo-*p*-terphenyl^[4]



A mixture of *p*-terphenyl (4.65 g, 20 mmol), iodine (5.076 g, 20 mmol) and H_5IO_6 (1.86 g, 8 mmol) was added to a solvent mixture of AcOH/ H_2O / H_2SO_4 (10:2:0.3 vol. (121.95/24.39/3.66 ml), 75 ml) and heated to 100 °C with stirring. A fresh colored precipitated gradually formed and thickened and later more of the same solvent mixture was added (38 ml) to maintain efficient stirring. The reaction mixture was heated for 24 h and subsequently cooled and filtered. The resulting light-tan product was washed with 10 % aq sodium thiosulfate (500 ml) and then dried. The crude product was purified by refluxing with two separate portions of toluene (2 x 250 ml) each for 15 min. The dissolved product crystallized from the hot extracts in white flaky crystals. The undissolved fraction was then extracted in a Soxhlet apparatus for 48 h using toluene (150 ml) and upon cooling yielded more of the same crystalline product. Yield: 60 %. MS (FD, 8 kV) $m/z = 481.9$ g/mol - calculated: 482.10 g/mol for $C_{18}H_{12}I_2$; 1H NMR (250 MHz, $CDCl_3$, RT, δ in ppm) 7.81 (d, $J = 8.5$ Hz, 4 H), 7.67 (s, 4 H), 7.41 (d, $J = 8.5$ Hz, 4 H); ^{13}C NMR (75 MHz, CD_2Cl_2 , RT, δ in ppm) 138.53, 129.54, 129.36, 128.73, 127.87; IR: $\nu = 3090, 3060$ (CH), 1580, 1470, 1380 (C=C arom), 1130, 1060, 995, 796 (CH) cm^{-1} .

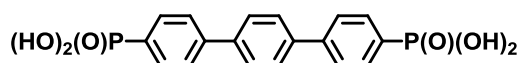
6.4.2 4,4'-Diethylphosphonato-*p*-terphenyl



4,4'-Diiodo-*p*-terphenyl (**7**) (0.48 g, 1 mmol) was dissolved in anhydrous toluene (100 ml) and stirred under argon until it is dissolved. Diethyl phosphite (0.56 g, 0.53 ml,

4 mmol) and triethylamine (0.41 g, 0.56 ml, 4 mmol) were added with a syringe, and the mixture is stirred for an additional 10 min; finally with a high argon purge tetrakis(triphenylphosphine)palladium (0.2918 g, 0.25 mmol) was added and the mixture heated at 75 °C during 12 h. After cooling to RT diethyl ether was added to the reaction mixture to precipitate the triethylamine hydroiodide, which was removed by filtration. The filtrate was evaporated to give a yellow oil. The crude product was purified by column chromatography on silica gel with ethyl acetate as eluent. Yield: 97 %. MS (FD, 8 kV) $m/z = 501.9$ g/mol - calculated: 502.48 g/mol for $C_{26}H_{32}O_6P_2$; 1H NMR (250 MHz, CD_2Cl_2 , RT, δ in ppm) 7.88 (dd, $J = 8.3$ Hz, 12.5, 4 H), 7.81 – 7.71 (m, 8 H), 7.71 – 7.43 (m, 4 H), 4.24 – 3.95 (m, 8 H), 1.40 – 1.20 (m, 12 H); ^{13}C NMR (75 MHz, CD_2Cl_2 , RT, δ in ppm) 132.91, 132.78, 128.98, 128.36, 127.67, 127.47, 62.71, 16.80; ^{31}P NMR (202 MHz, CD_2Cl_2 , RT, δ in ppm) 18.75 (s).

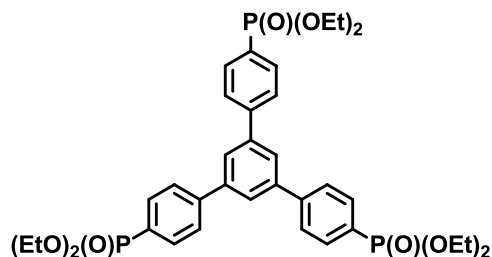
6.4.3 (*p,p'*-Terphenyl-4,4''-diyl)bisphosphonic acid



9

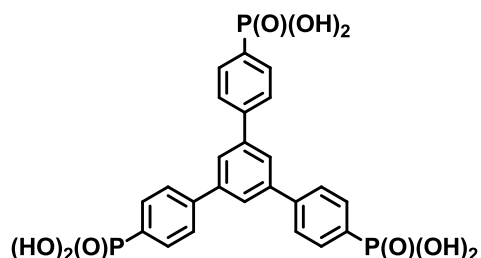
4,4'-Diethylphosphonato-*p*-terphenyl (**8**) (0.486 g, 0.967 mmol) was treated with trimethylsilylbromide (1.209 g, 7.74 mmol) in 150 ml of DCM for 48 h. Then, DCM was evaporated and the product of this first step dried under vacuum. The product of the first step was treated with MeOH (200 ml) for another 48 h. The final product was washed with water several times. Yield: 72 % (272 mg). 1H NMR (250 MHz, DMSO, RT, δ in ppm) 7.88 – 7.72 (m, 12 H); ^{13}C NMR (75 MHz, DMSO, RT, δ in ppm) 141.67, 138.85, 131.27, 128.99, 127.44, 126.35; ^{31}P NMR (202 MHz, DMSO, RT, δ in ppm) 13.49 (s); EA found 54.51 % C, 3.4 % H - calculated: 55.4 % C, 4.13 % H, 24.6 % O, 15.87 % P.

6.4.4 1,3,5-Tris(*p*-diethylphosphonatophenyl)benzene

**11**

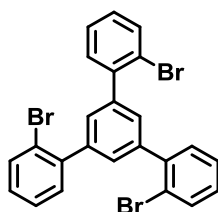
1,3,5-Tris(4-bromophenyl)benzene (**10**) (1.0 g, 1.84 mmol) was dissolved in anhydrous toluene (100 ml) and stirred under argon until it is dissolved. Diethyl phosphite (9.15 g, 8.54 ml, 66.3 mmol) and triethylamine (6.7 g, 9.24 ml, 66.3 mmol) were added with a syringe, and the mixture is stirred for an additional 10 min; finally with a high argon purge tetrakis(triphenylphosphine)palladium (0.76 g, 0.66 mmol) was added and the mixture heated at 75 °C during 12 h. After cooling to RT diethyl ether was added to the reaction mixture to precipitate the triethylamine hydroiodide, which was removed by filtration. The filtrate was evaporated to give a yellow oil. The crude product was purified by column chromatography on silica gel (ethyl acetate - MeOH 9:1). Yield: 75 %. MS (FD, 8 kV) $m/z = 713.7$ g/mol - calculated: 714.66 g/mol for $C_{36}H_{45}O_9P_3$; 1H NMR (250 MHz, CD_2Cl_2 , RT, δ in ppm) 8.03 – 7.72 (m, 12 H), 4.26 – 3.96 (m, 12 H), 1.38 – 1.23 (m, 18 H); ^{13}C NMR (75 MHz, CD_2Cl_2 , RT, δ in ppm) 144.92, 142.20, 132.98, 128.03, 127.52, 126.62, 62.75, 16.81; ^{31}P NMR (202 MHz, CD_2Cl_2 , RT, δ in ppm) 18.75 (s).

6.4.5 1,3,5-Tris(*p*-phosphonatophenyl)benzene

**12**

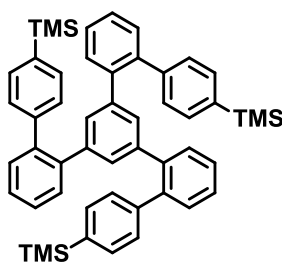
1,3,5-Tris(*p*-diethylphosphonatophenyl)benzene (**11**) (0.5 g, 0.70 mmol) was treated with trimethylsilylbromide (0.6 ml, 4.2 mmol) in 150 ml of DCM for 48 h. Then, DCM was evaporated and the product of this first step dried under vacuum. The product of the first step was treated with MeOH (200 ml) for another 48 h. The final product was washed with water several times. A white foam-like solid was obtained. Overall Yield: 90 % (344 mg). ^1H NMR (250 MHz, DMSO, RT, δ in ppm) 8.01 (d, $J = 8.6$ Hz, 9 H), 7.82 (dd, $J = 8.2$ and 12.6 Hz, 6 H); ^{13}C NMR (75 MHz, DMSO, RT, δ in ppm) 142.15, 141.08, 132.19, 131.26, 127.06, 125.18; ^{31}P NMR (202 MHz, DMSO, RT, δ in ppm) 13.48 (s); EA found 52.25 % C, 3.99 % H - calculated: 52.76 % C, 3.87 % H, 26.36 % O, 17.01 % P.

6.4.6 1,3,5-Tris-2'-bromophenylbenzene^[5]

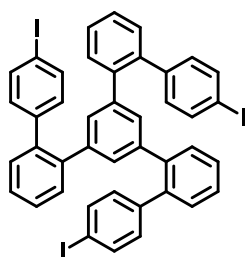


14

2-Bromoacetophenone (**13**) (20 g, 100.0 mmol) and trifluoromethanesulfonic acid 10 mol% were stirred at 130 °C until the total conversion of starting material (7 h). The resulting black solution was allowed to cool to RT and quenched by adding water. The mixture was then extracted with CH_2Cl_2 , and the organic layer was washed with water and brine, dried over MgSO_4 . The solvents were removed under vacuum and the residue was purified by column chromatography on silica gel (hexane - DCM 6:1) to afford 13.0 g (72 %) of a slight-yellow solid. Mp: 159 - 160 °C; MS (FD, 8 kV) $m/z = 543.80$ g/mol - calculated: 543.09 g/mol for $\text{C}_{24}\text{H}_{15}\text{Br}_3$; ^1H NMR (250 MHz, CD_2Cl_2 , RT, δ in ppm) 7.69 (d, $J = 7.8$ Hz, 3 H), 7.51 - 7.26 (m, 9 H), 7.22 (m, 3 H); ^{13}C NMR (75 MHz, CD_2Cl_2 , RT, δ in ppm) 142.26, 140.90, 133.59, 131.92, 130.05, 129.44, 127.99, 122.85; EA found 53.36 % C, 2.93 % H - calculated 53.08 % C, 2.78 % H, 44.14 % Br.

6.4.7 1,3,5-Tris[4''-(trimethylsilyl)-2'-biphenyl]ylbenzene^[5]**15**

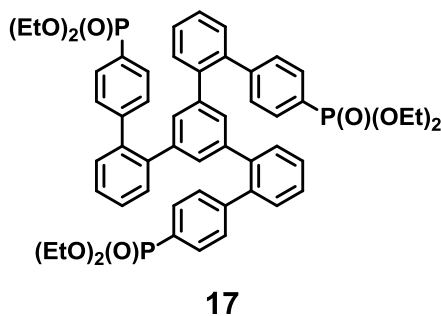
400 mg of 1,3,5-Tris-2'-bromophenylbenzene (**14**) (0.737 mmol), 515 mg 4-(trimethylsilyl) phenylboronic acid (2.652 mmol), 26 mg (3 mol %) Pd(PPh₃)₄, 1.02 g K₂CO₃, 25 ml toluene, 6 ml EtOH and 6 ml H₂O were added into a 50 ml Schlenk flask. The mixture was degassed by two "freeze-pump-thaw" cycles and then heated to reflux under argon overnight. After standard work-up and purification by column chromatography on silica gel (hexane - DCM 6:1), 514 mg white solid was obtained (93 %). MS (FD, 8 kV) m/z = 750.8 g/mol - calculated: 751.23 g/mol for C₅₁H₅₄Si₃; ¹H NMR (250 MHz, CD₂Cl₂, RT, δ in ppm) 7.47 (d, J = 8.2 Hz, 6 H), 7.33 - 7.30 (m, 6 H), 7.25 - 7.16 (m, 3 H), 7.02 (d, J = 7.8 Hz, 6 H), 6.74 - 6.70 (m, 6 H), 0.25 (s, 27 H); ¹³C NMR (75 MHz, CD₂Cl₂, RT, δ in ppm) 142.36, 141.11, 140.83, 140.61, 138.71, 133.23, 130.63, 130.20, 129.90, 127.74, 127.66, 0.988; EA found 81.45 % C, 7.18 % H - calculated 81.54 % C, 7.25 % H, 11.22 % Si.

6.4.8 1,3,5-Tris[4''-(iodo)-2'-biphenyl]ylbenzene^[5]**16**

500 mg of 1,3,5-Tris[4''-(trimethylsilyl)-2'-biphenyl]ylbenzene (**15**) (0.665 mmol) were dissolved in 130 ml CHCl₃, then degassed by bubbling through argon for 20 min, then 2.4 ml iodine monochloride (1.0 M in CH₂Cl₂) was added slowly. After stirring for 1 h,

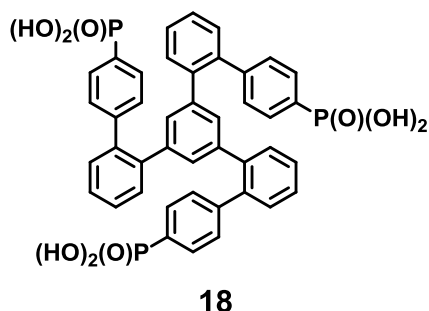
the reaction was quenched by adding aqueous sodium disulfite. The organic layer was washed by water three times and dried over MgSO_4 . The solution was concentrated to 10 ml and then 100 ml MeOH was added to precipitate the product. The white solid was collected and dried under vacuum to afford 564 mg product (93 %). Mp: 258 - 259 °C. MS (FD, 8 kV) $m/z = 912.8$ g/mol - calculated: 912.38 g/mol for $\text{C}_{42}\text{H}_{27}\text{I}_3$; ^1H NMR (250 MHz, CD_2Cl_2 , RT, δ in ppm) 7.66 - 7.61 (m, 6 H), 7.41 - 7.30 (m, 9 H), 6.86 - 6.83 (m, 3 H), 6.76 - 6.72 (m, 6 H), 6.67 (s, 3 H); ^{13}C NMR (75 MHz, CD_2Cl_2 , RT, δ in ppm) 141.66, 141.08, 140.45, 139.77, 137.37, 132.43, 130.78, 130.25, 130.18, 128.23, 127.97, 92.43; EA found 54.94 % C, 3.03 % H – calculated 55.29 % C, 2.98 % H, 41.73 % I.

6.4.9 1,3,5-Tris[4''-(diethylphosphonato)-2'-biphenyl]ylbenzene



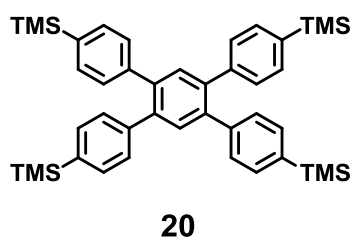
1,3,5-Tris(4''-iodo-2'-biphenyl)ylbenzene (**16**) (0.5 g, 0.65 mmol) was dissolved in anhydrous toluene (100 ml) and stirred under argon until it is dissolved. Diethyl phosphite (3.2 g, 3.0 ml, 23.3 mmol) and triethylamine (2.36 g, 3.25 ml, 23.3 mmol) were added with a syringe, and the mixture is stirred for an additional 10 min; finally with a high argon purge tetrakis(triphenylphosphine)palladium (0.270 g, 0.23 mmol) was added and the mixture heated at 75 °C during 12 h. After cooling to RT diethyl ether was added to the reaction mixture to precipitate the triethylamine hydroiodide, which was removed by filtration. The filtrate was evaporated to give a yellow oil. The crude product was purified by column chromatography on silica gel (ethyl acetate - MeOH 8:2). Yield: 63 %. MS (FD, 8 kV) $m/z = 942.6$ g/mol - calculated: 942.95 g/mol for $\text{C}_{54}\text{H}_{57}\text{O}_9\text{P}_3$; ^1H NMR (250 MHz, CD_2Cl_2 , RT, δ in ppm) 7.74 (dd, $J = 8.1$ and 13.0 Hz, 6 H), 7.46 – 7.24 (m, 9 H), 7.15 (dd, $J = 3.7$ and 7.9 Hz, 6 H), 6.79 (d, $J = 7.3$ Hz, 3 H), 6.71 (s, 3 H), 4.15 – 3.84 (m, 12 H), 1.22 (t, $J = 7.0$ Hz, 18 H); ^{13}C NMR (75 MHz, CD_2Cl_2 , RT, δ in ppm) 146.12, 140.84, 140.25, 139.73, 131.72, 130.43, 128.51, 128.01, 62.37, 16.50; ^{31}P NMR (202 MHz, CD_2Cl_2 , RT, δ in ppm) 17.78 (s).

6.4.10 1,3,5-Tris[4''-(phosphonato)-2'-biphenyl]ylbenzene



1,3,5-Tris[4''-diethylphosphonato-2'-biphenyl]ylbenzene (**17**) (0.3 g, 0.32 mmol) was treated with trimethylsilylbromide (0.29 g, 1.91 mmol) in 150 ml of DCM for 48 h. Then, DCM was evaporated and this product of the first step dried under vacuum. The product of the first step was treated with MeOH (200 ml) for another 48 h. The final product was washed with water several times. A white powder was obtained. Overall yield: 72 % (179 mg). ^1H NMR (75 MHz, DMSO, RT, δ in ppm) 7.70 (s, 6 H), 7.43 – 7.31 (m, 9 H), 7.06 (s, 6 H), 6.85 (s, 3 H), 6.66 (s, 3 H); ^{13}C NMR (126 MHz, DMSO, RT, δ in ppm) 143.02, 140.06, 139.15, 129.88, 129.54, 128.79, 127.61, 127.21; ^{31}P NMR (202 MHz, DMSO, RT, δ in ppm) 12.50 (s); EA found 63.12 % C, 3.48 % H – calculated 65.12 % C, 4.29 % H, 18.59 % O, 12.0 % P.

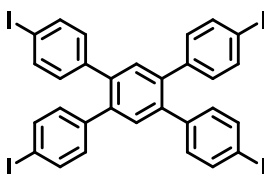
6.4.11 1,2,4,5-Tetrakis(4-trimethylsilylphenyl)benzene



A mixture of 1,2,4,5-tetrabromobenzene (**19**) (0,79 g, 1.89 mmol), palladium (II) acetate (0.022 g, 0.094mmol), tri(o-tolyl)phosphine (0.058 g, 0.19 mmol), phenylboronic acid (2.19 g, 11.32 mmol), toluene (60 ml), methanol (20 ml), and 2 M K_2CO_3 (16 ml) was heated at 75 °C during 12 h under a Argon atmosphere while maintaining with good stirring (tri(o-tolyl)phosphine was added once all the chemicals were in the flask under high Ar purge). After the reaction mixture was cooled to room temperature, it was poured into water and extracted with dichloromethane (3 x 100 ml).

The combined organic layer was dried with anhydrous Na_2SO_4 and evaporated to dryness. The crude product was further purified by column chromatography in petroleum ether to afford 0.52 g of a white powder (41.5 %). MS (FD, 8 kV) $m/z = 670.1$ g/mol - calculated: 671.22 g/mol for $\text{C}_{42}\text{H}_{54}\text{Si}_4$; ^1H NMR (250 MHz, CDCl_3 , RT, δ in ppm) 7.52 (s, 2 H), 7.38 (d, $J = 8.1$ Hz, 8 H), 7.20 (d, $J = 8.1$ Hz, 8 H), 0.27 - 0.21 (m, 36 H); ^{13}C NMR (75 MHz, CDCl_3 , RT, δ in ppm) 141.30, 139.54, 138.38, 133.20, 132.91, 129.17, -1.08; EA found 75.56 % C, 8.11 % H – calculated 75.15 % C, 8.11 % H, 16.74 % Si.

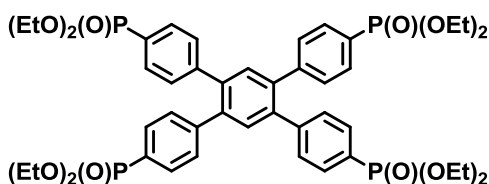
6.4.12 1,2,4,5-Tetrakis(*p*-iodophenyl)benzene



21

1.34 g of 1,2,4,5-Tetrakis(4-trimethylsilylphenyl)benzene (**20**) (2.0 mmol) were dissolved in 130 ml CHCl_3 , and the solution was degassed by bubbling through argon for 20 min. Then 9 ml iodine monochloride (1.0 M in CH_2Cl_2) were added slowly. After stirring for 1h, the reaction was quenched by adding aqueous sodium disulfite. The organic layer was washed by water three times and dried over MgSO_4 . The solution was concentrated to 10 ml and then 100 ml MeOH was added to precipitate the product. The white solid was collected and dried under vacuum to afford 1.432 g product (81 %). MS (FD, 8 kV) $m/z = 884.1$ g/mol - calculated: 886.08 g/mol for $\text{C}_{30}\text{H}_{18}\text{I}_4$; ^1H NMR (250 MHz, CDCl_3 , RT, δ in ppm) 7.59 (d, $J = 8.3$ Hz, 8 H), 7.39 (s, 2 H), 6.91 (d, $J = 8.4$ Hz, 8 H); ^{13}C NMR (75 MHz, CDCl_3 , RT, δ in ppm) 139.74, 138.84, 137.40, 132.69, 131.56, 93.03.

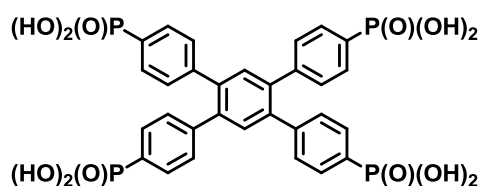
6.4.13 1,2,4,5-Tetrakis(*p*-diethylphosphonatophenyl)benzene



22

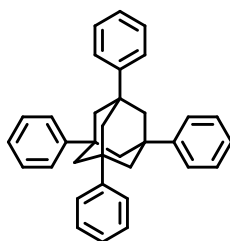
1,2,4,5-Tetrakis(*p*-iodophenyl)benzene (**21**) (1.0 g, 1.43 mmol) was dissolved in anhydrous toluene (100 ml) and stirred under argon until it is dissolved. Diethyl phosphite (9.5 g, 8.9 ml, 68.8 mmol) and triethylamine (6.9 g, 9.59 ml, 68.8 mmol) were added with a syringe, and the mixture is stirred for an additional 10 min; finally with a high argon purge tetrakis(triphenylphosphine)palladium (0.79 g, 0.69 mmol) was added and the mixture heated at 75 °C during 12 h. After cooling to RT diethyl ether was added to the reaction mixture to precipitate the triethylamine hydroiodide, which was removed by filtration. The filtrate was evaporated to give a yellow oil. The crude product was purified by column chromatography on silica gel (ethyl acetate - MeOH 8:2). Yield: 68 %. MS (FD, 8 kV) $m/z = 926.1$ g/mol - calculated: 926.84 g/mol for $C_{46}H_{58}O_{12}P_4$; 1H NMR (250 MHz, CD_2Cl_2 , RT, δ in ppm) 7.66 (dd, $J = 8.3$ and 13.0 Hz, 8 H), 7.55 (s, 2 H), 7.38 – 7.27 (m, 8 H), 4.18 – 3.92 (m, 16 H), 1.28 (t, $J = 7.1$ Hz, 24 H); ^{13}C NMR (75 MHz, CD_2Cl_2 , RT, δ in ppm) 144.66, 133.27, 131.80, 130.16, 129.15, 126.65, 62.44, 16.56; ^{31}P NMR (202 MHz, CD_2Cl_2 , RT, δ in ppm) 17.40 (s).

6.4.14 1,2,4,5-Tetrakis(*p*-phosphonatophenyl)benzene

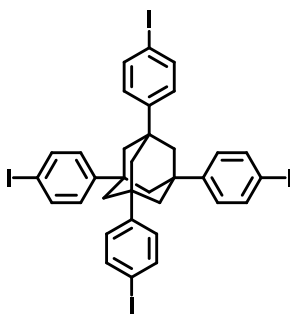


23

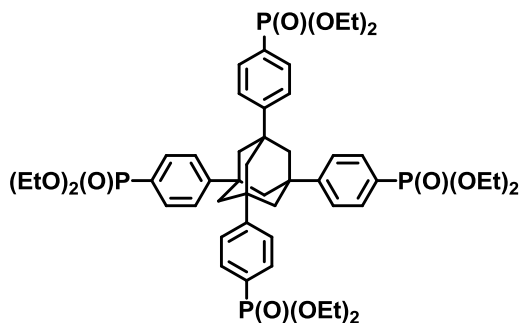
1,2,4,5-Tetrakis(*p*-diethylphosphonatophenyl)benzene (**22**) (0.8 g, 0.86 mmol) was treated with trimethylsilylbromide (1.06 g, 6.9 mmol) in 150 ml of DCM for 48 h. Then, DCM was evaporated and the product of this first step dried under vacuum. The product of the first step was treated with MeOH (200 ml) for another 48 h. The final product was washed with water several times. Yield: 83 % (501 mg). 1H NMR (300 MHz, DMSO, RT, δ in ppm) 7.62 (dd, $J = 8.1$ and 12.7 Hz, 8 H), 7.47 (s, 2 H), 7.34 (d, $J = 5.0$ Hz, 8 H); ^{13}C NMR (126 MHz, DMSO, RT, δ in ppm) 142.15, 138.70, 131.55, 130.60, 129.39, 128.05; ^{31}P NMR (202 MHz, DMSO, RT, δ in ppm) 11.72 (s); EA found 46.28 % C, 3.23 % H – calculated 51.3 % C, 3.73 % H, 27.33 % O, 17.64 % P.

6.4.15 1,3,5,7-Tetrakisphenyladamantane^[6]**25**

A dry 1000-ml three neck round-bottom flask was fitted with two condensers, a magnetic stirbar, a nitrogen inlet, and two outlets running to a 30 % NaOH solution. The flask was placed in an ice bath and cooled. To this flask were added 1-bromoadamantane (**24**) (30.0 g, 0.14 mol), benzene (300 ml) and tert-butyl bromide (38.2 g, 0.28 mol). AlCl_3 (1.6 g, 0.012 mol) was added in four portions over 30 min to the chilled, stirring solution. The ice bath was replaced with a heating mantle and the reaction mixture allowed to warm to RT. The solution was then heated at reflux for 1 h, during which time large amounts of a white solid (1,3,5,7-tetraphenyladamantane) formed. The heterogeneous reaction mixture was cooled to room temperature and poured into acidic ice. Benzene (300ml) was added and the slurry stirred for about an hour. The solution was decanted into a separatory funnel, leaving behind as much of the solid as possible. The layers were separated, and the organic layer was filtered to remove the 1,3,5,7-tetraphenyladamantane. The solids were combined and Soxhlet extracted overnight with chloroform. The desired product was insoluble in chloroform: 32.0 - 43.0 g (50 - 70 %). Mp 417 - 419 °C; MS (FD, 8 kV) $m/z = 439.8$ g/mol - calculated: 440.62 g/mol for $\text{C}_{34}\text{H}_{32}$; IR (KBr) 3025, 2907, 2848, 1590, 1490, 1349, 1079, 769, 750, 703 cm^{-1} ; ^{13}C NMR (75 MHz, CD_2Cl_2 , RT, δ in ppm) 149.8, 129.2, 127.3, 124.8, 45.3, 39.4; EA found 56.00 % C, 4.68 % H – calculated 55.66 % C, 4.67 % H.

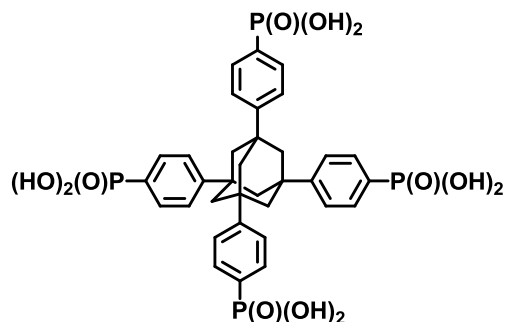
6.4.16 1,3,5,7-Tetrakis(*p*-iodophenyl)adamantane^[6]**26**

1,3,5,7-Tetraphenyladamantane (**25**) (2.0 g, 0.0045 mol) and iodine (2.3 g, 0.009 mol) were ground together with a mortar and pestle. The finely ground pink solid was transferred to a 100 ml one neck round-bottom flask containing a magnetic stirbar and equipped with a nitrogen inlet. The mortar was rinsed with 20 ml of chloroform which was also transferred to the flask. Bis-(trifluoroacetoxy)iodobenzene (BFIB; 3.9 g, 0.009 mol) was added and the reaction mixture flushed with nitrogen. A static atmosphere of nitrogen was maintained while the dark red mixture stirred for 4 h, after which the mixture was filtered to remove a pink solid (mix of product and starting material). The solid was Soxhlet extracted with chloroform overnight. The chloroform solutions were combined and washed sequentially with 5 % NaHSO₃ (to remove the iodine), water, and saturated NaCl solution. The solvent was removed under reduced pressure to give a yellow solid which was recrystallized from CHCl₃/MeOH (9:1) to give 50 – 70 % of the white crystalline product. MS (FD, 8 kV) *m/z* = 944.0 g/mol - calculated: 944.20 g/mol for C₃₄H₂₈I₄; IR (KBr) 3049,2919,2848,1484,1443, 1390,1355,1179,1076,1002,820,779,703 cm⁻¹; ¹³C NMR (75 MHz, CD₂Cl₂, RT, δ in ppm) 148.4, 137.5, 127.1, 91.7, 46.6, 39.0; EA found 43.24 % C, 3.08 % H – calculated 43.25 % C, 2.99 % H, 53.76 % I.

6.4.17 1,3,5,7-Tetrakis(*p*-diethylphosphonatophenyl)adamantane^[7]

27

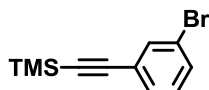
To an Ace Glass pressure tube containing a solution of 1 g (1 mmol) of tetrakis-1,3,5,7-(4-iodophenyl)adamantane (**26**) in 10 ml of dry benzene, 2.48 ml (19.4 mmol) of diethyl phosphite, 5 ml of triethylamine and 0.02 g (0.032 mmol) of dichlorobis(triphenylphosphine)palladium (II) were added under an argon atmosphere. A stirring bar was added and the pressure tube was sealed. The mixture was heated at 80 °C for 72 h with stirring, and then cooled; the precipitated triethylammonium iodide was filtered off. The filtrate was concentrated by evaporation and the residual oil was diluted with 100 ml of cold water. The precipitate obtained was filtered, washed twice with water and dried under high vacuum for 72 h. This gave 1,3,5,7-(4-diethylphosphonatophenyl)adamantane as a pale-yellow slightly hygroscopic solid 0.75 g (76 %). The product was sufficiently pure enough to use without further purification. MS (FD, 8 kV) $m/z = 983.4$ g/mol - calculated: 984.96 g/mol for $C_{50}H_{68}O_{12}P_4$; 1H -NMR (250 MHz, $CDCl_3$, RT, δ in ppm) 7.8 (m, 8 H), 7.6 (d, $J = 4$ Hz, 8 H), 4.1 (m, 16 H), 2.2 (s, 12 H), 1.3 (t, $J = 7$ Hz, 24 H); ^{13}C -NMR (75 MHz, $CDCl_3$, RT, δ in ppm) 152.98, 132.06, 126.04, 125.12, 62.08, 62.08, 46.50, 39.46; ^{31}P -NMR (202 MHz, $CDCl_3$, RT, δ in ppm) 14.88 (s); EA found 57.94 % C, 6.75 % H – calculated 60.97 % C, 6.96 % H, 19.49 % O, 12.58 % P.

6.4.18 1,3,5,7-Tetrakis(*p*-phosphonatophenyl)adamantane**28**

1,3,5,7-Tetrakis(*p*-diethylphosphonatophenyl)adamantane (**27**) (0.7 g, 0.71 mmol) was treated with trimethylsilylbromide (0.87 g, 5.7 mmol) in 150 ml of DCM for 48 h (first step). Then, DCM was evaporated and the product of the first step dried under vacuum. The product of the first step was treated with MeOH (200 ml) for another 48 h. The final product was washed with water several times (second step). Overall yield: 72 %. ¹H NMR (700 MHz, DMSO, 100 °C, δ in ppm) 7.75 – 7.60 (m, 16 H), 2.12 (d, J = 30.6 Hz, 12 H); ¹³C NMR (176 MHz, DMSO, 100 °C, δ in ppm) 151.63, 131.74, 130.17, 124.32, 45.75, 38.77; ³¹P NMR (202 MHz, DMSO, RT, δ in ppm) 13.94 (s); EA found 50.71 % C, 4.34 % H – calculated 53.69 % C, 4.77 % H, 25.24 % O, 16.29 % P.

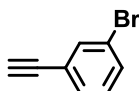
6.5 Substituted Hexaphenylbenzene Molecules

6.5.1 ((3-Bromophenyl)ethynyl)trimethylsilane

**30**

1-Bromo-3-iodobenzene (**29**) (2.26 ml, 5.0 g, 17.67 mmol), CuI (5 mol %, 0.88 mmol, 168.3 mg) and dichloro-bis(triphenylphosphine)palladium (620.3 mg, 0.88 mmol, 5 mol %) were dissolved in 10 ml of dry toluene. 5 ml of diisopropylamine were added and the mixture was degassed with Ar during 20 min. Afterwards 2.26 ml (1.56 g, 15.9 mmol, 0.9 eq) of trimethylsilylacetylene were added dropwise and the mixture was stirred during 1 h at RT. The solution was neutralized with a diluted HCl solution. The organic layer was dried over MgSO₄ and dried under reduced pressure. The crude product was purified by column chromatography on silica gel (hexane) to give the desired product as a yellow oil in 87 % yield (3.9 g). MS (FD, 8 kV) m/z = 254.1 g/mol - calculated: 253.21 g/mol for C₁₁H₁₃BrSi; ¹H NMR (250 MHz, CD₂Cl₂, RT, δ in ppm) 7.62 (t, J = 1.6 Hz, 1H), 7.47 (ddd, J = 1.1, 2.0 and 8.0 Hz, 1 H), 7.43 – 7.37 (m, 1 H), 7.20 (t, J = 7.9 Hz, 1 H), 0.33 – 0.16 (m, 9 H); ¹³C NMR (75 MHz, CD₂Cl₂, RT, δ in ppm) 135.16, 134.89, 132.40, 132.25, 131.47, 131.02, 130.87, 130.59, 130.42, 125.81, 122.58, 103.70, 96.50, 0.11.

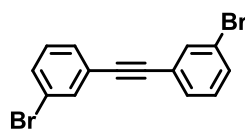
6.5.2 1-Bromo-3-ethynylbenzene

**31**

[(3-Bromophenyl)ethynyl]trimethylsilane (**30**) (11.85 mmol, 3.0 g) was diluted in 10 ml of dry THF. 23.69 ml of TBAF (23.69 mmol, 2 eq, 1 M) were added and the contents were allowed to react during 15 min at RT. The dark blue/brown solution was then dried under vacuum and the crude product purified by column chromatography on silica

gel (hexane) to give the desired product as a yellow oil in 78 % yield (1.7 g). MS (FD, 8 kV) $m/z = 181.1$ g/mol - calculated: 181.03 g/mol for C_8H_5Br ; 1H NMR (250 MHz, CD_2Cl_2 , RT, δ in ppm) 7.65 (t, $J = 1.7$ Hz, 1 H), 7.51 (ddd, $J = 1.1, 1.9$ and 8.0, 1 H), 7.43 (dt, $J = 1.3$ and 7.7 Hz, 1H), 7.27 – 7.16 (m, 1 H), 3.19 (s, 1 H); ^{13}C NMR (75 MHz, CD_2Cl_2 , RT, δ in ppm) 135.97, 133.09, 131.78, 130.84, 123.18, 79.23.

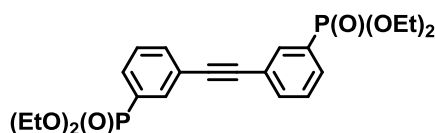
6.5.3 1,2-Bis(3-bromophenyl)ethyne



32

1-Bromo-3-ethynylbenzene (**31**) (5.46 mmol, 1.0 g), CuI (5 mol %, 0.27 mmol, 52 mg) and dichloro-bis(triphenylphosphine)palladium (5 mol %, 0.27 mol, 192 mg) were dissolved in 10 ml of dry toluene. 10 ml of NEt_3 were added and the mixture was degassed with Ar during 20 min. Afterwards 0.63 ml (1.4 g, 4.92 mmol, 0.9 eq) of 1-bromo-3-iodobenzene (**29**) were added dropwise and the mixture was stirred during 12 h at 60 °C. The solution was neutralized with a diluted HCl solution. The organic layer was dried over $MgSO_4$ and dried under reduced pressure. The crude product was purified by column chromatography on silica gel (hexane) to give the desired product as a yellow oil which crystallized upon cooling in 87 % yield (1.6 g). MS (FD, 8 kV) $m/z = 336.1$ g/mol - calculated: 336.02 g/mol for $C_{14}H_8Br_2$; 1H NMR (250 MHz, CD_2Cl_2 , RT, δ in ppm) 7.69 (t, $J = 1.7$ Hz, 2 H), 7.57 – 7.43 (m, 4 H), 7.26 (t, $J = 7.9$ Hz, 2 H); ^{13}C NMR (75 MHz, CD_2Cl_2 , RT, δ in ppm) 134.85, 132.37, 130.85, 130.56, 125.33, 122.71, 89.45, 54.72, 54.36, 54.00, 53.64, 53.28; EA found 50.31 % C, 2.37 % H – calculated 50.04 % C, 2.40 % H, 47.56 % Br.

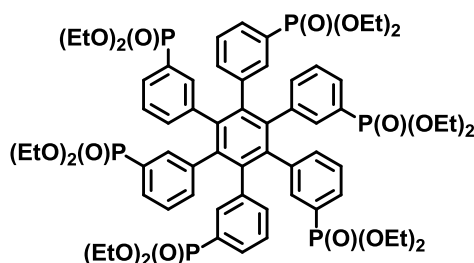
6.5.4 1,2-Bis(3-diethylphosphonatophenyl)ethyne



33

1,2-Bis(3-bromophenyl)ethyne (**32**) (1.0 g, 2.22 mmol) was dissolved in anhydrous toluene (10 ml) and stirred under argon. Diethyl phosphite (3.4 ml, 26.7 mmol) and triethylamine (3.7 ml, 26.7 mmol) were added and the mixture was degassed with Ar during 20 min; finally tetrakis(triphenylphosphine)palladium (0) (257 mg, 0.22 mmol, 10 mol %) was added with a high argon purge and the mixture heated at 75 °C overnight. After cooling to RT, diethyl ether was added to the reaction mixture to precipitate the triethylamine hydroiodide, which was removed by filtration. The filtrate was evaporated to give a yellowish oil. The crude product was purified by column chromatography on silica gel (ethyl acetate – MeOH 10:1). 0.68 g (68 %) of a white solid was obtained. MS (FD, 8 kV) $m/z = 450.1$ g/mol - calculated: 450.4 g/mol for $C_{22}H_{28}O_6P_2$; 1H NMR (250 MHz, CD_2Cl_2 , RT, δ in ppm) 7.97 (dt, $J = 1.3$ and 13.6 Hz, 2 H), 7.83 – 7.66 (m, 4 H), 7.57 – 7.41 (m, 2 H), 4.27 – 3.95 (m, 8 H), 1.39 – 1.25 (m, 12 H); ^{13}C NMR (176 MHz, CD_2Cl_2 , RT, δ in ppm) 135.61, 135.59, 135.37, 135.31, 132.08, 132.02, 130.74, 129.68, 129.30, 129.21, 123.99, 123.89, 89.87, 62.85, 62.82, 54.31, 54.15, 54.00, 53.85, 53.69, 16.75, 16.71; ^{31}P NMR (284 MHz, CD_2Cl_2 , RT, δ in ppm) 16.81 (s); EA found 58.21 % C, 6.05 % H – calculated 58.67 % C, 6.27 % H, 21.31 % O, 13.75 % P.

6.5.5 Hexakis(*m*-diethylphosphonatophenyl)benzene

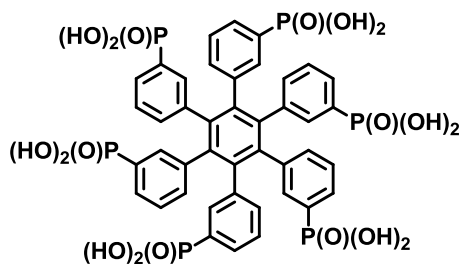


34

1,2-Bis(3-diethylphosphonatophenyl)ethyne (**33**) (0.5 g, 1.11 mmol) and dioxane (7 ml) were introduced in a round flask and the solution was degassed with Ar during 20 min. $Co_2(CO)_8$ (37.96 mg, 0.11 mmol, 10 mol %) was introduced and the mixture heated at 125 °C during the night under Ar atmosphere. The solvent was evaporated under vacuum. The dark blue oil was purified by column chromatography (ethyl acetate – MeOH 7:3) to give 310 mg (62 %) of a yellowish solid. MS (FD, 8 kV) $m/z = 1350.7$ g/mol - calculated: 1351.2 g/mol for $C_{66}H_{84}O_{18}P_6$; 1H NMR (250 MHz, $C_2D_2Cl_4$, RT, δ in ppm) 7.38 – 7.21 (m, 6 H), 7.06 (s, 6 H), 6.93 (d, $J = 17.4$ Hz, 6 H), 3.79 (dd, $J = 14.8$ and 23.3 Hz, 24 H), 1.22 (ddd, $J = 5.2, 12.3$ and 19.9 Hz, 36 H); ^{13}C NMR (176 MHz,

$C_2D_2Cl_4$, RT, δ in ppm) 140.26, 140.10, 140.05, 139.92, 139.85, 139.77, 135.37, 135.23, 135.05, 134.38, 129.70, 128.23, 127.59, 127.18, 62.33, 62.31, 62.20, 16.62, 16.59; ^{31}P NMR (283 MHz, CD_2Cl_2 , RT, δ in ppm) 17.47 – 17.01 (m).

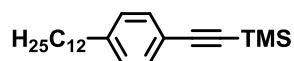
6.5.6 Hexakis(*m*-phosphonatophenyl)benzene



35

Hexakis(*m*-diethylphosphonatophenyl)benzene (**34**) (0.3 g, 0.22 mmol) was treated with trimethylsilylbromide (0.76 ml, 5.33 mmol) in 25 ml of DCM for 48 h. Then, DCM was evaporated and the product of this first step dried under vacuum. The product of the first step was treated with MeOH (100 ml) for another 48 h. 196 mg (87 % yield) of a yellowish powder were obtained. 1H NMR (500 MHz, DMSO, 100 °C, δ in ppm) 7.74 – 7.37 (m, 6 H), 7.13 (s, 6 H), 6.91 (s, 12 H); ^{13}C NMR (176 MHz, RT, δ in ppm) 140.61, 140.23, 140.09, 139.89, 139.53, 139.46, 139.29, 134.01, 132.97, 132.21, 132.00, 131.77, 131.25, 130.97, 130.75, 128.14, 127.24; ^{31}P NMR (202 MHz, DMSO, 100 °C, δ in ppm) 12.62 (s); EA found 47.14 % C, 3.73 % H – calculated 49.72 % C, 3.58 % H, 28.39 % O, 18.32 % P.

6.5.7 [(4-Dodecylphenyl)ethynyl]trimethylsilane

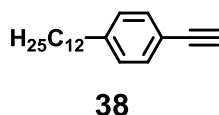


37

3.6 ml of [(4-bromophenyl)ethynyl]trimethylsilane (**36**) (5.27 mmol, 1.4 g), 215.22 mg (5 mol %) of $Pd(dppf)Cl_2$ and 10 ml THF were added in the flask. Then the Grignard reagent $C_{12}H_{25}MgBr$ (2 eq, 10.54 mmol, 10.542 ml) was added dropwise. The reaction was kept at 60 °C overnight and quenched by adding methanol. The solvent was removed under vacuum and purified by column chromatography (hexane) to provide

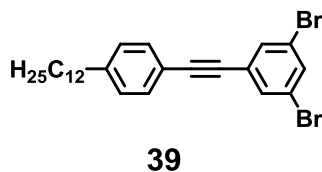
1.6 g a light yellow oil (90 %). MS (FD, 8 kV) $m/z = 339.7$ g/mol - calculated: 342.63 g/mol for $C_{23}H_{38}Si$; 1H NMR (250 MHz, CD_2Cl_2 , RT, δ in ppm) 7.46 – 7.34 (m, 2 H), 7.15 (d, $J = 8.4$ Hz, 2 H), 2.67 – 2.54 (m, 2 H), 1.60 (s, 2 H), 1.29 (d, $J = 10.2$ Hz, 18 H), 0.89 (t, $J = 6.6$ Hz, 3 H), 0.33 – 0.16 (m, 9 H).

6.5.8 1-Dodecyl-4-ethynylbenzene



[(4-Dodecylphenyl)ethynyl]trimethylsilane (**37**) (2.92 mmol, 1 g) was diluted in 10 ml of dry THF. 5.8 ml of a 1 M TBAF solution (5.8 mmol, 2 eq) were added and the contents were allowed to react during 15 min at RT. The dark blue/brown solution was then dried under vacuum and the crude product purified by column chromatography on silica gel (hexane) to give the desired product as a yellow oil in 89 % yield (0.7 g). MS (FD, 8 kV) $m/z = 268.9$ g/mol - calculated: 270.45 g/mol for $C_{20}H_{30}$; 1H NMR (250 MHz, CD_2Cl_2 , RT, δ in ppm) 7.46 – 7.34 (m, 2 H), 7.15 (d, $J = 8.4$ Hz, 2 H), 3.08 (s, 1 H), 2.67 – 2.54 (m, 2 H), 1.60 (s, 2 H), 1.29 (d, $J = 10.2$ Hz, 18 H), 0.89 (t, $J = 6.6$ Hz, 3 H).

6.5.9 1,3-Dibromo-5-[(4-dodecylphenyl)ethynyl]benzene

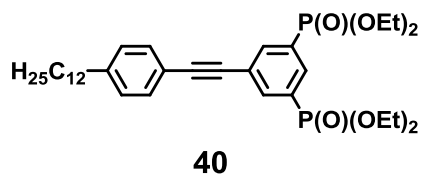


1,3,5-Tribromobenzene (4.64 mmol, 1.49 g), 2 mol % of CuI (0.08356 mmol, 15.9 mg) and 2 mol % of dichloro-bis(triphenylphosphine)palladium (0.08356 mmol, 58.65 mg) were dissolved in 10 ml of dry toluene. 10 ml of NEt_3 were added and the mixture was degassed with Ar during 20 min. Afterwards 1.13 g (4.18 mmol, 0.9 eq) of 1-dodecyl-4-(ethynyl)benzene (**38**) were added dropwise and the mixture was stirred during 12 h at 60 °C. The solution was neutralized with a diluted HCl solution. The organic layer was dried over $MgSO_4$ and dried under reduced pressure. The crude product was purified by column chromatography on silica gel (hexane) to give the desired product as white crystals in 74 % yield (1.73 g). MS (FD, 8 kV) $m/z = 504.1$

g/mol - calculated: 503.34 g/mol for $C_{26}H_{32}Br_2$; 1H NMR (250 MHz, CD_2Cl_2 , RT, δ in ppm) 7.72 – 7.58 (m, 3 H), 7.50 – 7.38 (m, 2 H), 7.20 (d, $J = 8.4$ Hz, 2 H), 2.71 – 2.54 (m, 2 H), 1.59 (dd, $J = 11.2$ Hz, 18.7, 2 H), 1.35 – 1.20 (m, 18 H), 0.89 (t, $J = 6.7$ Hz, 3 H); ^{13}C NMR (75 MHz, CD_2Cl_2 , RT, δ in ppm) 145.20, 134.27, 133.65, 133.48, 132.19, 129.22, 127.55, 125.99, 123.87, 123.13, 119.83, 92.78, 86.23, 36.46, 32.52, 31.82, 30.67, 30.26, 30.23, 30.16, 30.04, 29.94, 29.83, 23.28, 14.47.

6.5.10 Tetraethyl 5-[(4-dodecylphenyl)ethynyl]-1,3- phenylene diphosphonate

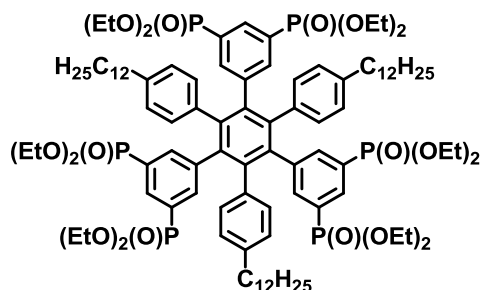
diphosphonate



1.73 g of 1,3-dibromo-5-[(4-dodecylphenyl)ethynyl]benzene (**39**) (3.43 mmol) was dissolved in anhydrous toluene (10 ml) and stirred under argon. Diethyl phosphite (2.63 ml, 20.58 mmol) and triethylamine (2.87 ml, 20.58 mmol) were added and the mixture was degassed with Ar during 20 min; finally tetrakis(triphenylphosphine)palladium (0) (396 mg, 0.343 mmol) was added with a high argon purge and the mixture heated at 75 °C overnight. After cooling to RT, diethyl ether was added to the reaction mixture to precipitate the triethylamine hydroiodide, which was removed by filtration. The filtrate was evaporated to give a yellowish oil. The crude product was purified by column chromatography on silica gel (hexane - EtAc 1:1). 1.5 g (70 %) of a yellow oil was obtained. MS (FD, 8 kV) $m/z = 619.4$ g/mol - calculated: 618.72 g/mol for $C_{34}H_{52}O_2P_2$; 1H NMR (250 MHz, CD_2Cl_2 , RT, δ in ppm) 8.20 – 7.99 (m, 3 H), 7.47 (d, $J = 8.2$ Hz, 2 H), 7.21 (d, $J = 8.3$ Hz, 2 H), 4.31 – 3.99 (m, 8 H), 2.75 – 2.57 (m, 2 H), 1.61 (s, 2 H), 1.45 – 1.19 (m, 30 H), 0.88 (t, $J = 6.6$ Hz, 3 H); ^{13}C NMR (75 MHz, CD_2Cl_2 , RT, δ in ppm) 145.40, 138.79, 138.69, 138.65, 138.60, 138.50, 134.46, 134.33, 134.19, 132.46, 132.30, 129.99, 129.81, 129.52, 125.53, 120.31, 92.92, 87.52, 63.44, 63.40, 63.36, 36.75, 32.79, 32.10, 30.53, 30.50, 30.43, 30.32, 30.21, 30.11, 23.55, 17.06, 17.02, 16.98, 14.73; ^{31}P NMR (284 MHz, CD_2Cl_2 , RT, δ in ppm) 15.07 (s).

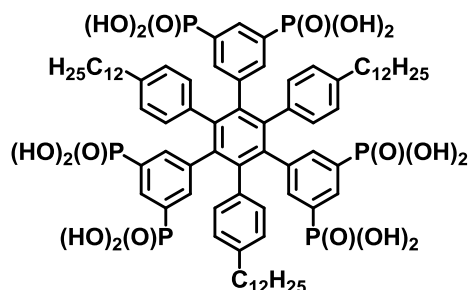
6.5.11 1,3,5-Tris(3,5-bidiethylphosphonatophenyl)-2,4,6-tris(4-

dodecylphenyl)-benzene

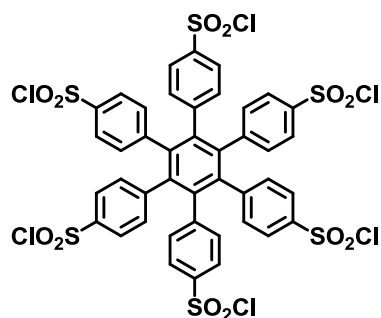


41

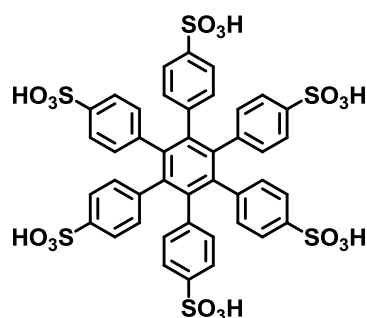
1.0 mg of tetraethyl 5-[(4-dodecylphenyl)ethynyl]-1,3-phenylenediphosphonate (**40**) (1.6 mmol) and dioxane (14 ml) were introduced in a round flask and the solution was degassed with Ar during 20 min. 10 mol % of $\text{Co}_2(\text{CO})_8$ (55 mg, 0.16 mmol) was introduced and the mixture heated at 125 °C during the night under Ar atmosphere. The solvent was evaporated under vacuum. The dark blue oil was purified by column chromatography (EtAc/MeOH 8/2) to give 0.6 g (61 %) of a yellow oil. MS (FD, 8 kV) $m/z = 1861.4$ g/mol - calculated: 1856.16 g/mol for $\text{C}_{102}\text{H}_{156}\text{O}_{18}\text{P}_6$; ^1H NMR (250 MHz, CD_2Cl_2 , RT, δ in ppm) 7.78 – 7.60 (m, 3 H), 7.47 (s, 6 H), 6.73 (dd, $J = 8.1$ and 29.2 Hz, 12 H), 3.98 – 3.60 (m, 24 H), 3.20 – 3.04 (m, 6 H), 2.35 – 2.18 (m, 6 H), 1.39 – 1.15 (m, 90 H), 0.97 – 0.77 (m, 9 H); ^{13}C NMR (176 MHz, CD_2Cl_2 , RT, δ in ppm) 141.66, 141.43, 141.29, 139.54, 138.26, 136.94, 133.06, 131.40, 129.10, 129.02, 128.06, 127.98, 127.54, 62.56, 46.79, 37.63, 35.91, 33.32, 32.49, 31.61, 30.60, 30.27, 30.14, 29.95, 27.63, 23.27, 16.69, 14.45; ^{31}P NMR (284 MHz, CD_2Cl_2 , RT, δ in ppm) 15.81 (s).

6.5.12 1,3,5-Tris(3,5-biphosphonatophenyl)-2,4,6-tris(4-dodecyl**phenyl)-benzene****42**

1,3,5-Tris(3,5-bidiethylphosphonatophenyl)-2,4,6-tris(4-dodecylphenyl)-benzene (**41**) (0.5 g, 0.27 mmol) was treated with trimethylsilylbromide (0,034 ml, 40 mg, 3.3 mmol) in 10 ml of DCM for 48 h. Then, DCM was evaporated and the product of this first step dried under vacuum. The product of the first step was treated with MeOH (100 ml) for another 48 h. 397 mg (97 % yield) of a white powder were obtained. ¹H NMR (700 MHz, DMSO, RT, δ in ppm) 7.49 (t, J = 12.9 Hz, 3 H), 7.29 (d, J = 14.0 Hz, 3 H), 6.81 (d, J = 22.4 Hz, 3 H), 6.64 (dd, J = 8.0 and 31.0 Hz, 12 H), 2.26 – 2.19 (m, 6 H), 1.33 (s, 6 H), 1.24 (dd, J = 11.6 and 31.3 Hz, 54 H), 0.85 (dd, J = 5.6 and 8.4 Hz, 9 H); ¹³C NMR (176 MHz, DMSO, RT, δ in ppm) 141.66, 141.43, 141.29, 139.54, 138.26, 136.94, 133.06, 131.40, 129.10, 129.02, 128.06, 127.98, 127.54, 46.79, 37.63, 35.91, 33.32, 32.49, 31.61, 30.60, 30.27, 30.14, 29.95, 27.63, 23.27, 14.45; ³¹P NMR (284 MHz, DMSO, RT, δ in ppm) 13.31 (d, J = 24.1 Hz), 12.53 (d, J = 39.5 Hz); EA found 58.60 % C, 7.04 % H – calculated 61.65 % C, 7.16 % H, 18.95 % O, 12.23 % P.

6.5.13 Hexaphenylbenzene hexasulfonyl chloride^[8]**44**

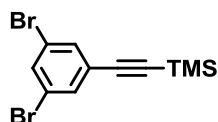
A 50 ml round-bottom flask was charged with 2.0 g of hexaphenylbenzene (**43**) and 25 ml of CH_2Cl_2 . The flask was placed in an ice bath. Chlorosulfonic acid (15 ml, 60 eq.) was added slowly to the stirred reaction mixture under Argon protection. The reaction was allowed to return to RT and continued for 24 h. Then the mixture was carefully poured into ice/water. The precipitate was collected and dissolved in acetone. The acetone solution was dried over MgSO_4 , filtered, and evaporated to dryness. After drying under vacuum overnight, 4.0 g of hexaphenylbenzene hexasulfonyl chloride was achieved as yellow solid (yield: 97 %). MS (FD, 8 kV) $m/z = 1126.5$ g/mol - calculated: 1125.74 g/mol for $\text{C}_{42}\text{H}_{24}\text{Cl}_6\text{O}_{12}\text{S}_6$; ^1H NMR (250 MHz, $(\text{CD}_3)_2\text{CO}$, RT, δ in ppm) 7.77 (d, $J = 8.6$ Hz, 12 H), 7.57 (d, $J = 8.6$ Hz, 12 H); ^{13}C NMR (75 MHz, DMSO, RT, δ in ppm) 146.98, 143.63, 140.28, 133.95, 127.36.

6.5.14 Hexakis(*p*-sulfonatophenyl)benzene**45**

66 ml of 1.0 M NaOH (38 eq.) was added to a 100 ml round-bottom flask containing 2.0 g of hexaphenylbenzene hexasulfonyl chloride (**44**) at RT. The mixture was stirred at 50 °C for 36 h. Afterwards the reaction mixture is cooled to RT and hexakis(*p*-

sulfonatophenyl)benzene (**45**) was precipitated in acetone. 1.7 g of the product were obtained (95 % yield). ^1H NMR (250 MHz, D_2O , RT, δ in ppm) 7.23 (d, $J = 8.4$ Hz, 12 H), 6.99 (d, $J = 8.4$ Hz, 12 H); ^{13}C NMR (75 MHz, D_2O , RT, δ in ppm) 160.09, 157.97, 157.22, 149.28, 141.90.

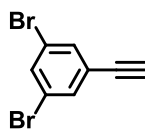
6.5.15 [(3,5-Dibromophenyl)ethynyl]trimethylsilane



47

1,3,5-Tribromobenzene (**46**) (15.89 mmol, 5 g), 5 mol % CuI (0.79 mmol, 151.2 mg) and 5 mol % dichloro-bis(triphenylphosphine)palladium (0.79 mmol, 557.4 mg) were dissolved in 25 ml of dry toluene. 10 ml of diisopropylamine were added and the mixture was degassed with Ar during 20 min. Afterwards 2.03 ml (1.4 g, 14.3 mmol, 0.9 eq) of trimethylsilylacetylene were added dropwise and the mixture was stirred during 1 h at RT. The solution was neutralized with a diluted HCl solution. The organic layer was dried over MgSO_4 and dried under reduced pressure. The crude product was purified by column chromatography on silica gel (hexane) to give the desired product as a yellow oil in 57 % yield (3 g). MS (FD, 8 kV) $m/z = 331.7$ g/mol - calculated: 332.11 g/mol for $\text{C}_{11}\text{H}_{12}\text{Br}_2\text{Si}$; ^1H NMR (250 MHz, CD_2Cl_2 , RT, δ in ppm) 7.64 (t, $J = 1.8$ Hz, 1 H), 7.55 (d, $J = 1.8$ Hz, 2 H), 0.30 – 0.23 (m, 9 H).

6.5.16 1,3-Dibromo-5-ethynylbenzene

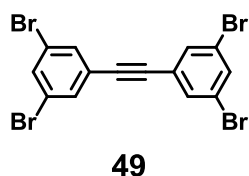


48

[(3,5-Dibromophenyl)ethynyl]trimethylsilane (**47**) (6.02 mmol, 2 g) was diluted in 10 ml of dry THF. 12.04 ml of a 1 M TBAF solution (12.04 mmol, 2 eq) were added and the contents were allowed to react during 15 min at RT. The dark blue/brown solution was then dried under vacuum and the crude product purified by column chromatography on silica gel (hexane) to give the desired product as a yellow oil in 89

% yield (0.7 g). MS (FD, 8 kV) $m/z = 259.7$ g/mol - calculated: 259.93 g/mol for $C_8H_4Br_2$; 1H NMR (250 MHz, CD_2Cl_2 , RT, δ in ppm) 7.64 (t, $J = 1.8$ Hz, 1 H), 7.55 (d, $J = 1.8$ Hz, 2 H), 3.08 (s, 1 H).

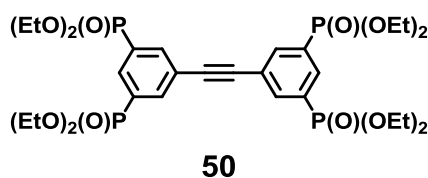
6.5.17 1,2-Bis(3,5-dibromophenyl)ethyne



1,3-Dibromo-5-ethynylbenzene (**48**) (1.92 mmol, 0.5 g), 5 mol % CuI (0.096 mmol, 18.3 mg) and 5 mol % dichloro-bis(triphenylphosphine)palladium (0.096 mmol, 67.5 mg) were dissolved in 20 ml of dry toluene. 10 ml of NEt_3 were added and the mixture was degassed with Ar during 20 min. Afterwards 545.1 mg (1.73 mmol, 0.9 eq) of 1,3,5-tribromobenzene (**46**) were added dropwise and the mixture was stirred during 12 h at 60 °C. The solution was neutralized with a diluted HCl solution. The organic layer was dried over $MgSO_4$ and dried under reduced pressure. The crude product was purified by column chromatography on silica gel (hexane) to give the desired product as a yellow oil in 73 % yield (0.7 g). MS (FD, 8 kV) $m/z = 492.8$ g/mol - calculated: 493.81 g/mol for $C_{14}H_6Br_4$; 1H NMR (250 MHz, CD_2Cl_2 , RT, δ in ppm) 7.71 (t, $J = 1.8$ Hz, 2 H), 7.63 (d, $J = 1.8$ Hz, 4 H); ^{13}C NMR (75 MHz, CD_2Cl_2 , RT, δ in ppm) 152.66, 142.78, 135.53, 134.02, 123.55.

6.5.18 Octaethyl 5,5'-(ethyne-1,2-diyl)bis(benzene-5,3,1-triyl)

tetraphosphonate

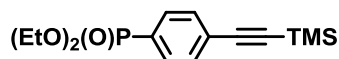


0.5 g of 1,2-bis(3,5-dibromophenyl)ethyne (**49**) (1.01 mmol) were dissolved in anhydrous toluene (10 ml) and stirred under argon. Diethyl phosphite (0.77 ml, 6.06 mmol) and triethylamine (0.85 ml, 6.06 mmol) were added and the mixture was

degassed with Ar during 20 min; finally tetrakis(triphenylphosphine)palladium (0) (233 mg, 0.202 mmol) was added with a high argon purge and the mixture heated at 75 °C overnight. After cooling to RT, diethyl ether was added to the reaction mixture to precipitate the triethylamine hydroiodide, which was removed by filtration. The filtrate was evaporated to give a yellowish oil. The crude product was purified by column chromatography on silica gel (ethyl acetate - MeOH 8:2). 0.46 g (63 %) of a yellow oil was obtained. MS (FD, 8 kV) $m/z = 723.4$ g/mol - calculated: 722.57 g/mol for $C_{30}H_{46}O_{12}P_4$; 1H NMR (300 MHz, CD_2Cl_2 , RT, δ in ppm) 8.19 – 8.03 (m, 6 H), 4.28 – 4.03 (m, 16 H), 1.40 – 1.28 (m, 24 H); ^{13}C NMR (75 MHz, CD_2Cl_2 , RT, δ in ppm) 138.92, 135.19, 132.79, 132.63, 130.36, 130.18, 124.77, 124.41, 124.36, 63.58, 63.55, 17.14, 17.10, 17.06; ^{31}P NMR (284 MHz, CD_2Cl_2 , RT, δ in ppm) 14.72 (s).

6.6 Expanding the Periphery of the Hexaphenylbenzene

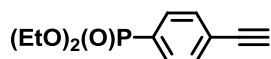
6.6.1 Diethyl 4-[(trimethylsilyl)ethynyl]phenylphosphonate



53

5 g of [(4-bromophenyl)ethynyl]trimethylsilane (**52**) (19.7 mmol) were dissolved in anhydrous toluene (25 ml) and stirred under argon. Diethyl phosphite (7.6 ml, 59.2 mmol) and triethylamine (8.2 ml, 59.2 mmol) were added and the mixture was degassed with Ar during 20 min; finally tetrakis(triphenylphosphine)palladium(0) (1.1 mg, 0.99 mmol) was added with a high argon purge and the mixture heated at 75 °C overnight. After cooling to RT, diethyl ether was added to the reaction mixture to precipitate the triethylamine hydroiodide, which was removed by filtration. The filtrate was evaporated to give a yellow oil. The crude product was purified by column chromatography on silica gel (hexane). 3.7 g (60 %) of a yellow oil which crystallized upon cooling was obtained. MS (FD, 8 kV) $m/z = 311.0$ g/mol - calculated: 310.40 g/mol for $C_{15}H_{23}O_3PSi$; 1H NMR (250 MHz, CD_2Cl_2 , RT, δ in ppm) 7.66 (tdd, $J = 5.9, 9.0$ and 11.6 Hz, 2 H), 7.58 – 7.41 (m, 2 H), 4.19 – 3.99 (m, 4 H), 1.40 – 1.22 (m, 6 H), 0.30 – 0.20 (m, 9 H); EA found 58.01 % C, 5.83 % H – calculated 58.04 % C, 7.47 % H, 15.46 % O, 9.98 % P; 9.05 % Si.

6.6.2 Diethyl 4-ethynylphenylphosphonate



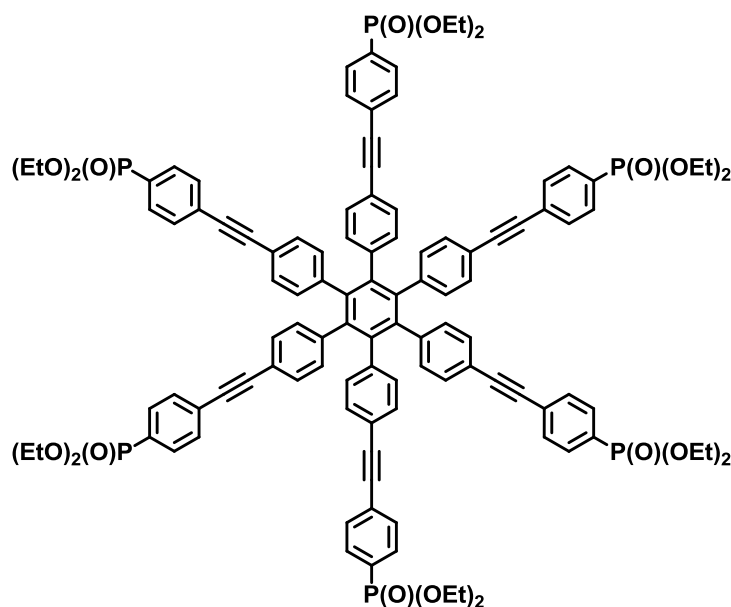
54

Diethyl 4-[(trimethylsilyl)ethynyl]phenylphosphonate (**53**) (2 g, 6.5 mmol) was diluted in 10 ml of dry THF. 13 ml of a 1 M TBAF solution (13 mmol, 2 eq) were added and the contents were allowed to react during 40 min at RT. The dark blue/brown solution was then dried under vacuum and the crude product purified by column chromatography on silica gel (ethyl acetate) to give the desired product as a yellow oil in 83 % yield (1.3 g).

MS (FD, 8 kV) $m/z = 239.0$ g/mol - calculated: 238.22 g/mol for $C_{12}H_{15}O_3P$; 1H NMR (250 MHz, CD_2Cl_2 , RT, δ in ppm) 7.85 – 7.67 (m, 2 H), 7.65 – 7.50 (m, 2 H), 4.20 – 3.96 (m, 4 H), 3.31 (s, 1 H), 1.30 (td, $J = 0.4$ and 7.1 Hz, 6 H); ^{13}C NMR (176 MHz, CD_2Cl_2 , RT, δ in ppm) 133.00, 132.91, 132.64, 132.58, 132.30, 132.24, 130.63, 129.56, 129.26, 129.19, 126.02, 81.99, 76.21, 63.17, 63.14, 16.68, 16.65; ^{31}P NMR (284 MHz, CD_2Cl_2 , RT, δ in ppm) 16.39 (s).

6.6.3 Hexakis[*p*-(*p*-diethylphosphonatophenylethynyl)phenyl]

benzene

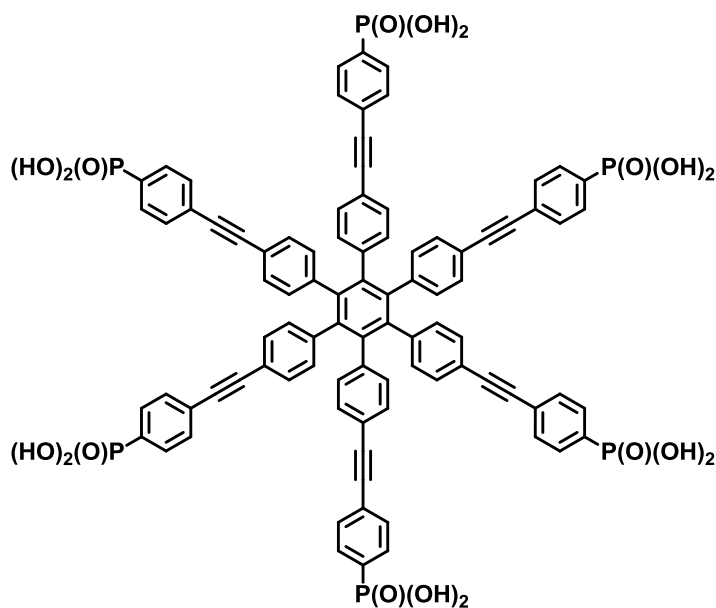


58

50 mg of hexaiodohexaphenylbenzene (**57**) (0.03876 mmol), 92.3 mg of diethyl 4-ethynylphenylphosphonate (**54**) (0.3876 mmol, 10 eq) and 4.4 mg CuI (0.0232 mmol, 60 mol %) were dissolved in 10 ml of dry toluene. 10 ml of NEt_3 were added and the mixture was degassed with Ar during 20 min. Afterwards 13.44 mg (0.0116 mmol, 30 mol %) of tetrakis(triphenylphosphine)palladium(0) were added and the mixture was stirred during 12 h at 65 °C. The solution was neutralized with a diluted HCl solution. The organic layer was dried over $MgSO_4$ and dried under reduced pressure. The crude product was purified by column chromatography on silica gel (ethyl acetate – MeOH 7:3) to give the desired product as a yellow oil in 43 % yield (32 mg). 1H NMR (250 MHz, CD_2Cl_2 , RT, δ in ppm) 7.71 (dd, $J = 8.3$ and 12.9 Hz, 12 H), 7.59 – 7.46 (m, 12

H), 7.16 (d, $J = 8.3$ Hz, 12 H), 6.91 (d, $J = 8.3$ Hz, 12 H), 4.06 (dd, $J = 7.1$ and 13.4 Hz, 24 H), 1.28 (t, $J = 7.1$ Hz, 36 H); ^{13}C NMR (176 MHz, CD_2Cl_2 , RT, δ in ppm) 141.35, 140.63, 132.34, 132.28, 132.14, 132.05, 131.97, 131.16, 129.75, 128.68, 127.87, 120.83, 92.38, 89.29, 62.92, 62.89, 16.86, 16.82; ^{31}P NMR (122 MHz, CD_2Cl_2 , RT, δ in ppm) 16.86 (s).

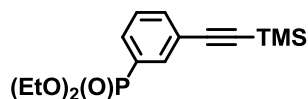
6.6.4 Hexakis[*p*-(*p*-phosphonatophenylethynyl)phenyl]benzene



59

Hexakis[*p*-(*p*-diethylphosphonatophenylethynyl)phenyl]benzene (**58**) (100 mg, 0.051 mmol) was treated with trimethylsilylbromide (0.18 ml, 0.12 g, 1.23 mmol) in 10 ml of DCM for 48 h. Then, DCM was evaporated and the product of this first step dried under vacuum. The product of the first step was treated with MeOH (100 ml) for another 48 h. 81 mg (98 % yield) of a white powder were obtained. ^1H NMR (500 MHz, DMSO, RT, δ in ppm) 7.64 (d, $J = 12.3$ Hz, 12 H), 7.56 (s, 12 H), 7.18 (d, $J = 7.6$ Hz, 12 H), 7.00 (d, $J = 7.8$ Hz, 12 H); ^{13}C NMR (126 MHz, DMSO, RT, δ in ppm) 140.19, 139.50, 135.09, 133.66, 131.33, 131.00, 130.89, 130.71, 130.64, 130.30, 130.21, 128.81, 128.70, 124.51, 119.45, 90.72, 89.09; ^{31}P NMR (202 MHz, DMSO, RT, δ in ppm) 12.37 (s); EA found 65.04 % C, 3.18 % H – calculated 66.92 % C, 3.74 % H, 17.83 % O, 11.51 % P.

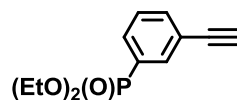
6.6.5 Diethyl 3-[(trimethylsilyl)ethynyl]phenylphosphonate



55

2.0 g of [(3-bromophenyl)ethynyl]trimethylsilane (**30**) (7.9 mmol) were dissolved in anhydrous toluene (15 ml) and stirred under argon. Diethyl phosphite (6.1 ml, 47.4 mmol) and triethylamine (6.6 ml, 47.4 mmol) were added and the mixture was degassed with Ar during 20 min; finally tetrakis(triphenylphosphine)palladium(0) (456 mg, 0.39 mmol) was added with a high argon purge and the mixture heated at 75 °C overnight. After cooling to RT, diethyl ether was added to the reaction mixture to precipitate the triethylamine hydroiodide, which was removed by filtration. The filtrate was evaporated to give a yellow oil. The crude product was purified by column chromatography on silica gel (ethyl acetate). 1.6 g (67 %) of a yellow oil which crystallized upon cooling was obtained. MS (FD, 8 kV) $m/z = 311.0$ g/mol - calculated: 310.40 g/mol for $C_{15}H_{23}O_3PSi$; 1H NMR (250 MHz, CD_2Cl_2 , RT, δ in ppm) 7.88 (ddd, $J = 1.2, 4.2$ and 13.6 Hz, 1 H), 7.78 – 7.58 (m, 2 H), 7.47 – 7.30 (m, 1 H), 4.21 – 3.94 (m, 4 H), 1.38 – 1.21 (m, 6 H), 0.31 – 0.18 (m, 9 H); ^{13}C NMR (126 MHz, CD_2Cl_2 , RT, δ in ppm) 135.95, 135.62, 135.59, 135.46, 135.39, 135.31, 134.77, 134.68, 134.10, 133.94, 132.33, 132.25, 132.15, 132.08, 131.76, 131.68, 130.65, 130.59, 130.52, 130.42, 130.27, 129.08, 128.92, 128.86, 128.79, 124.11, 123.98, 123.14, 122.98, 103.96, 96.05, 78.75, 62.75, 62.70, 62.60, 62.55, 16.51, 16.46, -0.15; ^{31}P NMR (202 MHz, CD_2Cl_2 , RT, δ in ppm) 16.86 (s); EA found 58.01 % C, 5.83 % H – calculated 58.04 % C, 7.47 % H, 15.46 % O, 9.98 % P; 9.05 % Si.

6.6.6 Diethyl 3-ethynylphenylphosphonate



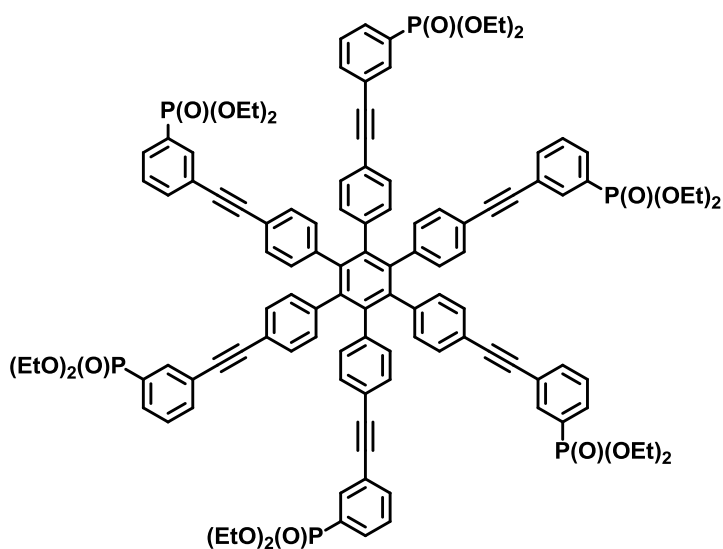
56

Diethyl 3-[(trimethylsilyl)ethynyl]phenylphosphonate (**55**) (1.0 g, 3.22 mmol) was diluted in 10 ml of dry THF. 6.5 ml of a 1 M TBAF solution (6.44 mmol, 2 eq) were added and the contents were allowed to react during 15 min at RT. The dark blue/brown solution was then dried under vacuum and the crude product purified by

column chromatography on silica gel (ethyl acetate) to give the desired product as a yellow oil in 91 % yield (698 mg). MS (FD, 8 kV) $m/z = 238.0$ g/mol - calculated: 238.22 g/mol for $C_{12}H_{15}O_3P$; 1H NMR (250 MHz, CD_2Cl_2 , RT, δ in ppm) 8.02 – 7.85 (m, 1 H), 7.85 – 7.61 (m, 2 H), 7.51 – 7.27 (m, 1 H), 4.24 – 3.93 (m, 4 H), 3.23 (s, 1 H), 1.30 (td, $J = 0.4, 7.1, 6$ H); ^{13}C NMR (126 MHz, CD_2Cl_2 , RT, δ in ppm) 135.93, 135.91, 135.61, 135.59, 135.54, 135.45, 134.76, 134.68, 132.15, 132.07, 131.10, 130.65, 130.63, 130.58, 130.51, 129.15, 128.99, 128.86, 123.13, 123.04, 122.97, 122.91, 82.68, 78.71, 62.73, 62.68, 62.62, 62.57, 16.50, 16.45; ^{31}P NMR (202 MHz, CD_2Cl_2 , RT, δ in ppm) 16.61 (s).

6.6.7 Hexakis[*p*-(*m*-diethylphosphonatophenylethynyl)phenyl]benzene

benzene

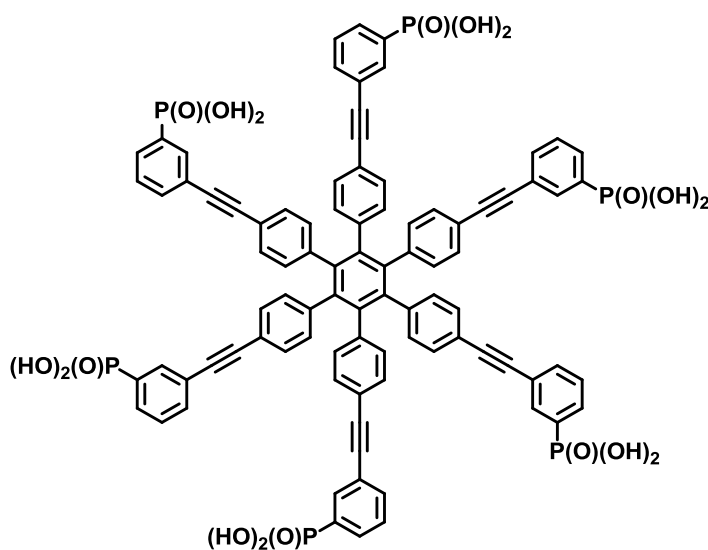


60

50 mg of hexaiodohexaphenylbenzene (**57**) (0.03876 mmol), 92.3 mg of diethyl 3-ethynylphenylphosphonate (**59**) (0.3876 mmol, 10 eq) and 4.4 mg CuI (0.0232 mmol, 60 mol %) were dissolved in 10 ml of dry toluene. 10 ml of NEt_3 were added and the mixture was degassed with Ar during 20 min. Afterwards 13.44 mg (0.0116 mmol, 30 mol %) of tetrakis(triphenylphosphine)palladium(0) were added and the mixture was stirred during 12 h at 60 °C. The solution was neutralized with a diluted HCl solution. The organic layer was dried over $MgSO_4$ and dried under reduced pressure. The crude product was purified by column chromatography on silica gel (ethyl acetate – MeOH

7:3) to give the desired product as a yellow oil in 50 % yield (38 mg). ^1H NMR (250 MHz, CD_2Cl_2 , RT, δ in ppm) 7.77 (d, $J = 13.7$ Hz, 6 H), 7.67 – 7.48 (m, 12 H), 7.34 (d, $J = 4.2$ Hz, 6 H), 7.07 (d, $J = 8.3$ Hz, 12 H), 6.83 (d, $J = 8.3$ Hz, 12 H), 3.97 (dq, $J = 7.1$ and 14.0 Hz, 24 H), 1.18 (dd, $J = 5.2$ and 12.2 Hz, 36 H); ^{13}C NMR (75 MHz, CD_2Cl_2 , RT, δ in ppm) 141.10, 140.52, 135.48, 135.18, 135.05, 132.01, 130.93, 129.24, 129.03, 120.81, 90.76, 88.51, 62.83, 62.76, 16.74, 16.65; ^{31}P NMR (202 MHz, CD_2Cl_2 , RT, δ in ppm) 16.85 (s).

6.6.8 Hexakis[*p*-(*m*-phosphonatophenylethynyl)phenyl]benzene

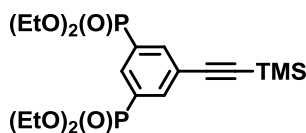


61

Hexakis[*p*-(*m*-diethylphosphonatophenylethynyl)phenyl]benzene (**60**) (100 mg, 0.051 mmol) was treated with trimethylsilylbromide (0.18 ml, 0.12 g, 1.23 mmol) in 10 ml of DCM for 48 h. Then, DCM was evaporated and the product of this first step dried under vacuum. The product of the first step was treated with MeOH (100 ml) for another 48 h. 76 mg (92 % yield) of a white powder were obtained. ^1H NMR (500 MHz, DMSO, RT, δ in ppm) 7.64 (dd, $J = 45.9$ and 103.2 Hz, 36 H), 7.18 (s, 6 H), 7.01 (s, 6 H); ^{13}C NMR (75 MHz, DMSO, RT, δ in ppm) 140.51, 139.49, 136.26, 133.75, 131.57, 130.45, 128.94, 127.12, 122.22, 119.68, 90.05, 89.08; ^{31}P NMR (202 MHz, DMSO, RT, δ in ppm) 11.73 (s); EA found 65.91 % C, 3.57 % H – calculated 66.92 % C, 3.74 % H, 17.83 % O, 11.51 % P.

6.6.9 Tetraethyl 5-[(trimethylsilyl)ethynyl]-1,3-phenylene

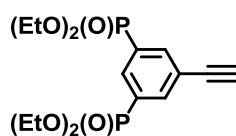
diphosphonate



62

1.0 g of [(3,5-dibromophenyl)ethynyl]trimethylsilane (**47**) (3.01 mmol) and 131.6 mg of NiBr₂ (0.60 mmol, 20 mol %) were dissolved in 20 ml mesitylene and stirred under Ar. The mixture was heated up to 160 °C and then 1.55 ml of triethyl phosphite (1.50 g, 9.03 mmol) were added dropwise. The reaction mixture was let during 12 h at 160 °C under Ar. After cooling to RT, the filtrate was evaporated to give a yellowish oil. The crude product was purified by column chromatography on silica gel (ethyl acetate – methanol 9:1). 955 mg (71 %) of a yellow oil was obtained. MS (FD, 8 kV) m/z = 445.4 g/mol - calculated: 446.49 g/mol for C₁₉H₃₂O₆P₂Si; ¹H NMR (250 MHz, CD₂Cl₂, RT, δ in ppm) 8.09 (dd, J = 5.5 and 6.9 Hz, 1 H), 8.07 – 7.95 (m, 2 H), 4.21 – 3.97 (m, 8 H), 1.36 – 1.21 (m, 12 H), 0.29 – 0.19 (m, 9 H); ¹³C NMR (126 MHz, CD₂Cl₂, RT, δ in ppm) 138.61, 138.55, 138.53, 138.50, 138.44, 134.32, 134.24, 134.16, 131.37, 131.26, 129.87, 129.76, 124.72, 124.59, 124.47, 102.85, 97.67, 62.90, 62.86, 62.84, 62.81, 62.77, 62.61, 16.55, 16.51, 16.49, 16.46, 16.42, 16.31, 16.26, - 0.25; ³¹P NMR (202 MHz, CD₂Cl₂, RT, δ in ppm) 15.36 (s).

6.6.10 Tetraethyl 5-ethynyl-1,3-phenylenediphosphonate



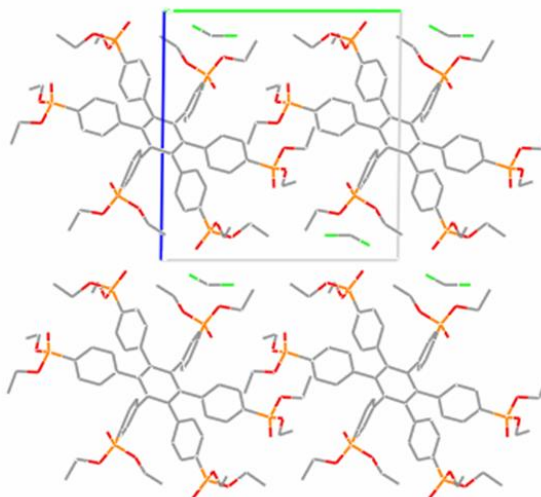
63

Tetraethyl 5-[(trimethylsilyl)ethynyl]-1,3-phenylenediphosphonate (**62**) (0.8 g, 1.8 mmol) was diluted in 10 ml of dry THF. 3.6 ml of a 1 M TBAF solution (3.6 mmol, 2 eq) were added and the contents were allowed to react during 15 min at RT. The dark blue/brown solution was then dried under vacuum and the crude product purified by column chromatography on silica gel (ethyl acetate – methanol 9:1) to give the desired

product as a yellow oil in 83 % yield (557 mg). MS (FD, 8 kV) $m/z = 375.0$ g/mol - calculated: 374.31 g/mol for $C_{16}H_{24}O_6P_2$; 1H NMR (250 MHz, CD_2Cl_2 , RT, δ in ppm) 8.16 (d, $J = 1.3$ Hz, 1 H), 8.07 (ddd, $J = 1.4, 7.3$ and 9.6 , 2 H), 4.28 – 3.94 (m, 8 H), 3.31 (s, 1 H), 1.39 – 1.22 (m, 12 H); ^{13}C NMR (75 MHz, CD_2Cl_2 , RT, δ in ppm) 139.14, 139.05, 139.00, 138.95, 138.86, 135.07, 134.94, 134.80, 132.36, 132.18, 129.86, 129.68, 124.01, 123.80, 123.58, 81.99, 80.21, 63.18, 63.14, 63.10, 16.75, 16.71, 16.67; ^{31}P NMR (202 MHz, CD_2Cl_2 , RT, δ in ppm) 15.11 (s).

6.7 Crystal Structures

6.7.1 Hexakis(*p*-diethylphosphonatophenyl)benzene (3)



$C_{68}H_{88}Cl_4O_{18}P_6$

Space group: $P\bar{1}$ triclinic

Cell lengths: $a = 7.9859(2)$ Å; $b = 14.8979(5)$ Å and $c = 15.7927(4)$ Å

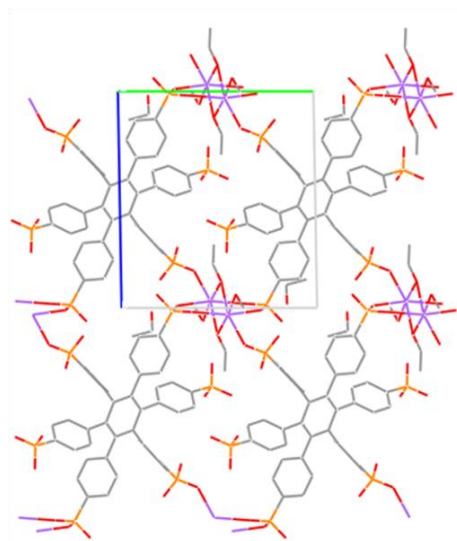
Cell angles: $\alpha = 90.7281(12)$ °; $\beta = 96.1445(17)$ ° and $\gamma = 90.1439(16)$ °

Cell volume: 1867.95

Z: 1 Z': 0

R factor: 5.17 %

6.7.2 Hexakis(*p*-phosphonatophenyl)benzene (4)



$C_{26}H_{33}NaO_{12}P_3$

Space group: P1 triclinic

Cell lengths: $a = 7.9133(2) \text{ \AA}$; $b = 12.7498(4) \text{ \AA}$ and $c = 13.9783(5) \text{ \AA}$

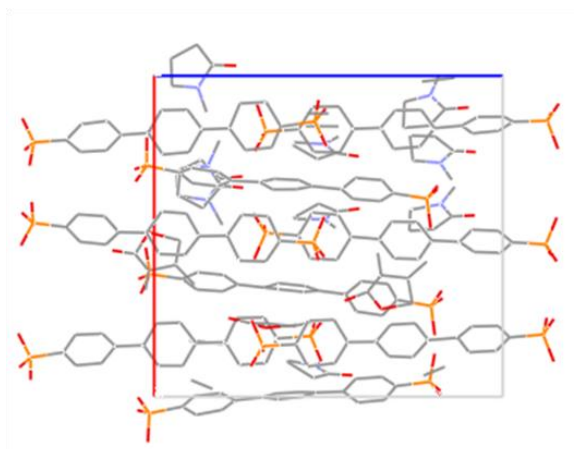
Cell angles: $\alpha = 88.1338(14)^\circ$; $\beta = 84.4238(19)^\circ$ and $\gamma = 80.653(2)^\circ$

Cell volume: 1384.8

Z: 2 Z': 0

R factor: 8.08 %

CCDC 799981.

6.7.3 (*p,p'*-Terphenyl-4,4''-diyl)bisphosphonic acid (9)

$C_{26}H_{18}N_2O_8P_2$

Space group: trigonal $P\bar{3}_1$

Cell lengths: $a = 19.6890(2)$ Å; $b = 19.6890(2)$ Å and $c = 18.5040(2)$ Å

Cell angles: $\alpha = 90^\circ$; $\beta = 90^\circ$ and $\gamma = 120.00^\circ$

Cell volume: 6212.17

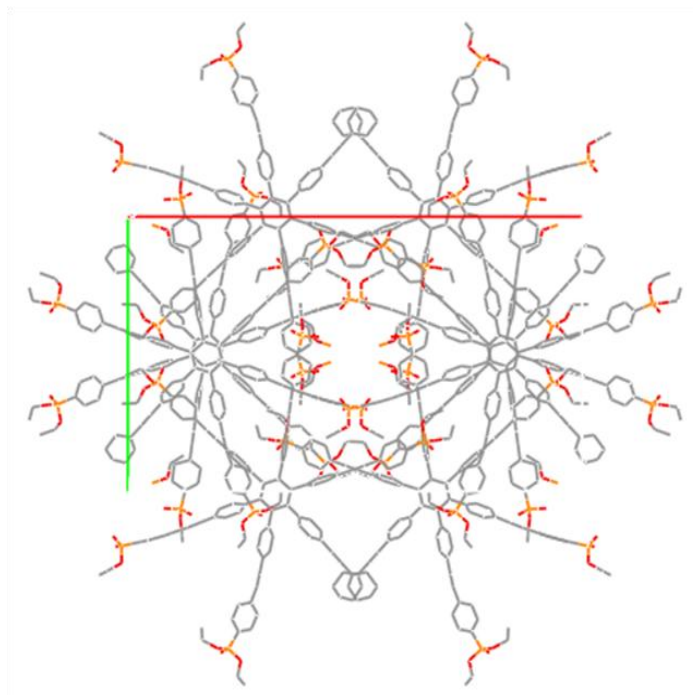
Z: 12 Z': 0

R factor: 21.12 %

CCDC 799980

6.7.4 Hexakis[*p*-(*p*-diethylphosphonatophenylethynyl)

phenyl]benzene (58)



$C_{108}O_{16}P_6$

Space group: monoclinic C 2/c

Cell lengths: $a = 40.259(2) \text{ \AA}$; $b = 24.1310(14) \text{ \AA}$ and $c = 21.4220(13) \text{ \AA}$

Cell angles: $\alpha = 90^\circ$; $\beta = 97.649(3)^\circ$ and $\gamma = 90^\circ$

Cell volume: 20626.1

Z: 8 Z': 0

R factor: 18.74 %

6.8 Phosphonic Acid based Organic-Inorganic Hybrid Materials

The necessary amounts of 1,3,5-tris(*p*-phosphonatophenyl)benzene (**12**) and salt were dissolved separately and mixed together in an Ace Glass pressure tube. The formed suspensions were heated or kept refluxed at the temperatures and times given in Tables 3.1 to 3.5. The precipitated products were filtered off, washed with water followed by centrifugation and Soxhlet extracted during 12 h in THF. Finally, the obtained products were dried under vacuum at 120 °C. Synthetic details and yields are also given in Tables 3.1 to 3.5 for all materials.

6.8.1 Copper based Organic-Inorganic Hybrid Materials

Table 6.1: Synthetic details and yields of copper based organic-inorganic hybrid materials.

	M9-R11	M22-R11	M28-R11	M31-R11
n (12) (mmol)	0.28	0.18	0.14	0.092
m (12) (mg)	150	100	75	50
n (Cu(NO ₃) ₂ ·3H ₂ O) (mmol)	1.65	1.1	0.82	0.55
m (Cu(NO ₃) ₂ ·3H ₂ O) (mg)	399	265	199	133
Solvent	H ₂ O	DMSO	DMSO/H ₂ O	H ₂ O
V (solvent 12) (ml)	3	3	3	3
V (solvent salt) (ml)	3	3	3	3
Time (d)	3	3	3	3
Temperature (°C)	150	150	200	90
Yield (%)	34	13	26	42

6.8.2 Zinc based Organic-Inorganic Hybrid Materials

Table 6.2: Synthetic details and yields of zinc based organic-inorganic hybrid materials.

	M10-R11	M24-R11	M25-R11	M29-R11	M32-R11
n (12) (mmol)	0.27	0.14	0.14	0.14	0.092
m (12) (mg)	150	75	75	75	50
n (ZnCl ₂) (mmol)	1.65	0.82	0.82	0.82	0.55
m (ZnCl ₂) (mg)	225	112	112	112	76
Solvent	H ₂ O	DMSO	DMSO/H ₂ O	DMSO/H ₂ O	H ₂ O
V (solvent 12) (ml)	3	3	3	3	3
V (solvent salt) (ml)	3	3	3	3	3
Time (d)	5	3	3	3	3
Temperature (°C)	95	150	150	200	150
Yield (%)	32	34	27	18	

6.8.3 Aluminum based Organic-Inorganic Hybrid Materials

Table 6.3: Synthetic details and yields of aluminum based organic-inorganic hybrid materials.

	M5-R11	M6-R11	M13-R11*	M14-R11
n (12) (mmol)	0.28	0.28	0.46	0.18
m (12) (mg)	150	150	250	100
n (Al(NO ₃) ₃ ·9H ₂ O) (mmol)	1.1	1.1	1.2	0.73
m (Al(NO ₃) ₃ ·9H ₂ O) (mg)	411	411	282	274
Solvent	DMSO/H ₂ O	DMSO/H ₂ O	DMSO/H ₂ O	H ₂ O
V (solvent 12) (ml)	3	3	5	3
V (solvent salt) (ml)	3	3	5	3
Time (d)	3	3	3	3
Temperature (°C)	150	200	150	90
Yield (%)	15	23	25	12

* Al(NO₃)₃·1H₂O instead of Al(NO₃)₃·9H₂O

6.8.4 Zirconium based Organic-Inorganic Hybrid Materials

Table 6.4: Synthetic details and yields of zirconium based organic-inorganic hybrid materials.

	M11-R11	M12-R11	M15-R11	M16-R11	M17-R11	M26-R11	M30-R11
n (12) (mmol)	0.28	0.28	0.28	0.28	0.28	0.28	0.28
m (12) (mg)	150	150	150	150	150	150	150
n (ZrOCl ₂ ·8H ₂ O) (mmol)	0.82	0.82	0.82	0.82	0.82	0.82	0.82
m (ZrOCl ₂ ·8H ₂ O) (mg)	265	265	265	265	265	265	265
Solvent	DMSO	DMSO	H ₂ O	DMSO/H ₂ O	DMSO/H ₂ O	DMSO/H ₂ O	DMSO
V (solvent 12) (ml)	3	3	3	3	3	3	3
V (solvent salt) (ml)	3	3	3	3	3	3	3
Time (d)	3	3	3	3	3	3	3
Temperature (°C)	90	150	90	90	150	200	200
Yield (%)	7	5	26	46	43	50	79

6.8.5 Tin based Organic-Inorganic Hybrid Materials

Table 6.5: Synthetic details and yields of tin based organic-inorganic hybrid materials.

	M7-R11	M8-R11	M20-R11	M27-R11
n (12) (mmol)	0.28	0.28	0.18	0.18
m (12) (mg)	150	150	100	100
n (SnCl ₄ .5H ₂ O) (mmol)	1.65	1.65	1.1	1.1
m (SnCl ₄ .5H ₂ O) (mg)	578	578	385	385
Solvent	H ₂ O/BuOH	DMSO/H ₂ O	DMSO	DMSO/H ₂ O
V (solvent 12) (ml)	3	3	3	3
V (solvent salt) (ml)	3	3	3	3
Time (d)	3	3	3	3
Temperature (°C)	150	150	150	200
Yield (%)	41	3	60	8

6.10 Bibliography

- [1] H. E. Gottlieb, V. Kotlyar, A. Nudelman, *J. Org. Chem.* **1997**, 62, 7512
- [2] *CIL NMR Solvent Data Chart.*
- [3] L. Greenspan, *J. Res. Natl. Bur. Stand., A Phys. Chem.* **1976**, 81A, 89
- [4] J. Zauhar, A. D. Bandrauk, K. D. Truong, A. Michel, *Synthesis* **1995**, 703
- [5] X. Feng, J. Wu, V. Enkelmann, K. Müllen, *Org. Lett.* **2006**, 8, 1145
- [6] V. R. Reichert, L. J. Mathias, *Macromolecules* **1994**, 27, 7015
- [7] M. V. Vasylyev, D. Astruc, R. Neumann, *Adv. Synth. Catal.* **2005**, 347, 39
- [8] F. M. Menger, L. Shi, *J. Am. Chem. Soc.* **2009**, 131, 6672

7 List of Publications

1. L. Jiménez-García, M. Klapper, K. Müllen. „Proton-Conducting Organic Materials“. PCT/EP2010/003375.
2. L. Jiménez-García, A. Kaltbeitzel, W. Pisula, J. S. Gutmann, M. Klapper, K. Müllen. „Phosphonic Acid-Containing Hexaphenylbenzene - A Crystalline Proton Conductor“. *Angew. Chem. Int. Ed.* **2009**, *48*, 9951 - 9953.
3. L. Jiménez-García, A. Kaltbeitzel, V. Enkelmann, J. S. Gutmann, M. Klapper, K. Müllen. „Organic Proton-Conducting Molecules as Solid State Separator Materials for Fuel Cell Applications“. *Adv. Funct. Mater* **2011**, *accepted*.
4. L. Jiménez-García, V. Enkelmann, J. Shu, R. Graf, M. Klapper, K. Müllen. „Crystalline and Microporous Phosphonated Open-Frameworks“. *In preparation*.

